

¹ A Search in the Two-Photon Final State for
² Evidence of New Particle Production in pp
³ Collisions at $\sqrt{s} = 7$ TeV

⁴ Rachel P. Yohay
University of Virginia
`rpy3y@virginia.edu`

⁵ June 11, 2012

6 Contents

7	1	Introduction	4
8	2	Motivation for Physics Beyond the Standard Model	7
9	2.1	The Standard Model and Electroweak Symmetry Breaking	8
10	2.2	Implications of the Higgs Mechanism	12
11	2.3	Addressing Problems of the Standard Model with Supersymmetry . .	14
12	3	The Supersymmetric Extension to the Standard Model	18
13	3.1	Supermultiplet Representation	18
14	3.2	The Unbroken SUSY Lagrangian	19
15	3.3	Soft SUSY Breaking	25
16	3.4	Gauge-Mediated SUSY Breaking	27
17	3.5	Phenomenology of General Gauge Mediation	30
18	3.6	Experimental Status of SUSY	34
19	4	The Large Hadron Collider	38
20	4.1	Design Considerations and Performance Limitations	39
21	4.2	Beam Injection	42
22	4.3	Magnets and Cryogenics	44
23	4.4	Radiofrequency Cavities	47

²⁴	5 The Compact Muon Solenoid Experiment	49
²⁵	5.1 The Detectors and Their Operating Principles	53
²⁶	5.1.1 Tracking System	53
²⁷	5.1.2 Electromagnetic Calorimeter	62
²⁸	5.1.3 Hadronic Calorimeter	67
²⁹	5.1.4 Muon System	71
³⁰	5.2 Triggering, Data Acquisition, and Data Transfer	76
³¹	5.2.1 Level 1 and High Level Trigger Systems	76
³²	5.2.2 Data Acquisition System	80
³³	5.2.3 Data Processing and Transfer to Computing Centers	83
³⁴	6 Event Selection	86
³⁵	6.1 Object Reconstruction	87
³⁶	6.1.1 Photons	87
³⁷	6.1.2 Electrons	98
³⁸	6.1.3 Jets and Missing Transverse Energy	98
³⁹	6.2 HLT	104
⁴⁰	6.3 Event Quality	107
⁴¹	6.4 Photon Identification Efficiency	110
⁴²	6.4.1 Tag and Probe Method	111
⁴³	6.4.2 Photon Efficiency Scale Factor $\epsilon_e^{\text{data}}/\epsilon_e^{\text{MC}}$	114
⁴⁴	7 Data Analysis	119
⁴⁵	7.1 Modeling the QCD Background	123
⁴⁶	7.1.1 Outline of the Procedure	123
⁴⁷	7.1.2 Reweighting	124
⁴⁸	7.1.3 Normalization	135
⁴⁹	7.2 Modeling the Electroweak Background	135

50	7.3 Errors on the Background Prediction	141
51	7.4 Results	147
52	8 Interpretation of Results in Terms of GMSB Models	153
53	8.1 Simplified Models	153
54	8.2 Upper Limit Calculation and Model Exclusion	155
55	8.2.1 Signal Acceptance \times Efficiency	155
56	8.2.2 CL_s and the Profile Likelihood Test Statistic	159
57	8.3 Cross Section Upper Limits	166
58	8.4 Exclusion Contours	167
59	A Monte Carlo Samples	172
60	A.0.1 List of Samples	172
61	A.0.2 Explanation of Naming Conventions	173

⁶² Chapter 1

⁶³ Introduction

⁶⁴ Although the Standard Model of particle physics has passed every experimental test
⁶⁵ to date, it leaves some very fundamental questions unanswered. Why do particles have
⁶⁶ mass? Why are their masses so different? Up to what energy scale is the Standard
⁶⁷ Model a valid description of nature? Many competing theories have been proposed to
⁶⁸ answer these questions. Establishing the existence of any one of them requires careful
⁶⁹ searches for deviations from Standard Model predictions of particle production or
⁷⁰ decay rates. The stellar performance of the Large Hadron Collider, the 7 TeV center-
⁷¹ of-mass energy proton collider located at the European Organization for Nuclear
⁷² Research (CERN) in Geneva, Switzerland, presents a golden opportunity to do such
⁷³ a search for evidence of new physical phenomena.

⁷⁴ One nearly universal prediction of theories of physics beyond the Standard Model
⁷⁵ is that at a high enough collision energy, heavy particles introduced by the new theory
⁷⁶ will be produced. The heavy particles will then decay, leading to distinctive signatures
⁷⁷ in the hermetic detectors that completely surround the collision points. By comparing
⁷⁸ the observed rate of processes with a particular signature to the expected rate from
⁷⁹ the Standard Model alone, the existence of a particular theory of new physics can be
⁸⁰ confirmed or ruled out.

81 This thesis presents a search for evidence of new heavy particles decaying to a final
82 state with two photons, jets, and a striking momentum imbalance that implies the
83 existence of a new kind of particle that can easily pass through matter without leaving
84 a trace. The signature is motivated by theories that incorporate supersymmetry, a
85 new symmetry of nature that predicts supersymmetric antiparticles to the known
86 particles, just as charge symmetry predicts a positively charged antiparticle for every
87 negatively charged particle and vice versa. Supersymmetry can provide answers to
88 all of the questions posed in the first paragraph. Besides its theoretical motivation,
89 the choice of signature is also driven by the low rate of expected Standard Model
90 background.

91 The search is performed at the Compact Muon Solenoid experiment, a detector ca-
92 pable of identifying photons, electrons, muons, quark jets, τ leptons, and momentum
93 imbalances with high efficiency. The central feature of the experiment is a supercon-
94 ducting solenoid, which, at a length of 13 m and a diameter of 7 m [1], is one of the
95 largest superconducting magnets ever built. By bending the paths of charged parti-
96 cles in the final state under the Lorentz force, the magnetic field produced by the
97 solenoid allows charged particle momenta to be accurately measured. Highly granular
98 calorimeters sit inside the solenoid for the purpose of measuring the energy of neutral
99 final state particles.

100 This thesis is organized as follows. Chapters 2 and 3 motivate the search for physics
101 beyond the Standard Model and the specific signature of two photons, as well as give
102 an overview of the Standard Model and supersymmetric theoretical frameworks. A
103 description is given of the Large Hadron Collider in Chapter 4 and the Compact Muon
104 Solenoid detector in Chapter 5. Chapters 6 and 7 explain in detail the experimental
105 techniques used in the search. Chapter 6 shows how collisions that are likely to have
106 produced a new particle are selected from the enormous amount of data collected, then
107 Chapter 7 shows the data analysis in detail and presents the results. An interpretation

¹⁰⁸ of the results in terms of new physics models is given in Chapter 8. Finally, the thesis
¹⁰⁹ is concluded in Chapter ??.

₁₁₀ **Chapter 2**

₁₁₁ **Motivation for Physics Beyond the
₁₁₂ Standard Model**

₁₁₃ In the 1960s, Sheldon Glashow, Steven Weinberg, and Abdus Salam proposed a math-
₁₁₄ ematical framework that unified the electromagnetic and weak forces at an energy
₁₁₅ scale in the hundreds of GeV/c, as well as a mechanism for breaking the electroweak
₁₁₆ symmetry at low energies [2]. At the same time, Murray Gell-Mann introduced the
₁₁₇ concept of quarks to describe hadron spectroscopy, a concept that would later grow
₁₁₈ into quantum chromodynamics (QCD), the full theory of the strong force [3]. These
₁₁₉ two key developments motivated the unified representation of particle physics as a set
₁₂₀ of fields whose dynamics are invariant under the Standard Model (SM) gauge group

$$SU(3)_C \otimes SU(2)_L \otimes U(1)_Y \quad (2.1)$$

₁₂₁ where $SU(3)_C$ describes the quark QCD interactions, $SU(2)_L$ describes the weak
₁₂₂ interactions among quarks and leptons, and $U(1)_Y$ describes the electromagnetic in-
₁₂₃ teraction.

₁₂₄ The Standard Model has been an extremely successful predictor of particle pro-
₁₂₅ duction and interaction cross-sections and decay rates, as well as of the exact masses

¹²⁶ of the electroweak force carriers. The case for the validity of the Standard Model was
¹²⁷ bolstered by the many precision QCD and electroweak measurements carried out at
¹²⁸ the Large Electron-Positron (LEP) collider, which ran from 1989-2000 at center-of-
¹²⁹ mass energies between 65 and 104 GeV/ c [4]. Figure 2.1 shows some of the highlights
¹³⁰ of the LEP program.

¹³¹ However, there are still deep theoretical problems with the Standard Model,
¹³² stemming from the introduction of the Higgs scalar into the theory to break elec-
¹³³ troweak symmetry [5]. Since the Higgs self-energy diagram is quadratically sensitive
¹³⁴ to the ultraviolet cutoff scale, and assuming that there are no new important en-
¹³⁵ ergy scales of physics between the weak scale ($\mathcal{O}(10^2 \text{ GeV}/c)$) and the Planck scale
¹³⁶ ($\mathcal{O}(10^{19} \text{ GeV}/c)$), in order to be consistent with experimental measurements, this dia-
¹³⁷ gram must include a remarkable 17-orders-of-magnitude cancellation that is otherwise
¹³⁸ poorly motivated [6]. The quest to find new physics at an intermediate energy scale
¹³⁹ between the weak and Planck scales, and thus extend the Standard Model, was the
¹⁴⁰ driving force behind the construction of the Large Hadron Collider (LHC) in 2009,
¹⁴¹ the world's highest energy particle accelerator to date.

¹⁴² Section 2.1 of this chapter gives a brief overview of the Standard Model and
¹⁴³ electroweak symmetry breaking. Sections 2.2 and 2.3 examine the issues raised by
¹⁴⁴ electroweak symmetry breaking that the Standard Model is as yet ill-prepared to
¹⁴⁵ address.

¹⁴⁶ **2.1 The Standard Model and Electroweak Symme- ¹⁴⁷ try Breaking**

¹⁴⁸ All of the elementary matter particles (fermions)—quarks, charged leptons, and neutrinos—
¹⁴⁹ can be put in fundamental representations of the SM gauge groups. The fermion con-
¹⁵⁰ tent of the Standard Model is summarized in Table 2.1. The left-handed doublets are

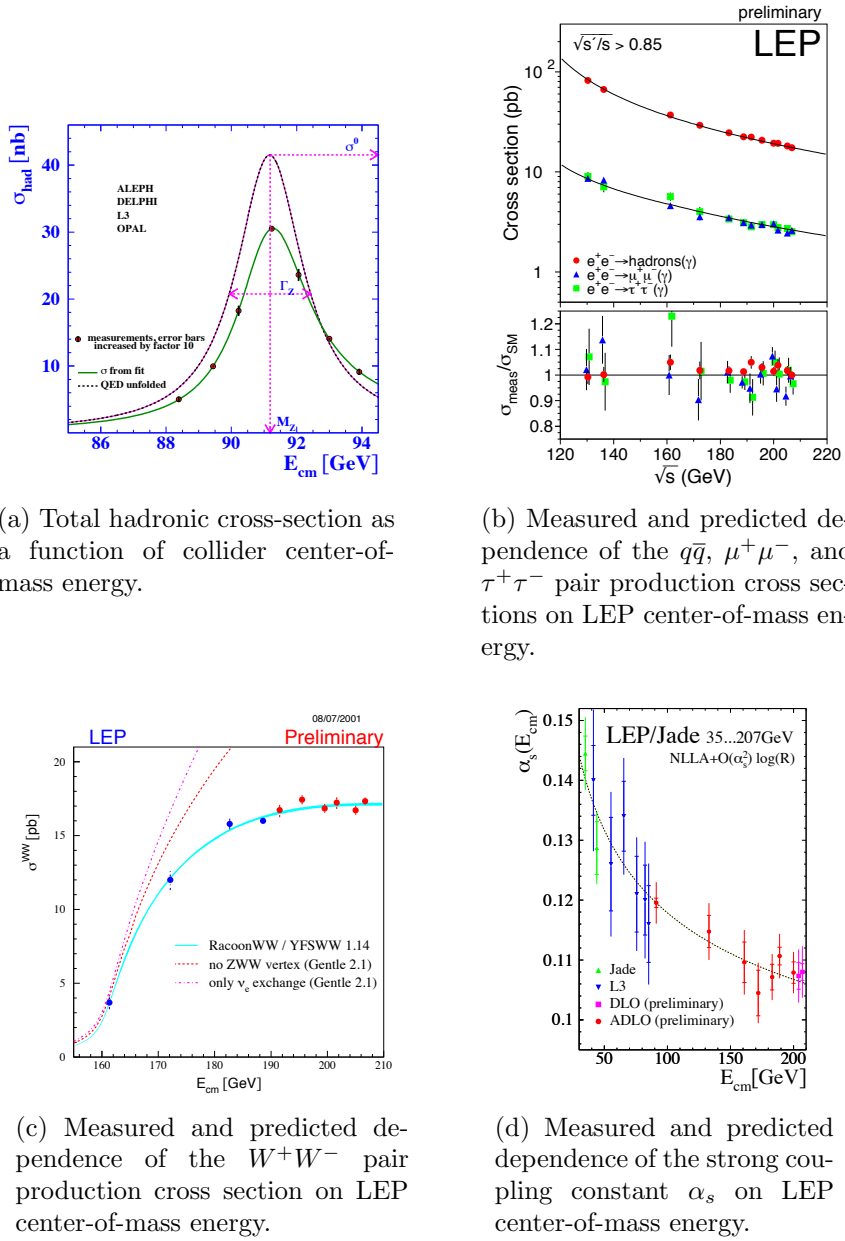


Figure 2.1: Selected LEP measurements demonstrating its contribution to the precise understanding of the Standard Model. Reprinted from ref. [4].

151 analogous to the spinors of non-relativistic quantum mechanics, with the z compo-
 152 nent of “weak isospin” I_3 equal to $+1/2(-1/2)$ for the upper(lower) component of the
 153 doublet.

Table 2.1: Fermion content of the Standard Model.

Type	Notation	Representation under $SU(3)_C \otimes SU(2)_L \otimes U(1)_Y$	Couples to
Left-handed quark doublet	$\begin{pmatrix} u_L \\ d_L \\ c_L \\ s_L \\ b_L \\ t_L \end{pmatrix}$	(3, 2, $\frac{1}{6}$)	g, W, γ
Right-handed up-type quark singlet	$\begin{pmatrix} u_R^\dagger \\ c_R^\dagger \\ b_R^\dagger \end{pmatrix}$	($\bar{3}$, 1, $-\frac{2}{3}$)	g, W, Z, γ
Right-handed down-type quark singlet	$\begin{pmatrix} d_R^\dagger \\ s_R^\dagger \\ t_R^\dagger \end{pmatrix}$	($\bar{3}$, 1, $\frac{1}{3}$)	g, W, Z, γ
Left-handed lepton doublet	$\begin{pmatrix} \bar{\nu}_{eL} \\ e_L \\ \bar{\nu}_{\mu L} \\ \mu_L \\ \bar{\nu}_{\tau L} \\ \tau_L \end{pmatrix}$	(1, 2, $-\frac{1}{2}$)	W, γ
Right-handed charged lepton singlet	$\begin{pmatrix} e_R^\dagger \\ \mu_R^\dagger \\ \tau_R^\dagger \end{pmatrix}$	($\bar{1}$, 1, 1)	W, Z, γ

154 There are two types of weak interactions: flavor-changing charged currents, in
 155 which an up-type and down-type quark or charged lepton and neutrino couple to
 156 a charged W , and neutral currents, in which a fermion couples to another of the
 157 same flavor and to a neutral Z . The charged current interaction is maximally parity
 158 violating—it only couples left-handed fermion doublets. The neutral current inter-
 159 action has a term coupling left-handed doublets and a term coupling right-handed
 160 singlets. There are no mass terms of the form $m_f^2(f_L \bar{f}_R + f_R \bar{f}_L)$ in the electroweak
 161 part of the Lagrangian, as these would violate gauge invariance [7]. The simplest

₁₆₂ way to link the left-handed and right-handed fermions is via a Yukawa interaction
₁₆₃ $-\xi [\bar{f}_R(\phi^\dagger f_L) + (\bar{f}_L \phi) f_R]$ where ϕ is a doublet of complex scalar fields [7].

₁₆₄ The fermion interaction part of the Lagrangian is [7]

$$\begin{aligned} \mathcal{L}_{\text{int}} = & \bar{f}_R i\gamma^\mu (\partial_\mu + i\frac{g_Y}{2} A_\mu Y) f_R \\ & + \bar{f}_L i\gamma^\mu (\partial_\mu + i\frac{g_Y}{2} A_\mu Y + i\frac{g_L}{2} \vec{\tau} \cdot \vec{b}_\mu) f_L \end{aligned} \quad (2.2)$$

₁₆₅ where g_Y and g_L are the electromagnetic and weak coupling constants, respectively;
₁₆₆ Y is the weak hypercharge; A_μ is the EM gauge field; \vec{b}_μ is a three-component
₁₆₇ vector of weak gauge fields; and $\vec{\tau}$ is a three-component vector of the three Pauli
₁₆₈ matrices. Before electroweak symmetry breaking, the three weak gauge fields and the
₁₆₉ one EM gauge field are massless. The three weak gauge fields correspond to the three
₁₇₀ generators (the Pauli matrices) of $SU(2)_L$. The one EM gauge field corresponds to the
₁₇₁ one generator (the real scalar Y) of $U(1)_Y$, where $Y = 2(Q - I_3)$ (Q is electric charge).
₁₇₂ For the $SU(3)_C$ part of the Lagrangian, there are eight massless gauge fields (the
₁₇₃ gluons) corresponding to the eight generators of $SU(3)_C$ (the Gell-Mann matrices).

₁₇₄ To break the electroweak symmetry implicit in the massless gauge bosons, a dou-
₁₇₅ blet of complex scalar fields (the Higgs) is introduced. It has a potential [7]

$$V(\phi^\dagger \phi) = \mu^2 \phi^\dagger \phi + |\lambda| (\phi^\dagger \phi)^2. \quad (2.3)$$

₁₇₆ Since $\mu^2 < 0$, the potential has the shape of a sombrero, as shown in Figure 2.2.
₁₇₇ At the minimum of the potential, the scalar fields are not zero, but have some positive
₁₇₈ vacuum expectation value (VEV) (it can be chosen such that one component is zero
₁₇₉ and the other is $\sqrt{-\mu^2/2|\lambda|}$). Nature spontaneously chooses one of the infinitely many
₁₈₀ vacua along the circle of minimum V in $(\Re[\phi], \Im[\phi])$ space.

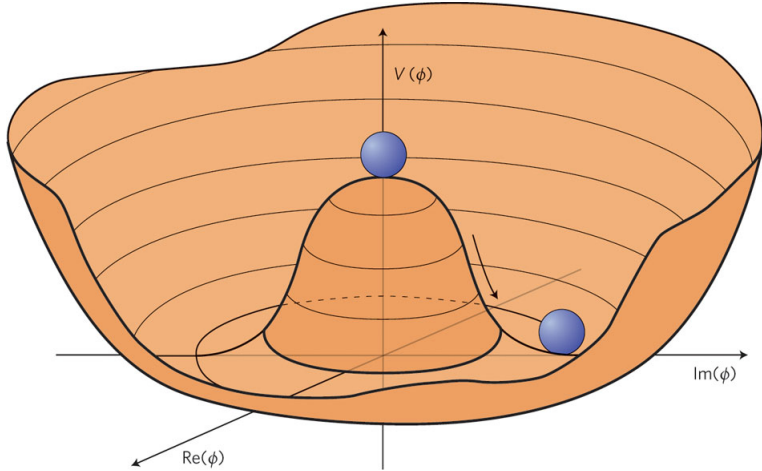


Figure 2.2: Higgs potential (the sombrero) as a function of the real and imaginary parts of the complex scalar field. The movement of the balls shows that the symmetry $\phi = 0$ is spontaneously broken, the stable vacuum state of nature being somewhere along the circle of minimum potential. Reprinted from Fig. 1 of ref. [8].

181 Expanding ϕ about its VEV v in the Lagrangian introduces one massive scalar, the
 182 Higgs, and new mass terms for the gauge bosons. However, the terms with positive
 183 mass are not the original b_1 , b_2 , b_3 , and A (spacetime indices dropped), but the
 184 observable W^\pm and Z^0 . The W^\pm are linear combinations of b_1 and b_2 . The Z^0 is
 185 one of the linear combinations of b_3 and A , the other being the massless photon γ .
 186 After electroweak symmetry breaking (EWSB), the only remaining symmetry of the
 187 vacuum is electric charge, because the value of the electric charge operator acting on
 188 the Higgs VEV is zero. As expected, there is one massless photon in the SM to reflect
 189 this symmetry. The SM fermions can also acquire masses as a by-product of the Higgs
 190 mechanism via Yukawa terms.

191 2.2 Implications of the Higgs Mechanism

192 Before the formulation of the Higgs mechanism, physicists suspected that a heavy
 193 boson mediated the weak force from observations of β decay, but had no way of
 194 putting a mass term into the Lagrangian without breaking gauge symmetry. The

195 Higgs mechanism of EWSB provided a way to generate masses for the $SU(2)_L$ gauge
 196 bosons. Furthermore, it predicted the W and Z masses in terms of g_L , g_Y , and v . g_L
 197 and g_Y could be measured in scattering experiments, and in 1983 the W and Z were
 198 first observed at the Super Proton-Antiproton Synchrotron (Sp \bar{p} S) at the European
 199 Organization for Nuclear Research (CERN) in Geneva, Switzerland [9, 10]. Crucially,
 200 the values of the coupling constants and the gauge boson masses predict that the
 201 Higgs VEV should be 246 GeV, so the Higgs mass should not be too much different
 202 than that if λ is to remain small enough to do perturbation theory [11].

203 The Higgs mechanism raises some interesting questions that cannot be immedi-
 204 ately answered by SM physics. First of all, why should μ^2 be negative? The form of
 205 the Higgs potential given in Eq. 2.3 is about the simplest renormalizable form that
 206 can be written for a scalar field, but the choice of $\mu^2 < 0$ is completely arbitrary.
 207 Second, how can the hierarchy problem be avoided?

208 The Higgs mass squared receives one-loop corrections from all the particles it
 209 couples to; namely, all particles with mass. Because the Higgs is a scalar particle,
 210 one-loop corrections are proportional to Λ_{UV}^2 , where Λ_{UV} is the ultraviolet cutoff
 211 energy of the loop integral. Λ_{UV} can be interpreted as the energy at which the SM
 212 can no longer describe particle physics and non-SM physics takes over. Ideally, Λ_{UV} is
 213 something like the Planck scale. However, taking $\Lambda_{\text{UV}} = M_{\text{Planck}}$ implies that in order
 214 to keep the Higgs mass of order a few hundred GeV, as required by experimental
 215 tests of EWSB, a very large and precise counterterm must be applied at all orders
 216 in perturbation theory to the bare m_H^2 . The quadratic sensitivity of the Higgs mass
 217 to the cutoff scale and the extremely fine-tuned counterterms it necessitates is called
 218 the hierarchy problem.

219 One of the most elegant ways to address these problems is to incorporate *super-*
 220 *symmetry* (SUSY) into the SM. Supersymmetry is new fundamental symmetry of
 221 nature between bosons and fermions, and will be discussed more thoroughly in Chap-

²²² ter 3. The next section just briefly describes how supersymmetry can mitigate some
²²³ of the problems of the Higgs mechanism.

²²⁴ 2.3 Addressing Problems of the Standard Model ²²⁵ with Supersymmetry

²²⁶ As in the ordinary Standard Model, the couplings and masses in supersymmetric
²²⁷ theory can be imposed at the supersymmetric scale and evolved down to the weak
²²⁸ scale by use of renormalization group equations. For many typical supersymmetric
²²⁹ scenarios (like the one shown in Figure 2.3), μ^2 is positive at the supersymmetric
²³⁰ scale but runs negative at the weak scale, leading to precisely the conditions needed
²³¹ for EWSB. This is a consequence of the fact that the evolution of m_H^2 depends on the
²³² top quark Yukawa coupling, which, since the top is very heavy compared to the other
²³³ quarks ($m_t \sim 42m_b$, $m_t \sim 136m_c$ [13]), is large. In some sense, then, supersymmetry
²³⁴ not only provides the conditions for EWSB, but also explains why the top quark must
²³⁵ be so much heavier than the other quarks.

²³⁶ SUSY's greatest strength, however, comes from the way it elegantly solves the
²³⁷ hierarchy problem. The Higgs squared mass corrections from fermion loops take the
²³⁸ form [12]

$$\Delta m_H^2 = -\frac{|\lambda_F|^2}{8\pi^2} \Lambda_{\text{UV}}^2 + \dots \quad (2.4)$$

²³⁹ while the corrections from scalar loops would take the form [12]

$$\Delta m_H^2 = \frac{|\lambda_S|^2}{16\pi^2} \Lambda_{\text{UV}}^2 + \dots \quad (2.5)$$

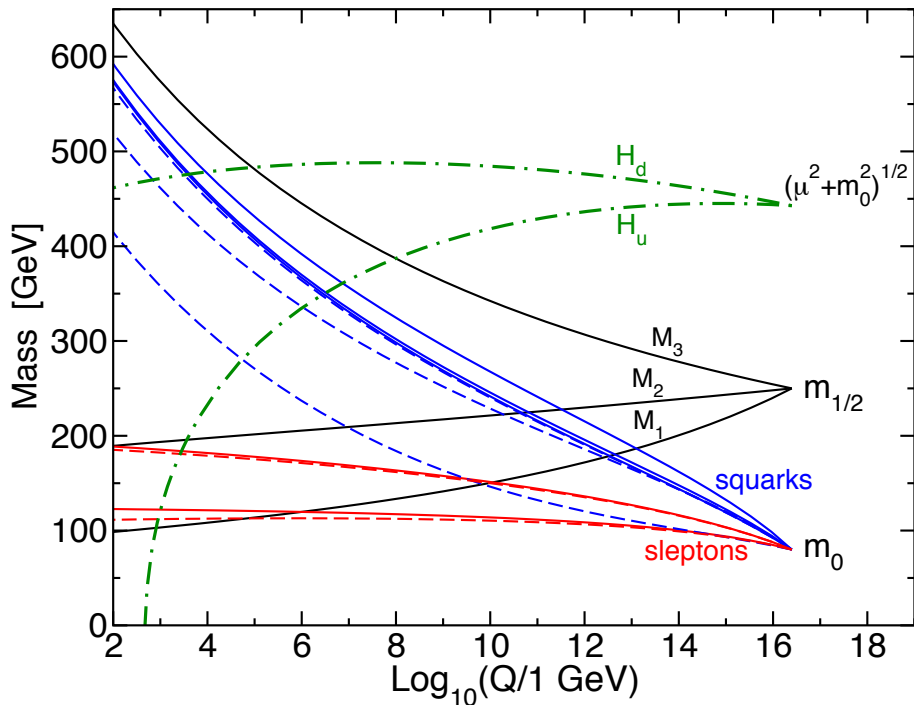


Figure 2.3: Predicted evolution of the free parameters of supersymmetry as a function of renormalization scale for a representative set of SUSY parameters. Note the dash-dotted line marked “ H_u ” that goes negative at ~ 1 TeV; this indicates μ^2 running negative. Reprinted from Fig. 7.4 of ref. [12].

240 where the ellipsis indicates terms proportional to $\ln \Lambda_{\text{UV}}$ that do not pose a prob-
 241 lem for the validity of the SM up to the Planck scale. Since the fermion and scalar
 242 contributions have opposite signs, if each SM fermion were accompanied by two as-
 243 yet-undiscovered scalar particles with $\lambda_S = |\lambda_F|^2$, then the problematic quadratic
 244 terms in Eqs. 2.4 and 2.5 would exactly cancel. This is precisely the foundation of su-
 245 persymmetry: for each fermion, there is a supersymmetric partner boson. This would
 246 remove the hierarchy problem altogether, and is the main reason physicists are eager
 247 to find evidence for the existence of supersymmetry at the LHC.

248 In addition to providing some rationale for the Higgs mechanism, SUSY makes two
 249 other very desirable predictions. The first is that the strong, weak, and electromag-
 250 netic coupling constants will exactly unify at an energy scale of 10^{16} GeV/c, as shown
 251 in Figure 2.4. Unification of forces is not required by any experimental consideration,
 252 but is an elegant result nonetheless. The second prediction of SUSY, explained in
 253 more detail in Sec. 3.5, is the existence of a new stable particle, undiscovered as of
 254 yet because of its extremely feeble interactions with ordinary matter. This particle
 255 might be what astronomers have observed as dark matter.

256 Everything discussed in this chapter assumes that the Higgs mechanism is indeed
 257 the origin of EWSB. It is important to remember that no experimental observation
 258 to date unequivocally establishes the existence of the Higgs scalar, although small
 259 excesses recently unearthed in the LHC data [14, 15] tentatively suggest a Higgs mass
 260 of ~ 125 GeV. The discovery of the Higgs scalar would place an important restriction
 261 on the types of SUSY theories that might be consistent with experiment. Operating at
 262 a 7 TeV center-of-mass energy, the LHC can thoroughly probe the scale of EWSB and
 263 the expected mass range of the Higgs, as well as the mass range of supersymmetric
 264 particles if SUSY is the solution to the hierarchy problem. Therefore, discovering or
 265 excluding SUSY is a key goal of the LHC physics program. The next chapter discusses
 266 SUSY more formally and shows what phenomenological consequences it entails.

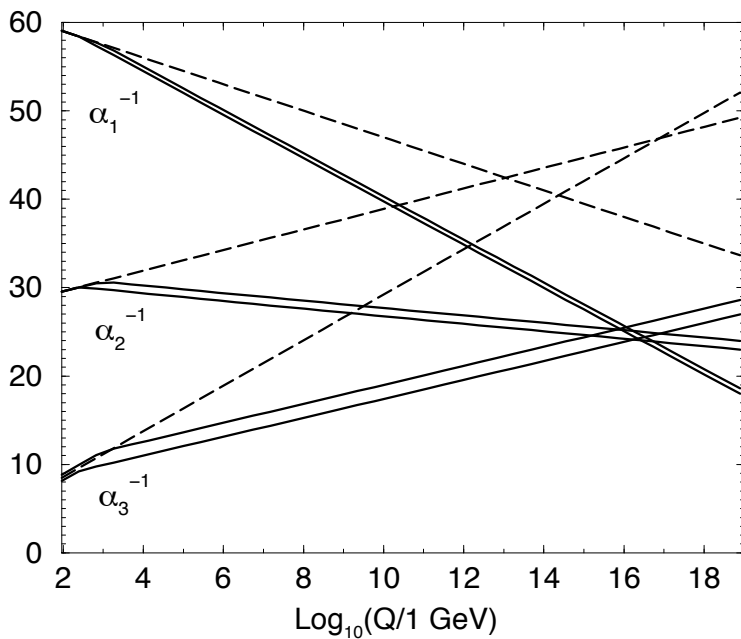


Figure 2.4: Inverse gauge couplings as a function of renormalization scale for the Standard Model assumption (dotted lines) and the SUSY assumption (solid lines; the double lines represent variations in SUSY parameters and in $\alpha_S(m_Z)$). Reprinted from Fig. 5.8 of ref. [12].

²⁶⁷ Chapter 3

²⁶⁸ **The Supersymmetric Extension to ²⁶⁹ the Standard Model**

²⁷⁰ The following introduction to SUSY focuses primarily on the aspects of the formalism that are relevant to phenomenology. In particular, most of the details of SUSY breaking (about which there is little theoretical consensus) are omitted, except where they are relevant to experiment. The notation is similar to that used in refs. [6] and [12], and much of the information presented is culled from those references.

²⁷⁵ **3.1 Supermultiplet Representation**

²⁷⁶ The Standard Model is extended to include supersymmetry by the introduction of a supersymmetry transformation that takes fermionic states to bosonic states and vice versa. The resulting model is called the *minimal supersymmetric Standard Model* (MSSM). In analogy with the known symmetries of the Standard Model, the SUSY transformation has associated generators that obey defining commutation and anti-commutation relations, and a fundamental representation. All SM particles and their superpartners fall into one of two *supermultiplet* representations. Using the property that

$$n_F = n_B, \quad (3.1)$$

284 where n_F is the number of fermionic degrees of freedom per supermultiplet and n_B is
 285 the number of bosonic degrees of freedom, the two types of supermultiplets are

- 286 1. *Chiral supermultiplets*: one Weyl fermion (two helicity states $\Rightarrow n_F = 2$) and
 287 one complex scalar field (with two real components $\Rightarrow n_B = 2$)
- 288 2. *Gauge supermultiplets*: One spin-1 vector boson (two helicity states $\Rightarrow n_B = 2$)
 289 and one Weyl fermion (two helicity states $\Rightarrow n_F = 2$)

290 In the gauge supermultiplet, the vector boson is assumed massless (i.e. before
 291 EWSB generates a mass for it). Since the superpartners to the SM particles have not
 292 yet been discovered, they must be significantly heavier than their SM counterparts.
 293 Unbroken SUSY predicts that the SM particles and their superpartners must have
 294 exactly the same mass, so ultimately a mechanism for SUSY breaking must be intro-
 295 duced to generate masses for the superpartners (see Sec. 3.3). Tables 3.1 and 3.2 show
 296 the chiral and gauge supermultiplets of the MSSM, respectively. Note that the scalar
 297 partners to the SM fermions are denoted by placing an “s” in front of their names,
 298 while the chiral fermion partners to the SM gauge bosons are denoted by appending
 299 “ino” to their names.

300 3.2 The Unbroken SUSY Lagrangian

301 The first piece of the full unbroken SUSY Lagrangian density consists of the kinetic
 302 and interacting terms related to the chiral supermultiplets. As explained in Sec. 3.1,
 303 a chiral supermultiplet consists of a Weyl fermion ψ (the ordinary fermion) and a
 304 complex scalar ϕ (the sfermion). For a collection of such chiral supermultiplets, the
 305 Lagrangian is

Table 3.1: Chiral supermultiplets of the supersymmetric Standard Model. Adapted from Table 1.1 of ref. [12].

Type of supermultiplet	Notation	Spin-0 component	Spin-1/2 component	Representation under $SU(3)_C \otimes SU(2)_L \otimes U(1)_Y$
Left-handed quark/squark doublet ($\times 3$ families)	Q	$(\tilde{u}_L \tilde{d}_L)$	$(u_L d_L)$	$(\mathbf{3}, \mathbf{2}, \frac{1}{6})$
Right-handed up-type quark/squark singlet ($\times 3$ families)	\bar{u}	\tilde{u}_R^*	u_R^\dagger	$(\bar{\mathbf{3}}, \mathbf{1}, -\frac{2}{3})$
Right-handed down-type quark/squark singlet ($\times 3$ families)	\bar{d}	\tilde{d}_R^*	d_R^\dagger	$(\bar{\mathbf{3}}, \mathbf{1}, \frac{1}{3})$
Left-handed lepton/slepton doublet ($\times 3$ families)	L	$(\tilde{\nu}_{eL} \tilde{e}_L)$	$(\bar{\nu}_{eL} e_L)$	$(\mathbf{1}, \mathbf{2}, -\frac{1}{2})$
Right-handed lepton/slepton singlet ($\times 3$ families)	\bar{e}	\tilde{e}_R^*	e_R^\dagger	$(\bar{\mathbf{1}}, \mathbf{1}, 1)$
Up-type Higgs/Higgsino doublet	H_u	$(H_u^+ H_u^0)$	$(\tilde{H}_u^+ \tilde{H}_u^0)$	$(\mathbf{1}, \mathbf{2}, \frac{1}{2})$
Down-type Higgs/Higgsino doublet	H_d	$(H_d^0 H_d^-)$	$(\tilde{H}_d^0 \tilde{H}_d^-)$	$(\mathbf{1}, \mathbf{2}, -\frac{1}{2})$

Table 3.2: Gauge supermultiplets of the supersymmetric Standard Model. Adapted from Table 1.2 of ref. [12].

Type of supermultiplet	Spin-1/2 component	Spin-1 component	Representation under $SU(3)_C \otimes SU(2)_L \otimes U(1)_Y$
Gluon/gluino	\tilde{g}	g	$(\mathbf{8}, \mathbf{1}, 0)$
W/wino	$\tilde{W}^\pm \tilde{W}^0$	$W^\pm W^0$	$(\mathbf{1}, \mathbf{3}, 0)$
B/bino	\tilde{B}^0	B^0	$(\mathbf{1}, \mathbf{1}, 0)$

$$\begin{aligned}\mathcal{L}_{\text{chiral}} = & -\partial^\mu \phi^{*i} \partial_\mu \phi_i - V_{\text{chiral}}(\phi, \phi^*) - i\psi^{\dagger i} \bar{\sigma}^\mu \partial_\mu \psi_i - \frac{1}{2} M^{ij} \psi_i \psi_j \\ & - \frac{1}{2} M_{ij}^* \psi^{\dagger i} \psi^{\dagger j} - \frac{1}{2} y^{ijk} \phi_i \psi_j \psi_k - \frac{1}{2} y_{ijk}^* \phi^{*i} \psi^{\dagger j} \psi^{\dagger k}\end{aligned}\quad (3.2)$$

where i runs over all supermultiplets in Table 3.1, $\bar{\sigma}^\mu$ are $-1 \times$ the Pauli matrices (except for $\sigma^0 = \bar{\sigma}^0$), M^{ij} is a mass matrix for the fermions, y^{ijk} are the Yukawa couplings between one scalar and two spinor fields, and $V_{\text{chiral}}(\phi, \phi^*)$ is the scalar potential

$$\begin{aligned}V_{\text{chiral}}(\phi, \phi^*) = & M_{ik}^* M^{kj} \phi^{*i} \phi_j + \frac{1}{2} M^{in} y_{jkn}^* \phi_i \phi^{*j} \phi^{*k} \\ & + \frac{1}{2} M_{in}^* y^{jkn} \phi^{*i} \phi_j \phi_k + \frac{1}{4} y^{ijn} y_{klm}^* \phi_i \phi_j \phi^{*k} \phi^{*l}.\end{aligned}\quad (3.3)$$

The Lagrangian can also be written as the kinetic terms plus derivatives of the *superpotential* W :

$$\begin{aligned}\mathcal{L}_{\text{chiral}} = & -\partial^\mu \phi^{*i} \partial_\mu \phi_i - i\psi^{\dagger i} \bar{\sigma}^\mu \partial_\mu \psi_i \\ & - \frac{1}{2} \left(\frac{\delta^2 W}{\delta \phi^i \delta \phi^j} \psi_i \psi_j + \frac{\delta^2 W^*}{\delta \phi_i \delta \phi_j} \psi^{\dagger i} \psi^{\dagger j} \right) - \frac{\delta W}{\delta \phi^i} \frac{\delta W^*}{\delta \phi_i}\end{aligned}\quad (3.4)$$

where

$$W = M^{ij} \phi_i \phi_j + \frac{1}{6} y^{ijk} \phi_i \phi_j \phi_k. \quad (3.5)$$

The second part of the Lagrangian involves the gauge supermultiplets. In terms of the spin-1 ordinary gauge boson A_μ^a and the spin-1/2 Weyl spinor gaugino λ^a of

³¹⁵ the gauge supermultiplet, where a runs over the number of generators for the SM
³¹⁶ subgroup (i.e. 1-8 for $SU(3)_C$, 1-3 for $SU(2)_L$, and 1 for $U(1)_Y$), this part of the
³¹⁷ Lagrangian is

$$\mathcal{L}_{\text{gauge}} = -\frac{1}{4}F_{\mu\nu}^a F^{\mu\nu a} - i\lambda^{\dagger a}\bar{\sigma}^\mu D_\mu \lambda^a + \frac{1}{2}D^a D^a \quad (3.6)$$

³¹⁸ where

$$F_{\mu\nu}^a = \partial_\mu A_\nu^a - \partial_\nu A_\mu^a + g f^{abc} A_\mu^b A_\nu^c \quad (3.7)$$

³¹⁹ (g is the coupling constant and f^{abc} are the structure constants for the particular SM
³²⁰ gauge group),

$$D_\mu \lambda^a = \partial_\mu \lambda^a + g f^{abc} A_\mu^b \lambda^c, \quad (3.8)$$

³²¹ and D^a is an auxiliary field that does not propagate (in the literature, it is used as a
³²² bookkeeping tool and can be removed via its algebraic equation of motion).

³²³ To build a fully supersymmetric and gauge-invariant Lagrangian, the ordinary
³²⁴ derivatives in $\mathcal{L}_{\text{chiral}}$ (Eq. 3.2) must be replaced by covariant derivatives

$$D_\mu \phi_i = \partial_\mu \phi_i - ig A_\mu^a (T^a \phi)_i \quad (3.9)$$

$$D_\mu \phi^{*i} = \partial_\mu \phi^{*i} + ig A_\mu^a (\phi^* T^a)^i \quad (3.10)$$

$$D_\mu \psi_i = \partial_\mu \psi_i - ig A_\mu^a (T^a \psi)_i. \quad (3.11)$$

³²⁵ This leads to the full Lagrangian

$$\begin{aligned}
\mathcal{L} &= \mathcal{L}_{\text{chiral}} + \mathcal{L}_{\text{gauge}} \\
&\quad - \sqrt{2}g(\phi^{*i}T^a\psi_i)\lambda^a - \sqrt{2}g\lambda^{\dagger a}(\psi^{\dagger i}T^a\phi_i) + g(\phi^{*i}T^a\phi_i)D^a \\
&= -\partial^\mu\phi^{*i}\partial_\mu\phi_i - i\psi^{\dagger i}\bar{\sigma}^\mu\partial_\mu\psi_i + ig\partial^\mu\phi^{*i}A_\mu^a(T^a\phi)_i - ig\partial_\mu\phi_iA^{\mu a}(\phi^*T^a)^i \\
&\quad - g^2A^{\mu a}(\phi^*T^a)^iA_\mu^a(T^a\phi)_i - g\psi^{\dagger i}\bar{\sigma}^\mu A_\mu^a(T^a\psi)_i - V_{\text{chiral}}(\phi, \phi^*) \\
&\quad - \frac{1}{2}M^{ij}\psi_i\psi_j - \frac{1}{2}M_{ij}^*\psi^{\dagger i}\psi^{\dagger j} - \frac{1}{2}y^{ijk}\phi_i\psi_j\psi_k - \frac{1}{2}y_{ijk}^*\phi^{*i}\psi^{\dagger j}\psi^{\dagger k} \\
&\quad - \frac{1}{4}F_{\mu\nu}^aF^{\mu\nu a} - i\lambda^{\dagger a}\bar{\sigma}^\mu\partial_\mu\lambda^a - ig\lambda^{\dagger a}\bar{\sigma}^\mu f^{abc}A_\mu^b\lambda^c + \frac{1}{2}D^aD^a \\
&\quad - \sqrt{2}g(\phi^{*i}T^a\psi_i)\lambda^a - \sqrt{2}g\lambda^{\dagger a}(\psi^{\dagger i}T^a\phi_i) + g(\phi^{*i}T^a\phi_i)D^a. \tag{3.12}
\end{aligned}$$

³²⁶ Writing out $F_{\mu\nu}^a$ and $V_{\text{chiral}}(\phi, \phi^*)$ explicitly combining the D^a terms using the equation

³²⁷ of motion $D^a = -g\phi^{*i}T^a\phi_i$, and rearranging some terms, the final unbroken SUSY

³²⁸ Lagrangian is

$$\begin{aligned}
\mathcal{L} = & -\partial^\mu \phi^{*i} \partial_\mu \phi_i - i\psi^{\dagger i} \bar{\sigma}^\mu \partial_\mu \psi_i \\
& - \frac{1}{4} (\partial_\mu A_\nu^a - \partial_\nu A_\mu^a) (\partial^\mu A^{\nu a} - \partial^\nu A^{\mu a}) - i\lambda^{\dagger a} \bar{\sigma}^\mu \partial_\mu \lambda^a \\
& - M_{ik}^* M^{kj} \phi^{*i} \phi_j - \frac{1}{2} M^{ij} \psi_i \psi_j - \frac{1}{2} M_{ij}^* \psi^{\dagger i} \psi^{\dagger j} \\
& + ig \partial^\mu \phi^{*i} A_\mu^a (T^a \phi)_i - ig \partial_\mu \phi_i A^{\mu a} (\phi^* T^a)^i - g \psi^{\dagger i} \bar{\sigma}^\mu A_\mu^a (T^a \psi)_i \\
& - ig \lambda^{\dagger a} \bar{\sigma}^\mu f^{abc} A_\mu^b \lambda^c \\
& - \frac{1}{4} g f^{abc} [(\partial_\mu A_\nu^a - \partial_\nu A_\mu^a) A^{\mu b} A^{\nu c} + A_\mu^b A_\nu^c (\partial^\mu A^{\nu a} - \partial^\nu A^{\mu a})] \\
& - \frac{1}{2} M_{in}^* y^{jkn} \phi^{*i} \phi_j \phi_k - \frac{1}{2} M^{in} y_{jkn}^* \phi_i \phi^{*j} \phi^{*k} \\
& - \frac{1}{2} y^{ijk} \phi_i \psi_j \psi_k - \frac{1}{2} y_{ijk}^* \phi^{*i} \psi^{\dagger j} \psi^{\dagger k} \\
& - \sqrt{2} g (\phi^{*i} T^a \psi_i) \lambda^a - \sqrt{2} g \lambda^{\dagger a} (\psi^{\dagger i} T^a \phi_i) \\
& - g^2 A^{\mu a} (\phi^* T^a)^i A_\mu^a (T^a \phi)_i - \frac{1}{4} g^2 f^{abc} A_\mu^b A_\nu^c f^{abc} A^{\mu b} A^{\nu c} \\
& - \frac{1}{4} y^{ijn} y_{kln}^* \phi_i \phi_j \phi^{*k} \phi^{*l} - \frac{1}{2} g^2 (\phi^{*i} T^a \phi_i)^2.
\end{aligned} \tag{3.13}$$

329 The above Lagrangian applies to chiral supermultiplets interacting with one kind
 330 of gauge supermultiplet (i.e. one SM gauge group). In the general case, there are
 331 additional terms corresponding to interactions with all three SM gauge groups.

332 The following list gives a description of the terms in Eq. 3.13:

- 333 • First two lines: kinetic terms for the four types of fields ϕ_i , ψ_i , A_μ^a , and λ^a
- 334 • Third line: mass terms for the ϕ_i and ψ_i (see Figs. 3.1(a) and 3.1(b))
- 335 • Fourth and fifth lines: cubic couplings in which ϕ_i , ψ_i , or λ^a radiates an A_μ^a (see
 336 Figs. 3.1(c), 3.1(d), and 3.1(e))
- 337 • Sixth line: triple gauge boson couplings (see Fig. 3.1(f))
- 338 • Seventh line: triple sfermion couplings (see Fig. 3.1(g))

- 339 • Eighth line: cubic couplings in which ψ_i radiates a ϕ_i (see Fig. 3.1(h))
- 340 • Ninth line: ϕ_i - ψ_i - λ^a vertices (see Fig. 3.1(i))
- 341 • 10th line: A_μ^a - A_μ^a - ϕ_i - ϕ_i and quadruple gauge boson couplings (see Figs. 3.1(j)
342 and 3.1(k))
- 343 • 11th line: ϕ_i^4 vertices (see Figs. 3.1(l) and 3.1(m))

344 3.3 Soft SUSY Breaking

345 Since quadratic divergences in sfermion masses vanish to all orders in perturbation
 346 theory in plain unbroken SUSY [12] due to the presence of gauge and Yukawa inter-
 347 actions with the necessary relationships between coupling constants, it is desirable
 348 that the terms that break SUSY not disturb this property. In addition, SUSY should
 349 be broken spontaneously, as electroweak symmetry is broken in the Standard Model,
 350 so that it is only made manifest at high energies. To satisfy these constraints, SUSY-
 351 breaking terms are simply added to the unbroken SUSY Lagrangian in Eq. 3.13 such
 352 that $\mathcal{L}_{\text{total}} = \mathcal{L}_{\text{unbroken}} + \mathcal{L}_{\text{breaking}}$. The coefficients of terms in $\mathcal{L}_{\text{breaking}}$ must have
 353 positive mass dimension in order not to contribute quadratically divergent loop cor-
 354 rections to the scalar masses (like the Higgs mass).¹ This form of SUSY breaking is
 355 called *soft*, and all coefficients of soft SUSY breaking terms are expected to be of
 356 order m_{soft} or m_{soft}^2 .

¹This point can be argued via dimensional analysis. Radiative corrections take the form Δm_S^2 , where m_S is the mass of the scalar particle in question. The dimensions of Δm_S^2 are mass². Δm_S^2 is proportional to some coupling constant or mass coefficient k multiplied by a function of Λ_{UV} , the high energy cutoff scale. The function of Λ_{UV} is determined by a loop integral, and thus typically takes the form Λ_{UV}^2 (quadratically divergent) or $\ln \frac{\Lambda_{\text{UV}}}{m_{\text{low}}}$ (logarithmically divergent, where m_{low} is some other lower-mass scale in the problem). Now, if k already contributes at least one power of mass to Δm_S^2 , then the high-energy behavior—the function of Λ_{UV} —can only contribute at most one power of the dimensionful parameter Λ_{UV} . However, there are typically no loop integrals that diverge linearly in Λ_{UV} , so by forcing k to have positive mass dimension, the form of the radiative corrections contributed by SUSY-breaking terms is limited to $\Delta m_S^2 \sim m_{\text{low}}^2 \ln \frac{\Lambda_{\text{UV}}}{m_{\text{low}}}$. In effect, the possibility of dangerous corrections proportional to Λ_{UV}^2 is excluded by dimensional analysis if the requirement that k contribute at least one power of mass is enforced.

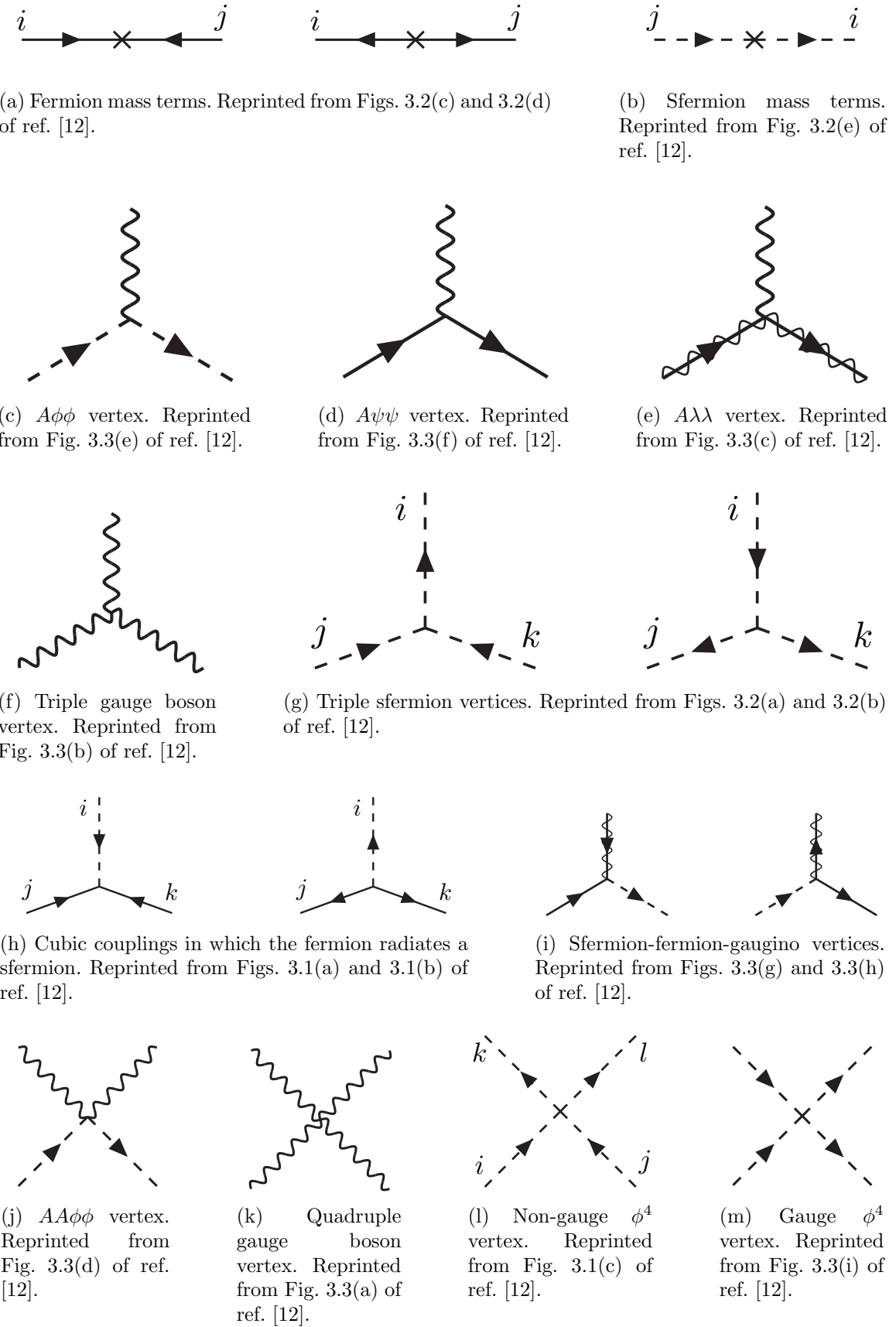


Figure 3.1: Interactions in the unbroken SUSY Lagrangian.

³⁵⁷ Soft SUSY breaking terms give masses to the sfermions and gauginos and introduce
³⁵⁸ a cubic sfermion vertex. The soft terms are given by

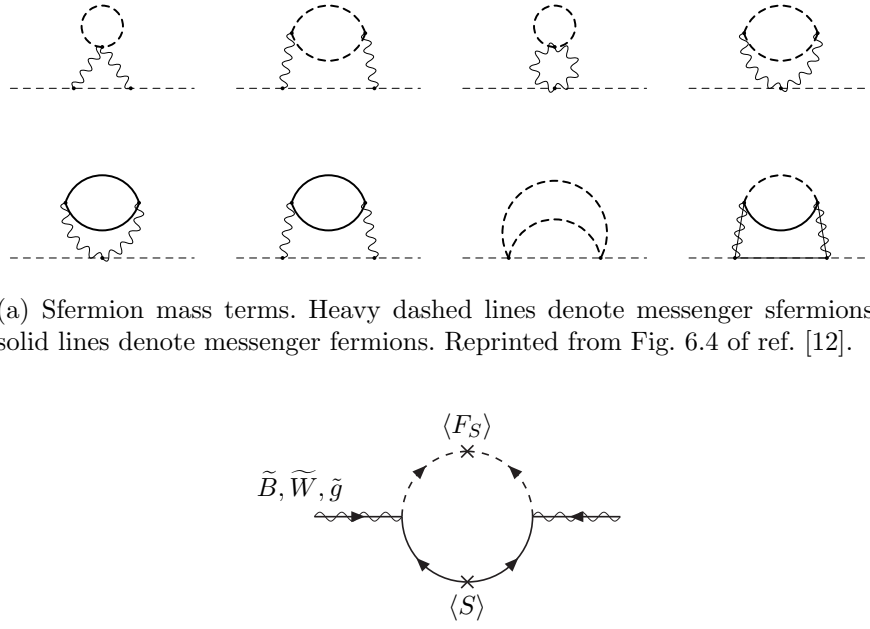
$$\begin{aligned}
 \mathcal{L}_{\text{soft}} = & -\frac{1}{2}(M_3\tilde{g}^a\tilde{g}^a + M_2\tilde{W}^a\tilde{W}^a + M_1\tilde{B}\tilde{B} + \text{h.c.}) \\
 & - (a_u^{ij}\tilde{u}_{Ri}^*\tilde{Q}_j H_u - a_d^{ij}\tilde{d}_{Ri}^*\tilde{Q}_j H_d - a_e^{ij}\tilde{e}_{Ri}^*\tilde{L}_j H_d + \text{h.c.}) \\
 & - m_{\tilde{Q}_{ij}}^2 \tilde{Q}_i^\dagger \tilde{Q}_j - m_{\tilde{L}_{ij}}^2 \tilde{L}_i^\dagger \tilde{L}_j \\
 & - m_{\tilde{u}_{ij}}^2 \tilde{u}_{Ri} \tilde{u}_{Rj}^* - m_{\tilde{d}_{ij}}^2 \tilde{d}_{Ri} \tilde{d}_{Rj}^* - m_{\tilde{e}_{ij}}^2 \tilde{e}_{Ri} \tilde{e}_{Rj}^* \\
 & - m_{H_u}^2 H_u^* H_u - m_{H_d}^2 H_d^* H_d - (b H_u H_d + \text{h.c.})
 \end{aligned} \tag{3.14}$$

³⁵⁹ where a runs from 1-8 for \tilde{g}^a and from 1-3 for \tilde{W}^a , and i, j run over the three families.
³⁶⁰ The color indices are not shown. The first line of Eq. 3.14 contains the gaugino mass
³⁶¹ terms. The second line contains cubic scalar couplings that contribute to mixing
³⁶² between the left- and right-handed third generation sfermions (it is assumed in the
³⁶³ supersymmetric Standard Model that the a_u^{ij} , a_d^{ij} , and a_e^{ij} are negligible unless $i =$
³⁶⁴ $j = 3$). The third and fourth lines of Eq. 3.14 contain squark and slepton mass terms,
³⁶⁵ and finally the last line contains the Higgs mass terms.

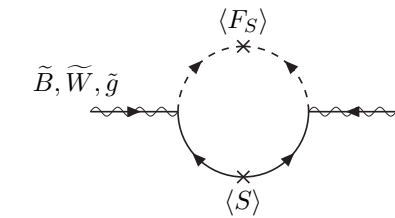
³⁶⁶ Many viable models of achieving soft SUSY breaking have been studied over the
³⁶⁷ last 30 years. For an overview, see Sec. 6 of ref. [12]. However, this thesis will only cover
³⁶⁸ *gauge-mediated SUSY breaking* (GMSB), because the two-photon search performed
³⁶⁹ is far more sensitive to this model than to other models of SUSY breaking.

³⁷⁰ 3.4 Gauge-Mediated SUSY Breaking

³⁷¹ In gauge-mediated models [16], “hidden” fields spontaneously break the supersymme-
³⁷² try of very heavy chiral *messenger* supermultiplets. There are a number of compet-
³⁷³ ing models (see ref. [16]) that explain the precise mechanism of spontaneous SUSY



(a) Sfermion mass terms. Heavy dashed lines denote messenger sfermions; solid lines denote messenger fermions. Reprinted from Fig. 6.4 of ref. [12].



(b) Gaugino mass term. The $\langle S \rangle$ part of the loop is a messenger fermion contribution; the $\langle F_S \rangle$ part is a messenger sfermion contribution. Reprinted from Fig. 6.3 of ref. [12].

Figure 3.2: Contributions to sfermion and gaugino masses from loop interactions with messenger particles in the GMSB framework.

374 breaking, but fortunately the details of those models mostly decouple from the phe-
 375 nomenology of GMSB. The messengers then communicate the SUSY breaking to the
 376 sparticles via loop diagrams of gauge interaction strength (i.e. via vertices like those
 377 shown in Figs. 3.1(c), 3.1(d), 3.1(i), 3.1(j), and 3.1(m), which are proportional to
 378 the SM gauge couplings constants). Feynman diagrams corresponding to gaugino and
 379 sfermion mass terms are shown in Figure 3.2.

380 Historically, GMSB and gravity-mediated SUSY breaking, or mSUGRA [17], have
 381 been the two most thoroughly experimentally studied scenarios of SUSY breaking.
 382 One advantage of GMSB over mSUGRA is that it naturally suppresses flavor vio-
 383 lation, a generic prediction of supersymmetry. Flavor violation is introduced in the
 384 scalar³ couplings and sfermion mass terms of $\mathcal{L}_{\text{soft}}$ (second, third, and fourth lines of

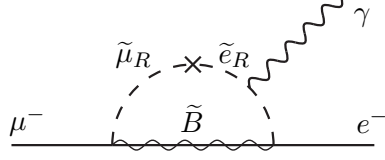


Figure 3.3: Possible contribution to $\mu \rightarrow e\gamma$ from $m_{\tilde{e}ij}$ soft term. Reprinted from Fig. 5.6(a) of ref. [12].

385 Eq. 3.14). Since a_u^{ij} , a_d^{ij} , a_e^{ij} , m_{Qij} , m_{Lij} , $m_{\tilde{u}ij}$, $m_{\tilde{d}ij}$, and $m_{\tilde{e}ij}$ are matrices in family
 386 space, any nonzero off-diagonal elements will lead to mixing between sfermions of
 387 different families. This can lead, for example, to contributions to the diagram $\mu \rightarrow e\gamma$
 388 (Figure 3.3) exceeding the experimental bounds. To avoid this disaster, *universality*
 389 conditions are assumed:

$$\mathbf{m}_{\tilde{\mathbf{Q}}}^2 = m_{\tilde{Q}}^2 \mathbf{1}, \mathbf{m}_{\tilde{\mathbf{L}}}^2 = m_{\tilde{L}}^2 \mathbf{1}, \mathbf{m}_{\tilde{\mathbf{u}}}^2 = m_{\tilde{u}}^2 \mathbf{1}, \mathbf{m}_{\tilde{\mathbf{d}}}^2 = m_{\tilde{d}}^2 \mathbf{1}, \mathbf{m}_{\tilde{\mathbf{e}}}^2 = m_{\tilde{e}}^2 \mathbf{1} \quad (3.15)$$

390 i.e. all sfermion mass matrices arising from the soft terms are assumed to be propor-
 391 tional to the unit matrix $\mathbf{1}$, such that there can be no flavor mixing from these terms
 392 and contributions to flavor-changing processes are drastically reduced.² In mSUGRA
 393 models, universality is assumed from the beginning, while in GMSB it is a natural
 394 consequence of the fact that the sparticle-messenger vertices are flavor-blind.

395 In minimal GMSB (mGMSB), there are four messenger supermultiplets q, \bar{q}, l, \bar{l}
 396 providing the messenger (s)quarks and (s)leptons. There is one breaking scale Λ . The
 397 gaugino masses computed from diagrams like Fig. 3.2(b) are given by

$$M_a = \frac{\alpha_a}{4\pi} \Lambda \quad (3.16)$$

²Universality also includes some assumptions about the form of a_{uij} , a_{dij} , and a_{eij} and the stipulation that the soft terms not introduce any CP-violating phases.

³⁹⁸ where a runs from 1-3 and the α_a are the SM gauge coupling constants. The sfermion
³⁹⁹ masses computed from diagrams like Fig. 3.2(a) are given by

$$m_{\phi_i}^2 = 2\Lambda^2 \sum_{a=1}^3 \left(\frac{\alpha_a}{4\pi}\right)^2 C_a(i) \quad (3.17)$$

⁴⁰⁰ where $C_a(i)$ are group theory factors that are identical for all particles residing in
⁴⁰¹ the same type of supermultiplet (e.g. for all left-handed (s)quarks or left-handed
⁴⁰² (s)leptons). As explained in the previous paragraph, the gaugino and sfermion masses
⁴⁰³ do not depend on fermion family.

⁴⁰⁴ In recent years, much theoretical progress has been made in unifying models of
⁴⁰⁵ gauge mediation and developing less restrictive models than mGMSB. *General gauge*
⁴⁰⁶ *mediation* (GGM) [18] retains the essential features of mGMSB, such as flavor de-
⁴⁰⁷ generacy and communication of SUSY breaking via messengers, but does not make
⁴⁰⁸ assumptions about the specific messenger sector or SUSY breaking scale. Many dif-
⁴⁰⁹ ferent collider final states can be interpreted in terms of GGM, and conversely, GGM
⁴¹⁰ implies a wealth of signatures, only a small fraction of which have been searched for
⁴¹¹ at colliders [19, 20, 21]. The following section discusses the aspects of GGM collider
⁴¹² phenomenology relevant to this thesis.

⁴¹³ 3.5 Phenomenology of General Gauge Mediation

⁴¹⁴ The main distinguishing feature of all GMSB phenomenology is that the gravitino \tilde{G} is
⁴¹⁵ very light (eV-keV). In general, the gravitino mass is proportional to $\langle F \rangle / M_P$, where
⁴¹⁶ $\langle F \rangle$ is the vacuum expectation value (VEV) of a field F that spontaneously breaks
⁴¹⁷ SUSY in the vacuum state and M_P is the Planck mass. In GGM models, $\langle F \rangle \sim 10^8$
⁴¹⁸ GeV, leading to a very light gravitino. In contrast, mSUGRA predicts $\langle F \rangle \sim 10^{20}$
⁴¹⁹ GeV. The fact that the gravitino is so much lighter than any other particles in the

⁴²⁰ supersymmetric Standard Model, and that it interacts only gravitationally (and thus
⁴²¹ extremely feebly), leads to two important phenomenological consequences:

- ⁴²² 1. All sparticle decay chains end with the production of a gravitino.
- ⁴²³ 2. The gravitino escapes 4π , hermetic collider detectors without interacting, leav-
⁴²⁴ ing a signature of “missing” momentum transverse to the beam direction.

⁴²⁵ Even if the gravitino were lighter than any other sparticle, but heavier than an
⁴²⁶ ordinary SM particle, it still could not decay to the SM particle due to *R-parity*. R-
⁴²⁷ parity is a conserved quantity of the supersymmetric Standard Model that enforces
⁴²⁸ baryon and lepton number conservation, which would otherwise be generically allowed
⁴²⁹ at levels in conflict with experiment (e.g. the non-observation of baryon- and lepton-
⁴³⁰ number-violating proton decay). All sparticles have R-parity -1, while all ordinary SM
⁴³¹ particles have R-parity +1, and R-parity conservation dictates that at any vertex, the
⁴³² product of the R-parities of each leg must be +1. This leads to two more important
⁴³³ consequences:

- ⁴³⁴ 1. Since conservation of energy only allows it to decay to ordinary SM particles,
⁴³⁵ but R-parity prevents a sparticle-particle-particle vertex, the *lightest supersym-
⁴³⁶ metric particle* (LSP) must be absolutely stable. All sparticle decays proceed
⁴³⁷ through the *next-to-lightest supersymmetric particle* (NLSP), which in turn de-
⁴³⁸ cays to the LSP. The fact that it is stable and only gravitationally interacting
⁴³⁹ makes the gravitino a candidate dark matter particle (see Sec. 3.6).
- ⁴⁴⁰ 2. In colliders, sparticles are produced in pairs (particle + particle \rightarrow sparticle +
⁴⁴¹ sparticle).

⁴⁴² In GMSB, then, the gravitino is the LSP. If the NLSP is a gaugino,³ then the
⁴⁴³ possible decays depend on mixing among the gauginos. Due to the effects of EWSB,

³In principle, the NLSP could be anything, but in most popular GGM models, it is either a gaugino or a stau. The stau NLSP search is not the subject of this thesis, so it will not be considered in this section.

444 the four neutral gauginos $\tilde{H}_u^0, \tilde{H}_d^0, \tilde{B}, \tilde{W}^0$ mix into four *neutralino* mass eigenstates
 445 $\tilde{\chi}_1^0, \tilde{\chi}_2^0, \tilde{\chi}_3^0, \tilde{\chi}_4^0$, and the four charged gauginos $\tilde{H}_u^+, \tilde{H}_d^-, \tilde{W}^+, \tilde{W}^-$ mix into two *chargino*
 446 mass eigenstates $\tilde{\chi}_1^\pm, \tilde{\chi}_2^\pm$ (two mass eigenstates each with two possible charges = four
 447 particles). In the limit that EWSB effects are small, the neutralino and chargino
 448 masses can be written as the gauge eigenstate masses plus a small perturbation:

$$m_{\tilde{\chi}_1^0} = M_1 - \frac{m_Z^2 \sin^2 \theta_W (M_1 + \mu \sin 2\beta)}{\mu^2 - M_1^2} + \dots \quad (3.18)$$

$$m_{\tilde{\chi}_2^0} = M_2 - \frac{m_W^2 (M_2 + \mu \sin 2\beta)}{\mu^2 - M_2^2} + \dots \quad (3.19)$$

$$m_{\tilde{\chi}_3^0} = |\mu| + \frac{m_Z^2 (\text{sgn}(\mu) - \sin 2\beta)(\mu + M_1 \cos^2 \theta_W + M_2 \sin^2 \theta_W)}{2(\mu + M_1)(\mu + M_2)} + \dots \quad (3.20)$$

$$m_{\tilde{\chi}_4^0} = |\mu| + \frac{m_Z^2 (\text{sgn}(\mu) + \sin 2\beta)(\mu - M_1 \cos^2 \theta_W - M_2 \sin^2 \theta_W)}{2(\mu - M_1)(\mu - M_2)} + \dots \quad (3.21)$$

$$m_{\tilde{\chi}_1^\pm} = M_2 - \frac{m_W^2 (M_2 + \mu \sin 2\beta)}{\mu^2 - M_2^2} + \dots \quad (3.22)$$

$$m_{\tilde{\chi}_2^\pm} = |\mu| + \frac{m_W^2 \text{sgn}(\mu)(\mu + M_2 \sin 2\beta)}{\mu^2 - M_2^2} + \dots \quad (3.23)$$

449 where $\tan \beta = \langle H_u^0 \rangle / \langle H_d^0 \rangle$.

450 The two scenarios studied in ref. [21] are the following:

451 • **Bino NLSP:** $M_1 \sim$ few hundred GeV, $M_2, |\mu| \gg M_1$. All but the lightest
 452 neutralino are effectively inaccessible at the LHC due to their large masses. The
 453 NLSP can always decay to $\gamma + \tilde{G}$, and if it is heavy enough, to $Z + \tilde{G}$ or $H + \tilde{G}$.

454 • **Wino NLSP:** $M_2 \sim$ few hundred GeV, $M_1, |\mu| \gg M_2$. The lightest neutralino
 455 and the lightest chargino are nearly degenerate in mass, and are the only two
 456 particles to play a role at the LHC. The decays described in the previous bullet
 457 point can happen, as well as chargino decays to $W + \tilde{G}$.

458 The subject of this thesis is the classic bino NLSP decay $\gamma + \tilde{G}$.

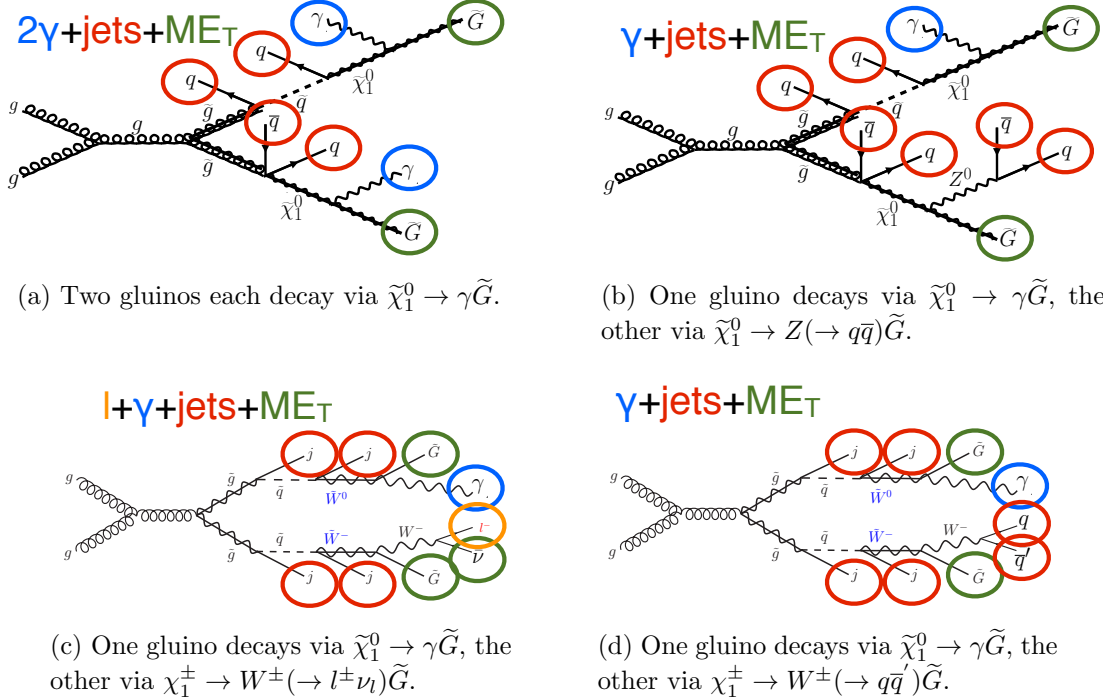


Figure 3.4: Typical LHC signatures of the bino and wino NLSP scenarios.

459 Since strong production of SUSY particles dominates over electroweak production
460 at the LHC due to the enhanced gg parton luminosity over the $q\bar{q}$ parton luminosity,
461 early LHC searches are particularly sensitive to light squarks and gluinos. General
462 gauge mediation makes no a priori restrictions on the mass splitting between the
463 strongly interacting sparticles and the weakly interacting sparticles, so models with
464 light squarks and gluinos are viable. In fact, such models could not be probed as
465 well at the Tevatron⁴ as they are at the LHC due to the aforementioned parton
466 luminosities.

467 Typical LHC signatures of the bino and wino NLSP scenarios are shown in Fig-
468 ure 3.4.

⁴Located on the Fermilab site in Batavia, Illinois, the Tevatron was a proton-antiproton collider operating at 1.96 TeV center-of-mass energy. The Tevatron ran from 1987 to 2011 [22].

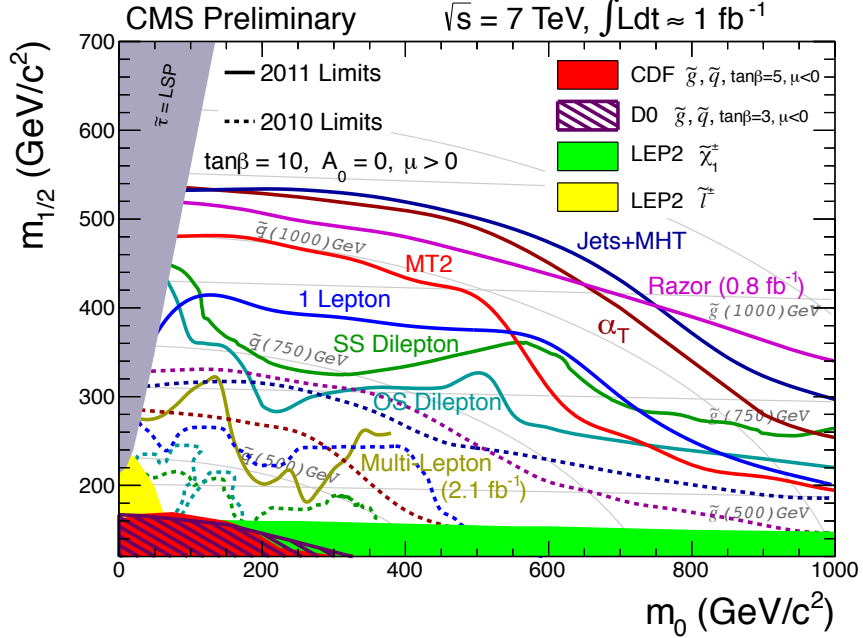


Figure 3.5: CMS limits on mSUGRA with $\tan \beta = 10$. The limits set by individual searches are shown as separate colored lines. Solid lines refer to 2011 searches (i.e. using an integrated luminosity of $\sim 1 \text{ fb}^{-1}$), while dashed lines refer to 2010 searches ($\sim 36 \text{ pb}^{-1}$). Reprinted from ref. [25].

469 3.6 Experimental Status of SUSY

470 Collider searches for evidence of supersymmetry began in earnest in the 1980s [23]
 471 and continue to this day. Most recently, the LHC and Tevatron experiments have set
 472 the strictest limits on a variety of SUSY breaking scenarios, including GMSB and
 473 mSUGRA.

474 Figure 3.5 shows the current limits set by the CMS experiment on the mSUGRA
 475 model (with $\tan \beta = 10$) in the m_0 - $m_{1/2}$ plane. (Note that although the plot is trun-
 476 cated at $m_0 = 1000 \text{ GeV}/c^2$, some searches are sensitive out to $m_0 \sim 2000 \text{ GeV}/c^2$.)
 477 Although the LHC has pushed m_0 above $\sim 1 \text{ TeV}/c^2$ for $m_{1/2}$ up to $\sim 400 \text{ GeV}/c^2$,
 478 casting some doubt onto the theory's prospects for solving the hierarchy problem,
 479 there is still a sizable chunk of mSUGRA parameter space that is not ruled out by
 480 collider experiments. Furthermore, parts of the CMS unexplored regions overlap with
 481 areas allowed by astrophysics experiments [24].

Removed

CMS

Moriond

result

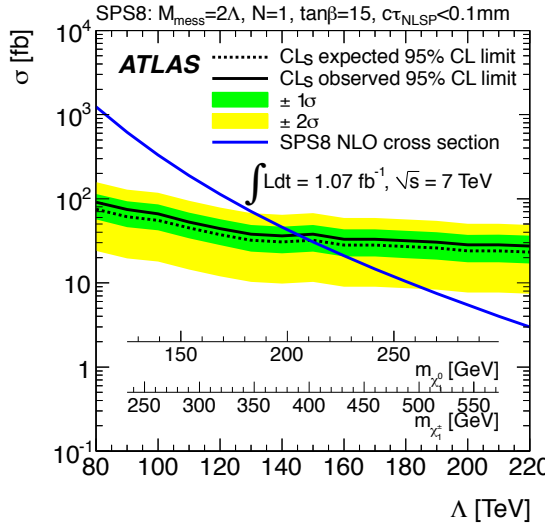


Figure 3.6: ATLAS cross section upper limit on the SPS8 [27] model of mGMSB as a function of SUSY breaking scale Λ , lightest neutralino mass $m_{\tilde{\chi}_1^0}$, or lightest chargino mass $m_{\tilde{\chi}_1^\pm}$. Values of Λ , $m_{\tilde{\chi}_1^0}$, or $m_{\tilde{\chi}_1^\pm}$ below the intersection point between the blue (predicted SPS8 cross section) and black (observed cross section upper limit) curves are excluded. The model parameters listed above the plot are defined in Secs. 3.4 and 3.5, except for τ_{NLSP} , which is the neutralino lifetime. Reprinted from ref. [19].

482 Figure 3.6 shows the most up-to-date limit (using 1 fb^{-1} of integrated luminos-
 483 ity collected by the ATLAS experiment [26] at the LHC) on the Snowmass Points
 484 and Slopes (SPS) model of mGMSB, dubbed SPS8 [27]. In general, the lifetime of
 485 the lightest neutralino in GMSB models can take on any value between hundreds of
 486 nanometers to a few kilometers depending on the mass of the lightest neutralino and
 487 the SUSY breaking scale [12]. The search published in ref. [19] (from which Figs. 3.6
 488 and ?? are culled) considers only *prompt* neutralino variants, i.e. with neutralino life-
 489 time short enough that the distance traveled by the neutralino before decay cannot be
 490 resolved by the detector. The most recent limits on non-prompt SPS8-style neutralino
 491 models were set by the Collider Detector at Fermilab (CDF) collaboration with 570
 492 pb^{-1} , and are shown in Figure 3.7 [20].

493 Finally, if the gravitino is to make up some or all of the dark matter, constraints
 494 on the form of gauge mediation must come from cosmological considerations and
 495 astronomical observations. The gravitino in gauge mediation models is usually very

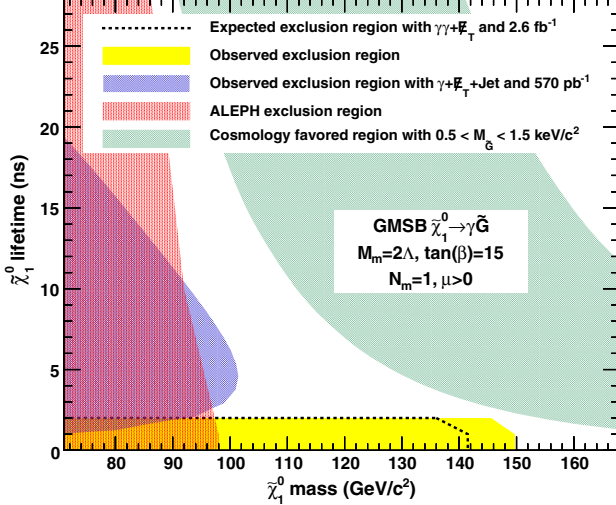


Figure 3.7: CDF exclusion contour in the $\tau_{\tilde{\chi}_1^0}$ - $m_{\tilde{\chi}_1^0}$ plane, where $\tau_{\tilde{\chi}_1^0}$ is the lifetime of the neutralino. Reprinted from ref. [20].

496 light ($\mathcal{O}(\text{eV-MeV})$) because it is proportional to the SUSY breaking scale divided
 497 by the Planck mass, and in GMSB the breaking scale is typically only of order a
 498 few hundred TeV ([12] and Sec. 3.5). A light, highly relativistic dark matter particle
 499 might have been produced, for instance, in the early, radiation-dominated period
 500 of the universe [29]. This *warm dark matter* (WDM) may be responsible for all of
 501 the dark matter needed to account for galactic structure, or it may share the duties
 502 with *cold dark matter* (CDM, weakly interacting particles with masses in the GeV
 503 range). In any viable model, the predicted relic density of the dark matter species
 504 must match the observed value of $\Omega h^2 \sim 0.1$ [30]. For many GMSB models, this
 505 measurement constrains the gravitino mass to the keV range [31]. This constraint,
 506 however, does not translate into a very strong bound on the lifetime of the lightest
 507 neutralino. Using the following equation (taken from [31]):

$$\tau_{\tilde{\chi}_1^0} \sim 130 \left(\frac{100 \text{ GeV}}{m_{\tilde{\chi}_1^0}} \right)^5 \left(\frac{\sqrt{\langle F \rangle}}{100 \text{ TeV}} \right)^4 \mu\text{m} \quad (3.24)$$

508 and applying the gravitino mass constraint $\sqrt{\langle F \rangle} \lesssim 3000 \text{ TeV}$ (cf. the first paragraph
 509 of Sec. 3.5 with $m_{\tilde{G}} \sim \text{keV}$) and $m_{\tilde{\chi}_1^0} = 100 \text{ GeV}$, the upper bound on the neutralino

510 lifetime is 100 meters. For $\sqrt{\langle F \rangle} \sim 100$ TeV, the neutralino lifetime is detectable on
511 collider time scales.

512 Recently, a lower bound on the WDM particle mass in either pure warm or mixed
513 warm and cold dark matter scenarios was set using observations of the Lyman- α for-
514 est. For pure WDM, $m_{\text{WDM}} > 8$ keV, while for some mixed WDM-CDM scenarios,
515 $m_{\text{WDM}} > 1.1\text{-}1.5$ keV [29, 32]. These bounds and others have motivated the develop-
516 ment of more complicated gauge mediation models [32]. However, rather than focus
517 on a specific GMSB model, of which there are many, the search detailed here is in-
518 terpreted in a minimally model dependent way. With this approach, the results can
519 be applied to many competing models. The remainder of this thesis is devoted to the
520 experimental details of the search, analysis strategy, and presentation of the results.
521 The work described in this thesis forms the basis for the CMS public result “Search
522 for Supersymmetry in Events with Photons and Missing Energy” [28], published in
523 April 2012.

524 **Chapter 4**

525 **The Large Hadron Collider**

526 At a 2010-2011 energy of 3.5 TeV/beam (7 TeV/beam design [33]) and maximum
527 instantaneous luminosity of $3.55 \times 10^{33} \text{ cm}^{-2} \text{ s}^{-1}$ [34] ($10^{34} \text{ cm}^{-2} \text{ s}^{-1}$ design [33]),
528 the CERN Large Hadron Collider (LHC) is the highest energy and highest intensity
529 proton-proton collider ever built. Its purpose is to allow the four LHC experiments to
530 explore TeV scale physics. For CMS and ATLAS, this implies examining the origins of
531 EWSB via searches for the SM Higgs boson and physical phenomena not predicted by
532 the SM that may explain the mass hierarchy in the SM. It also includes searches for
533 possible dark matter candidates that are often proposed to have masses at the weak
534 scale. The LHC needs to provide high energy proton collisions because the masses
535 of the sought-after particles are higher than those already incorporated into the SM.
536 It must also provide an unprecedented collision rate because signatures of the Higgs
537 boson and physics beyond the SM are very rare compared to SM processes.

538 The rest of this chapter is devoted to an overview of the LHC machine. Sec-
539 tion 4.1 gives the overall layout of the machine and design choices made in light of
540 energy and luminosity demands. Section 4.2 describes the LHC injection scheme. The
541 different types of magnets and their functions is illustrated in Section 4.3, and finally
542 the radiofrequency cavities are covered in Section 4.4. Unless otherwise noted, all

543 information in this chapter comes from ref. [33].

544 4.1 Design Considerations and Performance Lim- 545 itations

546 The layout of the 26.7-km long [35] LHC ring, located \sim 100 m underground on the
547 border between France and Switzerland northwest of Geneva, is shown in Figure 4.1.
548 The two circulating beams of protons travel in opposite directions, colliding only at
549 the experimental points. There are eight straight sections, each \sim 528 m long, and
550 eight arcs, each made of 23 106.9-m long arc cells. Beam crossings occur in four of
551 the straight sections. The arcs contain six 14.3-m long dipole magnets, the cryogenics
552 to cool the magnets, and short straight sections (SSS) with focusing and corrector
553 magnets. The high luminosity experiments CMS and ATLAS are located diametrically
554 opposite each other on the ring, ensuring that in principle each should receive the
555 same integrated luminosity from the LHC.

556 To achieve a maximum energy per beam of 7 TeV, the peak magnetic field pro-
557 duced by the dipole magnets must be 8.33 T, demanding the use of superconducting
558 technology. Due to the like charges of the two beams, two separate magnet systems
559 and evacuated beam pipes must be used to accelerate the protons in opposite direc-
560 tions. Space limitations in the LHC tunnel, which was previously used for the LEP
561 collider, prevent the installation of two separate rings of magnets, so each dipole in-
562 stead contains two beam pipe bores and two sets of superconducting coils to produce
563 two fields in opposite directions. In order to safely operate the magnets at 8.33 T,
564 the cryogenic bath temperature is chosen to be 1.9 K, colder than any other acceler-
565 ator cryogen and well below the critical temperature of the niobium-titanium (NbTi)
566 superconducting wires of 9.2 K [38]. The extremely low bath temperature leads to
567 a lessened heat capacity in the wires and consequently a lower energy threshold for

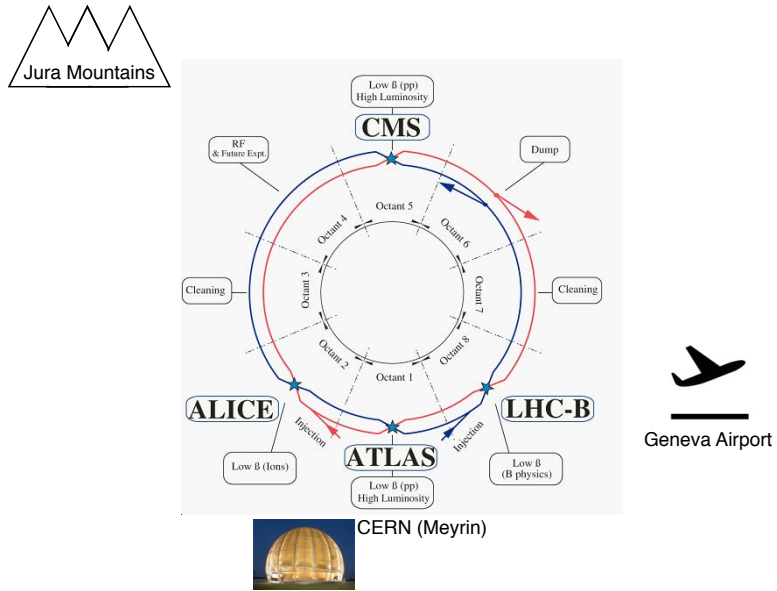


Figure 4.1: Bird's-eye view of the LHC ring, showing the locations of the experiments and local landmarks. Arrows show the beam direction. The ring figure is reprinted from Fig. 2.1 of ref. [33]. The CERN Globe of Innovation photo comes from ref. [36] and the airplane cartoon comes from ref. [37].

568 triggering a quench, so movements and heat dissipation within the cables must be
 569 controlled more tightly than in previous accelerators.

570 The LHC beams are arranged in bunches of protons, with each bunch separated
 571 by an integer multiple of the 25 ns minimum bunch spacing. The machine luminosity
 572 L is given by

$$L = \frac{N_b^2 n_b f_{\text{rev}} \gamma_r}{4\pi \epsilon_n \beta^*} F \quad (4.1)$$

573 where N_b is the number of protons per bunch (squared for the two beams), n_b is
 574 the number of bunches per beam, f_{rev} is the bunch revolution frequency, γ_r is the
 575 relativistic γ of the protons, ϵ_n is the normalized transverse beam emittance, β^* is
 576 the value of the β function at the collision point, and F is a geometrical factor less
 577 than one related to the *crossing angle* of the bunches with respect to the horizontal

578 (ATLAS) or vertical (CMS) planes and the beam size. The normalized transverse
 579 beam emittance is a measure of the RMS spread of the beam in the plane transverse
 580 to its direction of motion, irrespective of its energy. A smaller emittance implies that
 581 particles are squeezed into a smaller area in phase space, leading to larger luminosity.
 582 The β function is defined as the square of the transverse beam size divided by the
 583 emittance. It describes the oscillations of the transverse beam size as a function of
 584 position in the ring. To achieve high luminosity, β^* is the minimum of the β function,
 585 and it is related to the focusing strength of the triplet magnets near the interaction
 586 points. In accelerating sections of the ring, the β function gets large so that the proton
 587 momenta may be more uniform. Each piece of the luminosity is limited by safety or
 588 design considerations.

589 Above some saturated bunch intensity, nonlinear beam-beam interactions experi-
 590 enced by the protons during collisions cause the luminosity to scale as N_b , not N_b^2
 591 [39]. The scale of these interactions is set by N_b/ϵ_n , and the size of the beam pipe and
 592 maximum β function limit ϵ_n to $3.75 \mu\text{m}$. Instabilities are also introduced through
 593 interactions between the protons and the wall of the beam pipe that scale with the
 594 beam current. Last but not least, the beam dump and magnet safety systems limit the
 595 total stored energy in the ring. For these reasons, the maximum number of bunches
 596 is limited to 1.15×10^{11} . In bunches of this proton multiplicity, the average num-
 597 ber of proton-proton collisions per bunch crossing, or *pileup*, in CMS and ATLAS is
 598 approximately 20. This unprecedented level of pileup poses unique triggering, event
 599 reconstruction, and analysis challenges for the experiments.

600 n_b can range from zero to 2808 and had a maximum of ~ 1400 in 2011, corre-
 601 sponding to 50 ns bunch spacing. f_{rev} is set by the circumference of the ring to 11.2
 602 kHz [40]. γ_r is set by the beam energy, which was 3.5 TeV in 2011.

603 The mechanical aperture of the triplet assemblies of quadrupole magnets limit
 604 the minimum β^* to 0.55 [40] and maximum crossing angle to $285 \mu\text{rad}$ [40] at the

The LHC injection complex

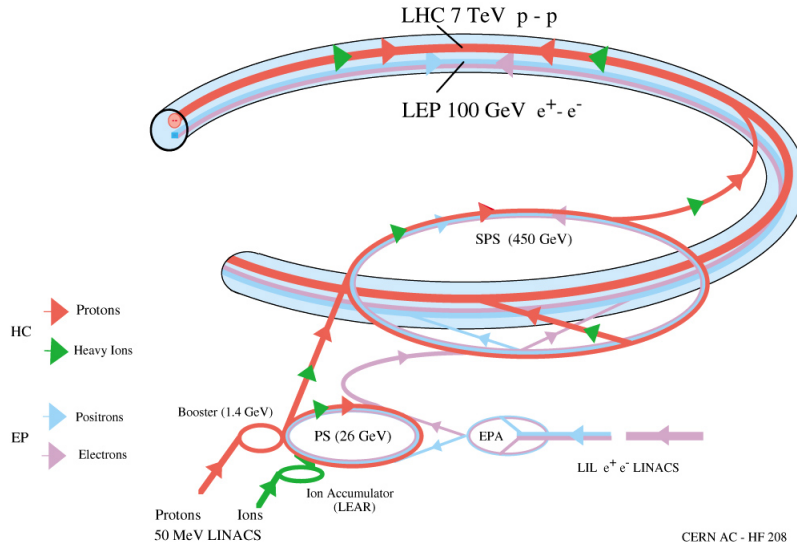


Figure 4.2: Overview of the LHC injector complex at CERN [41].

605 interaction points. The purpose of the crossing angle is to prevent parasitic collisions
 606 in the 23-m length of shared beam pipe upstream and downstream of the interaction
 607 points.

608 4.2 Beam Injection

609 The ultimate source of protons for the LHC is a bottle of hydrogen connected to the
 610 CERN Linac2 linear accelerator, which accelerates the protons up to 50 MeV. From
 611 there they enter the Proton Synchrotron Booster (PSB), which accelerates them to
 612 1.4 GeV, and then the Proton Synchrotron (PS) itself, which brings them to 25 GeV.
 613 The Super Proton Synchrotron (SPS) is the next stage, accelerating the protons to
 614 an energy of 450 GeV. Finally, they leave the SPS and enter the LHC, where they are
 615 accelerated to the desired beam energy (3.5 TeV in 2011). An overview of the LHC
 616 injector complex is shown in Figure 4.2.

617 The 25-ns spaced bunches (or 50 ns for 2011 operation) are produced in trains
 618 of 72 in the PS via a process of splitting six initial bunches into 12 smaller bunches

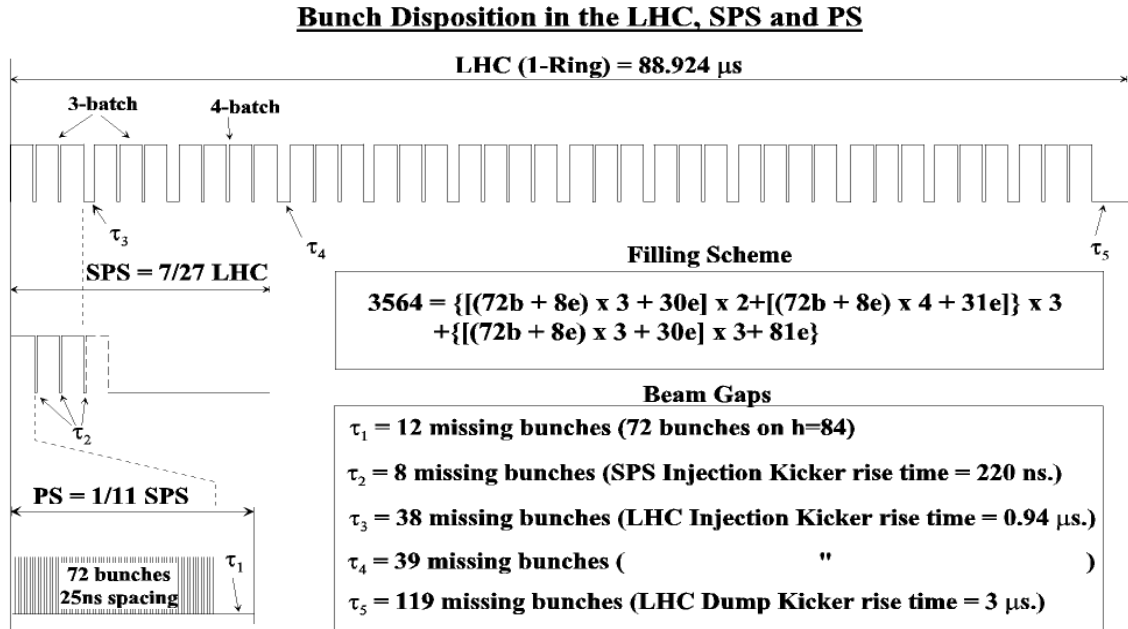


Figure 4.3: LHC injection scheme. Reprinted from Fig. 12.2 of ref. [33].

at specified points along the ring. At the end of each train is a 300 ns (12 bunch) gap, which is an artifact of the splitting process. The SPS is limited by its maximum allowed bunch intensity to storing three or four PS trains at a time. There is an 8 ns (8 bunch) gap at the end of each train due to the SPS injection kicker rise time. The LHC is filled three or four trains at a time from the SPS. At the end of each three-train and four-train group is a gap of 0.94 μ s (38 or 39 bunches) due to the LHC injection kicker rise time. Finally, at the end of an entire 88.924- μ s long LHC orbit is a gap of 3 μ s (119 bunches), known as the *abort gap*, to allow for the LHC dump kicker rise time. The injection scheme is shown in Figure 4.3.

LHC injection occurs at points 2 and 8. At the intersection of the SPS-LHC transfer line and the LHC beam pipe are five septum magnets that deflect the bunches 12 mrad horizontally into orbit. The septum magnets have a gap into which the beam is injected as well as two separate holes for the circulating beams, as shown in Figure 4.4. Four kicker magnets then deflect the bunches 0.85 mrad vertically into orbit. The kicker magnets supply a pulsed magnetic field with a 0.94 μ s rise time

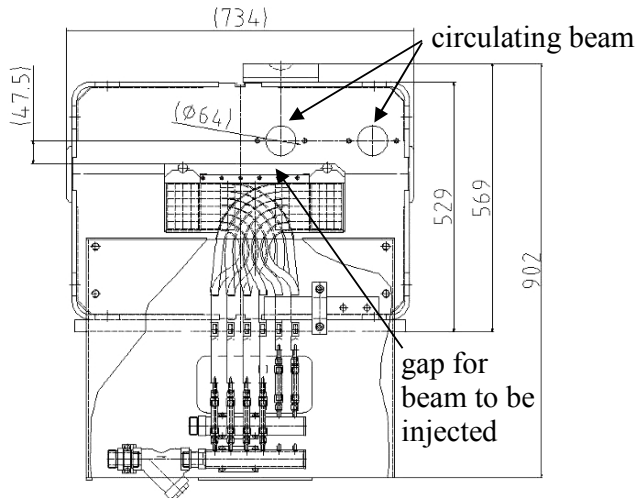


Figure 4.4: Cross-sectional view of septum magnet (beam direction is into or out of the page) showing the holes for the circulating beams and the separate gap for injected particles. Reprinted from Fig. 11.2 of ref. [33].

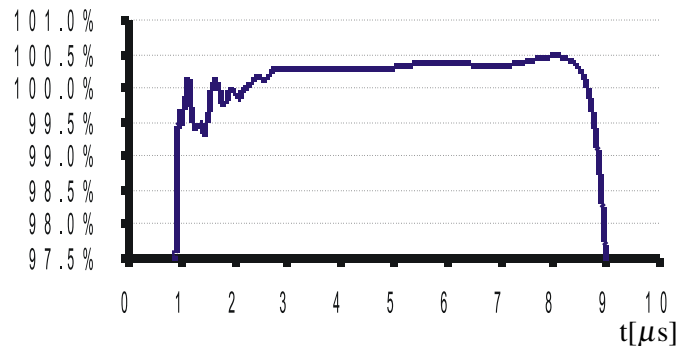


Figure 4.5: LHC injection kicker pulse shape. The *y*-axis measures percentage of maximum current. Reprinted from Fig. 11.7 of ref. [33].

634 (see Fig. 4.3) and a 5.84(7.86) μs flat top for three-train(four-train) injection (see
 635 Figure 4.5). To limit emittance growth at injection due to over- or under-kicking the
 636 injected bunches such that they miss the core of the LHC orbit, the kicker current is
 637 limited to $< 0.5\%$ flat top ripple in any direction.

638 4.3 Magnets and Cryogenics

639 There are 1232 twin-bore dipole magnets along the LHC ring used for establishing
 640 the circular orbit of the protons. They consist of two evacuated beam pipes, each

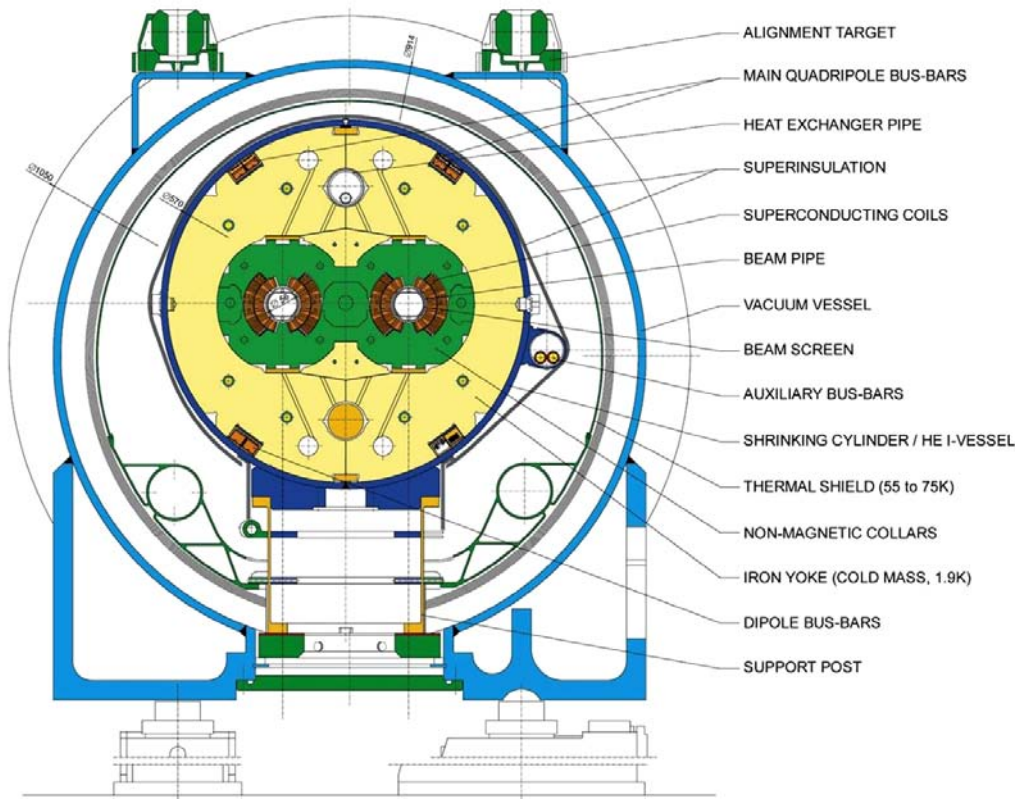


Figure 4.6: Cross-sectional view of LHC dipole + cryostat. Reprinted from Fig. 3.3 of ref. [33].

641 flanked by its own set of superconducting coils, inside an iron yoke which serves as
 642 the 1.9 K cold mass. The entire assembly sits inside a helium vessel, which is itself
 643 surrounded by a vacuum chamber thermally insulating the cold mass from the room
 644 temperature LHC cavern. The entire dipole + cryostat device is ~ 16.5 m long and
 645 weighs about 27.5 t. A cross-sectional view of the dipole is given in Figure 4.6.

646 To provide a centripetal Lorentz force on the protons, the dipole field points
 647 vertically up or down, depending on the sense of the beam. The magnetic field lines for
 648 a single beam pipe are shown in Figure 4.7. Figure 4.8 shows the coil windings in two
 649 bores. To provide the correct field direction, the coils are wound around blocks that
 650 are ~ 14 m long (the length of the dipole), so that each winding has a circumference
 651 of ~ 28 m.

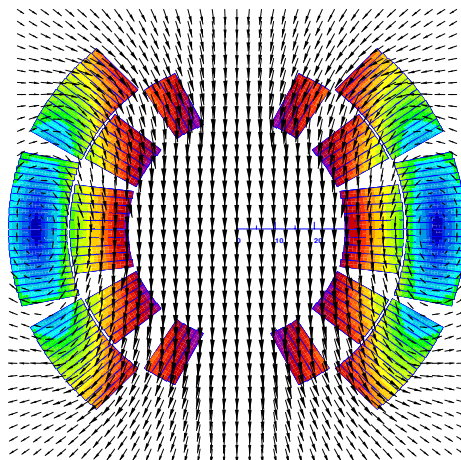


Figure 4.7: Magnetic field lines of the dipole field. The beam direction is into the page. Reprinted from Fig. 4 of ref. [42].

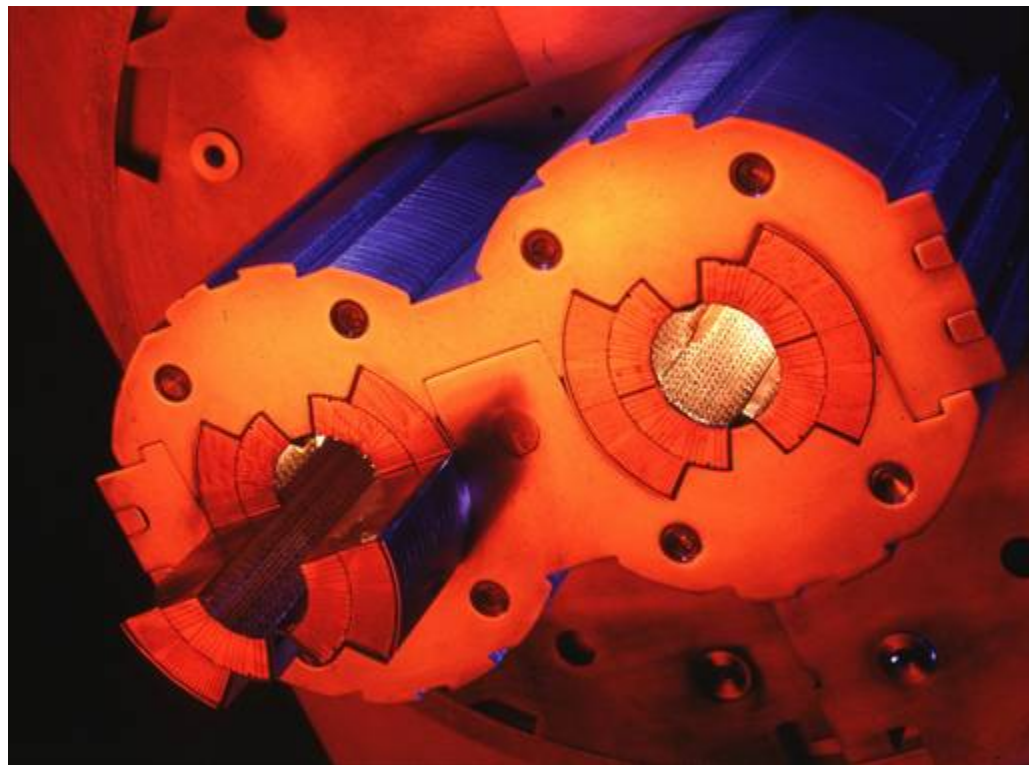


Figure 4.8: Superconducting coils in a twin-bore dipole [43].

652 In addition to the dipoles, a number of different types of orbit corrector magnets
 653 are installed throughout the ring. The main quadrupole magnets, as well as higher
 654 order field corrector magnets, are located in the arcs and short straight sections. The
 655 function of these magnets is to provide fine grained control over the magnetic field
 656 in order to keep the bunches in the proper orbit and control the emittance and β
 657 functions.

658 In the straight sections, there are four specialized types of magnets related to SPS
 659 extraction and bringing the beams into collision. Matching section quadrupoles near
 660 the transfer lines help to match the injected bunch orbit to the circulating bunch orbit.
 661 Dispersion suppressors, consisting of dipoles and quadrupoles, help to reduce beam
 662 dispersion near the collision points due to off-momentum protons. Matching section
 663 separation dipoles control the separation between the two beams near the collision
 664 points. The magnets that perform the final squeeze of the beams before collision,
 665 called the low- β inner triplets, must provide a very high field gradient of 215 T/m,
 666 withstand a high radiation dose, and sustain high heat loads in the superconducting
 667 coils.

668 The superfluid helium cryogen is delivered to the magnets via a distribution line
 669 from the main refrigerator. A cross section of the LHC tunnel, showing the cryogen
 670 delivery apparatus for a dipole, is shown in Figure 4.9.

671 4.4 Radiofrequency Cavities

672 LHC bunches are captured and accelerated in 400 MHz superconducting radiofre-
 673 quency (RF) cavities. 400 MHz defines the bunch length of $\lesssim 2$ ns. As bunches pass
 674 through the cavities, the oscillating electric field is at its peak and accelerates the
 675 protons through a potential difference of 2 MV per cavity (16 MV per turn). The
 676 finite bunch length is due to particles that arrive out of phase with the electric field

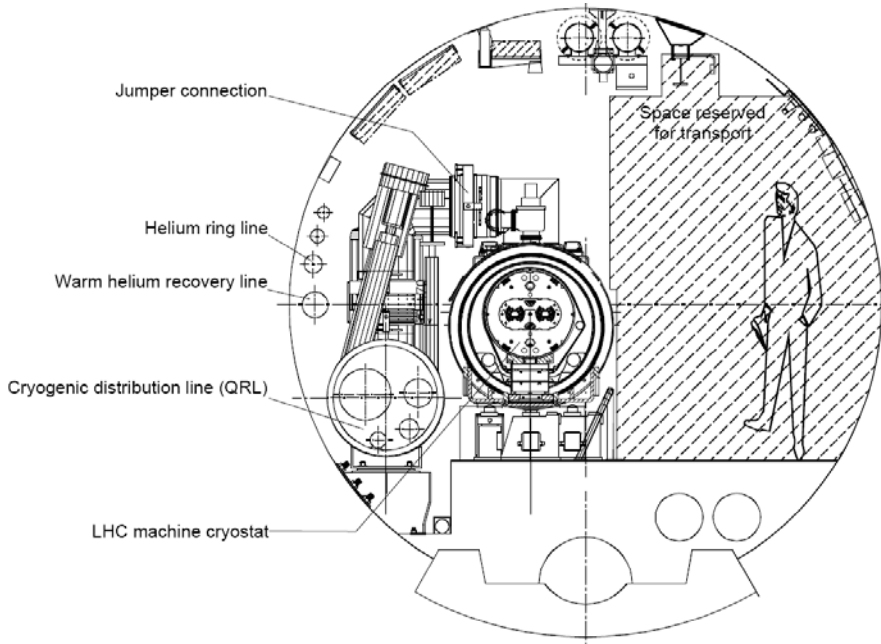


Figure 4.9: Cross section of the LHC tunnel, showing the cryogen delivery apparatus for a dipole. Reprinted from Fig. 7.1 of ref. [33].

677 due to deviations in their momenta from the nominal. During a ramp of the beam
 678 energy from 450 GeV to 3.5 or 7 TeV, bunches repeatedly travel around the ring, re-
 679 ceiving an energy kick each time, until the desired energy is reached. Feedback from
 680 the RF accelerating system causes an increase in magnet current to keep the bunches
 681 in a fixed orbit.

682 Superconducting material (niobium) coats the cylindrical walls of the cavity. RF
 683 power is coupled to the cavity via a klystron. The RF electric field standing wave is set
 684 up across the cavity in the beam direction. The transverse magnetic field dissipates
 685 some energy into the walls, but much less than in a normal conducting cavity.

686 **Chapter 5**

687 **The Compact Muon Solenoid**
688 **Experiment**

689 The Compact Muon Solenoid (CMS) detector sits at point 5 of the LHC ring, diamet-
690 rically opposite the ATLAS detector at point 1. It is a 4π hermetic general purpose
691 detector, meaning that it has the capability to detect charged and neutral hadrons,
692 photons, electrons, muons, taus, neutrinos, and non-Standard-Model particles pre-
693 dicted to escape the detector with good efficiency over a large range of rapidity.
694 Its main distinguishing feature is a superconducting solenoid that provides a 3.8T
695 magnetic field parallel to the beam line. This strong magnetic field allows precise de-
696 termination of the momentum and charge of muons and electrons up to a momentum
697 of ~ 1 TeV.

698 The origin of the CMS coordinate system is at the nominal interaction point. The
699 y -axis points skyward, the x -axis points towards the center of the LHC ring, and
700 the z -axis points counterclockwise along the LHC ring. r denotes radial distances
701 from the beam line, ϕ is the azimuthal angle measured with respect to the positive
702 x -axis, and θ is the polar angle measured with respect to the positive z -axis. The
703 *pseudorapidity* η is defined as $\eta = -\ln \tan(\theta/2)$, and is a good approximation to

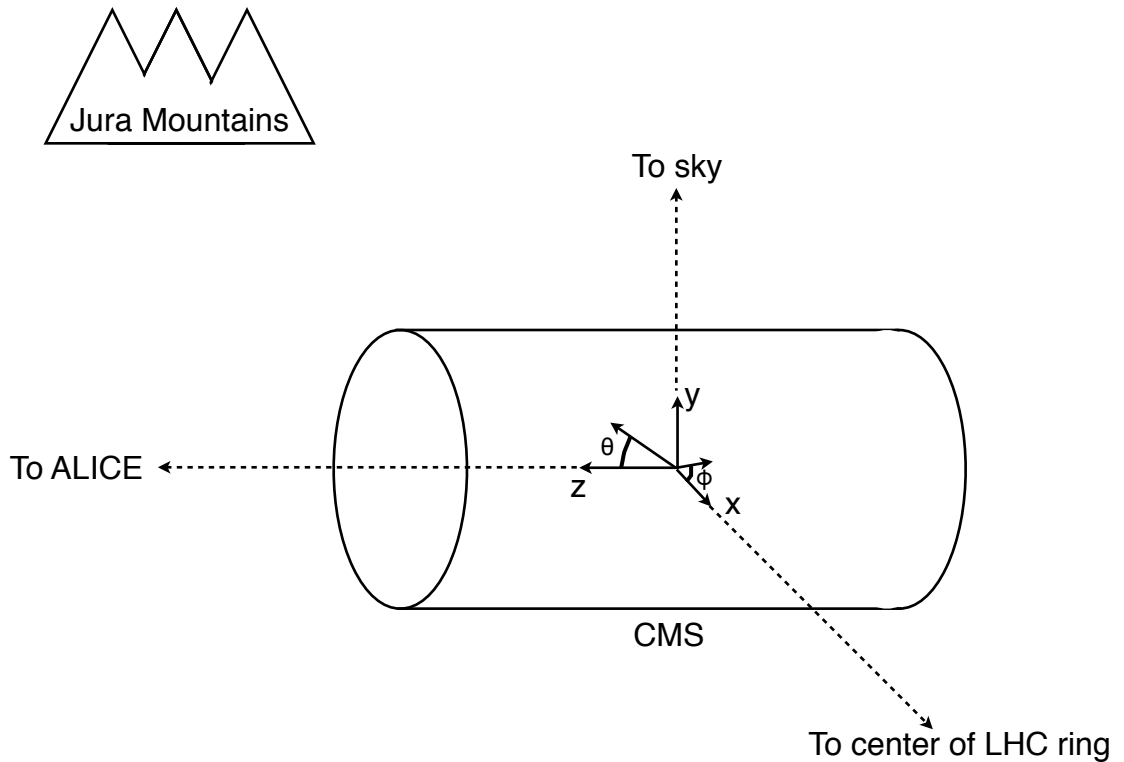


Figure 5.1: CMS coordinate system.

704 rapidity $y = (1/2) \ln((E + p_z c)/(E - p_z c))$ for relativistic particles. The transverse
 705 momentum and energy (p_T and E_T) of a particle are defined as $p_T = p \cos \phi$ and
 706 $E_T = E \cos \phi$, where p and E are the magnitude of the particle's momentum vector
 707 and the particle's total energy, respectively. A depiction of the CMS coordinate system
 708 is shown in Figure 5.1.

709 The CMS sub-detectors are arranged in concentric cylindrical layers, plus “end-
 710 caps,” around the beam line, as shown in Figure 5.2. Closest to the beam line are
 711 three layers of silicon pixel detectors, with the innermost at radius 4.4 cm and out-
 712 ermost at radius 10.2 cm [44]. Including the pixel endcaps, the total pixel coverage

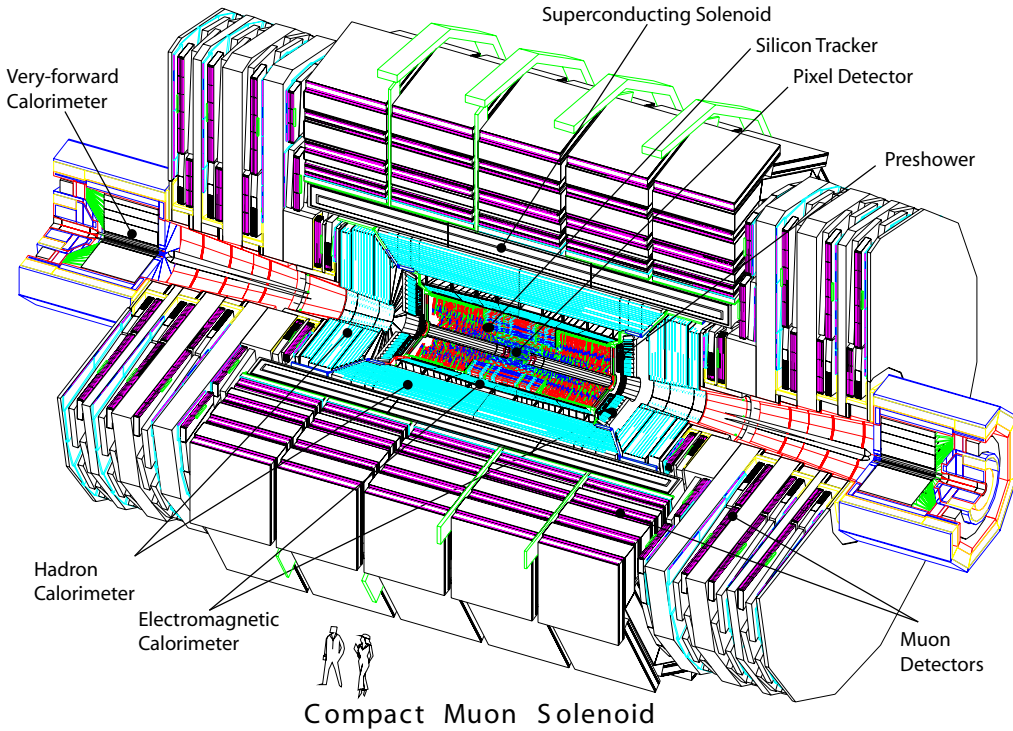


Figure 5.2: Cutaway view of CMS. Reprinted from Fig. 1.1 of ref. [44].

₇₁₃ extends to $\eta = 2.5$ [44]. The pixel detector plays an important role in determining the
₇₁₄ proton-proton interaction position (*beam spot*) and the impact parameters of charged
₇₁₅ particle trajectories, and is critical for the measurement of decay positions some dis-
₇₁₆ tance from the beam spot (*displaced vertices*), such as those due to the showering and
₇₁₇ hadronization of a b quark.

₇₁₈ The 10 next layers of CMS are comprised of silicon microstrip detectors, with the
₇₁₉ outermost layer at a radius of 1.3 m from the beam line [44]. As for the pixel detectors,
₇₂₀ the silicon strip endcap extended tracking coverage to $\eta = 2.5$. The silicon microstrip
₇₂₁ layers are the workhorse of the CMS tracking system, and provide excellent charged
₇₂₂ particle momentum resolution and track finding efficiency.

₇₂₃ Outside the tracking detectors are the calorimeters, starting with the single-layer
₇₂₄ lead tungstate crystal electromagnetic calorimeter at a radius of 1.3 m from the beam
₇₂₅ line (location of crystal front faces) [44]. Each crystal is 23 cm long, corresponding

726 to 25.8 radiation lengths (X_0) [44]. The crystal dimensions are such that most of one
 727 electromagnetic shower, and no more, can be contained in a single crystal, leading to
 728 excellent energy resolution for photons and electrons. The electromagnetic calorime-
 729 ter radial and endcap layers cover a pseudorapidity range up to 3.0. A lead/silicon
 730 sampling calorimeter sits in front of the crystal endcaps to provide better rejection
 731 of neutral pions.

732 The last layer of calorimetry inside the solenoid is the brass/scintillator sampling
 733 hadronic calorimeter, which has a radial extent from 1.77-2.95 m [44]. The hadronic
 734 barrel and endcap calorimeters cover up to $|\eta| = 3.0$, while the iron/quartz-fiber for-
 735 ward hadronic calorimeter covers the region $3.0 \leq |\eta| \leq 5.2$.¹ There is one more
 736 layer of hadronic calorimetry outside the solenoid in $|\eta| < 1.3$ which, together with
 737 the layers inside the solenoid, provides approximately 12 hadronic interaction lengths
 738 of instrumented absorber. Because of its large $|\eta|$ coverage and depth, the hadronic
 739 calorimeter provides good missing transverse energy resolution and accurate measure-
 740 ments of high energy jets.

741 The iron return yoke of the solenoidal magnetic field is interleaved with muon
 742 detectors from 4.1-7.4 m in r and 6.6-10.6 m in z , providing muon detection up to
 743 $|\eta| = 2.4$ [44]. In the barrel region of $|\eta| < 1.2$, drift tubes are used to read out the
 744 muon tracks, while in the endcaps cathode strip chambers are used. Due to their
 745 speed, resistive plate chambers are used throughout the muon system to provide
 746 an independent trigger and timing measurement. Combining the tracker and muon
 747 system hits, the momenta and charge of muons up to $p_T = 1$ TeV can be precisely
 748 reconstructed.

749 A longitudinal quarter cross-sectional view of CMS is shown in Figure 5.3. The
 750 remainder of this chapter is devoted to explaining the CMS subdetectors and readout

¹The Centauro and Strange Object Research (CASTOR) and Zero Degree Calorimeter (ZDC) detectors provide additional calorimetry beyond $|\eta| = 5.2$. However, they are mainly used in the heavy ion and diffractive physics programs of CMS, and play no role in the detection of heavy SUSY particles. Therefore, they will not be discussed here.

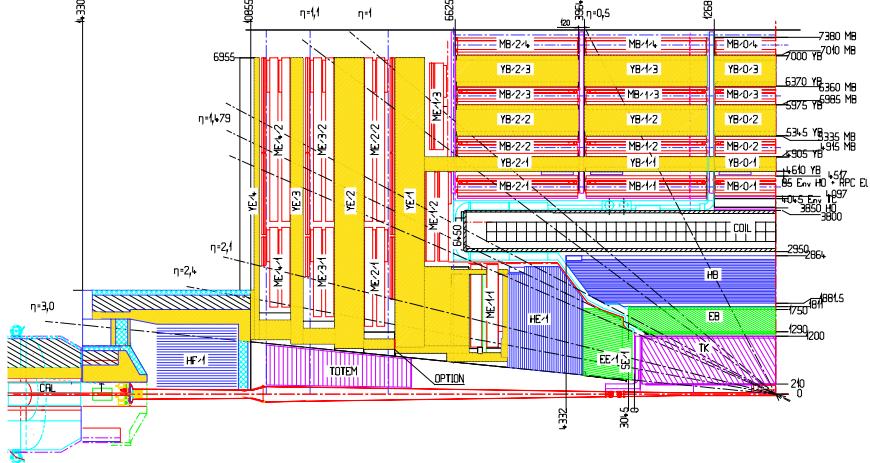


Figure 5.3: Longitudinal quarter cross-sectional view of CMS. The nominal interaction point is at the lower right-hand corner of the drawing. The tracker is shown in purple diagonal hashing, the electromagnetic calorimeter in green, the hadronic calorimeter in blue, and the muon stations in red. The solenoid is shown in black and white and labeled COIL, and the magnet return yoke is shown in yellow. Radial and longitudinal distances are measured in millimeters. Reprinted from Fig. CP 1 of ref. [45].

systems. Section 5.1 describes the subdetector technologies and performance benchmarks, while Section 5.2 details the CMS trigger and data acquisition systems and framework for promptly reconstructing and transferring data worldwide. For a thorough description of CMS, see ref. [44]. Unless otherwise noted, all information in this chapter comes from ref. [44].

5.1 The Detectors and Their Operating Principles

5.1.1 Tracking System

Given the LHC design instantaneous luminosity, efficient reconstruction of charged particle tracks from transverse momenta of 1 GeV up to 1 TeV can only be achieved with a low occupancy tracker. For $r < 10$ cm, the hit rate density is highest, leading to the choice of $100 \mu\text{m} \times 150 \mu\text{m}$ silicon pixel sensors for hit detection. For $20 \text{ cm} < r < 110 \text{ cm}$, the lower hit rate allows the use of silicon strips, with length along z of

763 order centimeters and length along the $r \cdot \phi$ curve of order hundreds of microns. This
 764 design leads to a pixel hit occupancy of $\sim 10^{-4}$ /pixel/BX and a strip hit occupancy
 765 of $\sim 10^{-2}$ /pixel/BX, where BX refers to 1 LHC bunch crossing.

766 As radiation dose from hadrons accumulates over the lifetime of the tracker, silicon
 767 leakage current through the semiconductor junctions increases, heating up the sensors.
 768 Since the leakage current itself depends on temperature, this can lead to *thermal*
 769 *runaway* that damages the detector. To avoid this, the tracker must be cooled to
 770 approximately -10°C . Operating at this temperature, the signal:noise ratio in the
 771 silicon sensors is 10:1, and should remain at that level over the 10-year lifetime of the
 772 tracker.

773 At its thickest ($|\eta| \sim 1.5$), the tracker depth (including services) is $\sim 1.8X_0$,
 774 and the depth falls off to $\sim 1X_0$ in thinner areas. Unfortunately, the large mass of
 775 the tracker degrades somewhat the performance of the electromagnetic calorimeter
 776 behind it, as $\sim 50\%$ of photons will convert to e^+e^- pairs in the tracker.

777 Pixel Detector

778 A longitudinal quarter view of the three barrel pixel (BPix) layers and two forward
 779 pixel (FPix) disks is shown in Figure 5.4. There are 768 BPix modules in total.
 780 Each BPix layer is divided into 32 ϕ -wedges, with eight modules per wedge arranged
 781 end-to-end in z . The ϕ -wedges operate nearly independently in terms of clock and
 782 readout. Each FPix disk consists of 24 ϕ -wedges, with pie-shaped modules attached
 783 to the front and back of the disk, for a total of 192 modules. The front- and back-side
 784 modules of the FPix disks are constructed of different sized *plaquettes*, or multi-pixel
 785 sensor chips, such that the gaps in the front-side module are covered by plaquette
 786 area in the back-side module and vice versa. An illustration of the BPix and FPix
 787 mechanical layouts is given in Figure 5.5.

788 Since the electric field in the depletion region of the BPix sensors is perpendicular

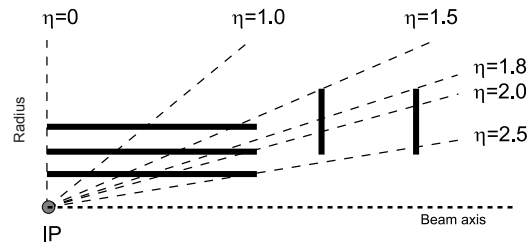
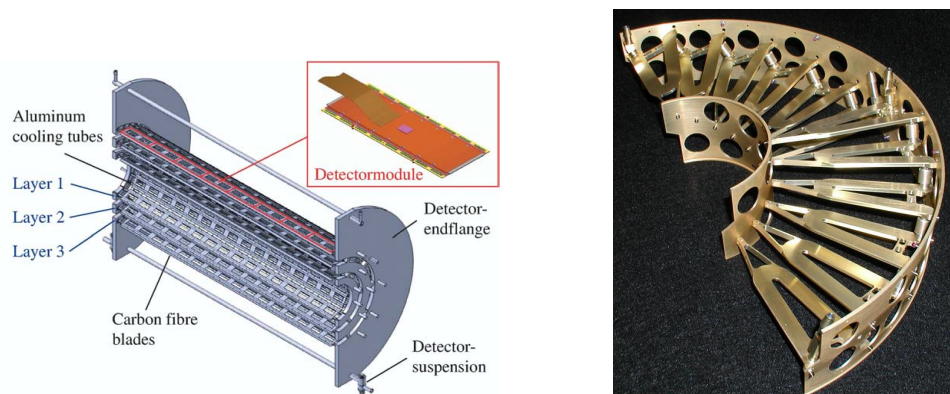


Figure 5.4: Longitudinal quarter view of the pixel detector. Reprinted from Fig. 3.6 of ref. [44].



(a) Cutaway view of the barrel pixel layers, showing the three layers and the eight end-to-end modules along z . Reprinted from Fig. 3.11 of ref. [44].

(b) Half-disk of the forward pixel detector, showing the 12 pie-shaped module mounts. Reprinted from Fig. 3.15 of ref. [44].

Figure 5.5: BPix and FPix mechanical structures.

789 (i.e. pointing along r) to the magnetic field of CMS (i.e. pointing along z), the charge
 790 carriers in the silicon experience a Lorentz drift along ϕ . The multi-pixel sensor pitch
 791 is such that this causes the charge from one particle hit to be shared among multiple
 792 pixels. Particle hits are reconstructed reading out the analog pixel signal and inter-
 793 polating between signals in multiple pixels. This method achieves a $15\text{-}20 \mu\text{m}$ spatial
 794 resolution, which is comparable to the sensor pitch. To induce this effect in FPix,
 795 the sensor wedges are tilted by the approximate BPix Lorentz angle of 20° [46] with
 796 respect to the y -axis.

797 Each multi-pixel sensor consists of an array of 52×80 n-type pixels implanted onto
 798 an n-type substrate with $320 \mu\text{m}$ thickness. The other face of the substrate is covered
 799 with a thin layer of p-type semiconductor. Except for the outer edges, which are held
 800 at ground potential to prevent sparking between the sensor edges and the connected
 801 readout chip [47], the p-side is reverse biased at 150 V (BPix) or 300 V (FPix). The
 802 pixels are held at ground potential. A particle entering through the p-side will cause
 803 a burst of current to flow across the p-n junction. The charge will be collected by the
 804 pixels, which are bump-bonded to the readout. The BPix and FPix sensors employ
 805 slightly different technologies for electrically isolating the individual pixels, but both
 806 rely on the idea of surrounding the pixels with a p-type material to provide a p-n
 807 junction that acts as a barrier to current flow.

808 Each 52×80 pixel sensor is bump bonded to a readout chip (ROC). The ROCs
 809 provide zero suppression and amplify, buffer, and communicate the signals from the
 810 sensors. A single token bit manager (TBM) controls ~ 16 ROCs in the barrel or ~ 24
 811 ROCs in the endcaps. Its purpose is to distribute the clock and trigger to the ROCs
 812 (the latter initiates a transmission of the signal further upstream to be assembled
 813 into the full event readout of CMS). The clock and trigger are supplied by the pixel
 814 front end controller (pFEC), which interfaces to the central clock and data acquisition
 815 systems. Analog signals that are collected from the pixel front ends are digitized by

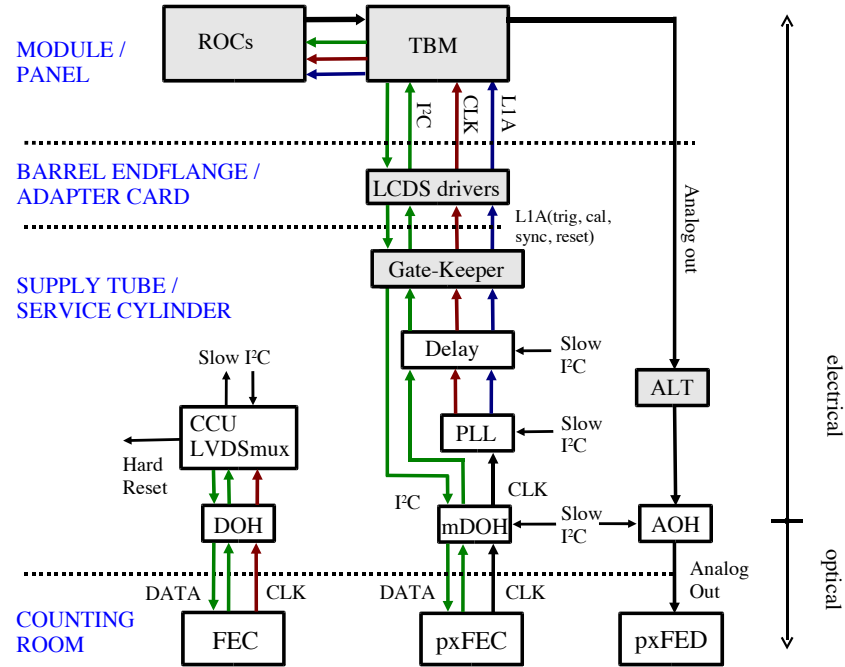


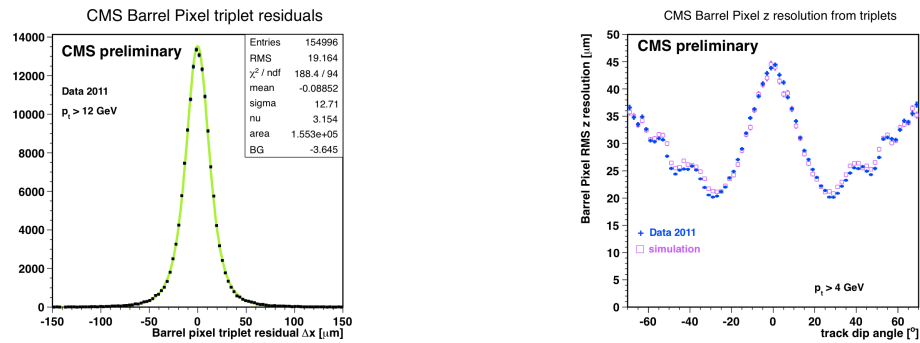
Figure 5.6: Pixel control and readout system. Reprinted from Fig. 3.9 of ref. [44].

816 the pixel front end digitizer (pxFED). A diagram of the readout system is shown in
 817 Figure 5.6.

818 Figure 5.7 shows some results highlighting the performance of the pixel detector.

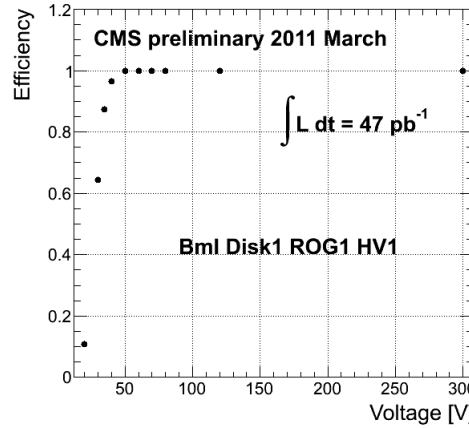
819 Silicon Strip Tracker

820 The silicon strip tracker is divided into four parts: the inner barrel (TIB) and inner
 821 disks (TID), covering the radial extent $20 \text{ cm} < r < 55 \text{ cm}$ and z extent $80 \text{ cm} <$
 822 $|z| < 90 \text{ cm}$; and the outer barrel (TOB) and endcap (TEC), covering the radial
 823 extent $61 \text{ cm} < r < 108 \text{ cm}$ and z extent $124 \text{ cm} < |z| < 282 \text{ cm}$. A number of the
 824 tracker layers and endcaps hold double-sided strip modules (shown as double lines
 825 in Figure 5.8), with the rear module tilted at an angle of 100 mrad with respect to
 826 the front module, to provide a measurement in two coordinates. There are a total of
 827 15,148 modules in the tracker, arranged as shown in the longitudinal cross-sectional
 828 view of Fig. 5.8. For the TIB and TOB, the modules are arranged in straight rows



(a) BPix hit resolution in the $r \cdot \phi$ coordinate [48].

(b) BPix hit resolution in the z coordinate vs. track dip angle, showing the effect of charge sharing on resolution [49].



(c) Pixel reconstruction efficiency vs. bias voltage for a group of three wedges in FPix [50].

Figure 5.7: Pixel detector performance highlights.

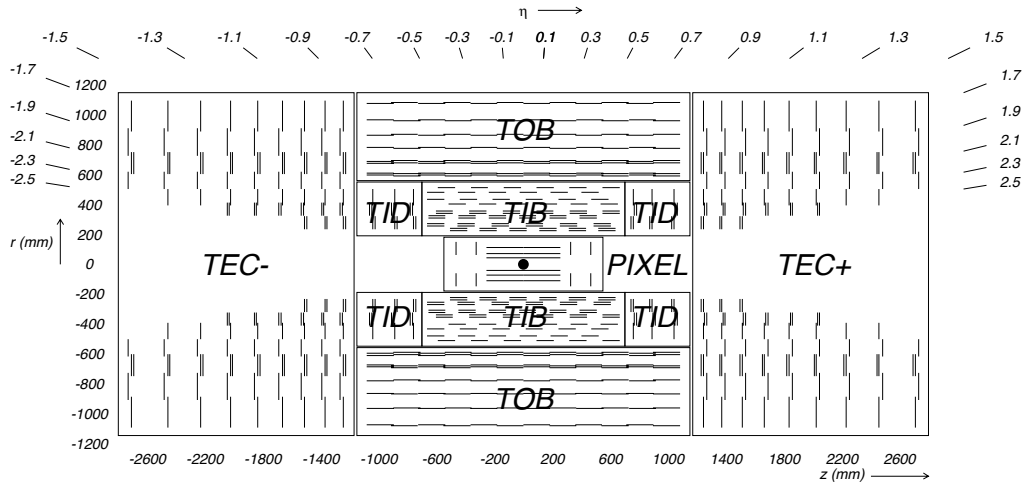


Figure 5.8: Longitudinal cross section of the silicon strip detector. Reprinted from Fig. 3.1 of ref. [44].

end-to-end along z , with repeating rows covering the full 2π extent in ϕ . In each of the TID disks, the modules are arranged into three concentric circular rings of increasing r . In the TEC, the modules are affixed to ϕ -wedges called *petals*. One side of the TEC and its petal structure is shown in Figure 5.9.

Like the pixels, the strip sensors generate a signal when current flows across a p-n junction in response to interaction with a charged particle. Whereas the pixels are n-type implants on an n-type substrate, with a solid p-type rear layer to which the high voltage is connected, the strips are p-type implants on an n-type substrate, with a solid n-type rear layer connecting to the high voltage. The p-n junction in the strip sensors is at the strip-substrate boundary, whereas in the pixel sensors it is at the boundary between the rear layer and the substrate. Each sensor has either 512 or 768 electrically isolated strips, with pitch varying from 80-205 μm depending on location. Strip lengths in z range from ~ 10 to ~ 25 cm. Thin (320 μm) sensors are used in the TIB, TID, and inner four rings of the TEC, while thick (500 μm) sensors are used in the TOB and the outer rings of the TEC. The thicker sensors compensate for the increased strip capacitance (and hence electronics noise) of the longer strips in the outer layers/disk of the tracker such that strip signal:noise is maintained above

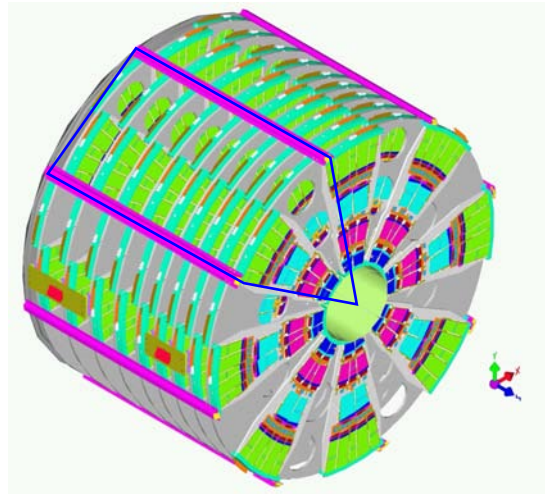


Figure 5.9: View of one tracker endcap, with the outline of a petal shown in blue. There are nine petals per wedge-shaped sector (one per TEC disk). Reprinted from Fig. 3.30 of ref. [44].

846 10 everywhere.

847 The strips are wire bonded to a front end readout chip called the APV25. The
 848 APV25 amplifies and shapes the strip signals before sending the full analog pulse
 849 information to an APVMUX, which multiplexes the output of two APV25s. Then,
 850 the electrical signal from the APVMUX is sent differentially a few centimeters to an
 851 optical driver, where it is converted to an optical signal and sent to one of the 450
 852 front end drivers (FEDs). The FEDs convert the signal back to an electrical pulse
 853 and digitize it for use in the global event assembly. As for the pixels, analog readout
 854 is used on detector so that hit reconstruction may benefit from charge sharing.

855 Clock, trigger, and control signals are sent from the front end controllers (FECs)
 856 to phase locked loop (PLL) chips on the front ends. The FECs interface to the global
 857 clock and trigger system. Four or six APV25s, an APVMUX, and a PLL chip all sit on
 858 a *hybrid*, two which one thin or two thick sensors are also affixed. The sensor-hybrid
 859 combination and its frame form a module. Figure 5.10 shows a diagram of a module,
 860 while Figure 5.11 shows a block diagram of the strip readout architecture.

861 As an example of the strip capabilities, strip hit resolution and signal:noise mea-

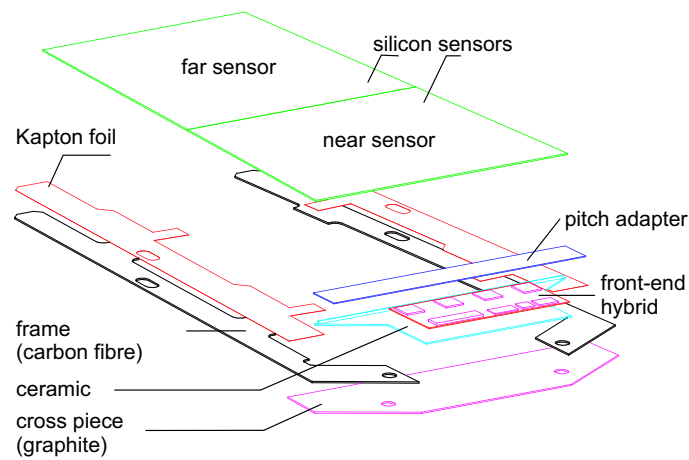


Figure 5.10: Exploded view of a strip module with two sensors. Reprinted from Fig. 3.22 of ref. [44].

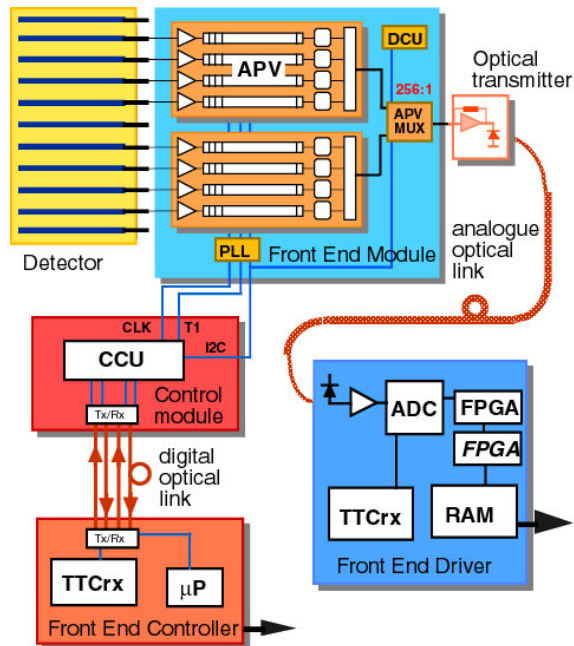


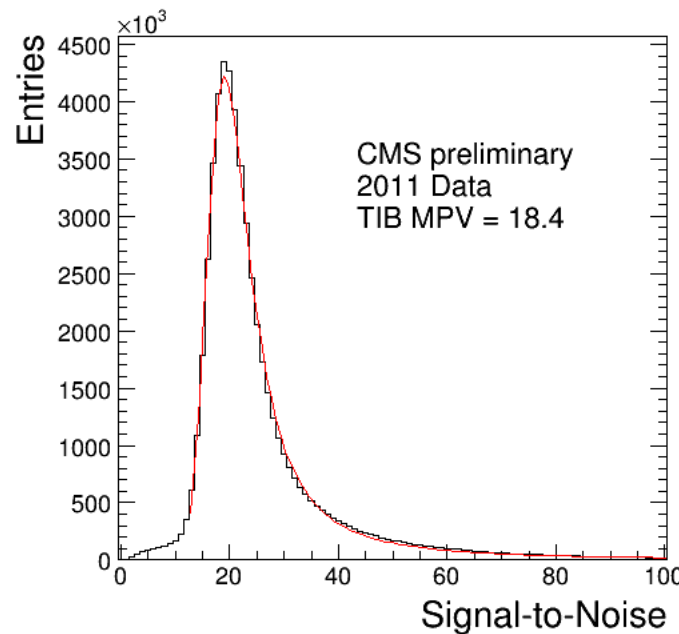
Figure 5.11: Block diagram of the strip readout architecture. Reprinted from Fig. 3.20 of ref. [44].

surements are shown in Figure 5.12. The entire pixel + strip tracker has been used successfully in the reconstruction of primary and secondary vertices, electrons, muons, tau decays, and charm and bottom hadron decays. In addition, the superior performance of the tracker over the hadronic calorimeter for low energy charged hadrons has been exploited in the the particle flow jet and \cancel{E}_T reconstruction technique (see Sec. 6.1.3). The CMS silicon strips, as well as the pixels, are well aligned and operating at close to design performance.

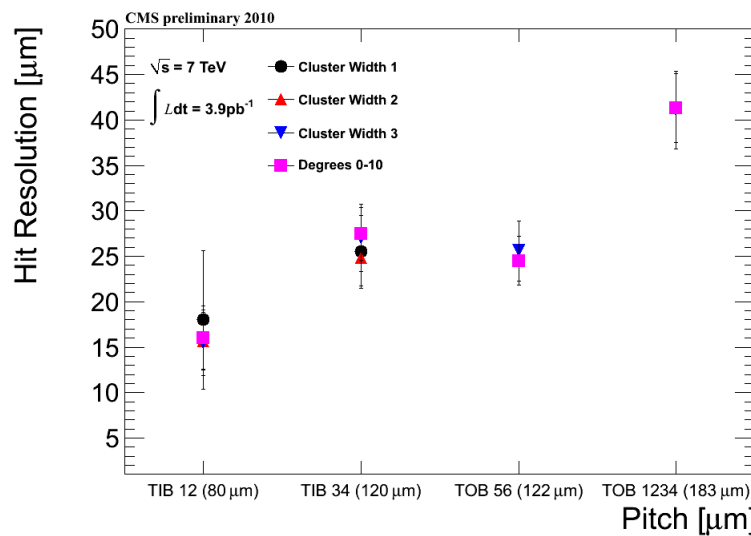
5.1.2 Electromagnetic Calorimeter

The electromagnetic calorimeter (ECAL) is composed of 68,524 lead tungstate (PbWO_4) crystals, divided into one barrel (EB) layer and two endcap (EE) disks. In EB, there are 1700 crystals per *supermodule* (SM), arranged in a 20×85 grid in $\phi \times \eta$. Two SMs are laid out end-to-end to form one row at fixed ϕ , with a total of 18 rows needed to cover the entire 2π extent in ϕ . The SMs may be operated independently. In EE, the independent unit is a wedge-shaped sector, with nine sectors covering each endcap side. The 7,324 EE crystals are divided approximately evenly between the 18 EE sectors. A two-layer preshower detector is placed in front of the EE disks, each layer consisting of a lead absorber followed by 1.9 mm pitch silicon strip detectors (the strips in the first layer are rotated 90° with respect to the second layer). The ECAL layout is shown in Figure 5.13.

The electromagnetic energy resolution can be parametrized as $(\sigma/E)^2 = (S/\sqrt{E})^2 + (N/E)^2 + (C)^2$, where S characterizes the size of photostatistical fluctuations, N characterizes the contribution from electronics noise, and C is a constant accounting for imperfect intercalibration between crystals, non-uniformity of crystal performance, and incomplete shower containment within one crystal. The design goal of the ECAL is to achieve $C = 0.5\%$. Therefore, fast, dense, and relatively radiation hard PbWO_4 was chosen as the crystal material. When a photon or electron strikes the crystal, it



(a) TIB signal:noise [51].



(b) TIB and TOB hit resolution as a function of strip pitch [52].

Figure 5.12: Strip detector performance highlights.

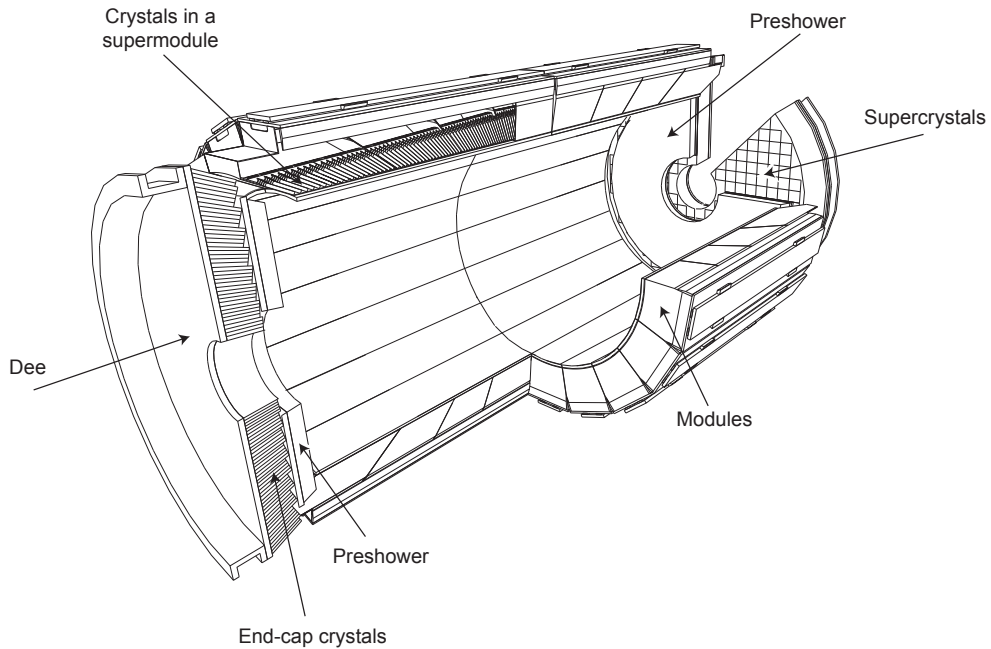


Figure 5.13: Layout of the ECAL detector. Reprinted from Fig. 4.5 of ref. [44].

888 initiates an electromagnetic (EM) shower. Due to the density, short radiation length,
 889 and small Molière radius of PbWO_4 , nearly the entirety of an EM shower can be
 890 contained in a single 23-cm long crystal with front face dimensions $2.2 \text{ cm} \times 2.2 \text{ cm}$.
 891 The crystals scintillate in the blue-green part of the spectrum, emitting $\sim 80\%$ of the
 892 scintillation light within 25 ns. Light is transmitted along the length of the crystals
 893 and collected at the rear with avalanche photodiodes (semiconductor diodes) in EB or
 894 vacuum phototriodes (conventional photomultipliers) in EE. Since the light output is
 895 low and varies with temperature, the crystals must be kept precisely at 18°C . The EB
 896 and EE crystals, which are slightly tapered to match the lateral shower development,
 897 are shown in Figure 5.14.

898 For each trigger, 10 samples, each separated by 25 ns, are read out. The 10-sample
 899 pulse is amplified and shaped by a multi-gain preamplifier (MGPA) residing on a very
 900 front end (VFE) card serving five crystals. The MGPA can switch between gains 1,
 901 6, and 12 to avoid saturation of the electronics, and affords a dynamic range up to

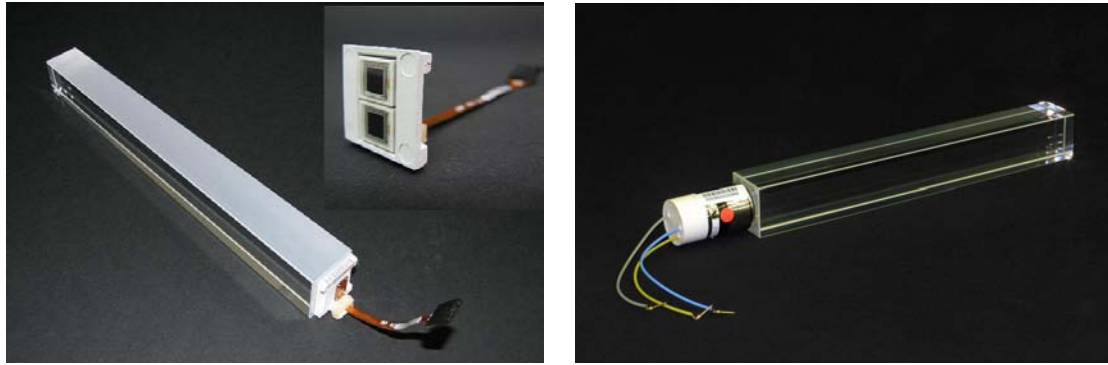


Figure 5.14: Left: EB crystal with attached APD. Right: EE crystal with attached VPT. Reprinted from Fig. 4.2 of ref. [44].

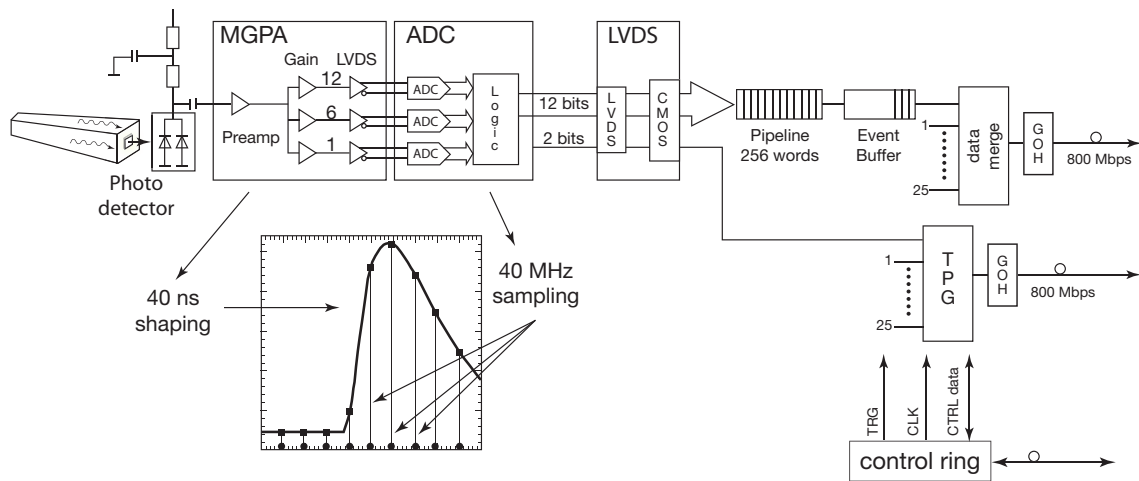


Figure 5.15: Flow chart of the crystal readout, showing the 10-sample pulse shape. Reprinted from Fig. 4.9 of ref. [44].

902 3 TeV. The samples are digitized on the VFE card, then sent to the front end (FE)
 903 card serving five VFEs. Digitized samples are buffered in the FE card until receipt
 904 of a trigger, when they are sent over an optical link to the data concentrator card
 905 (DCC) that interfaces to the global DAQ. The DCC interfaces to the *selective readout*
 906 processor, which decides whether a crystal should be read out with or without zero
 907 suppression based on its proximity to a high-energy hit. The clock is transmitted to
 908 the FE cards from the Clock and Control System (CCS) boards. A flow chart of the
 909 crystal readout is given in Figure 5.15.

At each bunch crossing, the trigger concentrator cards (TCC) of the ECAL compute *trigger primitives* from 5×5 non-overlapping transverse energy sums (in the endcaps the geometry is not always 5×5). This information, along with a special bit in EB only characterizing the transverse shower profile that is used for rejection of anomalous APD hits (see Sec. 6.1.1), is transmitted from the TCCs to the synchronization and link boards (SLBs), and then on to the global trigger system. The trigger decision is communicated to the DCCs, which request the buffered data from the front ends if the decision is affirmative.

Despite the radiation hardness of lead tungstate relative to other types of crystals, it still suffers from transparency loss due to radiation-induced lattice damage, as shown in Figure 5.16. In addition, any unforeseen change in the gains of the MGPAs and VPTs, or in the pedestal levels, will degrade the energy resolution. For this reason, a continuously running calibration system is installed with the ECAL. The system makes use of the LHC abort gaps to read out the pedestal levels, test pulses fired into the MGPAs, and laser (EB and EE) or LED (EE only) pulses fired into the crystals at regular intervals. Laser and LED events are used to compute corrections to the crystal gains for transparency loss, while the other types of calibration events serve to monitor changes in the electronics performance due to magnetic field or high voltage cycling. The mean time between transparency measurements is ~ 40 minutes. Figure 5.17 shows the architecture of the laser monitoring system.

The current ECAL energy resolution is somewhat worse than the design goal of 0.5%. An incomplete understanding of (a) the transparency loss and (b) the photon conversion and electron bremsstrahlung processes in the $\sim 1X_0$ of tracker material in front of the ECAL are the main limiting factors in improving the resolution. However, as more data accumulate, more refined models of transparency loss and EM interactions in the tracker can be built, leading to better resolution. Energy resolution vs. $|\eta|$ can be seen in Figure 5.18.

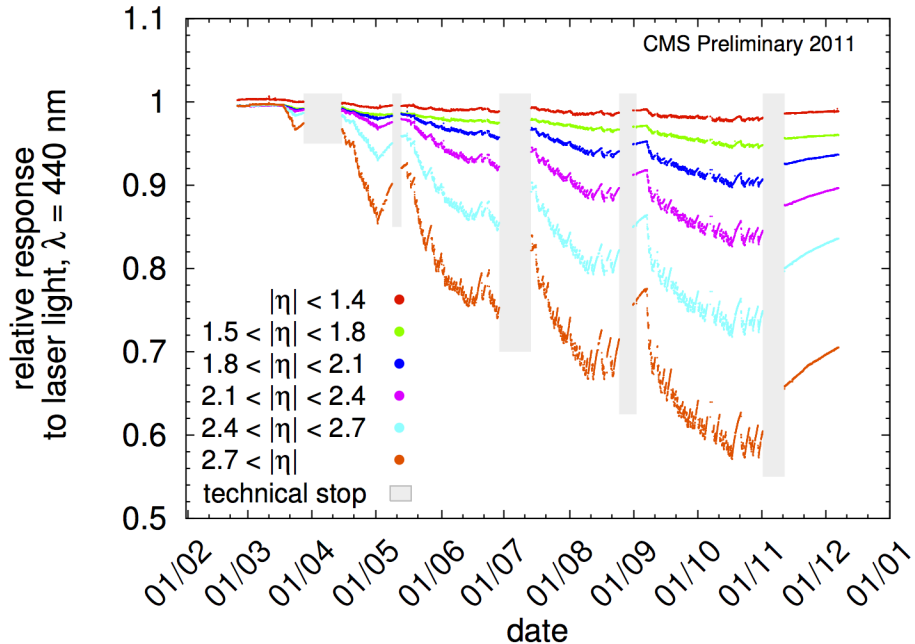


Figure 5.16: Relative response of the crystals to blue laser pulses from February 1, 2011 to January 1, 2012 [53]. Technical stops, during which the LHC is turned off for maintenance and development, are shown in gray. These periods of inactivity correspond to growth in the crystal response, as radiation damage recovery occurs.

937 The 10-sample readout coupled with the fast scintillation time of lead tungstate
 938 allows for a very precise reconstruction of the time of ECAL hits. ECAL timing is used
 939 for searches for long-lived particles that decay to photons or jets, such as long-lived
 940 neutralinos in GMSB [?]. Figure 5.19 shows the timing resolution in EE.

941 5.1.3 Hadronic Calorimeter

942 The CMS hadronic calorimeter (HCAL) has four parts: HCAL barrel (HB), HCAL
 943 endcap (HE), and HCAL outer (HO), which all utilize the same brass absorber /
 944 plastic scintillator sandwich technology; and HCAL forward (HF), which is a Čerenkov
 945 detector made of quartz fibers. A quarter longitudinal cross-sectional view of HCAL
 946 is shown in Figure 5.20. Like EB, HB is formed of 36 ϕ -wedges (18 cover 2π in positive
 947 η , 18 cover 2π in negative η). Each wedge is divided into 16 along η and four along
 948 ϕ , for a total of 64 readout towers per wedge (compare 1700 individually read out

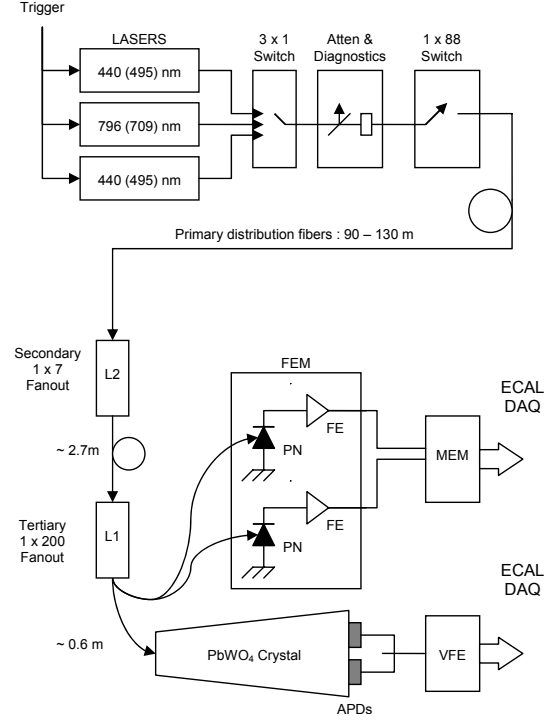


Figure 5.17: Architecture of the laser monitoring system. Reprinted from Fig. 4.16 of ref. [44].

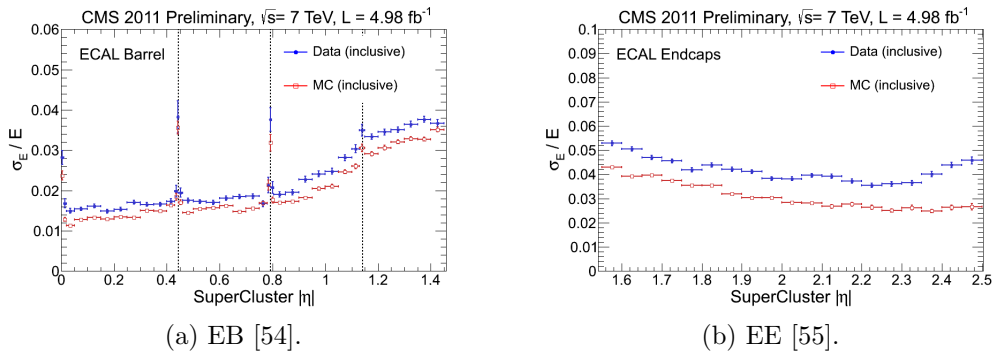


Figure 5.18: Energy resolution vs. $|\eta|$ for Z decay electrons for data (filled blue circles) and MC (empty red squares). The dotted lines show the locations of module gaps (three per SM).

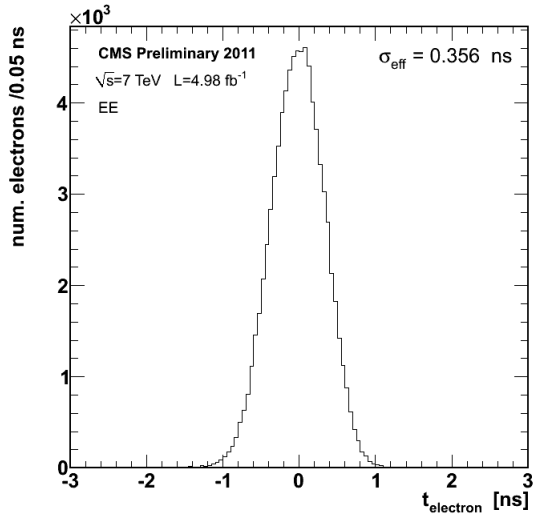


Figure 5.19: Distribution of reconstructed times of Z decay electrons in EE [56].

949 crystals per EB wedge). HE is divided into 36 ϕ -wedges containing 38 readout towers
 950 each. HO consists of five rings around HB and HE distributed symmetrically along z .
 951 There are 72 ϕ -slices per ring, with each ϕ -slice further divided into 5, 6, or 8 along
 952 z depending on ring. The HF fibers are distributed within the steel absorber. HF is
 953 divided into 18 ϕ -wedges per endcap side, each containing 24 readout towers. All HB
 954 towers have a single readout channel except for the two in each wedge at highest $|\eta|$,
 955 which are segmented into two longitudinal layers for readout. In HE, all towers have
 956 two longitudinal readout layers, except for the three rings of towers closest to the
 957 beam line, which have three. There are also two longitudinal depths of HF fibers.

958 HB, HE, and HO are all sampling calorimeters consisting of alternating layers of
 959 brass absorber and plastic scintillator. The absorber initiates the hadronic shower,
 960 and as shower particles travel through the scintillator the scintillation light is read
 961 out by wavelength-shifting (WLS) fibers connected to the scintillator tiles.² The full
 962 development of the shower is sampled by the layers of instrumented scintillator. The
 963 scintillator tiles are staggered so that there are no cracks in coverage along the direc-

²By contrast, in the ECAL, the crystal material acts as both absorber and scintillator, greatly reducing the contribution to energy resolution from sampling fluctuations.

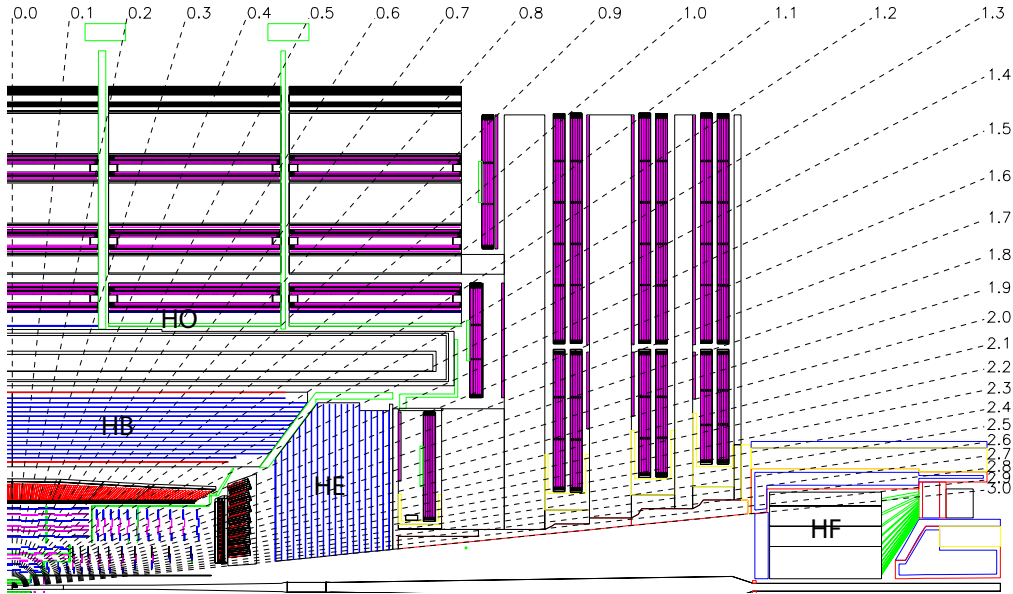


Figure 5.20: Quarter longitudinal cross-sectional view of HCAL (and muon stations in purple). Reprinted from Fig. 5.1 of ref. [44].

tion projected back to the beam spot. Light output from all tiles in a single readout tower is collected via the WLS fibers and merged into a single signal that is amplified by a hybrid photodiode (HPD). A diagram of the optical readout of HB (similar for HE and HO) is shown in Figure 5.21.

Due to the extremely harsh radiation environment near the beam line, HF is constructed of a 1.2-m thick, 1.7-m long ring of steel absorber with radiation hard quartz fibers distributed within the steel and running parallel to the beam line. Hadronic showers develop in the steel and are sampled in the quartz fibers when charged shower particles hit the the fibers and emit Čerenkov light. The light is transmitted by total internal reflection down the fibers to a photomultiplier tube (PMT), where the signals from all fibers in an HF tower are merged into one. Since only relativistic particles emit Čerenkov light in these fibers, it is mostly the EM component of the hadronic shower, consisting of neutral pions decaying to photons that interact electromagnetically with the absorber, that is sampled [57]. The charged hadrons produced in hadronic showers are typically too slow to generate Čerenkov light. Figure 5.22

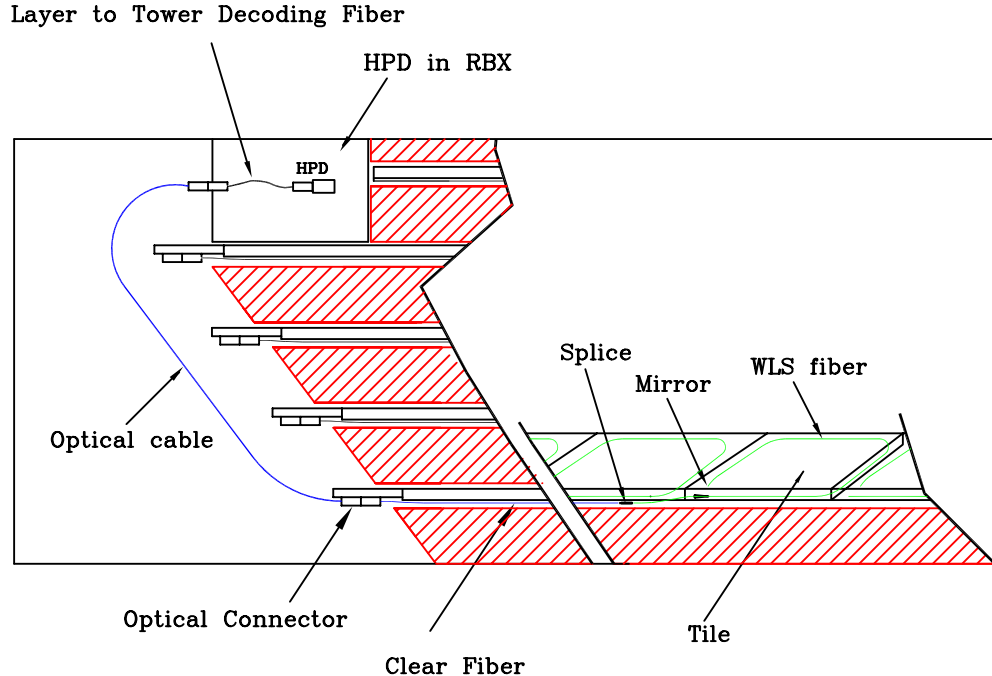


Figure 5.21: Diagram of the optical readout of HB. Reprinted from Fig. 5.7 of ref. [44].

979 shows a cross-sectional view of one side of HF.

980 Electrical signals from either HPDs (HB/HE/HO) or PMTs (HF) are digitized on
 981 the front ends by means of a fast charge-integrating ADC. The digitized signals are
 982 sent off-detector to the HCAL Trigger/Read-Out (HTR) boards, where they await a
 983 trigger decision. If the trigger is accepted, the signals are sent on to the HCAL data
 984 concentrator cards (DCCs), which interface to the global DAQ system. HCAL trigger
 985 primitives, consisting of transverse energy sums over an entire tower, are calculated
 986 in the HTR boards and sent to the global trigger system.

987 Selected HCAL performance results can be seen in Figure 5.23.

988 5.1.4 Muon System

989 Beginning at a radius of ~ 10 interaction lengths from the beam line, where all parti-
 990 cles except muons should have been stopped by the HCAL, are the muon chambers,
 991 interspersed with the iron return yoke of the CMS magnetic field. Three technologies

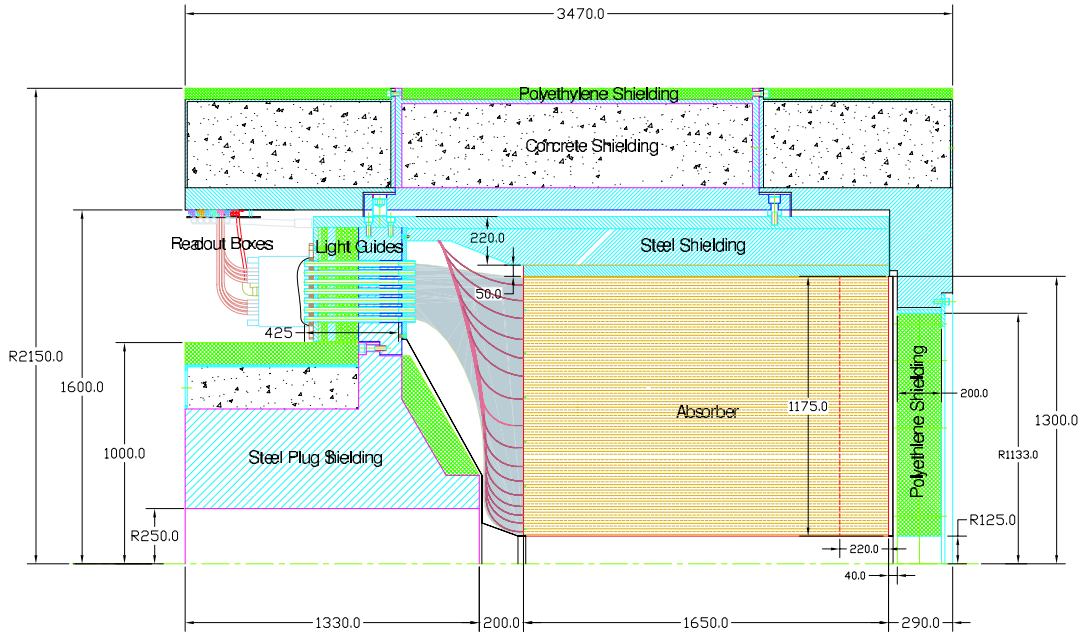
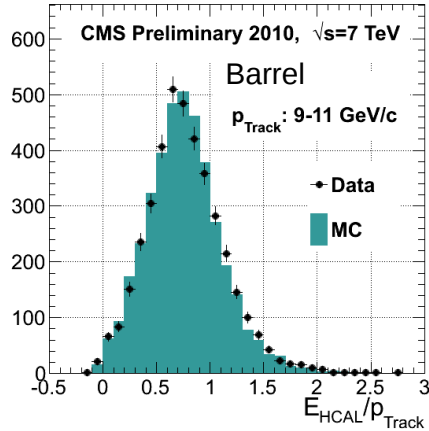


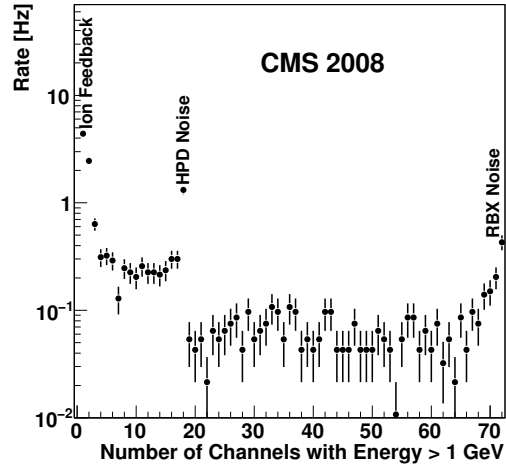
Figure 5.22: Cross-sectional view of one side of HF. The z -axis is horizontal. Reprinted from Fig. 5.28 of ref. [44].

are employed: drift tubes in the barrel section (MB), cathode strip chambers (CSCs) in the endcap section (ME), and resistive plate chambers (RPCs) in both sections to provide an independent trigger with superior time resolution. There are four barrel layers of stations extending out to $|\eta| = 1.2$. Each endcap consists of five disks of stations as shown in Figure 5.24b, covering $1.4 < |\eta| < 2.4$. RPCs populate the barrel and endcap muon systems alongside the DT chambers and CSCs. Since they have time resolution much better than a few ns, they are used to assign the bunch crossing of muon tracks and provide a p_T trigger with sharp turn-on.

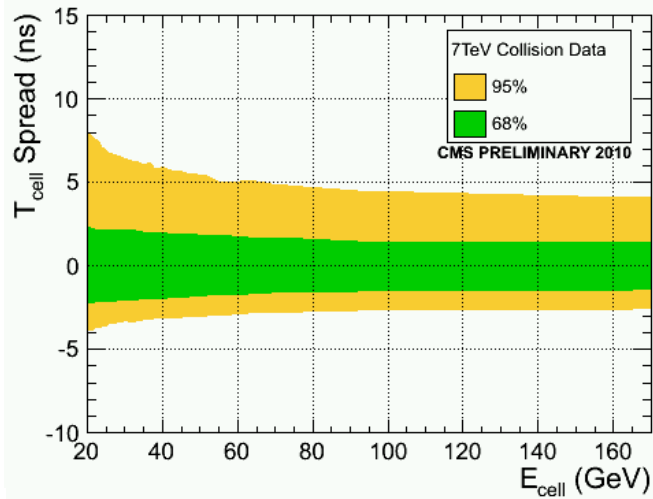
Each DT chamber consists of two $r \cdot \phi$ superlayers (SLs) and optionally one z SL (in all chambers except those in the fourth layer). The SLs contain four rows of drift tubes, with the rows staggered such that there are no gaps in the coverage. The $r \cdot \phi$ SLs have the tube axis parallel to the beam line, while the z SL is perpendicular to the beam line. The tubes are ~ 2.4 m in length and $13 \text{ mm} \times 42 \text{ mm}$ in cross section. Each chamber therefore records eight $r \cdot \phi$ tracking points and optionally four



(a) Data/MC comparison of HB response to charged tracks of 9-11 GeV/c momentum [58].

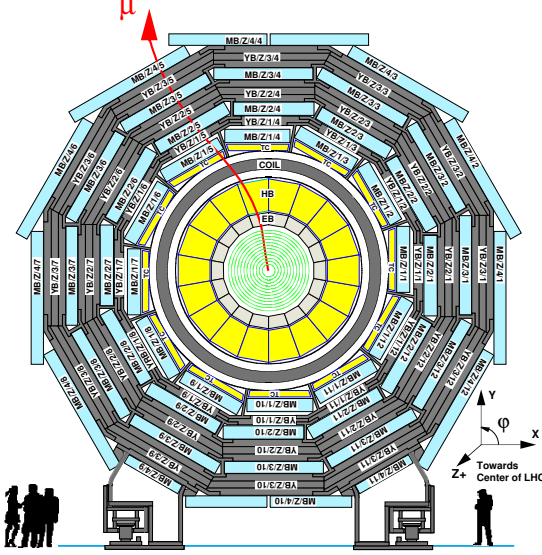


(b) Distribution of tower multiplicity, clearly showing three peaks in rate corresponding to noise sources (see Sec. 6.3) [98].

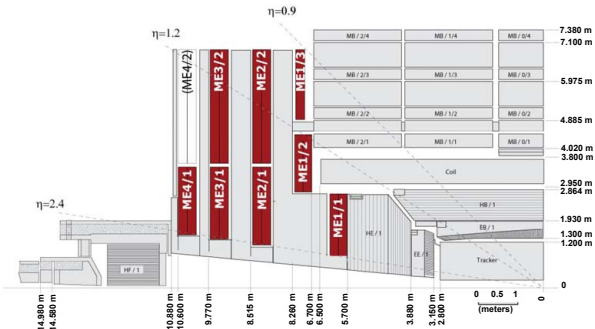


(c) Timing resolution vs. tower energy [58].

Figure 5.23: Selected HCAL performance results.



(a) One of the five wheels of MB, showing the four layers of muon stations. The five wheels are spaced symmetrically in z about $z = 0$. As a muon traverses the muon detectors, its curvature in the transverse plane changes direction and magnitude due to the magnetic field in the return yoke, which is of opposite sign and reduced strength relative to the field within the solenoid volume. Reprinted from Fig. 7.3 of ref. [44].



(b) Quarter longitudinal cross section of CMS highlighting the location of the ME disks. Reprinted from Fig. 7.47 of ref. [44].

Figure 5.24: View of the MB and ME layout in CMS.

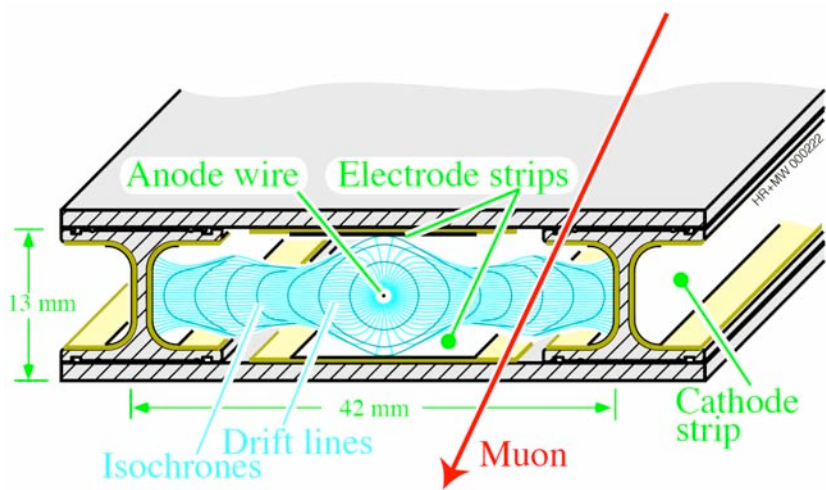


Figure 5.25: Electric field lines within a drift tube as well as the contours of equal drift time. Reprinted from Fig. 7.5 of ref. [44].

1006 z tracking points. The tubes are filled with an 85%Ar + 15% CO₂ gas mixture. An
 1007 anode wire at 3600 V runs the length of the tube, while the walls are covered with
 1008 electrodes held at 1800 V or -1200 V depending on wall. When a muon passes through
 1009 the tube, it ionizes the gas atoms. The liberated electrons drift along the electric field
 1010 lines created by the electrodes to the anode, which is read out. Figure 5.25 shows
 1011 the electric field lines within a drift tube as well as the contours of equal drift time.
 1012 The maximum drift time is 380 ns.

1013 CSCs consist of alternating layers of cathode strips (four planes oriented along r)
 1014 and anode wires (three planes oriented along ϕ). A 40%Ar + 50%CO₂ + 10%CF₄ gas
 1015 mixture fills the space between two successive planes, forming six gas gaps. When a
 1016 muon ionizes the gas atoms, the positive ions drift toward the anode and are read
 1017 out to provide a measurement of r , just as in the DTs. However, an image charge is
 1018 induced on the cathode strips, which is also read out to provide a measurement of ϕ .
 1019 The wires are spaced 3.2 mm apart. The cathode strips have pitch varying from 8.4
 1020 mm at the end closest to the beam line to 16 mm at the other end, and are spaced
 1021 0.5 mm apart. A trapezoidal CSC is shown in Figure 5.26.

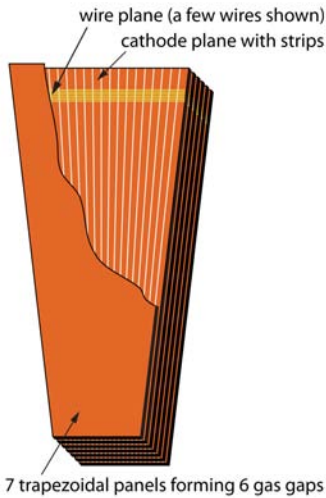


Figure 5.26: CSC wedge, showing the cathode and wire planes. Reprinted from Fig. 7.49 of ref. [44].

1022 Track stubs from the muon system are combined with tracks from the tracking
 1023 system to form more precise muon tracks than either system could form alone, as
 1024 shown in Figure 5.27. This leads to extremely good di-muon invariant mass resolution
 1025 (Figure 5.28) over a large p_T range.

1026 **5.2 Triggering, Data Acquisition, and Data Trans-** 1027 **fer**

1028 **5.2.1 Level 1 and High Level Trigger Systems**

1029 The Level-1 (L1) trigger system, which encompasses dedicated hardware processors
 1030 to construct trigger objects (typically high p_T jets, electrons, photons, taus, and
 1031 muons) out of the calorimeter and muon hits, distributes a L1 accept or reject to all
 1032 subdetectors at the LHC bunch crossing frequency of 40 MHz. Further data filtering
 1033 is performed by the High Level Trigger (HLT) system, a farm of ~ 1000 commercially
 1034 available processors running a slimmed down version of the CMS event reconstruction

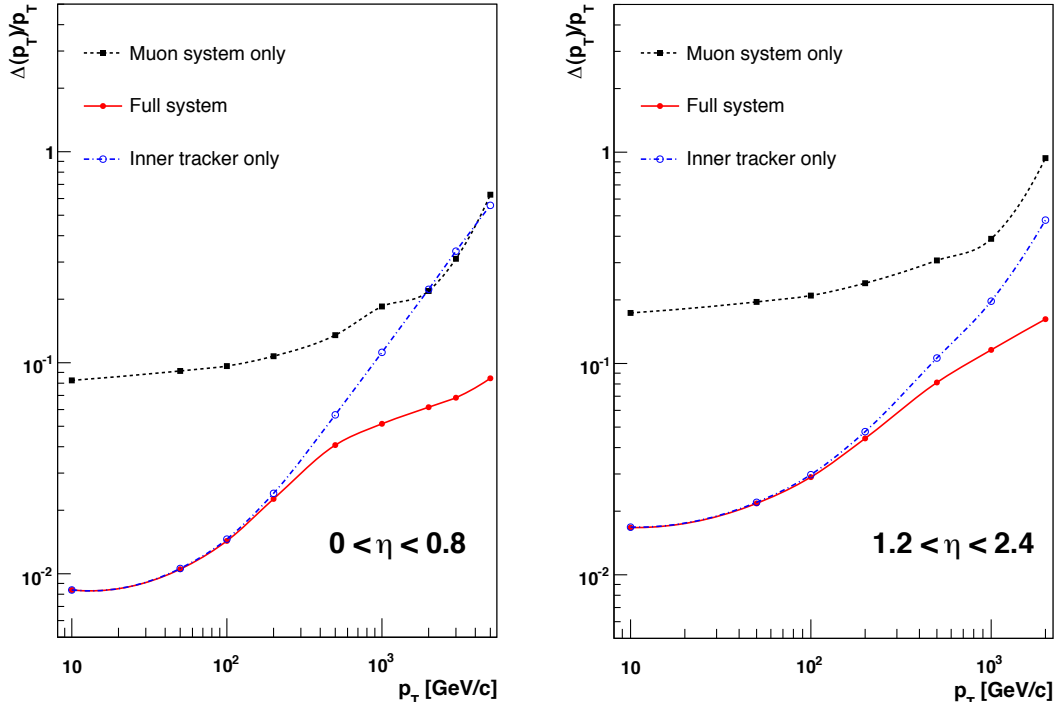


Figure 5.27: Muon p_T resolution as a function of muon p_T for tracker information only (blue), muon information only (black), and both tracker and muon information combined (red). Reprinted from Fig. 1.2 of ref. [44].

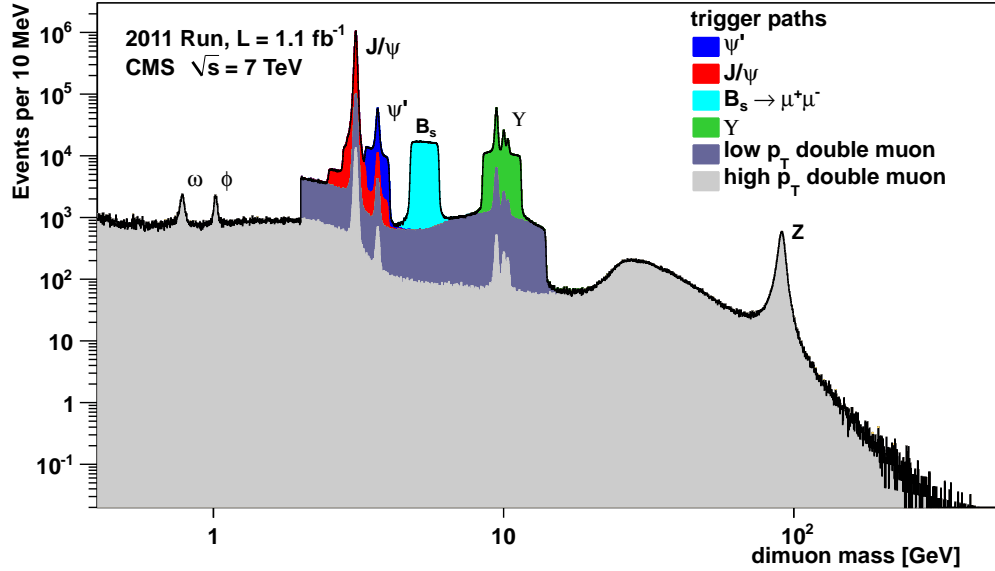


Figure 5.28: Di-muon invariant mass spectrum broken down by trigger path [59]. The light(dark) gray regions show the contribution from high- p_T (low- p_T) di-muon triggers. Note that no $B_s \rightarrow \mu^+\mu^-$ decays have been observed [60]; the light blue region just shows the amount of triggers dedicated to the $B_s \rightarrow \mu^+\mu^-$ search.

1035 software CMSSW. The data rate received by the HLT is ~ 100 kHz; the output rate of
 1036 events permanently written to disk is ~ 100 Hz. An L1 trigger *latency* (time between
 1037 the collision and the distribution of the L1 decision to the subdetectors) of $3.2\ \mu\text{s}$ is
 1038 achieved via the use of fast electronics and sufficiently deep buffers to pipeline trigger
 1039 primitives waiting to be analyzed. This latency corresponds to the length of the LHC
 1040 abort gap, so in principle CMS may be operated with zero *dead time* (during which
 1041 LHC bunches are missed because the L1 system is blocked while processing other
 1042 triggers).

1043 At the bottom, the L1 trigger consists of trigger primitive generators (TPGs) in
 1044 the calorimeter and muon systems that send E_T sums or muon track stubs to the
 1045 regional calorimeter trigger (RCT) or muon track finders, respectively. The RCT,
 1046 DT track finder (DTTF), and CSC track finder (CSCTF) sort and rank the regional
 1047 trigger primitives based on p_T and quality. The ranked RCT candidates and muon
 1048 track stubs are sent to the global calorimeter trigger (GMT) and global muon trigger
 1049 (GMT), respectively, where high-level objects like isolated and non-isolated muons
 1050 and EM candidates, jets, taus, and \cancel{E}_T are constructed from all the regional inputs
 1051 and ranked. Calorimeter isolation sums for muons are also sent from the RCT to
 1052 the GMT. The highest ranked global objects are sent to the global trigger (GT),
 1053 which sits at the top of the L1 trigger. The GT issues the final L1 accept or reject to
 1054 all subdetectors based on a comparison of the GMT and GCT candidates with the
 1055 requirements of its programmed trigger menu. A block diagram of the L1 trigger is
 1056 shown in Figure 5.29.

1057 A region in the RCT consists of a matrix of 4×4 trigger towers. A trigger tower
 1058 in EB/HB is one HCAL tower + the 5×5 matrix of ECAL crystals in front of it;
 1059 in EE/HE the idea is similar but the counting of crystals and HE towers is slightly
 1060 more complicated. An EM RCT candidate is built around a high E_T seed tower.
 1061 The E_T of the candidate is the sum of the tower E_T and the E_T of its highest- E_T

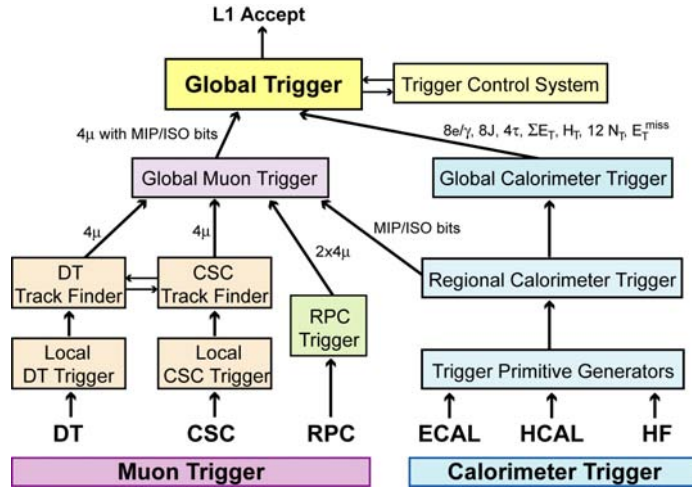


Figure 5.29: Block diagram of the L1 trigger. Reprinted from Fig. 8.1 of ref. [44].

1062 broad side neighbor (see Figure 5.30 for a definition of the broad side neighbors). Two
 1063 isolation criteria are defined based on (a) the ratio of the EM energy to the HCAL
 1064 energy in the tower and (b) the shower shape. For a non-isolated EM candidate, the
 1065 highest- E_T broad side neighboring tower must pass these two isolation criteria; for
 1066 an isolated EM candidate, all eight neighboring towers must the criteria, and there
 1067 must also be at least one quiet corner with the E_T of all five towers in the corner
 1068 below some threshold (see Fig. 5.30). The process is repeated until four isolated and
 1069 four non-isolated EM candidates are found, starting with the highest- E_T tower in the
 1070 region and moving down in tower E_T . An RCT region is flagged as consistent with
 1071 tau decay only if the pattern of tower transverse energy sums defines at most a 2×2
 1072 matrix of energetic towers within the 4×4 RCT region.

1073 From the tower transverse energy sums, eight EM candidates, and tau flag received
 1074 from each RCT, the GCT computes the total E_T in the calorimeter (and the total E_T
 1075 above some programmable threshold, called H_T), and the \cancel{E}_T . It also classifies the
 1076 towers into jets and determines the globally highest ranked isolated and non-isolated
 1077 EM candidates. The jet finding uses a clustering algorithm based on the energy of a
 1078 sub-cluster with respect to its neighbors [61]. Jets are classified as tau decays if all

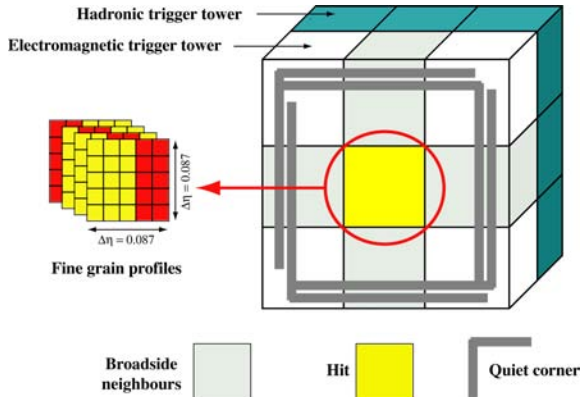


Figure 5.30: Geometry of an EM RCT candidate. Reprinted from Fig. 8.2 of ref. [44].

of the RCT regions participating in the jet clustering had energy patterns consistent with tau decay. Counts of jets above 12 different programmable E_T thresholds are calculated. The jet counts, energy sums, \mathcal{E}_T , and highest ranked EM candidates are sent to the GT, where the final L1 decision is taken and transmitted to the subdetectors. The GT can execute a maximum of 128 trigger algorithms in parallel. If any one of these algorithms yields an accept, the event is accepted, and all trigger information is sent on to the HLT for further filtering. The double-photon HLT paths used in this analysis (see Sec. 6.2) require isolated L1 seeds (i.e. EM candidates built by the RCT) with $E_T > 12$ or 20 GeV, depending on path.

No muon triggers are used in the two-photon analysis. A description of the muon trigger system can be found in ref.[44].

5.2.2 Data Acquisition System

The CMS data acquisition (DAQ) system takes event fragments (calorimeter hits, track hits, etc.) from each of the 626 subdetector front end drivers (FEDs), assembles them into a data structure representing the full event, and sends the event on to the HLT for further filtering. The DAQ must operate at an input rate of ~ 100 GB/s, corresponding to an input rate from the L1 trigger of ~ 100 kHz. To facilitate

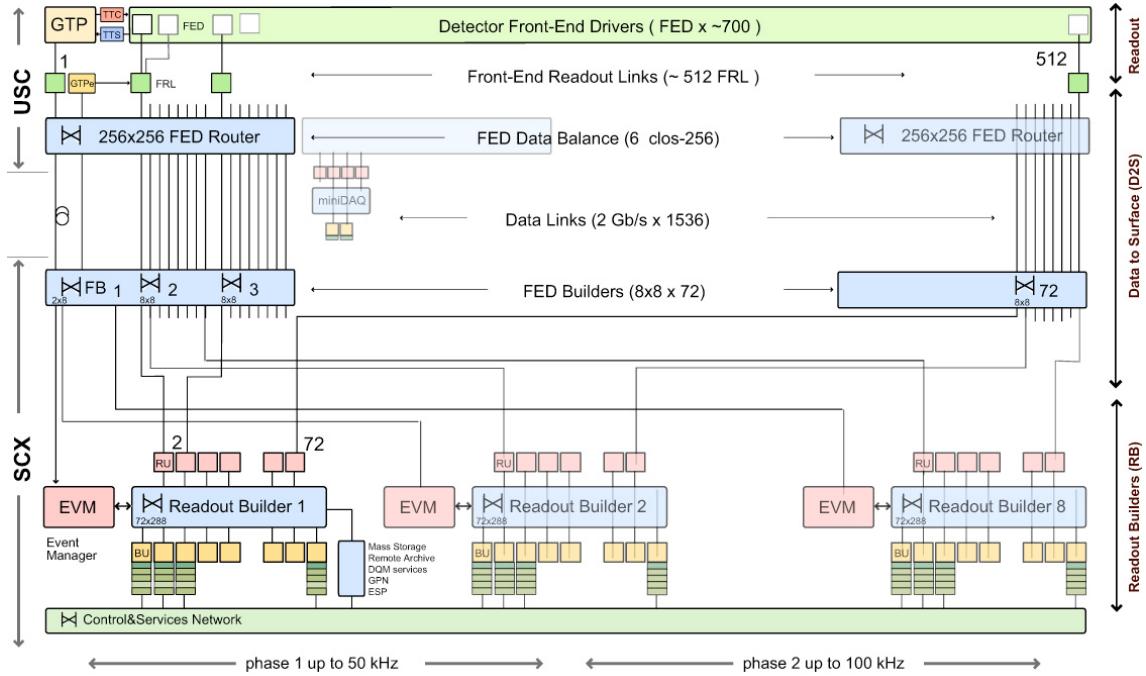


Figure 5.31: Diagram of the DAQ system. The identical event builder systems, shown as inputs and outputs to the boxes labeled “Readout Builder 1”, “Readout Builder 2”, etc., represent the eight slices. Within one slice, data can flow from the detector front ends to the readout systems to the builder network (which assembles the event fragments) to the filter systems (HLT) independently of the other slices. Reprinted from Fig. 9.8 of ref. [44].

1096 expansion of the system as the need arises, the DAQ is composed of eight nearly
 1097 independent slices. Each slice functions as a smaller version of the whole DAQ that
 1098 can handle an input event rate up to ~ 12.5 kHz. A diagram of the DAQ system,
 1099 showing schematically the eight slices, is given in Figure 5.31.

1100 Data from the front ends is collected by the FEDs and pushed to the front end
 1101 readout links (FRLs), which may take inputs from up to two FEDs simultaneously.
 1102 The FRLs check for transmission errors, generate event fragments with size ~ 2 kB,
 1103 buffer the fragments in 64 kB memories, and finally send them to the FED builders.
 1104 The FEDs, FRLs, and FED builders are located in the underground control room.
 1105 The 72 FED builders each construct one ~ 16 kB *super-fragment* from the input
 1106 event fragments, then send the super-fragment on to a readout unit (RU) located in

1107 the surface control room ~ 80 m away. Super-fragments belonging to the same event
 1108 are sent to RUs in the same DAQ slice. There are 72 RUs per readout builder, one
 1109 for each super-fragment of an event, with each DAQ slice built around one readout
 1110 builder (see Fig. 5.31). Each readout builder hosts a number of builder units (BUs)
 1111 that perform the final integration of super-fragments into complete events.

1112 Resource brokers (RBs) in the HLT filter farm request complete events from the
 1113 BUs and distribute those events to the filter units (FUs) for HLT selection. If an
 1114 event passes any one of the HLT paths in the predefined menu, it is sent back to
 1115 the RB for transfer to the storage manager (SM). The SM nodes transfer accepted
 1116 events to the CERN Tier-0 prompt reconstruction facility for unpacking of the raw
 1117 data into ROOT [62] files that can be accessed by physicists wishing analyze the data.
 1118 The lag time between recording of an event in the DAQ and availability of the fully
 1119 reconstructed event for analysis is typically 48 hours.

1120 If the buffers of the upstream DAQ elements (the filter farm, readout builders,
 1121 FED builders, or FRLs) are full, those elements will not request new events from
 1122 downstream. This can lead to a buildup of events in the downstream element buffers,
 1123 *back-pressuring* all the way down to the FEDs themselves. The CMS trigger throttling
 1124 system (TTS) consists of dedicated lines between the FEDs and the GT for the
 1125 purpose of sending predefined signals to the GT about the state of the FED buffers.
 1126 If the buffer of a particular FED is getting full, it can alert the GT to reduce the
 1127 trigger rate so as to prevent FED buffer overflows and loss of time synchronization
 1128 between event fragments. The TTS latency is $\sim 1\mu\text{s}$. Causes of back-pressure (hence
 1129 dead time) include: problems with the FED electronics (in this case, the upstream
 1130 elements request events but the FEDs have trouble sending them), increases in the
 1131 L1 accept rate (perhaps due to a noisy detector channel) beyond what the upstream
 1132 DAQ elements can handle, increases in the event size due to high pileup or a poor
 1133 quality beam that scrapes against the beam pipe, failures of the DAQ transmission

1134 lines or DAQ hardware such that events are not requested from the FEDs fast enough,
 1135 or bottlenecks at the SM nodes or filter farm due to hardware failures or large event
 1136 sizes.

1137 All components of the DAQ, from the FEDs up to the SMs, are controlled by
 1138 cross-platform DAQ (XDAQ) [63] processes, or *executives*. The Simple Object Access
 1139 Protocol (SOAP) [64] protocol is used to transmit control and monitoring data be-
 1140 tween XDAQ-enabled devices and to the end user, who can view the running of a
 1141 XDAQ executive via a Web interface called HyperDAQ [65]. The Run Control and
 1142 Monitoring System (RCMS) handles the configuration and control of all XDAQ exec-
 1143 utives via a hierarchical structure. At the top of the hierarchy is the Level-0 *function*
 1144 *manager* (FM), controlling the Level-1 sub-detector FMs, which in turn control their
 1145 Level-2 system-specific XDAQ executives. The central DAQ and L1 trigger each have
 1146 their own Level-1 FM. A unit of data acquisition, called a *run*, may be configured,
 1147 started, and stopped by an end user interacting with the RCMS Web interface.

1148 5.2.3 Data Processing and Transfer to Computing Centers

1149 Data leaving the filter farm are grouped into datasets based on HLT path, i.e. there
 1150 are different datasets for events passing diphoton triggers, jet triggers, muon + elec-
 1151 tron triggers, etc. At the Tier-0 facility, the datasets are go through three levels of
 1152 processing to create three *data tiers*. The first layer produces RAW data by unpack-
 1153 ing the detector byte streams sent from the DAQ and L1 trigger into data structures
 1154 holding the ADC counts recorded for each channel of the detector, digitized trigger
 1155 primitives, and the L1 decision. A single event has ~ 1.5 MB of RAW data. The next
 1156 layer of processing is the reconstruction, which forms channel energies in GeV, ap-
 1157 plies calibrations, and creates high-level objects like photons, electrons, muons, taus,
 1158 jets, E_T , and charged tracks. The RECO data tier occupies ~ 0.5 MB per event.
 1159 Finally, analysis object data (AOD) is a subset of the RECO data, comprising the

1160 high-level objects but usually excluding the individual channel hit information if it is
1161 not associated to a physics object. This tier occupies ~ 0.1 MB per event. One copy
1162 of the RAW data is stored permanently at CERN and another copy is distributed
1163 amongst the Tier-1 facilities (see below) for permanent storage. Changes in the re-
1164 construction algorithms periodically require reprocessing of the RAW data to form a
1165 new RECO tier. In general, only the AOD tier is available to physicists wishing to
1166 perform analyses due to the smaller size and faster replication and transfer time of
1167 AOD with respect to RAW or RECO.

1168 There are three tiers of computing and data storage sites within the Worldwide
1169 LHC Computing Grid (WLCG) [66]. The tier closest to CMS is Tier-0, which is
1170 located at CERN and performs archiving of the RAW data, prompt reconstruction
1171 of the data within ~ 48 hours of its being collected, and transferral of copies of the
1172 RECO datasets to Tier-1 facilities. There are a few Tier-1 centers worldwide, hosted
1173 by national computing facilities and laboratories. They store parts of the RAW dataset
1174 and copies of the RECO datasets, participate in subsequent reconstruction passes
1175 after the prompt reconstruction at Tier-0, and ship AOD datasets upon request to the
1176 Tier-2 centers. Analysts interact primarily with the Tier-2 centers, which store AOD
1177 datasets and run batch processing queues for running analysis jobs over the datasets.
1178 Different layers of WLCG software control data transfer between sites, data storage,
1179 and batch processing. A diagram of the WLCG tier system is given in Figure 5.32.

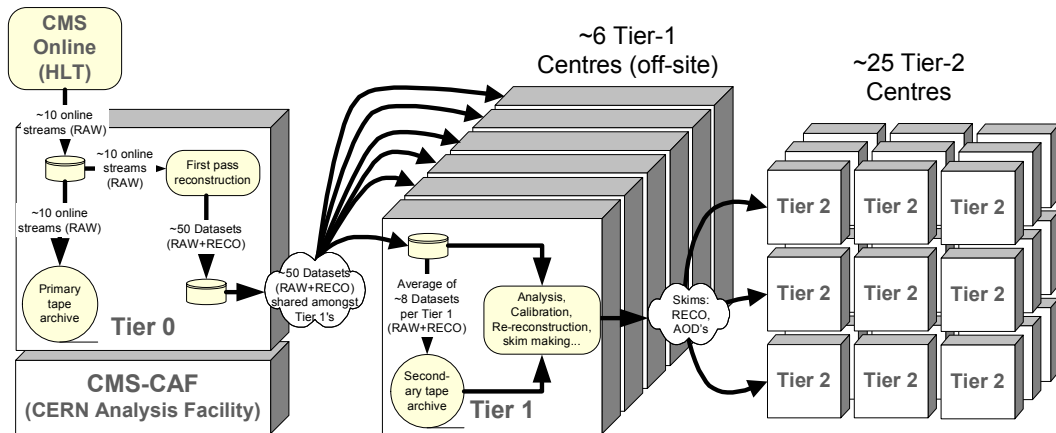


Figure 5.32: Diagram of the WLCG tier system showing data archival and reconstruction at each tier along with data transfer between tiers. Reprinted from Fig. 11.2 of ref. [44].

1180

Chapter 6

1181

Event Selection

1182 In keeping with the phenomenology described in Sec. 3.5, the candidate GGM events
1183 selected in this search consist of two high- E_T photons and a significant momentum
1184 imbalance transverse to the beam, indicating the production of an escaping gravitino.
1185 This momentum imbalance is usually referred to as *missing transverse energy* and is
1186 denoted by the symbol \cancel{E}_T .

1187 However, in order to use real CMS data (as opposed to simulation) to derive pre-
1188 dictions for the backgrounds to the search, *control samples* distinct from the *candidate*
1189 two-photon sample must be collected. These samples consist of different numerical
1190 combinations of photons, electrons, and jets, and are explained in more detail in
1191 Chapter 7. Since this search is performed in the high- \cancel{E}_T tail of the \cancel{E}_T distribution,
1192 where adequate detector simulation is very difficult, it is advantageous to use *data-
1193 driven* background estimates, which capture the true detector response, over numbers
1194 derived from simulation.

1195 In the following sections, the reconstruction of photons, electrons, jets, and \cancel{E}_T
1196 is explained. Sec. 6.1 begins with an explanation of the high level reconstruction.
1197 It is followed by Sec. 6.2, which describes the triggers used to collect the candidate
1198 and control samples. Sec. 6.3 describes event cleaning cuts that are applied to the

1199 candidate and control samples. Finally, the chapter concludes with a measurement of
1200 the photon identification efficiency in Sec. 6.4.

1201 6.1 Object Reconstruction

1202 This section describes the *offline* object reconstruction, i.e. the reconstruction of par-
1203 ticle objects from events that have already been triggered and written to permanent
1204 storage, as opposed to the building of trigger objects explained in Secs. 5.2.1 and 6.2.

1205 6.1.1 Photons

1206 Uncalibrated EB/EE Hits

1207 Photon reconstruction begins with the ADC count value for each of the 10 recorded
1208 time samples per ECAL crystal per trigger. To construct an *uncalibrated hit*, the
1209 gain (1, 6, or 12; see Sec. 5.1.2) of each sample is determined and the ADC count
1210 value scaled appropriately. The pedestal is estimated from the average of the first
1211 three samples, which, for a properly timed in hit, should contain no signal. This
1212 pedestal value is subtracted from the rest of the samples. Finally, the amplitude of the
1213 pulse is reconstructed using a predetermined weight for each sample [67]. The weights
1214 correspond to the pulse shape expected from the MGPA and shaping circuit response.
1215 The time of the hit is also reconstructed using the ratios between neighboring time
1216 samples [68]. A typical ECAL channel pulse shape is shown in Figure 6.1.

1217 Calibrated EB/EE Hits

1218 In the next phase of the photon reconstruction, calibrations are applied to the un-
1219 calibrated hits to form *calibrated hits* with energy measured in GeV. Channels are
1220 excluded from seeding calibrated hits if

- 1221 • they are excessively noisy,

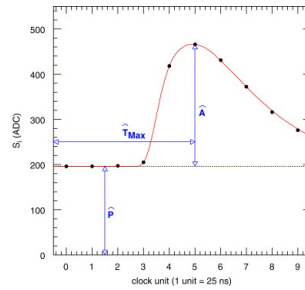


Figure 6.1: Typical ECAL channel pulse shape. \hat{P} is the pedestal value, \hat{A} is the pulse amplitude, and \hat{T}_{\max} is the hit time. The red line is the assumed pulse shape from which the weights are derived. Reprinted from ref. [67].

- 1222 • they are stuck in fixed gain (i.e. the MGPA gain does not change properly to
- 1223 avoid saturation),
- 1224 • they are totally dead,
- 1225 • they have one or more neighboring dead channels, or
- 1226 • they do not have good trigger primitives (i.e. trigger primitive is missing, satu-
- 1227 rated, or *spike-like*).

Added

1228 *ECAL spikes* are hits in which low energy protons and heavy ions from jets ionize this
 1229 in the sensitive volume of the EB APD, causing the APD to register a fake large- para-
 1230 amplitude hit. Because they are not the result of a real electromagnetic shower, spikes graph
 1231 tend to be isolated. They may also appear to arrive early or late with respect to the and the
 1232 nominal bunch crossing. Most spikes are reconstructed with a hit time ~ 10 ns earlier next
 1233 than real EM hits because unlike real hits, whose pulse shapes include the time about
 1234 constant associated with crystal scintillation, the reconstructed spikes only involve spikes
 1235 the rise time of the electronics. There also is a long tail of late arriving spikes due to
 1236 slow neutrons from jets [69].

1237 Because of their particular timing and topological characteristics, cuts have been
 1238 developed to effectively identify and reject spike-like hits. This analysis utilizes both
 1239 the “Swiss cross” cut $1 - E_4/E_1 > 0.95$, where E_1 is the energy of the spike candidate

1240 crystal and E_4 is the sum of the energies in the four crystals whose edges are parallel to
 1241 the four edges of the spike candidate crystal, and a timing cut $t \geq 3$ ns, to flag spikes.
 1242 More information about these cuts can be found in ref. [69]. A simpler algorithm
 1243 using the fine grain veto bit of the L1 TPG is used to reject spikes at the trigger level
 1244 **[insert citation]**.

1245 In addition to the trigger primitives, no uncalibrated hits that are spike-like are eli-
 1246 gible for calibration. The calibrations applied are crystal transparency loss corrections
 1247 measured continuously by the laser/LED system, energy intercalibrations (relative en-
 1248 ergy calibration between crystals), absolute scale calibrations between ADC counts
 1249 and GeV,¹ and time intercalibrations (relative time calibration between crystals).

1250 The ECAL crystals were pre-calibrated before installation in CMS using labora-
 1251 tory light yield and photodetector gain measurements [71]. In addition, some EB and
 1252 EE crystals were intercalibrated using test beams [72], and all EB crystals were inter-
 1253 calibrated with cosmic ray muons [73]. EE precalibrations were validated with LHC
 1254 *splash events* in 2009 [73, 74], in which the beam was dumped onto a collimator ap-
 1255 proximately 150 meters upstream of CMS, causing a spray of muons to enter CMS at
 1256 one endcap and exit at the other. Splash events were also used to derive time intercal-
 1257 ibration constants. Before colliding beam operations commenced, the intercalibration
 1258 precision was estimated to be 0.5%-2.2% in EB and 1%-5% in EE [75].

1259 Three calibration methods were employed once colliding beam operations began:

- 1260 • ϕ symmetry relative calibration between crystals, exploiting the azimuthal sym-
 1261 metry of CMS
- 1262 • π^0 and η relative calibration between crystals, using the diphoton decays of
 1263 these particles

¹The ADC-GeV scale factors (one for EB and one for EE) are defined such that the sum of fully calibrated and scaled hits in a particular 5×5 cluster of crystals (plus the associated energy deposited in ES) is 50 GeV for a 50 GeV incident unconverted photon [70].

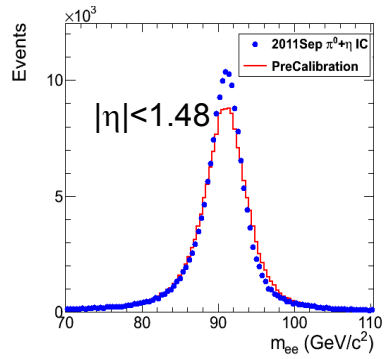


Figure 6.2: Z peak reconstructed using pre-LHC calibration constants (red) or September 2011 π^0/η -derived intercalibration constants (blue). Reprinted from ref. [76].

1264 • E/p absolute calibration, comparing the momentum measured in the tracker p
 1265 to the energy measured in the ECAL E of a sample of electrons from Z decay

1266 By September 2011, the intercalibration precision in EB was measured to be be-
 1267 tween 0.3% and 1.1% using the π^0/η method [76]. Figure 6.2 shows the improvement
 1268 in Z reconstruction from pre-LHC calibration constants to the latest π^0/η -derived
 1269 constants.

1270 Calibrated ES Hits

Added

1271 ES calibrated hits are formed from the three samples read out per sensor. Just as in the paren-
 1272 case of EB/EE crystals, ES uncalibrated hits gain-adjusted, pedestal-subtracted, and thetical
 1273 reconstructed using weights. To make a calibrated ES hit, intercalibration constants, remark
 1274 angle correction constants (for the non-uniformity of sensor angle with respect to the
 1275 vertical across ES), and a MIP-GeV absolute scale factor are applied.

1276 Clustering

1277 After calibrated ECAL hits are formed, they must be clustered into shapes that
 1278 represent the energy deposit from a single particle. *Basic clusters* are formed around
 1279 seed hits, defined as a hit that

- 1280 • has calibrated $E_T > 1(0.18)$ GeV in EB(EE),
- 1281 • does not originate from a dead channel or one with faulty hardware,
- 1282 • is not poorly calibrated,
- 1283 • was reconstructed with the standard algorithm (i.e. not a special recovery algo-
- 1284 rithm for channels with subpar data integrity),
- 1285 • is not saturated,
- 1286 • is not spike-like, and
- 1287 • is in time (EB).

1288 EB basic clusters are formed around the seeds via the *hybrid* algorithm, while EE basic
 1289 clusters are formed with the `multi5x5` algorithm [77]. In addition to non-radiating
 1290 electrons and unconverted photons, both algorithms are designed to also recover all of
 1291 the energy associated with electron bremsstrahlung deposits and photon conversions.
 1292 The geometry of the CMS magnetic field means that bremsstrahlung and conversions
 1293 will tend to spread the shower out in ϕ , not η . Both algorithms work by forming
 1294 basic clusters around seeds, then combining the basic clusters into *superclusters* (SC)
 1295 by searching in a window extended in the ϕ direction for all basic clusters consistent
 1296 with bremsstrahlung radiation from the primary electron, or with a photon conversion.
 1297 Figure 6.3 illustrates the hybrid algorithm in EB. In EE, the energy deposited in ES
 1298 must also be added into the total clustered energy sum.

1299 Figure 6.4 shows the effect of superclustering on $Z \rightarrow ee$ reconstruction.

1300 **Supercluster Corrections**

1301 The total clustered ECAL energy is defined as

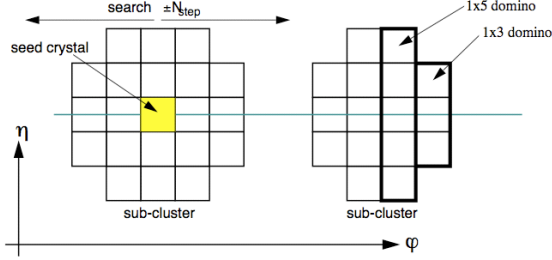


Figure 6.3: Hybrid algorithm in EB. The shower extent is essentially constant in η , but spreads out in ϕ as the two sub-clusters (or basic clusters) are grouped into the same supercluster. Reprinted from ref. [77].

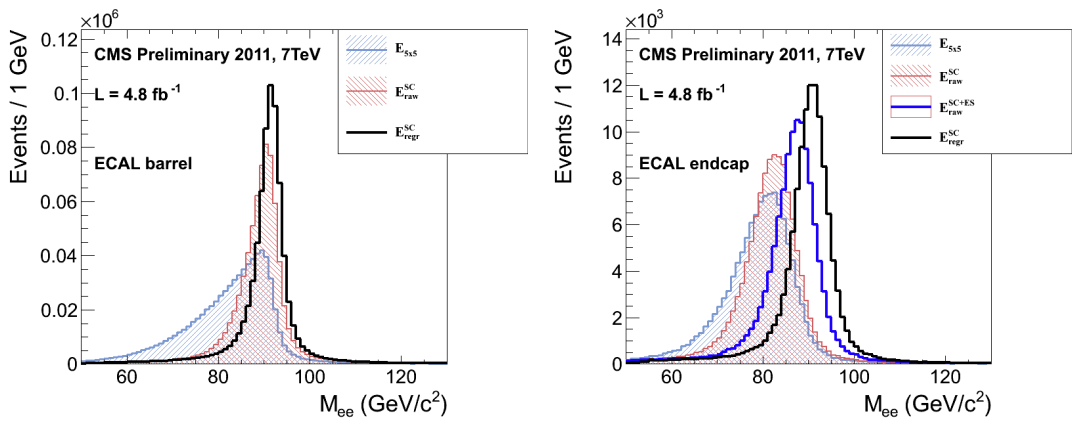


Figure 6.4: Z peak reconstructed in the dielectron channel for different kinds of clustering. The left plot is for EB and the right plot for EE. The constituent hits were calibrated with the best available intercalibrations and laser calibrations as of December 2011. The light blue histogram shows the reconstruction using a 5×5 energy sum, the red histogram shows the reconstruction using the SC energy for crystals only (the dark blue histogram on the right-hand side adds in the energy from ES), and the black histogram shows the reconstruction after the SCs are corrected using a multivariate method [?]. Reprinted from Fig. 30 of ref. [?].

$$E = F \times \sum_{i=1}^{n_{\text{crystal}}} G \times c_i \times A_i \quad (6.1)$$

1302 where G is the ADC-GeV or MIP-GeV scale factor, c_i are the intercalibration con-
 1303 stants, A_i is the uncalibrated hit amplitude in ADC counts, and F is a SC correction
 1304 factor. G and c_i were explained in Sec. 6.1.1. F is a product of three factors for hybrid
 1305 SCs (two for multi5x5 SCs) [77]:

- 1306 1. $C_{\text{EB}}(\eta)$, which compensates for lateral energy leakage due to the crystal off-
 1307 pointing in EB. These corrections are taken from MC simulation [77] and were
 1308 confirmed in test beams [72].
- 1309 2. $f(\text{brem})$, which corrects for biases in the clustering algorithms for showers char-
 1310 acterized by differing amounts of bremsstrahlung. These corrections are taken
 1311 from MC simulation [77].
- 1312 3. Residual correction $f(E_T, \eta)$, due to the variation in η of detector material
 1313 traversed by a primary electron or photon, and to any residual E_T dependence
 1314 of the reconstruction. These corrections are determined from MC and validated
 1315 on $Z \rightarrow ee$ data samples [78].

Changed

1316 As a benchmark of ECAL calibration performance, the extra energy smearing in
 1317 MC needed to achieve data/MC agreement in the Z width was between $\sim 0.9\%$ (in
 1318 the central part of EB for electrons with little bremsstrahlung) and $\sim 3.3\%$ (in the
 1319 outer part of EE for heavily radiating electrons) [79].

1320 From Supercluster to Photon

1321 The CMS photon object is any SC with $E_T > 10$ GeV and $H/E < 0.5$, unless the SC
 1322 $E_T > 100$ GeV, in which case the H/E requirement is dropped. H/E is defined as the

ratio of energy in the HCAL in a 0.15 cone around the SC centroid, directly behind
 the SC, to the SC energy. SCs with $R9 > 0.94(0.95)$ in EB(EE), where $R9$ is defined
 as the ratio of the energy in the central 3×3 cluster of crystals divided by the SC
 energy $E_{3 \times 3}/E_{\text{SC}}$, are the best calibrated and most accurate type of electromagnetic
 shower. Therefore, for these objects, the photon energy is defined as the energy sum
 of the fully calibrated hits in the central 5×5 cluster around the seed (with $C_{\text{EB}}(\eta)$
 applied for EB photons). For all other SCs, the photon energy is equal to the fully
 corrected SC energy (cf. Sec. 6.1.1).

Reorganized

In this search, candidate photons and *fake photons* (f , “fakes”) are further selected
 according to the criteria listed in Table 6.1. Fakes are used in the determination of
 the QCD background, as explained in Chapter 7.

next 3

para-

graphs;

edited

Ta-

ble 6.1

caption

Table 6.1: Selection criteria for photons and fakes. “Pixel seed,” I_{comb} , and $\sigma_{i\eta i\eta}$ are
 defined in the text.

Variable	Cut (γ)	Cut (f)
SC $ \eta $	< 1.4442	< 1.4442
H/E	< 0.05	< 0.05
$R9$	< 1	< 1
Has pixel seed	No	No
$I_{\text{comb}}, \sigma_{i\eta i\eta}$	$< 6 \text{ GeV} \&\& < 0.011$	$(\geq 6 \&\& < 20 \text{ GeV}) \parallel \geq 0.011$

I_{comb} is defined as

Updated

effective

area

$$I_{\text{comb}} = I_{\text{ECAL}} - 0.093\rho + I_{\text{HCAL}} - 0.0281\rho + I_{\text{track}} \quad (6.2)$$

where I_{ECAL} , I_{HCAL} , and I_{track} are E_T sums in the annular regions defined in Figure 6.5
 and ρ is the average pileup energy density in the calorimeters (per unit $\eta \cdot \phi$) as
 measured with the Fastjet algorithm [80, 81]. Note that the ECAL and track isolation
 veto strips at constant η ensure that the isolation cuts are similarly efficient for
 converted photons, radiating electrons, and unconverted photons.

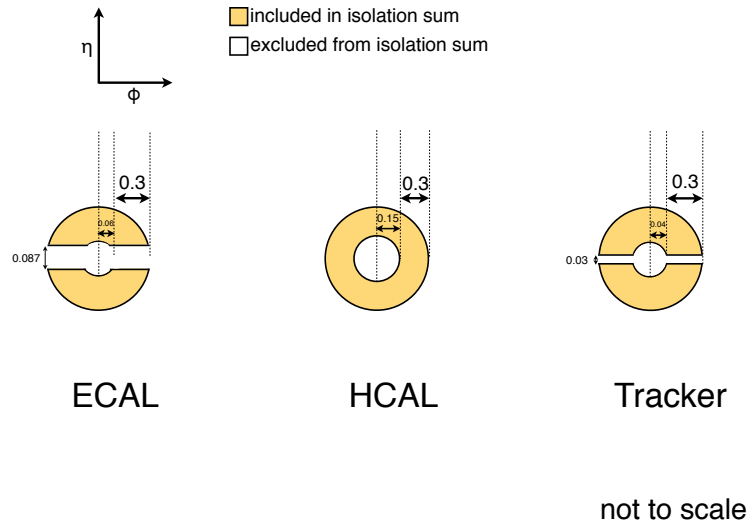


Figure 6.5: ECAL, HCAL, and track Isolation cones.

¹³⁴⁰ $\sigma_{i\eta i\eta}$ is the log energy weighted extent of the shower in η and is defined as Added $\sigma_{i\eta i\eta}$

$$\sigma_{i\eta i\eta} = \frac{\sum_{i=1}^{25} w_i (\eta_i - \bar{\eta})^2}{\sum_{i=1}^{25} w_i} \quad (6.3) \quad \text{defini-} \quad \text{tion}$$

¹³⁴¹ where the sums run over the 5×5 matrix of crystals surrounding the seed, $w_i =$
¹³⁴² $\max(0, 4.7 + \ln(E_i/E))$, E_i is the energy of the i^{th} crystal, E is the total energy in the
¹³⁴³ 25 crystals, η_i is the offset in η of the i^{th} crystal from the seed, and $\bar{\eta}$ is the weighted
¹³⁴⁴ average η of the 25 crystals (using the w_i as weights) [82]. Changed

¹³⁴⁵ Figure 6.6 shows the ρ distribution for a sample of two-photon events, with at average
¹³⁴⁶ least one 40 GeV and one 25 GeV photon, passing the selection requirements in ρ ; up-
¹³⁴⁷ Table 6.1 and the trigger requirements in Table 6.3. This sample represents the full dated
¹³⁴⁸ 2011 dataset of 4.7 fb^{-1} . Since the average ρ is $\sim 7.5 \text{ GeV}$, and there is a long tail fig. 6.6
¹³⁴⁹ above this average value, it is necessary to subtract pileup energy from the ECAL
¹³⁵⁰ and HCAL isolation cones to recover otherwise clean photons in events with large
¹³⁵¹ pileup. The ECAL and HCAL *effective areas* of 0.093 and 0.0281, respectively, are

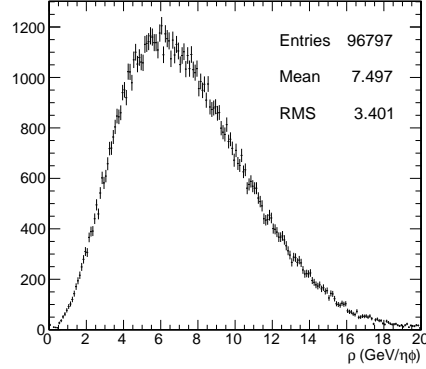


Figure 6.6: ρ distribution for a sample of two-photon events, with at least one 40 GeV and one 25 GeV photon, passing the selection requirements in Table 6.1 and the trigger requirements in Table 6.3. This sample covers the full 2011 dataset of 4.7 fb^{-1} .

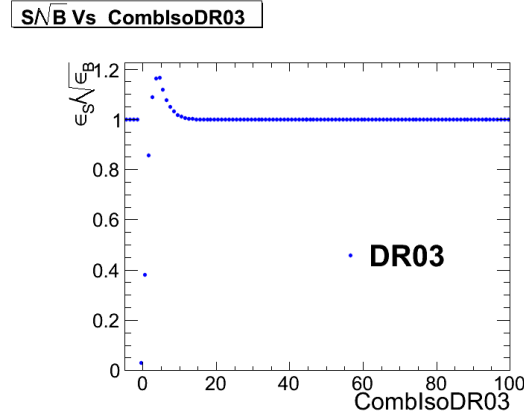


Figure 6.7: S/\sqrt{B} (S and B defined in the text) vs. combined isolation. Reprinted from Fig. 7 of ref. [83].

1352 calculated by fitting the average ECAL or HCAL isolation energy vs. ρ in a sample
 1353 of $Z \rightarrow ee$ events to a straight line. The slope of the line—which has the units of $\eta \cdot \phi$,
 1354 or area—is the effective area.

1355 The cut on combined isolation of 6 GeV (Table 6.1) is the result of an S/\sqrt{B}
 1356 optimization procedure [83]. S is a sample of photons in simulated GGM events that
 1357 are products of neutralino decay, while B is a sample of photons matched to generated
 1358 hadronic jets in simulated QCD events. Figure 6.7 shows the value of S/\sqrt{B} vs.
 1359 combined isolation, in particular the pronounced peak around 6 GeV.

New

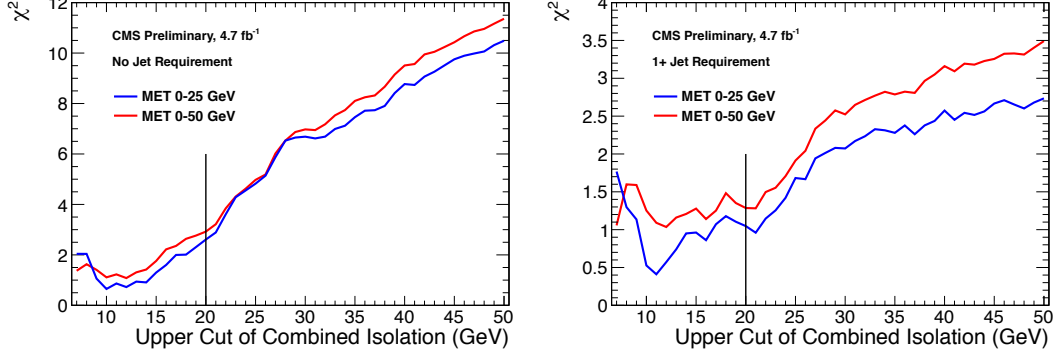


Figure 6.8: Neyman’s χ^2 between the ff and $\gamma\gamma$ \cancel{E}_T distributions, truncated at either 25 (red) or 50 (blue) GeV, vs. upper bound on fake combined isolation. The left plot includes all events; the right plot is for events with ≥ 1 jet defined as in Table 6.2, but with the ΔR cleaning criteria applied to the two primary EM objects and all additional electrons, photons, and fake photons. The full reweighting and normalization procedure is employed in the \cancel{E}_T calculation (see Sec. 7.1). Error bars include statistical, reweighting, and normalization error (see Sec. 7.3). Reprinted from Fig. 9 of ref. [83].

1360 The upper bound on fake photon combined isolation guarantees that poorly iso-
 1361 lated dijet events, with \cancel{E}_T resolution dissimilar to the candidate diphoton events,
 1362 do not enter the ff sample. The exact value of 20 GeV (cf. Table 6.1) arises from
 1363 a low- \cancel{E}_T $ff/\gamma\gamma$ χ^2 optimization procedure [83]. Figure 6.8 shows the value of the
 1364 Neyman’s χ^2 between the ff and $\gamma\gamma$ \cancel{E}_T distributions, truncated at either 25 or 50
 1365 GeV, vs. upper bound on fake combined isolation. As shown in the figure, 20 GeV
 1366 very nearly minimizes the χ^2 , while also being large enough that a sufficient number
 1367 of ff events may be collected.

1368 Finally, a “pixel seed” is defined as a hit in the pixel detector consistent with a
 1369 track extrapolated from the position of the ECAL SC back to the primary vertex.
 1370 Real photons, having no charge and therefore no bending in the magnetic field, should
 1371 not have a pixel seed.

1372 6.1.2 Electrons

1373 Electrons are reconstructed identically to photons, except that in the electron case
 1374 the presence of a pixel seed is enforced, rather than vetoed.² Photons and electrons
 1375 are defined by very similar criteria so that $Z \rightarrow ee$ events can be used to model
 1376 the QCD background in the two-photon sample without introducing any bias in the
 1377 electron energy measurement (cf. Sec. 7.1).

1378 6.1.3 Jets and Missing Transverse Energy

1379 Particle Flow

1380 In this analysis, jets and \cancel{E}_T are formed from *particle flow* (PF) candidates. The parti-
 1381 cle flow algorithm [87, 88] uses information from all CMS subdetectors to reconstruct
 1382 as accurately as possible the positions and momenta of all visible jet constituents,
 1383 exploiting the fine granularity of the tracker and ECAL to achieve a greatly improved
 1384 momentum resolution over calorimeter-only jets [89]. The PF algorithm is summa-
 1385 rized below [90].

1386 1. Reconstruct the fundamental detector objects via iterative procedures

- 1387 • Tracks in the inner silicon layers
 - 1388 – High efficiency and low fake rate for charged hadrons in jets
 - 1389 – Relaxed primary vertex constraint allows photon conversions, parti-
 1390 cles originating from nuclear interactions in the silicon, and long-lived
 1391 particles to be reconstructed
- 1392 • Calorimeter clusters
- 1393 • Muon tracks in the outer muon layers

²In many CMS analyses, electrons are reconstructed very differently from photons. In particular, a special tracking algorithm [86] is used to best follow a radiating electron. However, in this analysis, the electron tracking is not used.

1394 2. Create a “block” of linked fundamental objects

- 1395 • Link silicon tracks to calorimeter clusters via $\Delta R_{\text{track-cluster}}$ (account for
1396 electron bremsstrahlung)
- 1397 • Link clusters in one calorimeter layer to clusters in a separate layer via
1398 $\Delta R_{\text{cluster-cluster}}$
- 1399 • Link silicon tracks to muon tracks via global track χ^2

1400 3. ID the particles in the block

- 1401 • If global (silicon + muon layers) muon p_T is compatible with silicon track
1402 p_T , ID as a muon and remove corresponding tracks from block
- 1403 • ID electron tracks via special algorithm and removed all corresponding
1404 tracks and cluster from block
- 1405 • Remove fake tracks from the block Fixed
- 1406 • Remove excess track-cluster links via $\Delta R_{\text{track-cluster}}$ minimization (but al-
1407 low multiple tracks to be associated to one cluster) typo
- 1408 • If the cluster energy is significantly larger then the energy of the linked
1409 track, ID as a PF photon or PF neutral hadron and remove corresponding
1410 clusters from the block
- 1411 • If the cluster is not linked to a track, ID as a PF photon or PF neutral
1412 hadron and remove corresponding clusters from the block
- 1413 • Remaining track-cluster links are PF charged hadrons

1414 **Jets**

1415 PF candidates are clustered into jets by means of the anti- k_T algorithm with $R = 0.5$
1416 [91]. In this algorithm, all possible pairs of PF candidates i, j are looped over, and
1417 the momenta of the pair that minimize the distance variable

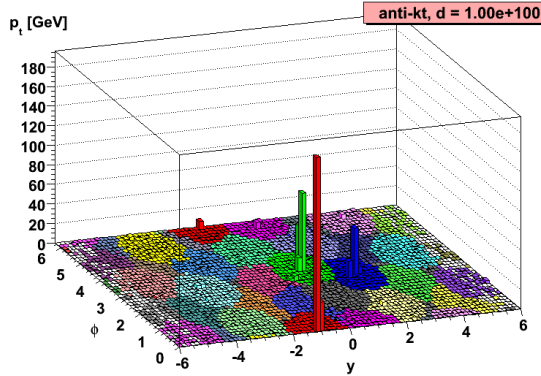


Figure 6.9: Example event display showing jets clustered via the anti- k_T algorithm. y is pseudorapidity. Reprinted from slide 85 of ref. [92].

$$d_{ij} = \frac{\Delta R_{ij}^2}{R^2 \max(k_{Ti}^2, k_{Tj}^2)} \quad (6.4)$$

1418 are combined, where k_{Ti} is the transverse momentum of “combined” PF candidate i .
 1419 The constituent PF candidates are clustered together. The process is repeated until
 1420 $d_{ij} > 1/k_{Ti}^2$ for all pairs of clustered PF momenta [92]. An illustration is given in Fig-
 1421 ure 6.9. The anti- k_T algorithm is infrared and collinear safe, leading to well-behaved Added
 1422 theoretical predictions and ease of comparison between data and MC simulation. It refer-
 1423 also tends to form circular jets, making it easy for experimental effects such as ex- ence to
 1424 pected out-of-cone energy and fiducial acceptance to be measured or simulated. For Fig. 6.9
 1425 these reasons, the anti- k_T jet clustering algorithm was chosen for this analysis.

1426 Once jets are clustered, they must be corrected for biases in the energy mea-
 1427 surement due to non-compensation [93], invisible energy (lost to overcoming nuclear
 1428 binding energy, in neutrinos, or in unclustered muons, for example) [93], detector
 1429 geometry and cracks [94], zero suppression and trigger inefficiencies [95], pileup, and
 1430 effects of the clustering algorithm [94]. Four multiplicative correction factors are ap-
 1431 plied to the raw jet four-momentum p_μ^{raw} [89]:

- 1432 • $C_{\text{offset}}(p_T^{\text{raw}})$, which accounts for extra energy due to noise, pileup, and the un-

1433 derlying event;

- 1434 • $C_{\text{MC}}(C_{\text{offset}} p_T^{\text{raw}}, \eta)$, which is derived from MC and accounts for most of the p_T
 1435 and η dependence;
- 1436 • $C_{\text{rel}}(\eta)$, which accounts for the remaining differences in uniformity over the
 1437 entire calorimeter between data and MC; and
- 1438 • $C_{\text{abs}}(C_{\text{rel}} C_{\text{MC}} C_{\text{offset}} p_T^{\text{raw}})$, which accounts for the remaining differences in linear-
 1439 ity over the full p_T range between data and MC.

1440 Figure 6.10 shows the total jet energy correction factor $C_{\text{offset}} C_{\text{MC}} C_{\text{rel}} C_{\text{abs}}$ vs. η
 1441 for jets reconstructed with the anti- k_T algorithm, $R = 0.5$. The PF jet corrections
 1442 are more uniform across η than those of CALO jets (composed of simple calorimeter
 1443 towers) or JPT jets (Jet Plus Tracks; composed of calorimeter energies replaced,
 1444 where possible, with matching track p_T) [96]. In addition, for p_T in the range 30-200
 1445 GeV and $|\eta|$ up to 2.0, the PF jet energy correction uncertainty is lower than that of
 1446 the other two types of jets, and never exceeds $\sim 3\%$ [89]. The superior performance
 1447 of PF jets motivates their use in this search.

1448 In this analysis, candidate and QCD control events are binned by number of jets
 1449 satisfying the criteria in Table 6.2.

1450 Missing Transverse Energy

1451 To be consistent with the jet reconstruction, \cancel{E}_T in this analysis is also reconstructed
 1452 from PF candidates. Raw \cancel{E}_T is defined as

$$\cancel{E}_{T\text{raw}} = \left| - \sum_{i=1}^{n_{\text{PF}}} \vec{p}_{Ti} \right| \quad (6.5)$$

Table 6.2: Definition of HB/HE hadronic jets.

Variable	Cut
Algorithm	L1FastL2L3Residual corrected PF
p_T	$> 30 \text{ GeV}$
$ \eta $	< 2.6
Neutral hadronic energy fraction	< 0.99
Neutral electromagnetic energy fraction	< 0.99
Number of constituents	> 1
Charged hadronic energy	$> 0.0 \text{ GeV}$ if $ \eta < 2.4$
Number of charged hadrons	> 0 if $ \eta < 2.4$
Charged electromagnetic energy fraction	< 0.99 if $ \eta < 2.4$
ΔR to nearest PF electron ^a , muon ^b , or one of the two primary EM objects	> 0.5

^aA PF electron is defined as an electron reconstructed with the PF algorithm [84] with $p_T > 15 \text{ GeV}$, $|\eta| < 2.6$, and $(I_{\text{charged}} + I_{\text{photon}} + I_{\text{neutral}})/p_T < 0.2$, where $I_{\text{charged}}(I_{\text{photon}})(I_{\text{neutral}})$ is the sum of PF charged hadron(PF photon)(PF neutral hadron) momenta in a $\Delta R = 0.4$ cone around the PF electron.

^bMuons are reconstructed [85] from a combination of muon station and inner tracker hits. Here, a muon must have track $\chi^2 < 10$, at least one good muon station hit, inner track transverse impact parameter $< 0.02 \text{ cm}$, inner track longitudinal impact parameter $< 0.5 \text{ cm}$, $p_T > 15 \text{ GeV}$, $|\eta| < 2.6$, and $(I_{\text{ECAL}} + I_{\text{HCAL}} + I_{\text{track}})/p_T < 0.2$, where $I_{\text{ECAL}}(I_{\text{HCAL}})(I_{\text{track}})$ is the sum of ECAL(HCAL)(track) momenta in a $\Delta R = 0.3$ cone around the muon.

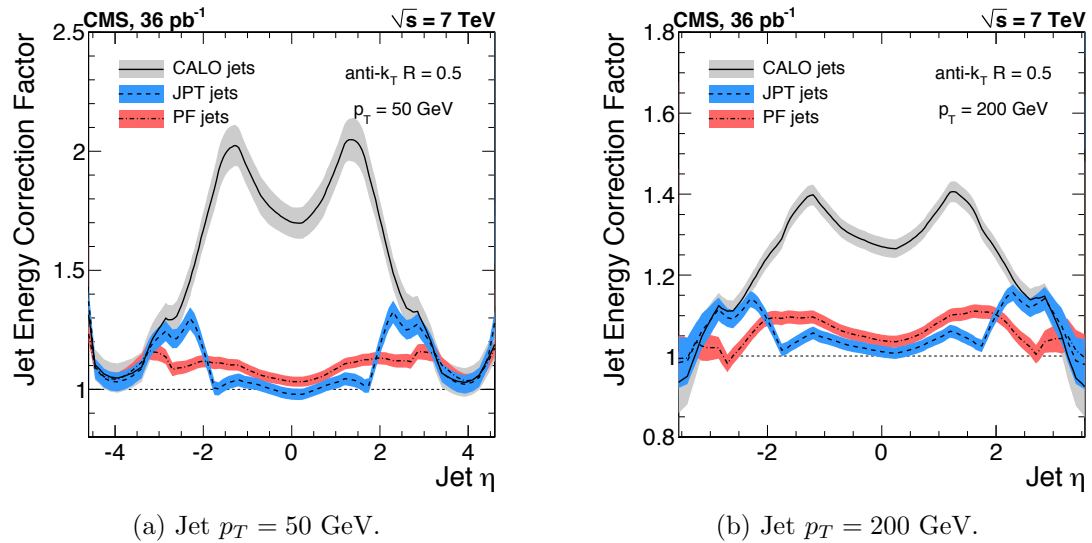


Figure 6.10: Total jet energy correction factor $C_{\text{offset}} C_{\text{MC}} C_{\text{rel}} C_{\text{abs}}$ vs. η , including uncertainty band, for jets reconstructed with the anti- k_T algorithm, $R = 0.5$. Reprinted from Fig. 26 of ref. [89].

where n_{PF} is the number of PF candidates in the event. \cancel{E}_{Raw} may be corrected for the same effects that necessitate jet corrections, since \cancel{E}_{Raw} is usually the result of jet mis-measurement (except, of course, in electroweak physics processes that include an energetic neutrino, or SUSY production). CMS *Type-I* \cancel{E}_T corrections simply involve replacing the PF jets with their corrected energies (cf. Sec 6.1.3) and recalculating \cancel{E}_T . Only jets with electromagnetic fraction (EMF) below 90% and $p_T > 20$ GeV are replaced. This ensures that very electromagnetic jets (as well as isolated leptons, which also receive no correction), which consist chiefly of neutral pions and are measured accurately by the ECAL, do not receive a correction derived for jets with a large fraction of their energy in charged hadrons. In addition, the p_T cut guarantees that jet corrections are only applied where they are known to within a few percent. For this search, the level of agreement between the SM background estimate and the two-photon search sample in a low- \cancel{E}_T control region is the same regardless of whether the \cancel{E}_T is corrected or not, so for simplicity the Type-I \cancel{E}_T corrections are not used (see Sec. ??).

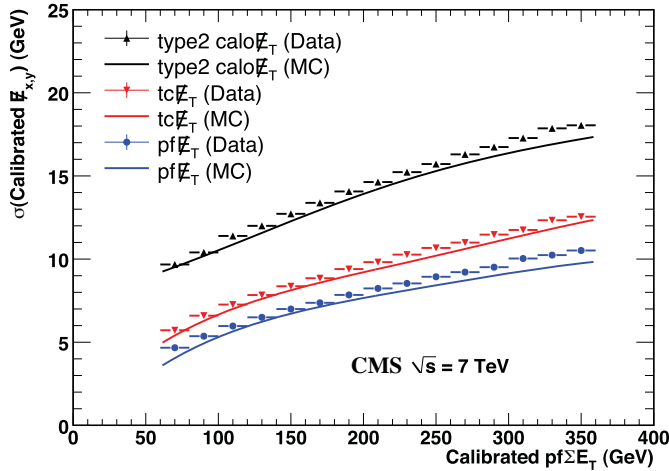


Figure 6.11: σ of a Gaussian fit to the x- and y-components of calibrated E_T vs. the calibrated PF E_T sum in a sample of events containing at least two jets with $p_T > 25$ GeV. σ is calibrated such that the E_T scale is equal for all three algorithms. PF $\sum E_T$ is corrected, on average, to the particle level using a Pythia v8 simulation [97]. The blue markers (data) and line (MC) refer to PF jets. Reprinted from Fig. 13 of ref. [95].

1468 Figure 6.11 shows the σ of a Gaussian fit to the x- and y-components of calibrated
 1469 E_T vs. the calibrated PF E_T sum in a sample of events containing at least two jets
 1470 with $p_T > 25$ GeV. Again, PF E_T outperforms E_T constructed of calorimeter towers
 1471 or track-corrected calorimeter deposits.

1472 6.2 HLT

1473 From the objects described in Sec. 6.1, four samples of events are formed:

- 1474 • $\gamma\gamma$ candidate sample, in which the two highest E_T objects are photons,
- 1475 • $e\gamma$ control sample, in which the two highest E_T objects are one electron and
 1476 one photon,
- 1477 • ee control sample, in which the two highest E_T objects are electrons, and
- 1478 • ff control sample, in which the two highest E_T objects are fakes.

¹⁴⁷⁹ In all samples, the leading EM object is required to have $E_T > 40$ GeV, while the
¹⁴⁸⁰ trailing EM object is required to have $E_T > 25$ GeV. The high level triggers used to
¹⁴⁸¹ select the four samples, by run range, are listed in Table 6.3. No trigger is prescaled.

Table 6.3: HLT paths triggered by the $\gamma\gamma$, $e\gamma$, ee , and ff samples, by run range. No triggers are prescaled.

Run range	$\gamma\gamma$	$e\gamma$	ee	ff
160404-163261	Photon26_ IsoVL_ Photon18	Photon26_ IsoVL_ Photon18	Photon26_ IsoVL_ Photon18	Photon26_ IsoVL_ Photon18
161216-166967	Photon36_ CaloIdL_ Photon22_ CaloIdL	Photon36_ CaloIdL_ Photon22_ CaloIdL	Photon36_ CaloIdL_ Photon22_ CaloIdL	Photon36_ CaloIdL_ Photon22_ CaloIdL
166347-180252	Photon36_ CaloIdL_ IsoVL_ Photon22_ CaloIdL_ IsoVL	Photon36_ CaloIdL_ IsoVL_ Photon22_ CaloIdL_ IsoVL	Photon36_ CaloIdL_ IsoVL_ Photon22_ R9Id	Photon36_ CaloIdL_ IsoVL Photon36_ CaloIdL_ IsoVL Photon36_ R9Id_ Photon22_ CaloIdL_ IsoVL Photon36_ R9Id_ Photon22_ R9Id

¹⁴⁸² Each piece of the HLT path name is defined as follows.

¹⁴⁸³ • Photon: Energy deposit in the ECAL that fired an L1 trigger (cf. Sec. 5.2.1).

1484 For Photon26_IsoVL_Photon18, the L1 seed E_T threshold is 12 GeV, while for Switched
 1485 all other triggers in Table 6.3 it is 20 GeV (cf. Sec. 5.2.1). HLT
 1486 • Integer following the word **Photon**: E_T threshold in GeV for offline reconstructed path
 1487 photon, using the full photon reconstruction of Sec. 6.1.1 minus the laser cali- names
 1488 brations and assuming the primary vertex at (0, 0, 0). to ver-
 1489 • **CaloIdL**: For EB photons, $H/E < 0.15$ and $\sigma_{in\eta} < 0.014$. batim
 1490 • **IsoVL**: $I_{ECAL} < 0.012E_T + 6$ GeV, $I_{HCAL} < 0.005E_T + 4$ GeV, and $I_{track} <$ font and
 1491 $0.002E_T + 4$ GeV. added
 1492 • **R9Id**: $R9 > 0.8$. reference
 1493 In addition, the versions of **HLT_Photon26_IsoVL_Photon18** and to L1
 1494 **Photon36_CaloIdL_Photon22_CaloIdL** that were active during runs 160404-163268 section
 1495 included a cut $E_{max}/E_{5\times5} < 0.98$ for spike rejection. E_{max} is the energy in the Switched
 1496 highest HLT path
 1497 energy crystal of the EM cluster and $E_{5\times5}$ is the energy in the 5×5 crystal matrix names
 1498 around the seed crystal. For runs after 163268, Swiss cross spike rejection of individual to ver-
 1499 crystals from HLT quantities was performed (cf. Sec. 6.1.1). All information about the batim
 1500 evolution of the CMS HLT settings can be found in the HLT configuration browser font
 1501 at <http://j2eeps.cern.ch/cms-project-confdb-hltdev/browser/>. Switched
 1502 As an example of the naming convention just described, the HLT path HLT
 1503 **Photon36_CaloIdL_IsoVL_Photon22_R9Id** is fired if one photon is found with $E_T >$ path
 1504 36 GeV passing the **CaloIdL** and **IsoVL** requirements, and another is found with names
 1505 $E_T > 22$ GeV passing the **R9Id** requirement. to ver-
 1506 For the offline E_T cuts described in this section, the triggers are $> 99\%$ efficient, batim
 1507 as shown in Figure 6.12 [83]. The efficiencies are measured with respect to triggers font
 1508 with lower E_T thresholds. Added
 1509 HLT ef-
 1510 ficiency
 1511 discus-
 1512 sion

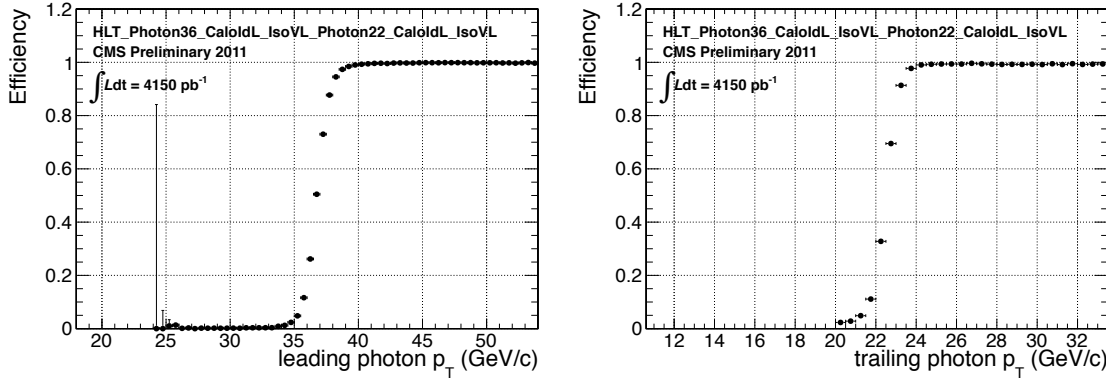


Figure 6.12: Efficiency of HLT_Photon36_CaloIdL_IsoVL_Photon22_CaloIdL_IsoVL for offline selected leading photon (left) and trailing photon (right) vs. photon p_T . Reprinted from Fig. 2 of ref. [83].

1508 6.3 Event Quality

1509 To suppress instrumental backgrounds, a set of event quality cuts are applied to the
 1510 $\gamma\gamma$, $e\gamma$, ee , and ff samples. First, all events are required to pass a good run selec-
 1511 tion, as determined by the CMS Physics Validation Team (<https://twiki.cern.ch/twiki/bin/view/CMS/PVTMain>, CERN computing ID needed). The good run selec-
 1512 tion excludes luminosity sections during which a sufficient part of the CMS detector
 1513 was unpowered or malfunctioning. Such conditions could occur if, for example, a high
 1514 voltage supply trips off in the middle of a run, or a DAQ error corrupts data quality
 1515 but is not spotted until after the data have been collected. The severity of a detec-
 1516 tor problem is judged by its effect on a wide range of analyses and reconstruction
 1517 algorithms. Of the $\sim 5 \text{ fb}^{-1}$ of integrated luminosity delivered by the LHC in 2011,
 1518 4.68 fb^{-1} passed the good run selection. This analysis is performed on the entire 2011
 1519 certified dataset.

1521 Second, all events must contain at least one good interaction vertex. The criteria
 1522 for a good vertex are:

- 1523 • $\chi^2 \neq 0 \parallel \text{ndof} \neq 0 \parallel N_{\text{tracks}} \neq 0$, where χ^2 and ndof are calculated for the track
 1524 fit to the vertex, and N_{tracks} is the number of tracks in the vertex fit

- 1525 • $\text{ndof} > 4$
- 1526 • $|z| < 24 \text{ cm}$, where z is the z -coordinate of the vertex position
- 1527 • $|\rho| < 2 \text{ cm}$, where ρ is the transverse displacement of the vertex position from
1528 the beam line

1529 The good vertex requirement eliminates non-collision backgrounds such as beam
1530 scraping, beam halo, cosmic muon interactions, and instrumental effects.

1531 Third, the two electromagnetic objects in the $\gamma\gamma$, $e\gamma$, ee , and ff events must
1532 be separated in ϕ by at least 0.05. This requirement protects against beam halo
1533 bremsstrahlung, in which a halo muon traveling parallel to the beam line radiates an
1534 energetic photon while itself depositing a large amount of energy in the ECAL. In
1535 this case, the two ECAL hits would likely be at the same ϕ (and ρ).

1536 Fourth, the two EM objects must be separated in R by at least 0.6. Since the
1537 isolation cone size used is 0.3, this ensures that the isolation energy of one EM object
1538 cannot be in the veto strip (Fig. 6.5) of the other.

1539 Finally, the $\gamma\gamma$, $e\gamma$, ee , and ff events must pass an HCAL noise filter and ECAL
1540 dead channel filter. The HCAL noise filter guarantees that all HCAL reconstructed
1541 hits are inconsistent with any noise source. Noise sources [98] include:

- 1542 • Ion feedback in the HPDs absent any true incident photons, in which a thermal
1543 electron ionizes a molecule in the HPD acceleration gap, faking a real signal
- 1544 • HPD discharge affecting nearly all channels in the same HPD [99], partially
1545 explained by the effect of the 4 T CMS magnetic field on the flashover voltage
1546 of the dielectric [101]
- 1547 • Concurrent signals in nearly all 72 channels of a single RBX, as yet unexplained
- 1548 • HF PMT window hits (as opposed to the usual quartz fiber hits)

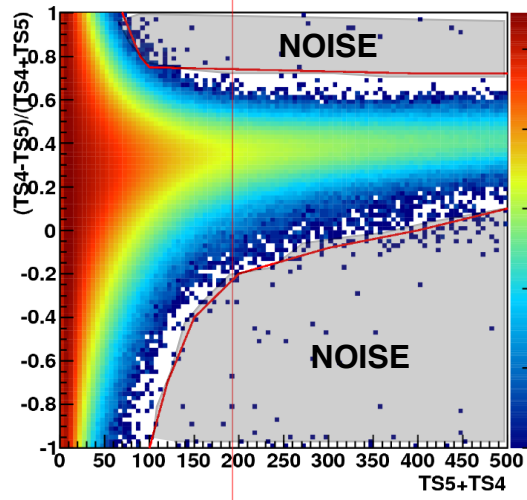


Figure 6.13: $(TS4 - TS5)/(TS4 + TS5)$ vs. $TS4 + TS5$ for a minimum bias sample. HB/HE hits are considered noisy if they lie in the sparsely populated gray region labeled "NOISE" defined by the curved red lines. Adapted from ref. [100].

- 1549 • ADC saturation

1550 Since HCAL noise may induce fake jets or E_T , events are rejected if any of the
1551 following criteria are true:

- 1552 • Any HPD has > 17 hits

- 1553 • A single HPD has > 10 hits, but every other HPD has zero hits

- 1554 • An RBX has > 10 zero-ADC-count hits

1555 • Any HB/HE reconstructed hit corresponding to an RBX with > 50 GeV of
1556 energy fails a two-dimensional cut defined by the variables $(TS4 - TS5)/(TS4 +$
1557 $TS5)$ vs. $TS4 + TS5$, where $TS4(TS5)$ is the hit amplitude in the fourth(fifth)
1558 time sample read out for that hit. The cut is defined in Fig. 6.13.

1559 The ECAL dead channel filter is designed to flag events in which significant EM
1560 energy was deposited in a masked region of the ECAL by using the trigger primitive
1561 information for the corresponding trigger tower. Energy deposited in a masked region

1562 of ECAL can cause fake E_T . Events are rejected if the trigger primitive E_T exceeds
1563 the maximum value of 63.75 GeV in any trigger tower that is masked in the readout.

1564 6.4 Photon Identification Efficiency

1565 In order to determine the cross section (or cross section upper limit) for a GGM
1566 signal, the photon identification efficiency is needed. Since no suitably large sample
1567 of $Z \rightarrow \mu\mu\gamma$ events in CMS exists yet, the efficiency calculation relies on the similarity
1568 between detector response to electrons and photons. A scale factor to correct the MC
1569 photon ID efficiency to the real photon efficiency for the data is obtained from the
1570 ratio of the electron efficiency from the data to the electron efficiency from MC.
1571 The different types of photon ID variables—calorimeter and track isolation, ratio of Removed
1572 hadronic to electromagnetic energy of the shower, and transverse shower shape—are refer-
1573 chosen so that their distributions for isolated electrons and photons are similar.³ ence to
1574 The photon selection efficiency is plots

$$\epsilon_\gamma = \epsilon_\gamma^{\text{MC}} \times \frac{\epsilon_e^{\text{data}}}{\epsilon_e^{\text{MC}}} \quad (6.6)$$

1575 where

- 1576 • ϵ_γ is the photon ID efficiency in data,
- 1577 • $\epsilon_\gamma^{\text{MC}}$ is the photon ID efficiency in MC,
- 1578 • ϵ_e^{data} is the electron ID efficiency obtained using $Z \rightarrow ee$ electrons in the data
1579 that satisfy the photon ID cuts, and

3 $R9$ differs between photons and radiating electrons, but the requirement $R9 < 1$ is loose enough not to introduce problems with the use of electrons to measure the photon ID efficiency.

- 1580 • ϵ_e^{data} is the electron ID efficiency obtained using $Z \rightarrow ee$ electrons in MC that
 1581 satisfy the photon ID cuts.

1582 The ratio $\epsilon_e^{\text{data}}/\epsilon_e^{\text{MC}}$ is defined as the scale factor by which the GGM signal MC
 1583 photon ID efficiency must be multiplied to give an estimate of the photon ID efficiency
 1584 in data. The photon ID requirements of Table 6.1 plus the IsoVL HLT requirement
 1585 described in Sec. 6.2 and Table 6.3 are repeated in Table 6.4.

Table 6.4: Candidate photon ID requirements.

Variable	Cut
I_{ECAL}	$< 0.012E_T + 6 \text{ GeV}$
I_{HCAL}	$< 0.005E_T + 4 \text{ GeV}$
I_{track}	$< 0.002E_T + 4 \text{ GeV}$
H/E	< 0.05
$\sigma_{i\eta i\eta}$	< 0.011
$I_{\text{ECAL}} - 0.0792\rho + I_{\text{HCAL}} - 0.0252\rho + I_{\text{track}}$	$< 6 \text{ GeV}$
$R9$	< 1

1586 6.4.1 Tag and Probe Method

1587 A *Z tag and probe* method is utilized to measure the efficiency of the photon ID
 1588 cuts in Table 6.1. The tag is a well-identified electron. The probe, by contrast, is as
 1589 loosely identified as possible, and all tags must pass the probe criteria in addition to
 1590 the stringent tag criteria. The tag and probe criteria used in this study are shown in
 1591 Table 6.5.

1592 The invariant mass of the tag and probe are required to be within a narrow window
 1593 around Z mass. Assuming that the probabilities of the tag and probe legs of the Z
 1594 decay to pass the photon ID cuts are uncorrelated, the efficiency can be estimated as

$$\epsilon = \frac{N_{\text{tag-pass}}}{N_{\text{tag-pass}} + N_{\text{tag-fail}}} \quad (6.7)$$

Table 6.5: Tag and probe criteria. The superscript 0.4 indicates that the isolation variable was calculated in a cone of $\Delta R = 0.4$ around the photon candidate. The isolations without superscripts use the standard $\Delta R = 0.3$ cones.

Variable	Cut	
	Tag	Probe
RECO object	photon	photon
HLT	HLT_Ele17_CaloIdVT_CaloIsoVT_TrkIdT_TrkIsoVT_SC8_Mass30_v* (must have fired the 17 GeV leg)	—
H/E	< 0.05	< 0.15
$I_{\text{ECAL}}^{0.4}$	$< 0.006E_T + 4.2 \text{ GeV}$	—
$I_{\text{HCAL}}^{0.4}$	$< 0.0025E_T + 2.2 \text{ GeV}$	—
$I_{\text{track}}^{0.4}$	$< 0.001E_T + 2.0 \text{ GeV}$	—
E_T	$> 25 \text{ GeV}$	—
SC E_T	—	$> 15 \text{ GeV}$
SC $ \eta $	< 1.4442	< 1.4442
$\sigma_{i\eta i\eta}$	< 0.009	—
Has pixel seed	Yes	—
Track match type	General track ^a	—
Track match ΔR	< 0.04	—
Track match p_T	$> 15 \text{ GeV}$	—
Track match $ \eta $	< 1.479	—

^aA general track is reconstructed with the CMS standard combinatorial track finder [102].

1595 where $N_{\text{tag-pass}}$ is the number of tag-probe pairs in which the probe leg passes the
 1596 photon ID cuts under study and $N_{\text{tag-fail}}$ is the number of tag-probe pairs in which
 1597 the probe leg fails the cuts. Implicit in these definitions is a double counting of pairs
 1598 in which both electrons pass the tag and probe criteria [103]. In addition, in the rare
 1599 circumstance (less than 1% in MC [103]) that two or more probes may be matched
 1600 to one tag, the pair with invariant mass closest to the Z mass is chosen.

1601 In practice, $N_{\text{tag-pass}}$ and $N_{\text{tag-fail}}$ are returned by a simultaneous unbinned maxi-
 1602 mum likelihood fit to the invariant mass distributions of tag-pass and tag-fail events,
 1603 with appropriate signal and background PDF assumptions. The fit form used is

$$\begin{aligned} f_{\text{tag-pass}}(m_{\text{tag-pass}}) &= \epsilon N_S f_S^{\text{pass}}(m_{\text{tag-pass}}) + N_B^{\text{pass}} f_B^{\text{pass}}(m_{\text{tag-pass}}) \\ f_{\text{tag-fail}}(m_{\text{tag-fail}}) &= (1 - \epsilon) N_S f_S^{\text{fail}}(m_{\text{tag-fail}}) + N_B^{\text{fail}} f_B^{\text{fail}}(m_{\text{tag-fail}}) \end{aligned} \quad (6.8)$$

1604 where $f_{\text{tag-pass}}(m_{\text{tag-pass}})$ and $f_{\text{tag-fail}}(m_{\text{tag-fail}})$ are the tag-pass and tag-fail PDFs,
 1605 respectively; ϵ is the efficiency; N_S is the total number of Z signal events summed over
 1606 both samples; $f_S^{\text{pass}}(m_{\text{tag-pass}})$ and $f_S^{\text{fail}}(m_{\text{tag-fail}})$ are the tag-pass and tag-fail signal
 1607 PDFs, respectively; N_B^{pass} and N_B^{fail} are the numbers of background events in the tag-
 1608 pass and tag-fail samples, respectively; and $f_B^{\text{pass}}(m_{\text{tag-pass}})$ and $f_B^{\text{fail}}(m_{\text{tag-fail}})$ are the
 1609 tag-pass and tag-fail background PDFs, respectively. This particular implementation
 1610 of the tag and probe methodology is based on tag `CMSSW_4_2_5` of the CMSSW
 1611 package `PhysicsTools/TagAndProbe`, and uses the MINUIT2 [104] library, as coded
 1612 in RooFit [105], for the likelihood maximization. For this study, CMSSWv4.2.8 was
 1613 used.

1614 For both samples, the signal shape is assumed to be a Crystal Ball function [106]
 1615 convoluted with the Z generated lineshape, while the background shape is a PDF
 1616 that describes the falling background as well as the kinematic turn-on at low invariant

1617 mass. The background PDF, called `RooCMSShape` [103], is given by

$$f_{\text{RooCMSShape}}(x) = \begin{cases} 1e20 & \text{for } (x - \mu)\gamma < -70 \\ 0 & \text{for } (x - \mu)\gamma > 70 \\ \text{erfc}((\alpha - x)\beta) \exp(-(x - \mu)\gamma) & \text{otherwise} \end{cases} \quad (6.9)$$

1618 where α , β , γ , and μ are parameters of the fit, most of which are held fixed. In the
 1619 three lowest E_T bins, all parameters of the tag-pass and tag-fail background PDFs
 1620 are left floating, because the effect of the relaxed E_T cuts has a significant effect on
 1621 the background shape. More details of the signal and background PDFs are given
 1622 in Table 6.6. The fixed signal and background parameter values were determined by
 1623 fitting a small sample ($0.0 \leq \eta < 0.25$) of `Fall11 MC signal (DYJetsToLL)` and back-
 1624 ground (`QCD_Pt-20to30_BCToE`, `QCD_Pt-30to80_BCToE`, `QCD_Pt-80to170_BCToE`,
 1625 `GJet_Pt-20_doubleEMEnriched`, `WJetsToLNu`, `TTJets`) with parameters left float-
 1626 ing.⁴

Added

1627 Some fit examples are shown in Figures 6.14 and 6.15. In Fig. 6.14, which shows fits
 1628 fits to data and MC for $15 \text{ GeV} \leq \text{probe } E_T < 20 \text{ GeV}$, the kinematic turn-on is below
 1629 the invariant mass range covered by the plot. The exponentially falling background
 1630 is easily seen underneath the signal, and is especially pronounced in the background-
 1631 dominated tag-fail sample.

1632 6.4.2 Photon Efficiency Scale Factor $\epsilon_e^{\text{data}}/\epsilon_e^{\text{MC}}$

1633 Figure 6.16 shows the dependence of the photon ID efficiency scale factor $\epsilon_e^{\text{data}}/\epsilon_e^{\text{MC}}$
 1634 on E_T , η , and N_{jet} , where jets are defined as in Table 6.2, but with only the two
 1635 Z electrons considered as candidates for overlap removal. Errors are statistical only.

⁴See Appendix A for a discussion of the MC samples.

Table 6.6: Parameter values (parameter definitions are in the text) for the signal and background PDFs for the different samples. The background PDF applies to all efficiency bins except the four lowest E_T bins, which use a floating `RooCMSShape` background. When a bracketed range is given, the parameter is allowed to float within that range. When a constant is given, the parameter is fixed to that constant.

PDF	Crystal Ball fit parameters				RooCMSShape fit parameters			
	μ	σ	α	n	μ	α	β	γ
Tag-pass signal	[-1.0, 1.0]	[1.0, 3.0]	0.87	97.0	N/A	N/A	N/A	N/A
Tag-fail signal	[-1.0, 1.0]	[1.0, 3.0]	0.73	134.9	N/A	N/A	N/A	N/A
Tag-pass background	N/A	N/A	N/A	N/A	65.0	61.949	0.04750	0.01908
Tag-fail background	N/A	N/A	N/A	N/A	α	[50.0, 100.0]	0.065	0.048

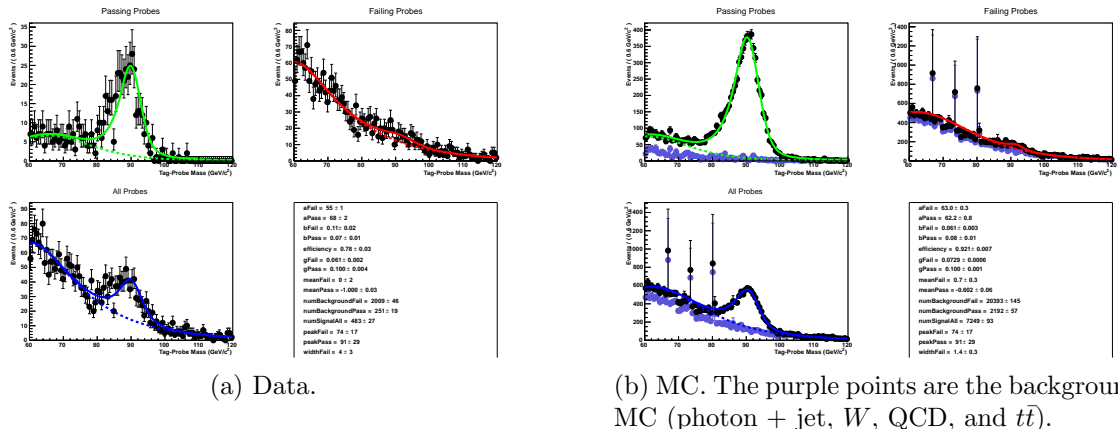


Figure 6.14: Tag and probe invariant mass fits for $15 \text{ GeV} \leq \text{probe } E_T < 20 \text{ GeV}$. Errors are statistical only. The tag-pass fit is shown in green, the tag-fail fit in red, and a fit to both samples in blue. Dotted lines are the background components of the fits; solid lines are signal plus background.

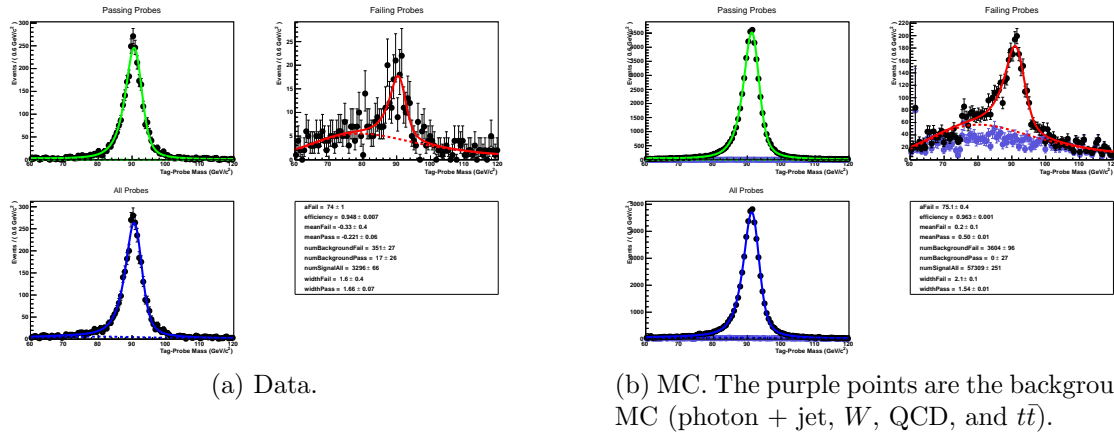


Figure 6.15: Tag and probe invariant mass fits for $-0.25 \leq \text{probe } \eta < -0.5$. Errors are statistical only. The tag-pass fit is shown in green, the tag-fail fit in red, and a fit to both samples in blue. Dotted lines are the background components of the fits; solid lines are signal plus background.

1636 There no significant dependence of the scale factor on these variables, so only one
1637 scale factor is computed from the entire dataset.

1638 The effect of pileup is studied by comparing the efficiencies ϵ_e^{data} and ϵ_e^{MC} vs. the
1639 number of primary vertices (N_{PV}) in the event. The efficiency only drops a few percent
1640 for events with large N_{PV} after using pileup-corrected isolation cuts, as can be seen in
1641 Figure 6.17a. The MC tracks the data, and the scale factor is flat vs. N_{PV} , as shown
1642 in Fig. 6.17b.

1643 The scale factor is measured to be $\epsilon_e^{\text{data}}/\epsilon_e^{\text{MC}} = 0.994 \pm 0.002(\text{stat.}) \pm 0.035(\text{syst.})$.
1644 Four main sources of systematic error, in addition to the statistical error of 0.2%, were
1645 studied.

1646 **Different behavior of electrons and photons in MC** Even though the photon
1647 ID cuts are designed to be similarly efficient for both electrons and photons,
1648 there might be a small difference in the performance between the two kinds
1649 of particles, e.g. because of electron bremsstrahlung. To check this effect, the
1650 MC electron ID efficiency was calculated using a $Z \rightarrow ee$ sample and the MC
1651 photon ID efficiency was calculated using a $\gamma + \text{jets}$ sample. Both samples were

Official
result
uses this
syst.
error, so
I am not
recheck-
ing
it

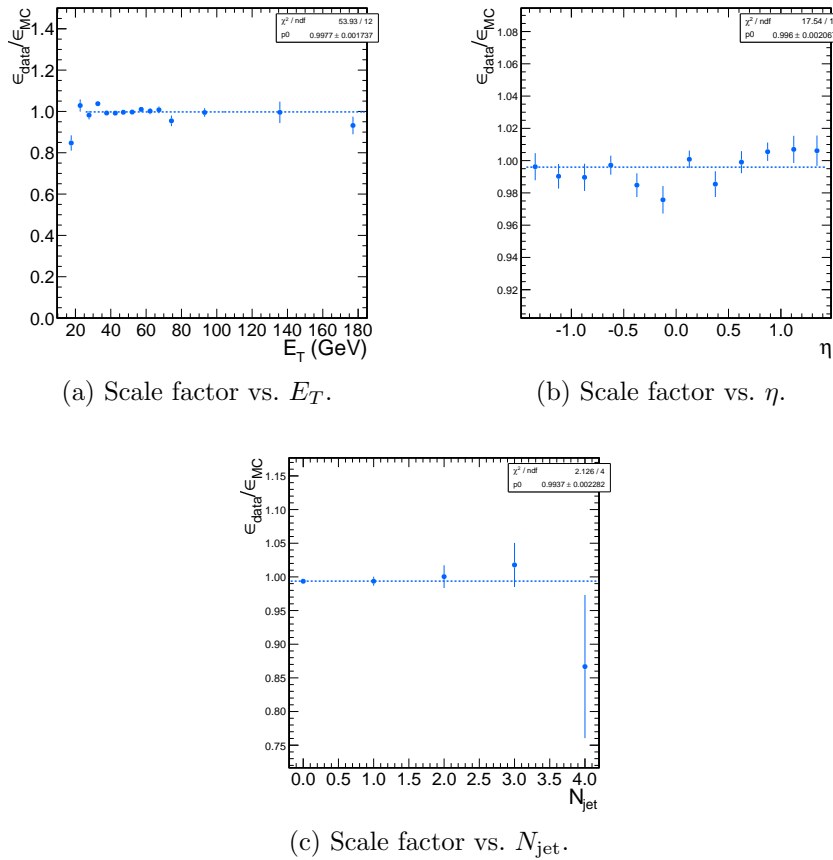


Figure 6.16: Dependence of the photon ID efficiency scale factor on some kinematic variables. Errors are statistical only.

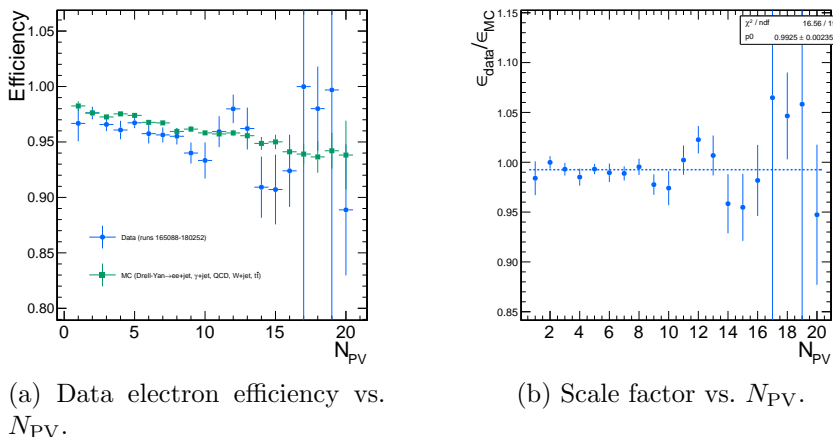


Figure 6.17: Dependence of the photon ID efficiency scale factor on the number of primary vertices per event. Errors are statistical only.

1652 reconstructed in CMSSWv3.6. Half the difference between these two results,
 1653 0.5%, was taken as an error on the scale factor.

Corrected

1654 **Pileup** To account for the possibility that the MC simulation may not adequately some of
 1655 reproduce the data in a high pileup environment, the data/MC scale factor these
 1656 for events with 1-4 good reconstructed primary vertices was calculated, along bullets
 1657 with the same for events with ≥ 5 good reconstructed primary vertices. The
 1658 difference between the scale factors from both samples, 2.4%, was taken as an
 1659 error on the scale factor from pileup.

1660 **Signal fit over/underestimation** It was found that the signal fit slightly under-
 1661 estimates the data in the tag-pass sample, and slightly overestimates it in the tag-fail sample. To cover this effect with a systematic error, the efficiencies in
 1662 data and MC, and then the scale factor, were recalculated using the background
 1663 (from fit) subtracted integrals of the tag-pass and tag-fail distributions, rather
 1664 than the fitted signal yields in those distributions. The difference between the
 1665 scale factor found in this way and the nominal scale factor, 1.9%, was taken as
 1666 an error on the scale factor.
 1667

1668 **Signal and background shape assumption** To assess the magnitude of the error
 1669 from the signal and background shape assumptions, the tag-pass and tag-fail
 1670 tail parameters (Crystal Ball α and n) were varied by $\pm 1\sigma$, and the background
 1671 shape was varied between `RooCMSShape`, exponential, power law, and quadratic.
 1672 All possible combinations of varied parameters were generated, and the data and
 1673 MC were refit and new scale factors generated according to those combinations.
 1674 The error was taken as the largest deviation of the scale factor from nominal,
 1675 1.8%.

1676 Finally, the pixel veto efficiency was estimated from MC to be 0.96 ± 0.005 (syst.),
 1677 with error due to varying assumptions of the tracker material distribution [107].

1678

Chapter 7

1679

Data Analysis

1680 The signature of GGM SUSY particle production in this search is an excess of two-
1681 photon events with high \cancel{E}_T . \cancel{E}_T is reconstructed using the particle flow algorithm
1682 as described in Sec. 6.1.3. Candidate two-photon events, as well as control events,
1683 are selected according to the offline object criteria presented in Secs. 6.1.1, 6.1.2,
1684 and 6.1.3; the event quality criteria in Sec. 6.3; and the trigger requirements in Sec. 6.2.
1685 These are summarized in Table 7.1.

Table 7.1: Selection criteria for $\gamma\gamma$, $e\gamma$, ee , and ff events.

Variable	Cut			
	$\gamma\gamma$	$e\gamma$	ee	ff
HLT match	IsoVL	IsoVL	IsoVL	IsoVL R9Id
E_T	$> 40/ > 25 \text{ GeV}$			
$\text{SC } \eta $	< 1.4442	< 1.4442	< 1.4442	< 1.4442
H/E	< 0.05	< 0.05	< 0.05	< 0.05
$R9$	< 1	< 1	< 1	< 1
Pixel seed	No/No	Yes/No	Yes/Yes	No/No
$I_{\text{comb}}, \sigma_{inj\eta}$	$< 6 \text{ GeV} \&& < 0.011$	$< 6 \text{ GeV} \&& < 0.011$	$< 6 \text{ GeV} \&& < 0.011$	$< 20 \text{ GeV} \&& (\geq 6 \text{ GeV} \parallel \geq 0.011)$
JSON	Yes	Yes	Yes	Yes
No. good PVs	≥ 1	≥ 1	≥ 1	≥ 1
ΔR_{EM}	> 0.6	> 0.6	> 0.6	> 0.6
$\Delta\phi_{\text{EM}}$	≥ 0.05	≥ 0.05	≥ 0.05	≥ 0.05

1686 This search utilizes 4.7 fb^{-1} of CMS data collected during the period April
 1687 December 2011, corresponding to the following datasets [108]:

- 1688 • /Photon/Run2011A-05Jul2011ReReco-ECAL-v1/AOD
- 1689 • /Photon/Run2011A-05Aug2011-v1/AOD
- 1690 • /Photon/Run2011A-03Oct2011-v1/AOD
- 1691 • /Photon/Run2011B-PromptReco-v1/AOD

1692 The search strategy is to model the backgrounds to the GGM SUSY signal using
 1693 \cancel{E}_T shape templates derived from the control samples, and then to look for a high- \cancel{E}_T
 1694 excess above the estimated background in the $\gamma\gamma$ sample. There are two categories
 1695 of backgrounds: QCD processes with no real \cancel{E}_T and electroweak processes with real
 1696 \cancel{E}_T from neutrinos. The relevant QCD background processes are multijet production
 1697 with at least two jets faking photons, photon + jet production with at least one jet
 1698 faking a photon, and diphoton production, and Z production with a radiated photon
 1699 where at least one of the Z decay products (typically a jet) fakes a photon. The
 1700 relevant electroweak background processes, which are small compared to the QCD
 1701 background, involve $W \rightarrow e\nu$ decay with a recoiling jet that fakes a photon or a
 1702 real radiated photon (the W may come from the decay of a top quark in $t\bar{t}$ events).
 1703 In both cases, the electron is misidentified as a photon due to a small inefficiency
 1704 in reconstructing the electron pixel seed. The main diagrams contributing to the
 1705 QCD(electroweak) backgrounds are shown in Figure 7.1(7.2).

1706 Data control samples are used to model all of the backgrounds. The primary
 1707 control sample used to model the QCD background is the ff sample, which is similar
 1708 to the candidate $\gamma\gamma$ sample but with combined isolation or $\sigma_{inj\eta}$ cuts inverted. The cuts
 1709 on these variables are used to distinguish between photons and jets, so by inverting
 1710 those cuts, the resulting ff sample becomes enriched with QCD dijets. Because the

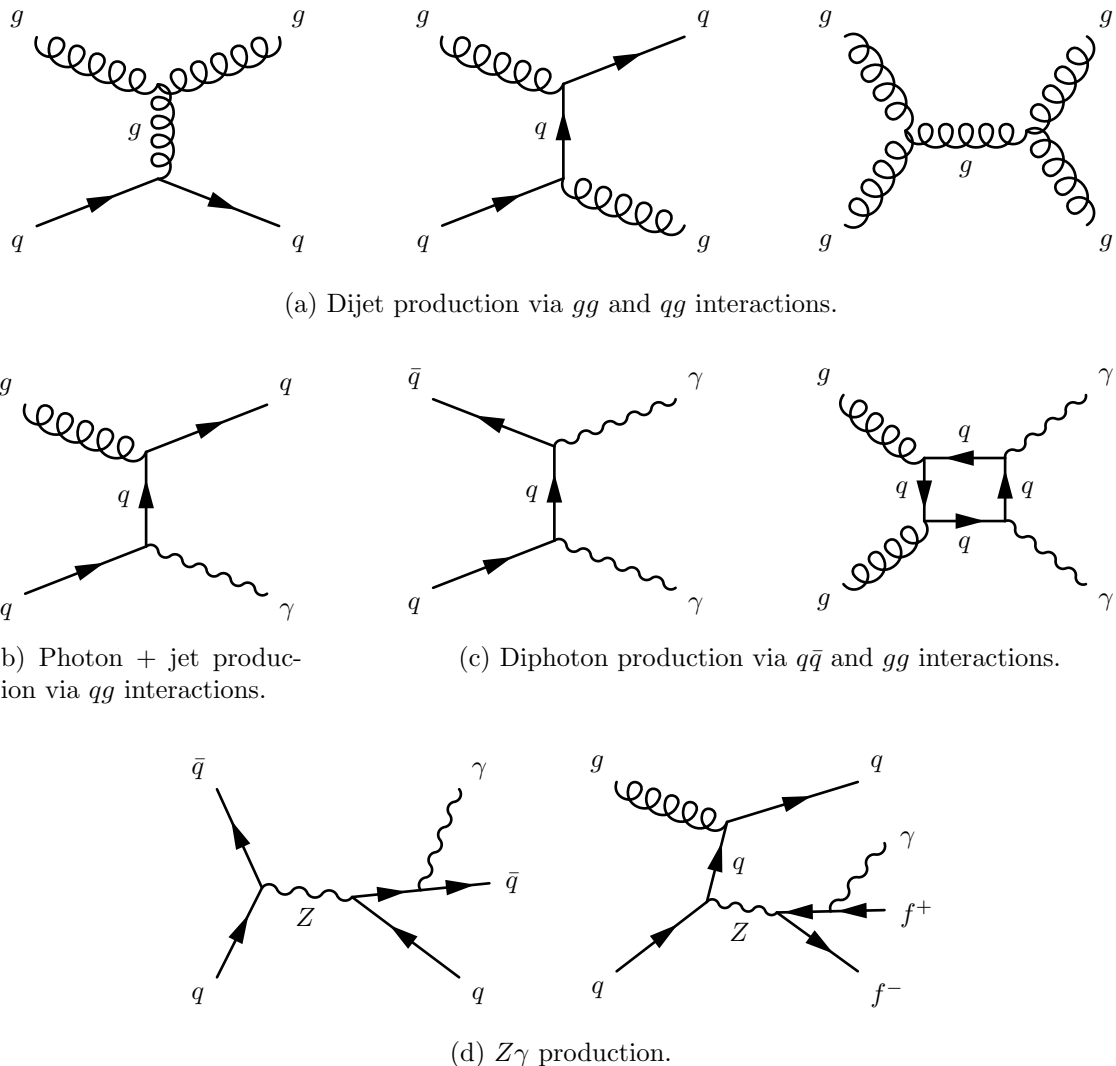


Figure 7.1: Representative Feynman diagrams of some QCD backgrounds to the GGM SUSY search.

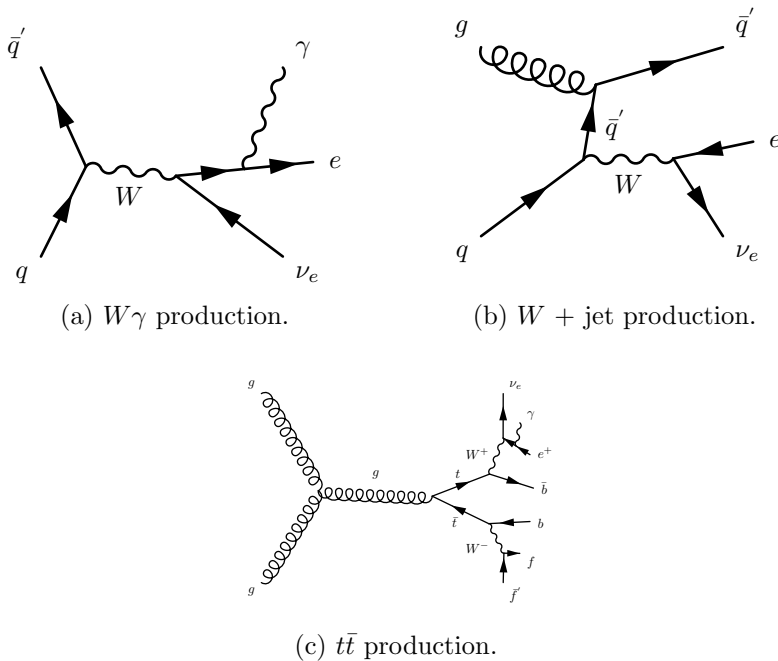


Figure 7.2: Representative Feynman diagrams of some electroweak backgrounds to the GGM SUSY search.

fake photons are still required to pass a tight cut on H/E , they are guaranteed to be very electromagnetic jets, with an EM energy scale and resolution similar to that of the candidate photons. This insures that the resulting estimate of the \cancel{E}_T shape does not have too long of a tail from severe HCAL mis-measurements that are actually rare in the $\gamma\gamma$ sample.

As a cross-check, the ee sample is also used to model the QCD background. This sample of Z decays should have no true \cancel{E}_T , just like the ff sample, and the electron definition (differing from the photon definition only in the presence of a pixel seed) insures that the electron energy scale and resolution is similar to that of the photon.

Finally, the $e\gamma$ sample is used to model the electroweak background from $W \rightarrow e\nu$ decays. The $e\gamma$ \cancel{E}_T distribution is scaled by the electron \rightarrow photon misidentification rate to predict the number of $W\gamma$, $W + \text{jet}$, and $t\bar{t}$ events in the $\gamma\gamma$ sample.

The remainder of this chapter describes the data analysis procedures and the final results of the search. Sec. 7.1 addresses the QCD background estimation. Sec. 7.2

1725 addresses the electroweak background estimation. The chapter concludes with a dis-
 1726 cussion of systematic errors in Sec. 7.3 and a presentation of the final results in
 1727 Sec. 7.4.

1728 7.1 Modeling the QCD Background

1729 7.1.1 Outline of the Procedure

1730 Due to the fact that the CMS ECAL energy resolution is much better than the
 1731 HCAL energy resolution, the energies of the two candidate photons in the events of
 1732 the $\gamma\gamma$ sample are typically measured to far greater accuracy and precision than the
 1733 energy of the hadronic recoil in those events. Therefore, fake E_T in the $\gamma\gamma$ sample
 1734 is almost entirely the result of hadronic mis-measurement in QCD dijet, photon +
 1735 jet, and diphoton events. The strategy employed to model this background is to find
 1736 a control sample in data consisting of two well-measured EM objects, just like the
 1737 candidate $\gamma\gamma$ sample, and assign each event a weight to account for the underlying
 1738 kinematic differences between the control and candidate samples. Once the reweighted
 1739 E_T spectrum of the control sample is created, it is then normalized in the low- E_T
 1740 region, the assumption being that GGM SUSY does not predict a significant amount
 1741 of events at low E_T . There are three aspects of this QCD background estimation
 1742 procedure that bear highlighting:

1743 **Choice of control sample** Since the underlying cause of E_T in the candidate sam-
 1744 ple is mis-measured hadronic activity, a control sample with similar hadronic
 1745 activity to the candidate sample should be chosen. Hadronic activity refers to
 1746 number of jets, jet E_T , pileup, etc.

1747 **Reweighting** The control sample is reweighted so that its E_T spectrum appears as it
 1748 would if the control sample had the same kinematic properties as the candidate

sample (i.e. particle p_T and η distributions, etc.). By choosing an appropriate control sample and reweighting it, the control \cancel{E}_T distribution should now match both the hadronic activity and the kinematics of the candidate sample.

Normalization Finally, the control E_T distribution is normalized in a region of low \cancel{E}_T , where contamination from the expected GGM SUSY signal is small. This implies an extrapolation of the low- \cancel{E}_T QCD background prediction to the high- \cancel{E}_T signal region.

As explained in the beginning of this chapter, the ff sample is used as the primary QCD control sample, while the ee sample is used as a cross-check. Both samples have two well-measured EM objects per event, no real \cancel{E}_T , and similar hadronic activity to the $\gamma\gamma$ sample. Figure 7.3 shows a comparison of the shapes of some distributions relevant to hadronic activity between the $\gamma\gamma$, ee , and ff samples. In general, the ee sample has less hadronic activity than the $\gamma\gamma$ and ff samples, as shown by the more steeply falling ee distributions in Figs. 7.3a, 7.3b, 7.3c, and 7.3d. In addition to the kinematic reweighting, there is also a reweighting by number of jets per event, which attempts to correct for this difference (see Sec. 7.1.2).

7.1.2 Reweighting

To reweight the control sample events to match the kinematics of the candidate sample events, a weight based on the p_T of the di-EM-object system and the number of jets in the event is used. As explained in Sec. 7.1.1, E_T in the $\gamma\gamma$, ff , and ee samples is due to the poorly measured hadronic recoil off the well-measured di-EM system. Therefore, the p_T of the di-EM system is a good handle on the true magnitude of the hadronic recoil, which affects the measured \cancel{E}_T . The di-EM system is depicted in Figure 7.4. As shown in Figure 7.5, \cancel{E}_T is largely uncorrelated with di-EM p_T , so there is little danger of reweighting away a true signal excess.

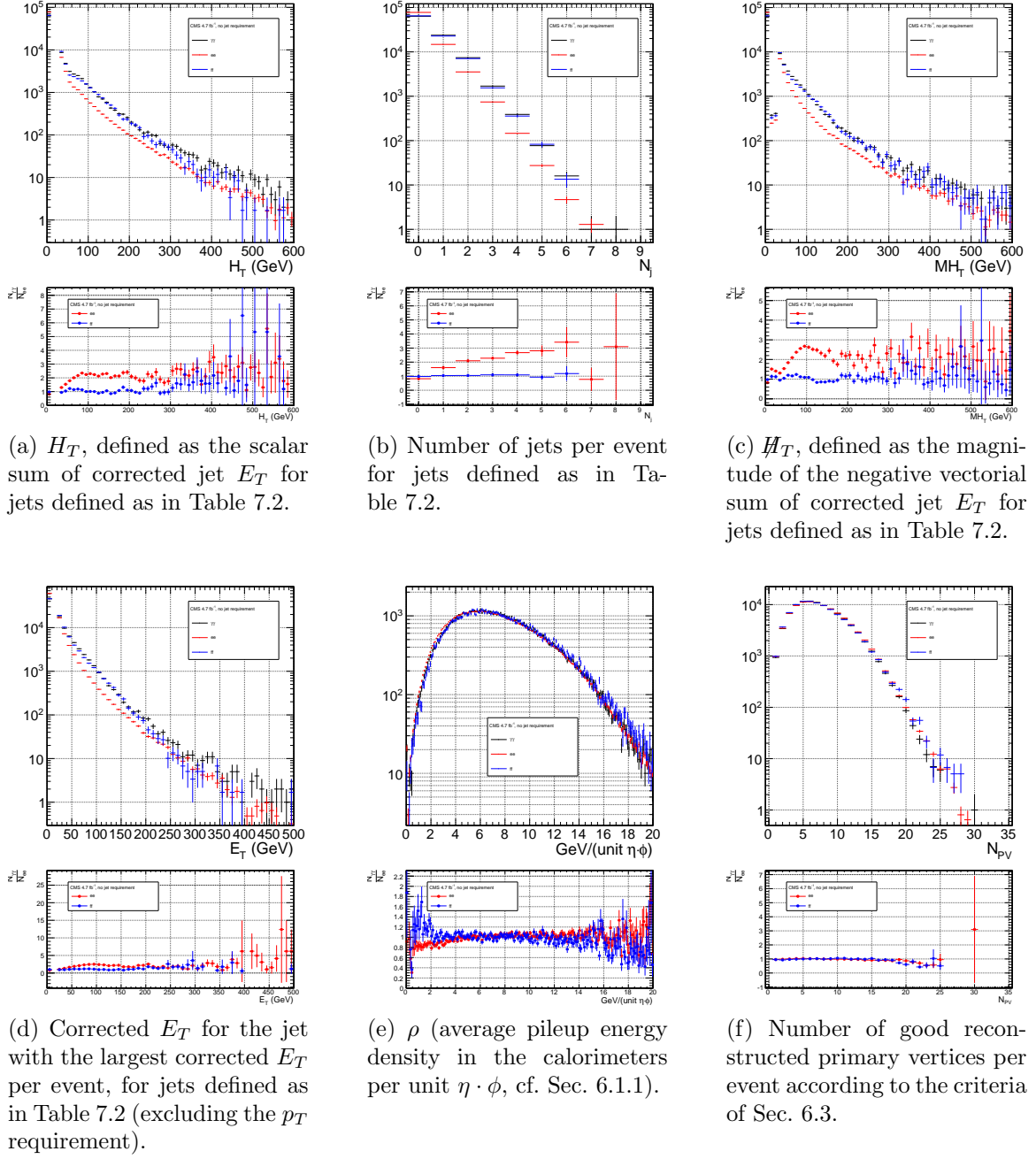


Figure 7.3: Comparison of the shapes of some distributions relevant to hadronic activity between the $\gamma\gamma$, ee ($81 \text{ GeV} \leq m_{ee} < 101 \text{ GeV}$), and ff samples. The ee and ff distributions are normalized to the number of events in the $\gamma\gamma$ distribution. Errors are statistical only.

Table 7.2: Definition of HB/HE/HF hadronic jets.

Variable	Cut
Algorithm	L1FastL2L3Residual corrected PF (cf. Sec. 6.1.3)
p_T	$> 30 \text{ GeV}$
$ \eta $	< 5.0
Neutral hadronic energy fraction	< 0.99
Neutral electromagnetic energy fraction	< 0.99
Number of constituents	> 1
Charged hadronic energy	$> 0.0 \text{ GeV}$ if $ \eta < 2.4$
Number of charged hadrons	> 0 if $ \eta < 2.4$
Charged electromagnetic energy fraction	< 0.99 if $ \eta < 2.4$
ΔR to nearest PF electron ^a , muon ^b , or one of the two primary EM objects	> 0.5

^aA PF electron is defined as an electron reconstructed with the PF algorithm [84] with $p_T > 15 \text{ GeV}$, $|\eta| < 2.6$, and $(I_{\text{charged}} + I_{\text{photon}} + I_{\text{neutral}})/p_T < 0.2$, where $I_{\text{charged}}(I_{\text{photon}})(I_{\text{neutral}})$ is the sum of PF charged hadron(PF photon)(PF neutral hadron) momenta in a $\Delta R = 0.4$ cone around the PF electron.

^bMuons are reconstructed [85] from a combination of muon station and inner tracker hits. Here, a muon must have track $\chi^2 < 10$, at least one good muon station hit, inner track transverse impact parameter $< 0.02 \text{ cm}$, inner track longitudinal impact parameter $< 0.5 \text{ cm}$, $p_T > 15 \text{ GeV}$, $|\eta| < 2.6$, and $(I_{\text{ECAL}} + I_{\text{HCAL}} + I_{\text{track}})/p_T < 0.2$, where $I_{\text{ECAL}}(I_{\text{HCAL}})(I_{\text{track}})$ is the sum of ECAL(HCAL)(track) momenta in a $\Delta R = 0.3$ cone around the muon.

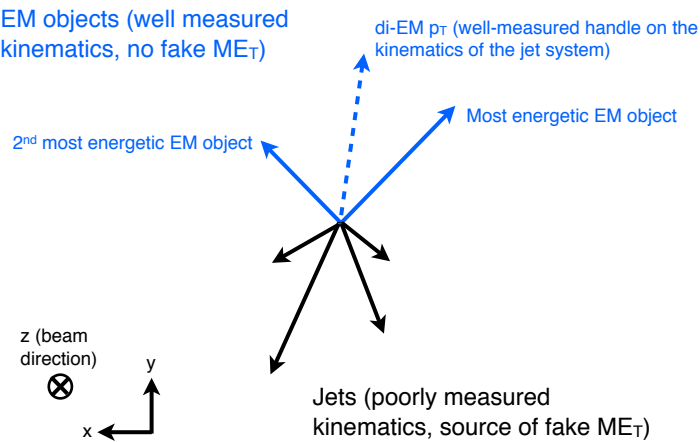


Figure 7.4: Cartoon showing the di-EM system in blue and the hadronic recoil in black. The di-EM p_T (dashed blue line) is used to reweight the control sample kinematic properties to match those of the candidate $\gamma\gamma$ sample.

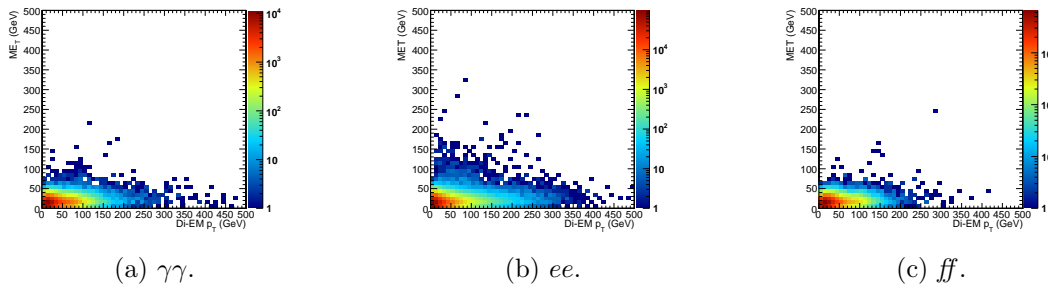


Figure 7.5: E_T vs. di-EM p_T .

Whereas the di-EM p_T reweighting accounts for differences in production kinematics between the control and $\gamma\gamma$ samples, a simultaneous reweighting based on the number of jets in the event accounts for differences in hadronic activity between the samples, especially between ee and $\gamma\gamma$ (cf. Fig. 7.3). Jets are defined as in Table 6.2. Figure 7.6 shows the effect of reweighting by number of jets per event, which is to increase(decrease) the tail of the $ee(ff)$ E_T spectrum.

1780 Although the electron and photon energies are well measured by the ECAL, the
 1781 ECAL-only measurement of the fake photon energy (cf. Sec 6.1.1) is biased slightly
 1782 low due to the fact that fakes (which are really jets) tend to deposit some energy in
 1783 the HCAL. This can be seen in Figs. 7.7 and 7.8, which show the relative difference
 1784 between the ECAL-only E_T measurement and the PF E_T measurement vs. EMF for
 1785 electrons, photons, and fakes. PF E_T is defined as the L1Fast-corrected E_T of the
 1786 nearest PF jet with $p_T \geq 20$ GeV (i.e., the E_T of the PF jet object reconstructed from
 1787 the same ECAL shower as the fake photon). On average, the fakes tend to deposit
 1788 a few percent more energy in the HCAL than the electrons or photons, which is
 1789 recovered by the PF algorithm. For this reason, the PF p_T is used in the calculation
 1790 of di-EM p_T rather than the ECAL-only p_T .¹ This leads to a modest improvement in
 1791 the agreement between the ee and ff E_T spectra, as shown in Figure 7.9.

1792 The control sample event weights are defined as

¹In the few events ($\mathcal{O}(10^{-3})$) in which two PF jet objects, corresponding to the two electrons or fakes, are not found, the ECAL-only p_T is used.

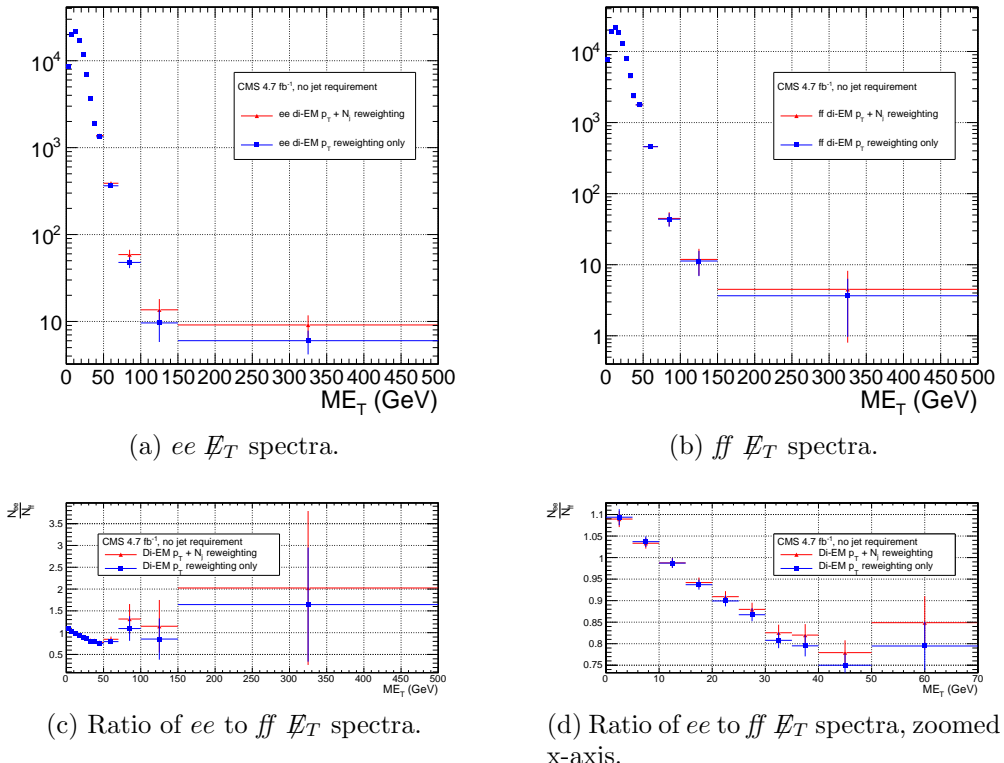


Figure 7.6: \cancel{E}_T spectra of the reweighted ee ($81 \text{ GeV} \leq m_{ee} < 101 \text{ GeV}$) and ff control samples. Blue squares indicate di-EM p_T reweighting only; red triangles indicate di-EM $p_T + \text{number of jets}$ reweighting. PF p_T (cf. p. 127) is used to calculate the di-EM p_T . The full normalization procedure is employed, along with ee sideband subtraction (discussed at the end of this section). Error bars are statistical only.

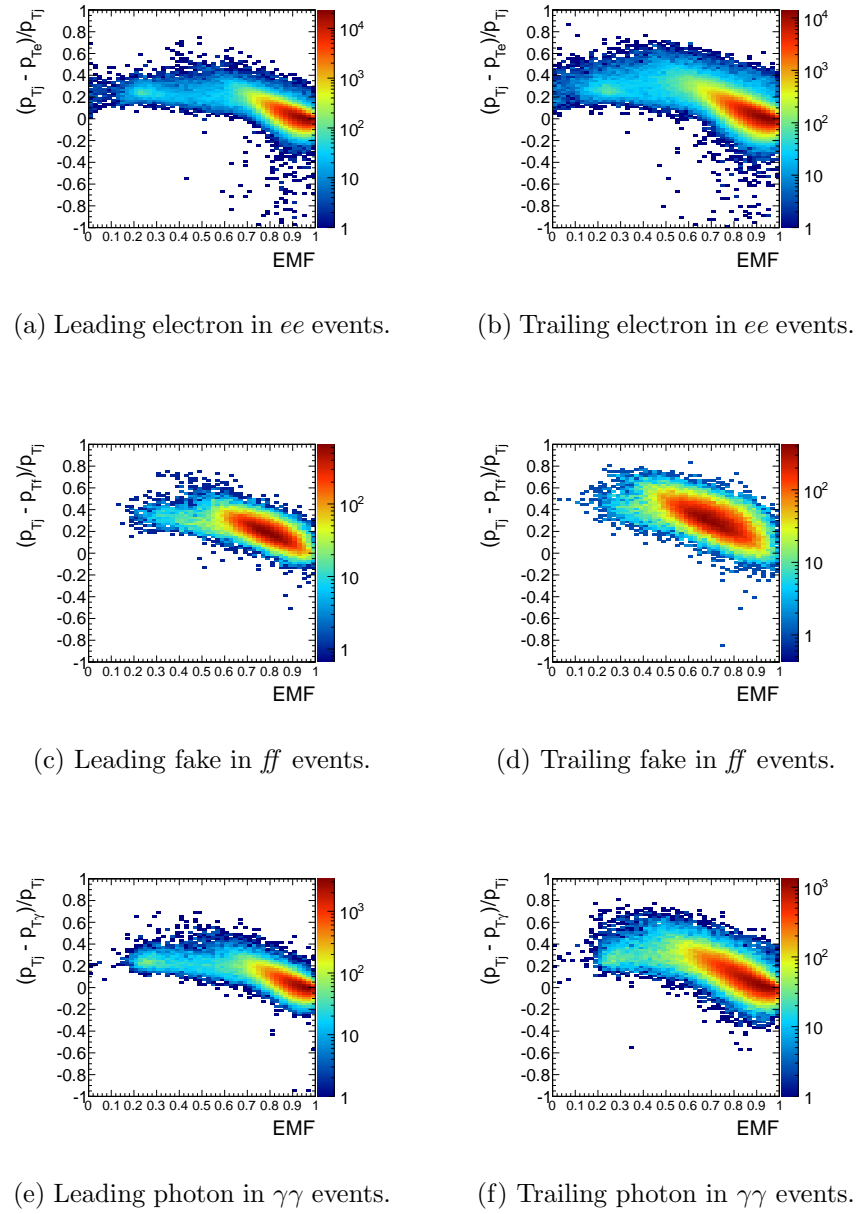


Figure 7.7: Relative difference between the ECAL-only E_T measurement and the PF E_T measurement vs. EMF. PF E_T is defined in the text.

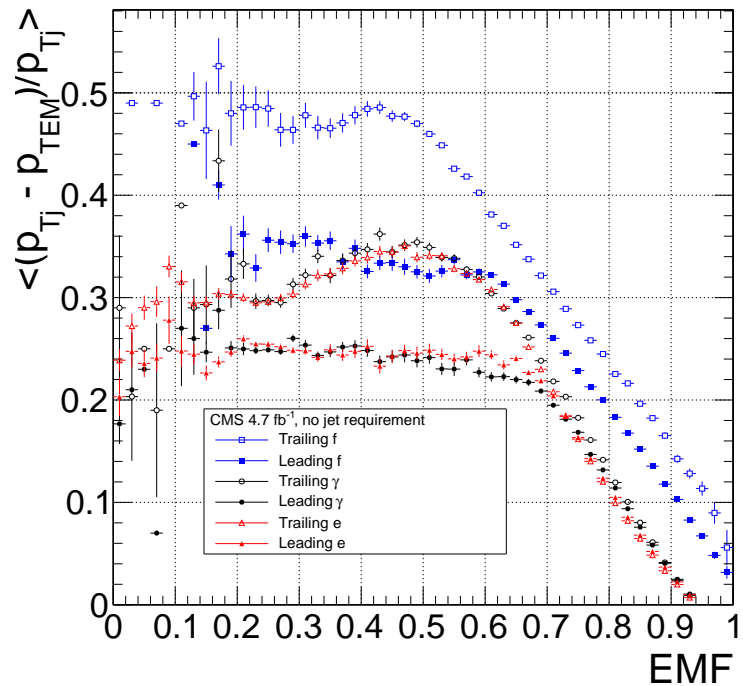


Figure 7.8: Average relative difference between the ECAL-only E_T measurement and the PF E_T measurement vs. EMF for the leading (filled marker) and trailing (open marker) electrons in ee events (red triangles), fakes in ff events (blue squares), and photons in $\gamma\gamma$ events (black circles). These are nothing more than profile histograms of Fig. 7.7. PF E_T is defined in the text. Error bars are statistical only.

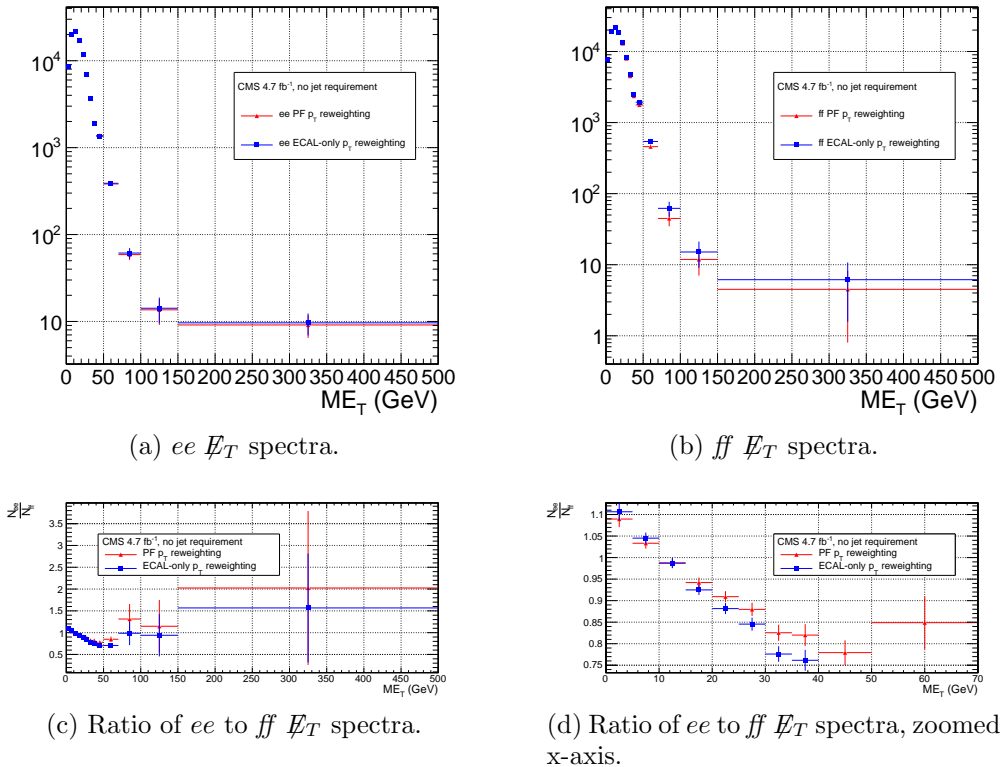


Figure 7.9: E_T spectra of the reweighted ee ($81 \text{ GeV} \leq m_{ee} < 101 \text{ GeV}$) and ff control samples. Blue squares indicate reweighting using the ECAL-only p_T estimate; red triangles indicate reweighting using the PF p_T estimate. The full reweighting and normalization procedure is employed, along with ee sideband subtraction (discussed at the end of this section). Error bars are statistical only.

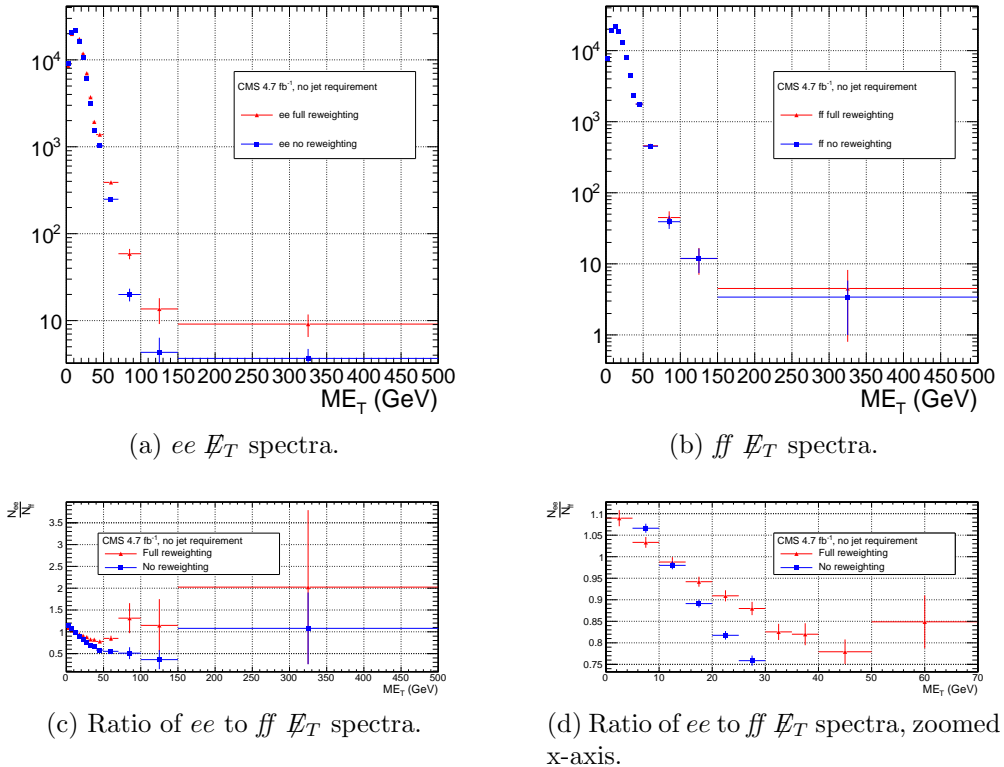


Figure 7.10: E_T spectra of the ee ($81 \text{ GeV} \leq m_{ee} < 101 \text{ GeV}$) and ff control samples. Red triangles indicate full di-EM $p_T +$ number of jets reweighting; blue squares indicate no reweighting. PF p_T (cf. p. 129) is used to calculate the di-EM p_T . The full normalization procedure is employed, along with ee sideband subtraction (discussed at the end of this section). Error bars are statistical only.

$$w_{ij} = \frac{N_{\text{control}}}{N_{\gamma\gamma}} \frac{N_{\gamma\gamma}^{ij}}{N_{\text{control}}^{ij}} \quad (7.1)$$

where i runs over the number of di-EM p_T bins, j runs over the number of jet bins,
 N_{control} is the total number of events in the control sample, $N_{\gamma\gamma}$ is the total number of
events in the $\gamma\gamma$ sample, $N_{\gamma\gamma}^{ij}$ is the number of $\gamma\gamma$ events in the i^{th} di-EM p_T bin and
 j^{th} jet bin, and N_{control}^{ij} is the number of control sample events in the i^{th} di-EM p_T
bin and j^{th} jet bin. The effect of the reweighting is more significant for the ee sample
than for the ff sample, as shown in Figure 7.10.

1799 The ee sample contains a non-negligible background of $t\bar{t}$ events in which both
 1800 W bosons decay to electrons. These events have significant real \cancel{E}_T from the two
 1801 neutrinos (unlike the $\gamma\gamma$ events), and therefore inflate the background estimate at
 1802 high \cancel{E}_T . In order to remove the $t\bar{t}$ contribution from the ee sample, a sideband
 1803 subtraction method is employed.

1804 Only events in the ee sample with $81 \text{ GeV} \leq m_{ee} < 101 \text{ GeV}$, where m_{ee} is the
 1805 di-electron invariant mass, are used in the QCD background estimate. This choice
 1806 maximizes the ratio of Z signal to background. The sidebands used to estimate the
 1807 background contribution within the Z window are defined such that $71 \text{ GeV} \leq m_{ee} <$
 1808 81 GeV and $101 \text{ GeV} \leq m_{ee} < 111 \text{ GeV}$.

1809 The full reweighting procedure is applied to the Z signal region and the two
 1810 sideband regions independently. Only Z signal events are used in the calculation of
 1811 the di-EM p_T weights for the Z signal region, and likewise only the events within
 1812 a given sideband region are used in the calculation of the weights for that region.
 1813 Assuming a constant $t\bar{t}$ background shape, the resulting reweighted sideband \cancel{E}_T
 1814 distributions are added together and subtracted from the reweighted Z signal \cancel{E}_T
 1815 distribution. The sideband subtracted Z signal \cancel{E}_T distribution is then normalized
 1816 as discussed in Secs. 7.1.1 and 7.1.3. The statistical and reweighting error from the
 1817 sideband regions is propagated to the error on the final ee QCD \cancel{E}_T estimate.

1818 The di-EM p_T weights for the two ee sideband regions are shown in Figure 7.11.
 1819 The overall scale of the weights, as well as the trend with di-EM p_T , is similar for
 1820 the two regions (except at high di-EM p_T , where the statistics are poor anyway).
 1821 Figure 7.12 shows the \cancel{E}_T spectra for the two sideband regions and the Z signal
 1822 region after subtraction. The shapes of the spectra indicate that the high- \cancel{E}_T $t\bar{t}$ tail,
 1823 present in the sideband distributions, was successfully subtracted from the Z signal
 1824 distribution.

1825 The ee ($81 \text{ GeV} \leq m_{ee} < 101 \text{ GeV}$), ff , and $\gamma\gamma$ di-EM p_T spectra for events with

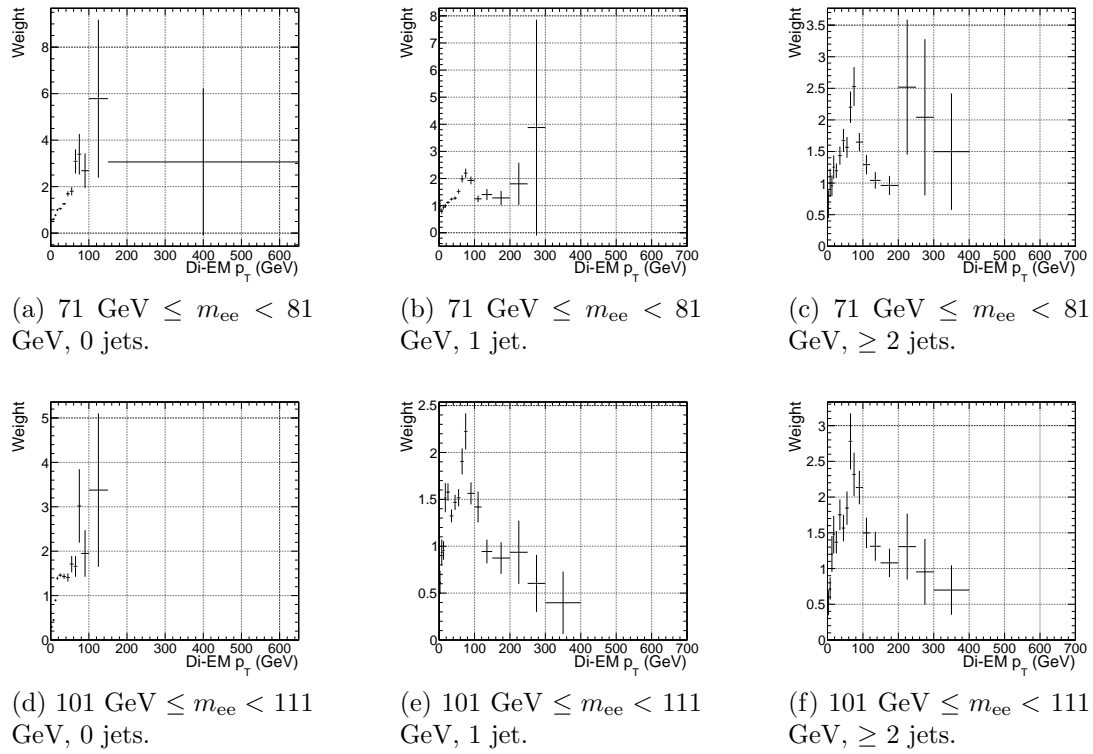


Figure 7.11: ee sideband di-EM p_T weights for events with 0, 1, or ≥ 2 jets (as in Table 6.2). Errors are statistical only.

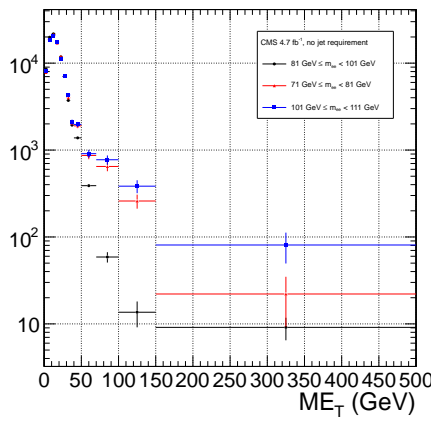


Figure 7.12: E_T spectra of the ee sample for $71 \text{ GeV} \leq m_{ee} < 81 \text{ GeV}$ (red triangles), $81 \text{ GeV} \leq m_{ee} < 101 \text{ GeV}$ (black circles), and $101 \text{ GeV} \leq m_{ee} < 111 \text{ GeV}$ (blue squares). The two sideband distributions (red and blue) and the Z signal distribution (black) are normalized to the total number of $\gamma\gamma$ events. Errors are statistical only.

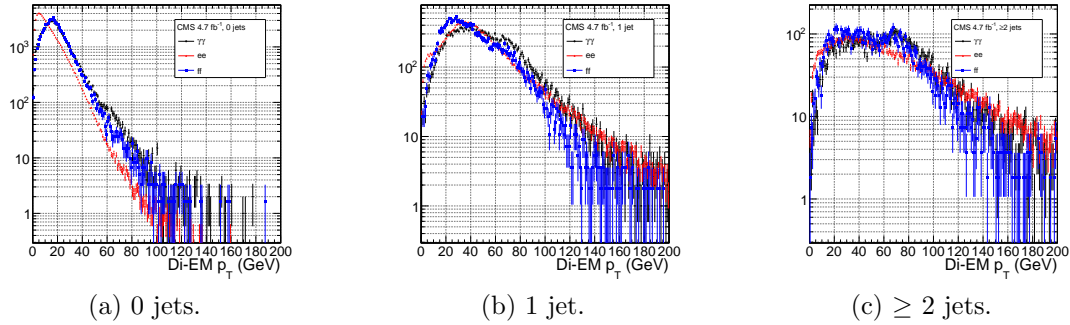


Figure 7.13: ee ($81 \text{ GeV} \leq m_{ee} < 101 \text{ GeV}$) (red triangles), ff (blue squares), and $\gamma\gamma$ (black circles) di-EM p_T spectra for events with 0, 1, or ≥ 2 jets (as in Table 6.2). Errors are statistical only.

1826 0, 1, or ≥ 2 jets (as in Table 6.2) are shown in Figure 7.13. Broad humps in the ff
 1827 and $\gamma\gamma$ spectra are due to kinematic ΔR and p_T turn-ons that are suppressed in the
 1828 ee sample due to the invariant mass cut. Figure 7.14 shows the weights applied to
 1829 the ee ($81 \text{ GeV} \leq m_{ee} < 101 \text{ GeV}$) and ff \cancel{E}_T spectra as a function of di-EM p_T and
 1830 number of jets per event.

1831 7.1.3 Normalization

After reweighting, the \cancel{E}_T distributions of the QCD control samples are normalized to the $\cancel{E}_T < 20$ GeV region of the candidate $\gamma\gamma \cancel{E}_T$ spectrum, where signal contamination is low. The normalization factor is $(N_{\gamma\gamma}^{\cancel{E}_T < 20 \text{ GeV}} - N_{e\gamma}^{\cancel{E}_T < 20 \text{ GeV}})/N_{\text{control}}^{\cancel{E}_T < 20 \text{ GeV}}$, where $N_{e\gamma}^{\cancel{E}_T < 20 \text{ GeV}}$ is the expected number of electroweak background events with $\cancel{E}_T < 20$ GeV (discussed in Section 7.2).

¹⁸³⁷ 7.2 Modeling the Electroweak Background

¹⁸³⁸ $W\gamma$, $W + \text{jet}$, and $t\bar{t}$ processes in which the W decay electron is misidentified as a
¹⁸³⁹ photon (due to a failure to properly associate a pixel seed to the electron candidate)
¹⁸⁴⁰ can contribute significantly to the high- \cancel{E}_T tail of the $\gamma\gamma$ \cancel{E}_T spectrum. To estimate

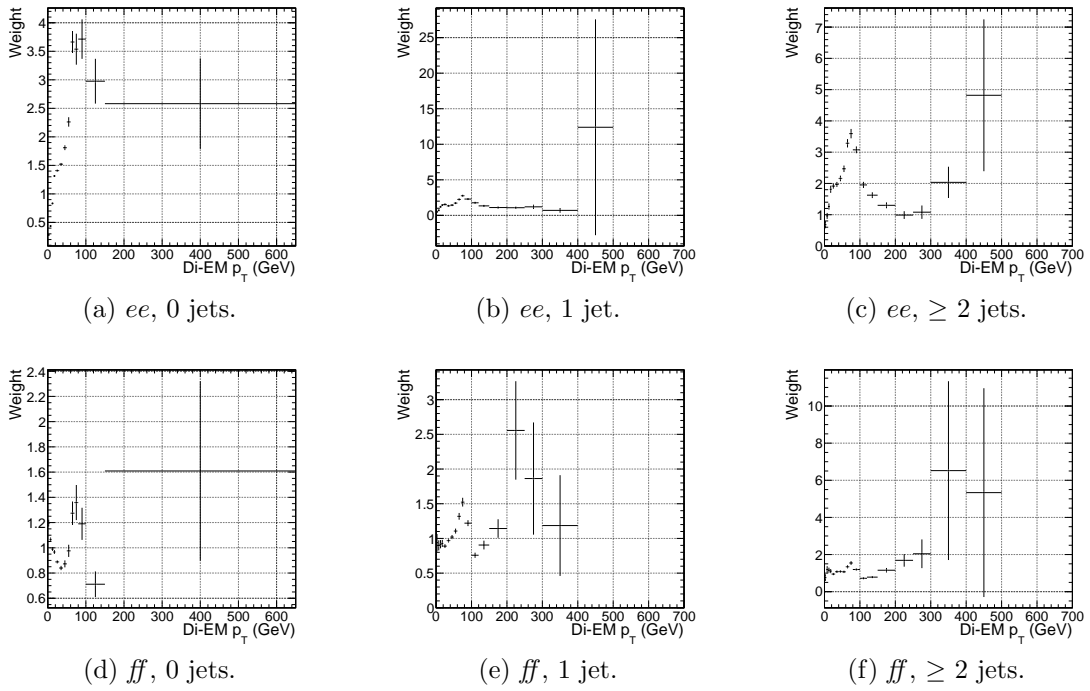


Figure 7.14: ee ($81 \text{ GeV} \leq m_{ee} < 101 \text{ GeV}$) and ff di-EM p_T weights for events with 0, 1, or ≥ 2 jets (as in Table 6.2). Errors are statistical only.

1841 this background, the $e\gamma$ sample, which is enriched in $W \rightarrow e\nu$ decays, is scaled by
 1842 $f_{e \rightarrow \gamma}/(1 - f_{e \rightarrow \gamma})$, where $f_{e \rightarrow \gamma}$ is the rate at which electrons are misidentified as photons.
 1843 The derivation of this scaling factor comes from the two equations

$$N_{e\gamma}^W = f_{e \rightarrow e} N_W \quad (7.2)$$

$$N_{\gamma\gamma}^W = (1 - f_{e \rightarrow e}) N_W \quad (7.3)$$

1844 where $N_{e\gamma}^W$ is the number of W events in the $e\gamma$ sample in which the electron was
 1845 correctly identified, $f_{e \rightarrow e}$ is the probability to correctly identify an electron, N_W is
 1846 the true number of triggered $W \rightarrow e\nu$ events, and $N_{\gamma\gamma}^W$ is the number of W events in
 1847 the $\gamma\gamma$ sample in which the electron was misidentified as a photon. The contribution
 1848 from $Z \rightarrow ee$ can be neglected (i.e. $f_{e \rightarrow \gamma}$ is small and the Z contribution involves
 1849 $f_{e \rightarrow \gamma}^2$, since both electrons have to be misidentified). Since $f_{e \rightarrow e} = 1 - f_{e \rightarrow \gamma}$, solving

1850 for $N_{\gamma\gamma}^W$ gives

$$N_{\gamma\gamma}^W = \frac{f_{e\rightarrow\gamma}}{1 - f_{e\rightarrow\gamma}} N_{e\gamma}^W \quad (7.4)$$

1851 $f_{e\rightarrow\gamma}$ is measured by fitting the Z peaks in the ee and $e\gamma$ samples. The number of
1852 Z events fitted in the ee and $e\gamma$ samples, respectively, is given by

$$N_{ee}^Z = (1 - f_{e\rightarrow\gamma})^2 N_Z \quad (7.5)$$

$$N_{e\gamma}^Z = 2f_{e\rightarrow\gamma}(1 - f_{e\rightarrow\gamma}) N_Z \quad (7.6)$$

1853 where N_Z is the true number of triggered $Z \rightarrow ee$ events. Solving for $f_{e\rightarrow\gamma}$ gives

$$f_{e\rightarrow\gamma} = \frac{N_{e\gamma}^Z}{2N_{ee}^Z + N_{e\gamma}^Z} \quad (7.7)$$

1854 A Crystal Ball function is used to model the Z signal shape in both the ee and
1855 $e\gamma$ samples, while an exponential convoluted with an error function (`RooCMSShape`,
1856 see Sec. 6.4.1) is used to model the background shape. The fixed fit parameters are
1857 identical for the two samples, but the other parameters are allowed to float indepen-
1858 dently. Table 7.3 shows the values and ranges of the fixed and floating fit parameters,
1859 respectively.

1860 Fits to the ee and $e\gamma$ invariant mass spectra are shown in Figure 7.15. Figure 7.16
1861 indicates that the dependence of $f_{e\rightarrow\gamma}$ on the electron p_T and η is small. (Note that all
1862 fit parameters are floating in the p_T -dependent fits.) Therefore, a constant misidenti-
1863 fication rate (derived from all ee and $e\gamma$ events), rather than a p_T - and η -dependent
1864 misidentification rate, is used in the final electroweak background estimate, with the

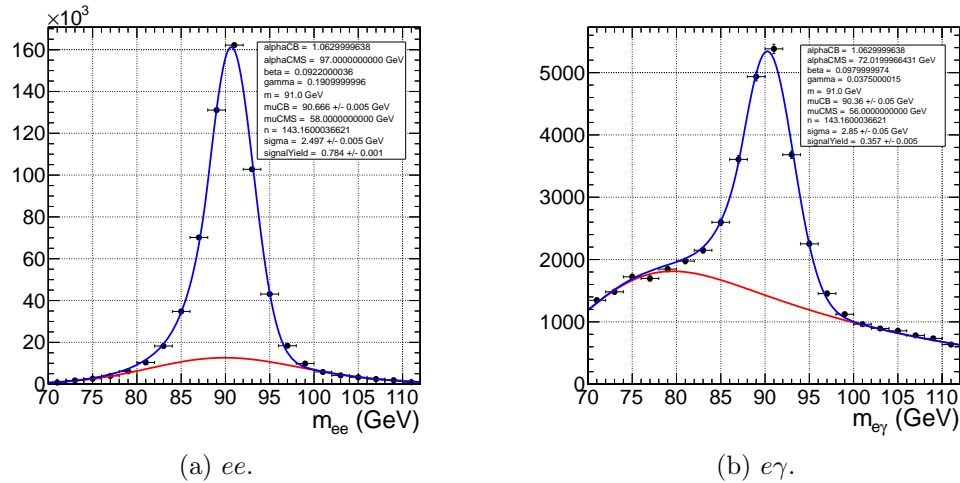


Figure 7.15: Fits to the ee and $e\gamma$ invariant mass spectra using the Crystal Ball RooCMSShape function described in the text and in Table 7.3. The total fit is shown in blue, while the background component is shown in red.

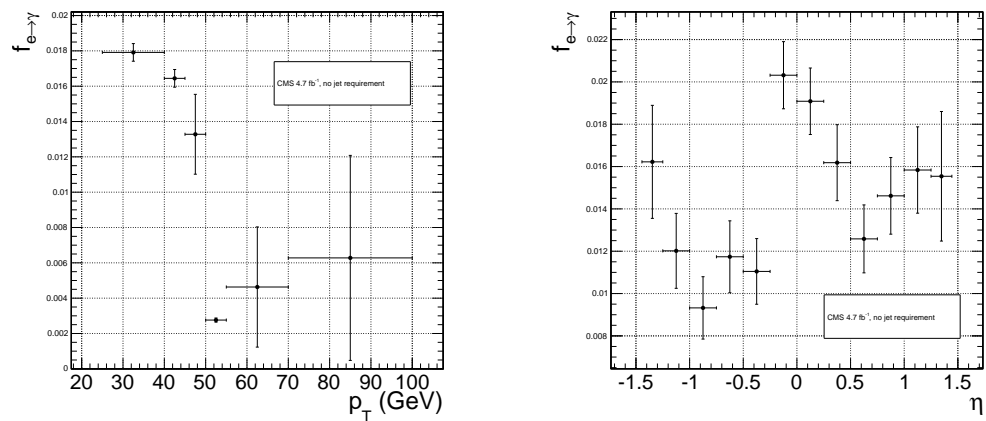
difference between the constant rate and the rate for electrons with p_T between 25 and 40 GeV (the range in which the bulk of the trailing photons in the $\gamma\gamma$ sample lie) taken as a systematic error.

Using the integrals of the Z fits shown in Fig. 7.15, Eq. 7.7, and the p_T systematic discussed above, $f_{e \rightarrow \gamma}$ is calculated to be $0.014 \pm 0.000(\text{stat.}) \pm 0.004(\text{syst.})$. The scaled $e\gamma$ MET distribution is shown in Figure 7.17.

In the 36 pb^{-1} version of this analysis [109], it was shown that the ee sample could accurately predict the QCD and real Z contribution to the $e\gamma$ sample at low \cancel{E}_T , and that the expectation from $W \rightarrow e\nu$ MC accounted for the remaining W contribution at high \cancel{E}_T . A plot of the \cancel{E}_T distributions of the 2010 $e\gamma$ sample and the predicted components is shown in Figure 7.18. This exercise helps to validate both the QCD and electroweak background prediction methods.

Table 7.3: Parameter values for the signal and background PDFs for the ee and $e\gamma$ samples. When a bracketed range is given, the parameter is allowed to float within that range. When a constant is given, the parameter is fixed to that constant.

PDF	Crystal Ball fit parameters				RooCMSShape fit parameters			
	μ	σ	α	n	μ	α	β	γ
ee signal	[86.2, 96.2]	[1.0, 5.0]	1.063	143.16	N/A	N/A	N/A	N/A
$e\gamma$ signal	[86.2, 96.2]	[1.0, 5.0]	1.063	143.16	N/A	N/A	N/A	N/A
ee background	N/A	N/A	N/A	N/A	58	97.0	0.0922	0.191
$e\gamma$ background	N/A	N/A	N/A	N/A	56	72.02	0.098	0.0375



(a) $f_{e \rightarrow \gamma}$ vs. electron p_T . For the lowest p_T bin, the fit to the $e\gamma$ spectrum does not converge well, so the Z signal fraction is fixed to the value in Fig. 7.15b.

(b) $f_{e \rightarrow \gamma}$ vs. electron η .

Figure 7.16: $f_{e \rightarrow \gamma}$ vs. electron p_T and η .

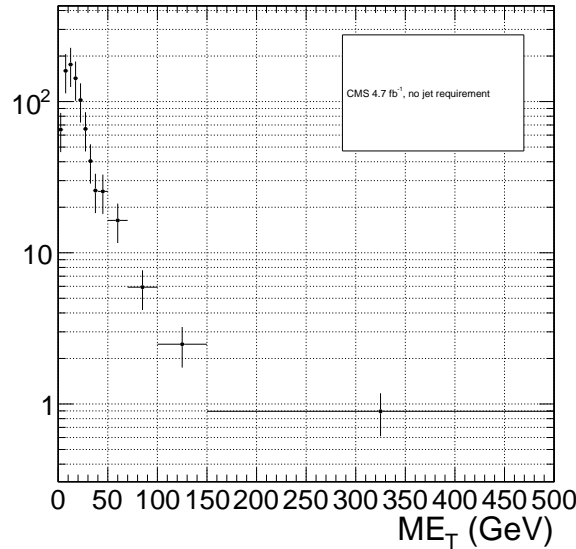


Figure 7.17: E_T spectrum of the $e\gamma$ sample after scaling by $f_{e \rightarrow \gamma}$. The total error on $f_{e \rightarrow \gamma}$ is propagated to the total error on the electroweak background estimate.

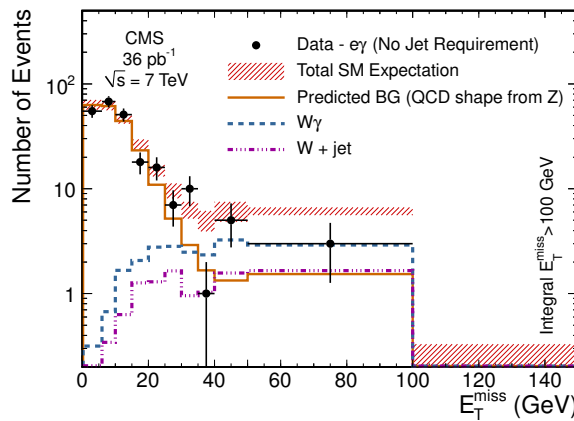


Figure 7.18: E_T spectrum of the $e\gamma$ sample in 36 pb^{-1} of 2010 LHC data scaled by the 2010 measured $f_{e \rightarrow \gamma}$ (black dots), QCD and real Z predicted background from the 2010 ee sample (solid orange line), MC $W + \text{jet}$ estimate (dash-dotted purple line), and MC $W\gamma$ estimate (dashed blue line). The total $e\gamma$ prediction (red band) is the sum of the ee , $W + \text{jet}$, and $W\gamma$ predictions. Reprinted from Fig. 2 of ref. [109].

1877 7.3 Errors on the Background Prediction

1878 The statistical error on the final background estimate in a particular \cancel{E}_T bin comes
 1879 from three sources: the number of control sample events collected in that bin, the
 1880 statistical error on the weights applied to events in that bin, and the statistics of the
 1881 normalization region. In the case of the ee control sample, there are contributions
 1882 from the statistics of the m_{ee} sidebands as well.

1883 In order to estimate the statistical error due to the reweighting procedure, 1000
 1884 toy sets of weights are generated. Each set includes a weight for each (di-EM p_T , N_j)
 1885 bin, with the values picked from a Gaussian distribution with mean and standard
 1886 deviation equal to the observed weight for that bin and its statistical error. The effect
 1887 of reweighting error is not correlated between \cancel{E}_T bins. For each of the 1000 exper-
 1888 iments, the control sample data are reweighted according to the generated weights,
 1889 and the background estimates are calculated for each \cancel{E}_T bin. Since the distribution
 1890 of the toy background estimates follows a Gaussian distribution in each \cancel{E}_T bin, the
 1891 RMS spread of the estimates is taken as the statistical error due to reweighting. This
 1892 procedure is carried out for the ff , ee , low sideband ee , and high sideband ee samples.

1893 The total statistical error on the background estimate per \cancel{E}_T bin is given by

$$\sigma_{\text{stat}}^2 = \sigma_{\text{stat,QCD}}^2 + \sigma_{\text{stat,EW}}^2 \quad (7.8)$$

1894 where $\sigma_{\text{stat,QCD}}^2$ is the square of the total statistical error on the QCD prediction in
 1895 the \cancel{E}_T bin

$$\sigma_{\text{stat,QCD}}^2 = \sigma_{\text{stat},s}^2 + \sigma_{\text{Poisson,QCD}}^2 + \sigma_{\text{reweight},s}^2 + \sigma_{\text{reweight,QCD}}^2 \quad (7.9)$$

1896 and $\sigma_{\text{stat,EW}}$ is the Poisson error on the number of $e\gamma$ events in the \cancel{E}_T bin ($= \sqrt{N_{e\gamma}}$,
 1897 where $N_{e\gamma}$ is the prediction in the \cancel{E}_T bin after scaling by $f_{e\rightarrow\gamma}$). The contributions
 1898 to $\sigma_{\text{stat,QCD}}^2$ are discussed below.

- 1899 • $\sigma_{\text{stat},s}^2$ is the statistical error contributed by the normalization factor s (i.e. from
 1900 Poisson error in the normalization region $\cancel{E}_T < 20$ GeV):

$$\begin{aligned}\sigma_{\text{stat},s}^2 = & \frac{N_{\text{control}}^2}{(N_{\gamma\gamma}^{\text{norm}} - N_{e\gamma}^{\text{norm}})^2} (\sigma_{\text{Poisson},\gamma\gamma}^{\text{norm}})^2 + (\sigma_{\text{Poisson},e\gamma}^{\text{norm}})^2 + \\ & \frac{N_{\text{control}}^2}{(N_{\text{control}}^{\text{norm}})^2} (\sigma_{\text{Poisson,control}}^{\text{norm}})^2\end{aligned}\quad (7.10)$$

1901 where N_{control} is the number of reweighted, normalized events in the \cancel{E}_T bin,
 1902 $N_{\gamma\gamma}^{\text{norm}}$ is the number of $\gamma\gamma$ events in the normalization region, $N_{e\gamma}^{\text{norm}}$ is the num-
 1903 ber of $e\gamma$ events in the normalization region (after scaling by $f_{e\rightarrow\gamma}$), $\sigma_{\text{Poisson},\gamma\gamma}^{\text{norm}}$
 1904 is the Poisson error on the number of $\gamma\gamma$ events in the normalization region
 1905 ($= \sqrt{N_{\gamma\gamma}^{\text{norm}}}$), $\sigma_{\text{Poisson},e\gamma}^{\text{norm}}$ is the Poisson error on the number of $e\gamma$ events in the
 1906 normalization region ($= \sqrt{N_{e\gamma}^{\text{norm}}}$), $N_{\text{control}}^{\text{norm}}$ is the number of QCD control (ee
 1907 or ff) events in the normalization region, and $\sigma_{\text{Poisson,control}}^{\text{norm}}$ is the Poisson error
 1908 on the number of QCD control (ee or ff) events in the normalization region
 1909 ($= \sqrt{\sum_{i=1}^{N_{\text{control}}^{\text{norm}}} w_i^2}$, where w_i is the di-EM p_T weight applied to event i). For
 1910 the ee control region, N_{control} and $N_{\text{control},\text{norm}}$ are sideband subtracted, and
 1911 $\sigma_{\text{Poisson,control}}^{\text{norm}}$ includes the Poisson error on the number of sideband events.

- 1912 • $\sigma_{\text{Poisson,QCD}}$ is the Poisson error due to the number of QCD control (ee or ff)
 1913 events in the \cancel{E}_T bin, equal to $\sqrt{\sum_{i=1}^{N_{\text{control}}^{\text{norm}}} w_i^2}$, where w_i is the di-EM p_T weight
 1914 applied to event i . For the ee control region, $\sigma_{\text{Poisson,QCD}}$ includes the Poisson
 1915 error on the number of subtracted sideband events.
- 1916 • $\sigma_{\text{reweight},s}$ is the error contributed by the control sample reweighting in the nor-

1917 malization region ($= \frac{N_{\text{control}}^2}{(N_{\text{control}}^{\text{norm}})^2} \sigma_{\text{reweight,control}}^{\text{norm}}$). $\sigma_{\text{reweight,control}}^{\text{norm}}$ is the quadrature
 1918 sum of the RMS of the 1000 toy reweighting experiments for each \cancel{E}_T bin in the
 1919 normalization region. For the ee control sample, it also includes (in quadrature)
 1920 the RMS of the toys in the sideband samples.

- 1921 • $\sigma_{\text{reweight,QCD}}$ is the error contributed by the control sample reweighting in the \cancel{E}_T
 1922 bin ($= s\sigma_{\text{reweight,control}}$). $\sigma_{\text{reweight,control}}$ is the RMS of the 1000 toy reweighting
 1923 experiments for the E_T bin. For the ee control sample, it also includes (in
 1924 quadrature) the RMS of the toys in the sideband samples.

1925 The dominant source of systematic error on the background estimate is the slight
 1926 difference in hadronic activity between the ee , ff , and $\gamma\gamma$ samples. This results in a
 1927 small bias (~ 1 GeV) of the ee \cancel{E}_T distribution towards lower values with respect to
 1928 the ff and $\gamma\gamma$ samples, as shown in Figure 7.19. Therefore, the ff sample is used as
 1929 the primary QCD background estimator, and the difference between the ee and ff
 1930 predictions is assigned as an error on the knowledge of the hadronic activity. For \cancel{E}_T
 1931 > 100 GeV, this error amounts to 43% of the total QCD + electroweak background
 1932 estimate.

1933 The second largest source of systematic error comes from the p_T dependence of the
 1934 $e \rightarrow \gamma$ misidentification rate (see 7.2). For $\cancel{E}_T > 100$ GeV, the expected electroweak
 1935 background is 3.4 ± 1.0 events, so this error amounts to 4.8% of the total QCD +
 1936 electroweak background estimate.

1937 The assumption of a constant $t\bar{t}$ and $W + \text{jets}$ background shape under the Z
 1938 peak in the ee sample induces a systematic error on the ee sideband-subtracted back-
 1939 ground prediction. To assess the magnitude of this error, the sideband subtraction
 1940 (see Sec. 7.1.2) is performed once using only the prediction from the high sideband,
 1941 and once using only the prediction from the low sideband. In each of these cases, the
 1942 prediction is weighted by a factor of two, to account for the fact that the sideband
 1943 regions are only half as wide (10 GeV) as the signal region (20 GeV). The maximum

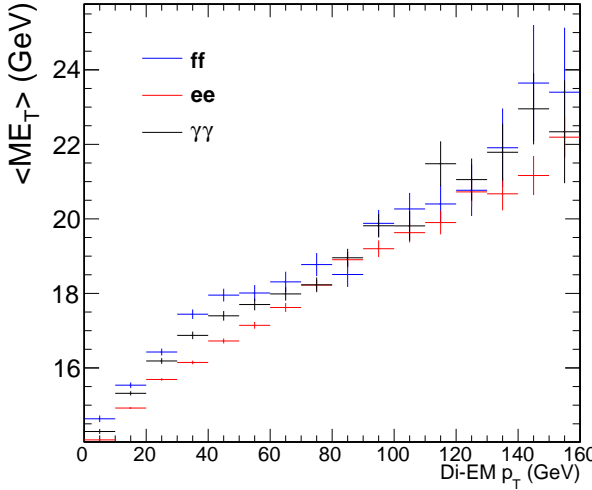


Figure 7.19: Average E_T vs. di-EM p_T for the ff (blue), ee (red), and $\gamma\gamma$ (black) samples.

1944 variation from the nominal ee estimate is taken as the error, which amounts to 11%
 1945 for $E_T > 100$ GeV. E_T distributions using the nominal ee sideband subtraction, the
 1946 low-sideband-only subtraction, and the high-sideband-only subtraction are shown in
 1947 Figure 7.20.

Added

1948 Finally, the few percent error on the jet energy correction factors introduces an this
 1949 error on the final background estimate through (a) the use of the PF p_T to measure para-
 1950 the di-EM p_T , (b) the counting of jets passing a 30 GeV p_T threshold for placement of graph
 1951 the event in an N_j bin for reweighting, and (c) the counting of jets above threshold for
 1952 the ≥ 1 -jet version of the selection. To estimate this error, 100 pseudo-experiments
 1953 are generated with identical properties as the true data sample, except with corrected
 1954 jet energies (in all events) all shifted by an amount $r\sigma(p_T, \eta)$. r is a random number
 1955 drawn from a Gaussian distribution with mean 0 and width 1, and $\sigma(p_T, \eta)$ is the
 1956 uncertainty on the jet energy correction factor (which, like the correction factor itself,
 1957 is a function of p_T and η). The same factor r is applied to all jets in all events in the
 1958 pseudo-experiment because the jet energy correction errors are correlated from jet to
 1959 jet (they result from e.g. uncertainties in MC simulation or uncertainties in ECAL

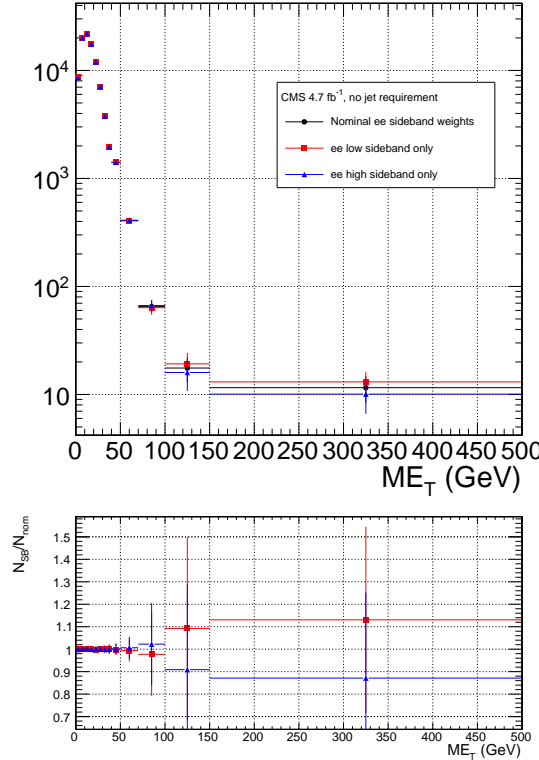


Figure 7.20: ee E_T distributions using the nominal sideband subtraction (black circles), low sideband only (red squares), and high sideband only (blue triangles). The bottom plot shows the ratio of the low sideband distribution to the nominal (red squares) and the ratio of the high sideband distribution to the nominal (blue triangles).

1960 energy scale [89]). The standard error of the mean of the 100 resulting background
 1961 estimates in each relevant E_T bin is taken as the error. The error in each E_T bin is
 1962 assumed to be uncorrelated. This process is repeated for both the inclusive and ≥ 1 -
 1963 jet selections. For $E_T \geq 100$ GeV, the jet energy correction uncertainty is 1.5% (2.2%)
 1964 of the total background for the inclusive (≥ 1 -jet) selection.

1965 The uncertainty in how to define the (di-EM p_T , N_j) bins, especially at high di-
 1966 EM p_T where the statistics are low, is covered by the 1000-toys procedure as long as
 1967 the bins are not too coarse. This is shown in Figure 7.21. If the bins are too coarse,
 1968 the details of the shape of the di-EM p_T spectra are lost, and the reweighting has a
 1969 smaller effect.

1970 The use of uncorrected instead of corrected PF E_T (see Sec. 6.1.3) makes no

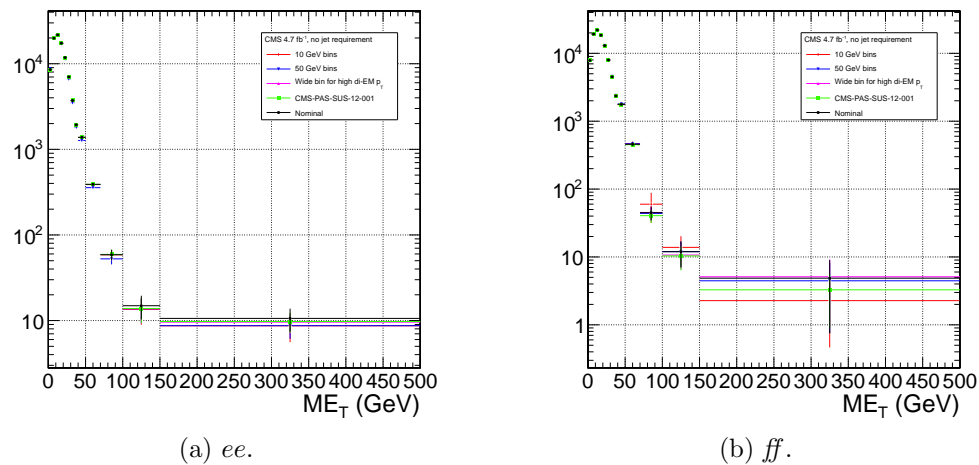


Figure 7.21: Comparison of \mathcal{F}_T distributions for five different di-EM p_T bin definitions: uniform bins of width 10 GeV (red diamonds); uniform bins of width 50 GeV (blue downward-pointing triangles); bins with lower edges $\{0.0, 5.0, 10.0, 15.0, 20.0, 30.0, 40.0, 50.0, 60.0, 70.0, 80.0, 100.0, 750.0\}$ GeV for 0-jet events and $\{0.0, 5.0, 10.0, 15.0, 20.0, 30.0, 40.0, 50.0, 60.0, 70.0, 80.0, 100.0, 150.0\}$ GeV for ≥ 1 -jet events (magenta upward-pointing triangles), i.e. a single wide bin at high di-EM p_T ; bins with lower edges $\{0.0, 5.0, 10.0, 15.0, 20.0, 30.0, 40.0, 50.0, 60.0, 70.0, 80.0, 100.0, 150.0\}$ GeV for 0-jet events and $\{0.0, 5.0, 10.0, 15.0, 20.0, 30.0, 40.0, 50.0, 60.0, 70.0, 80.0, 100.0, 120.0, 150.0, 200.0\}$ GeV for ≥ 1 -jet events (green squares), i.e. the bins used in ref. [28]; and the nominal bin definitions shown in Fig. 7.14 (black circles).

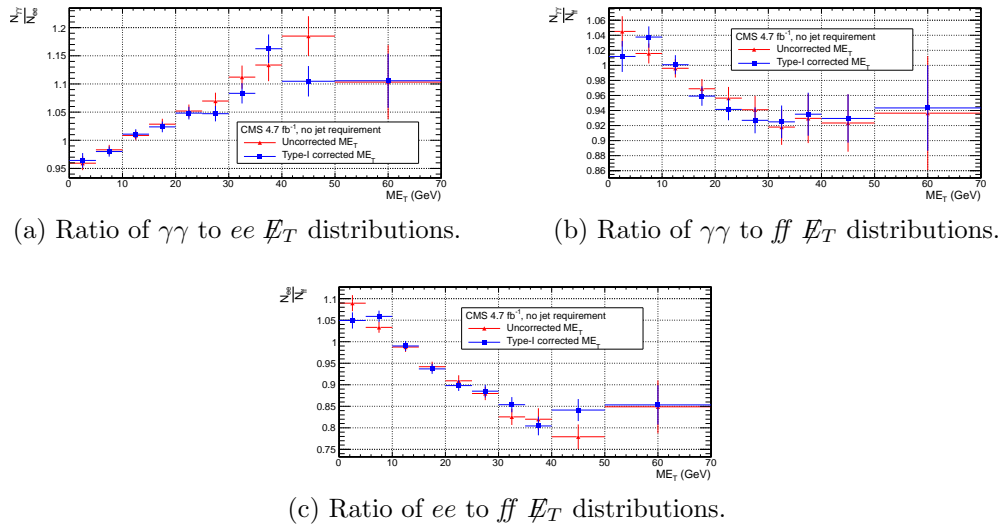


Figure 7.22: Agreement between $\gamma\gamma$, ee , and ff samples for uncorrected (red triangles) and corrected (blue squares) \not{E}_T .

1971 difference in the agreement of the background predictions and the search sample in
 1972 a control region at low \not{E}_T , as shown in Figure 7.22. Since the control samples are
 1973 derived from the same data as the search sample, any biases in the \not{E}_T reconstruction
 1974 due to jet energy scale are present equally in both samples.

1975 Tables 7.4 and 7.5 list all the errors on the ee and ff QCD background predictions,
 1976 respectively, for the \not{E}_T bins used in the search. Table 7.6 lists the errors on the
 1977 electroweak background prediction. Finally, Table 7.7 shows the errors on the total
 1978 QCD + electroweak background prediction, broken down by origin (statistical or
 1979 systematic) and QCD background estimation sample (ee or ff). In the final result,
 1980 only the ff QCD estimate is used.

1981 7.4 Results

1982 Figure 7.23(7.24) shows the \not{E}_T distribution of the inclusive(≥ 1 -jet) $\gamma\gamma$ search sample
 1983 along with the predicted \not{E}_T distributions of the QCD and electroweak backgrounds.
 1984 The observed number of two-photon events, background estimates and their errors,

Table 7.4: Errors on the ee QCD background prediction as a fraction of the ee prediction.

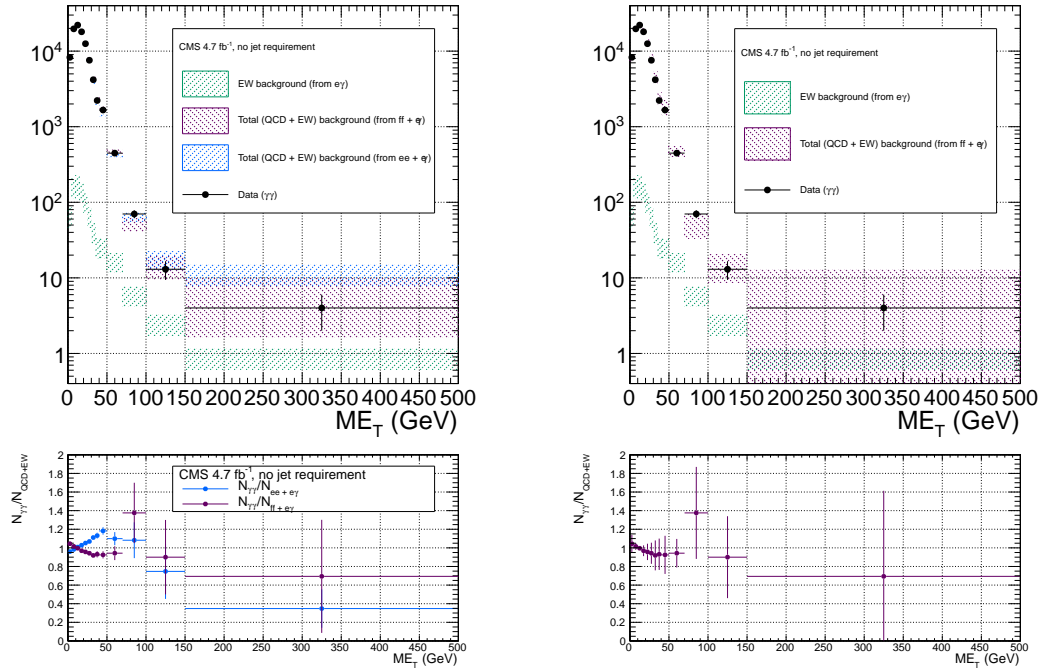
Source of error	Fractional uncertainty (%)				
	[50, 60)	[60, 70)	[70, 80)	[80, 100)	≥ 100
Total	3.9	8.1	16	25	25
Statistics	3.6	7.8	16	24	22
No. events	3.6	7.7	15	24	20
In norm. region	0.43	0.44	0.46	0.55	0.51
In this E_T bin	3.5	7.7	15	24	20
Reweighting	0.73	1.2	3.5	4.3	7.7
In norm. region	0.19	0.19	0.2	0.24	0.23
In this E_T bin	0.71	1.2	3.5	4.3	7.7
Systematics	2.6	4.4	1.2	7.5	14
$f_{e \rightarrow \gamma}$ (in norm. region)	0.0012	0.0012	0.0013	0.0015	0.0014
m_{ee} background shape	1.4	2	0.72	5.5	12
Jet energy scale	2.2	3.9	0.96	5.1	6.9

Table 7.5: Errors on the ff QCD background prediction as a fraction of the ff prediction.

Source of error	Fractional uncertainty (%)				
	[50, 60)	[60, 70)	[70, 80)	[80, 100)	≥ 100
Total	15	25	61	34	64
Statistics	7.2	14	30	33	38
No. events	7.1	14	29	33	36
In norm. region	0.64	0.64	0.64	0.64	0.64
In this E_T bin	7.1	14	29	33	36
Reweighting	0.85	2.7	5.1	6.9	13
In norm. region	0.27	0.27	0.27	0.27	0.27
In this E_T bin	0.81	2.6	5.1	6.9	13
Systematics	13	21	53	6.6	52
ee/ff difference	13	21	53	5.5	52
$f_{e \rightarrow \gamma}$ (in norm. region)	0.0012	0.0012	0.0012	0.0012	0.0012
Jet energy scale	0.099	1.7	1.8	3.5	1.8

Table 7.6: Errors on the $e\gamma$ electroweak background prediction as a fraction of the $e\gamma$ prediction.

Source of error	Fractional uncertainty (%)				
	[50, 60)	[60, 70)	[70, 80)	[80, 100)	≥ 100
Total	29	29	30	30	30
Statistics	3.6	5.2	6.7	7.2	6.5
Systematics ($f_{e \rightarrow \gamma}$)	29	29	29	29	29



(a) $ee + e\gamma$ and $ff + e\gamma$. The widths of the bands correspond to the errors given in Table 7.7, excluding the error associated with the difference between the ee and ff QCD estimates for the $ff + e\gamma$ E_T distribution.

(b) $ff + e\gamma$. The widths of the bands correspond to the errors given in Table 7.7, including the error associated with the difference between the ee and ff QCD estimates.

Figure 7.23: E_T distribution of the $\gamma\gamma$ search sample (black circles) along with the predicted E_T distributions of the QCD and electroweak backgrounds (blue band for ee QCD prediction + electroweak prediction, purple band for ff QCD prediction + electroweak prediction). The electroweak background prediction is shown in green. The bottom plots show the ratio of the $\gamma\gamma E_T$ distribution to the $ee + e\gamma$ background distribution (blue) and $ff + e\gamma$ background distribution (purple).

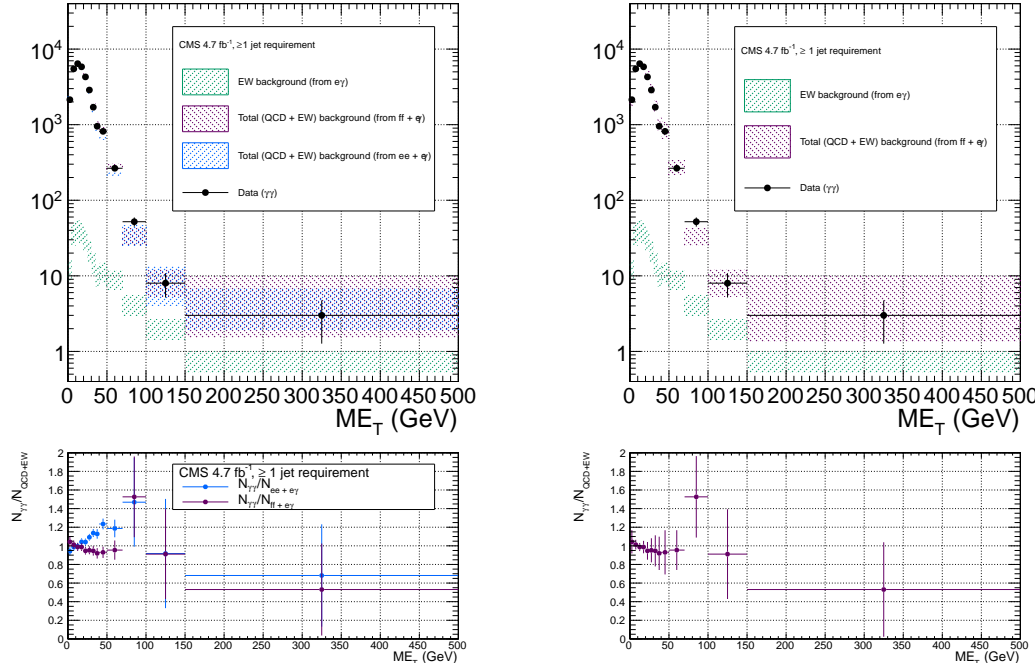
1985 and expected number of inclusive(≥ 1 -jet) two-photon events from two representative
 1986 GGM SUSY models are listed in Table 7.8(7.9). (Details of the SUSY MC production
 1987 are given in Chapter 8 and App. A.) No deviation from the Standard Model prediction
 1988 is observed in the $\gamma\gamma$ search sample.

Table 7.7: Errors on the total QCD + electroweak background prediction as a fraction of the total prediction.

Source of error	Fractional uncertainty (%)				
	[50, 60)	[60, 70)	[70, 80)	[80, 100)	≥ 100
Total ($ee + e\gamma$)	3.9	7.8	15	22	22
Statistics	3.4	7.3	14	21	18
QCD	3.4	7.3	14	21	18
Electroweak	0.13	0.3	0.53	0.79	0.76
Systematics	2.7	4.5	2.6	7.4	13
QCD	2.5	4.1	1.1	6.7	12
Electroweak	1	1.7	2.3	3.2	3.4
Total ($ff + e\gamma$)	14	24	54	30	54
Statistics	6.9	13	26	29	30
QCD	6.9	13	26	29	30
Electroweak	0.11	0.24	0.79	0.83	1.1
Systematics	12	20	47	6.7	43
QCD	12	20	47	5.8	43
Electroweak	0.9	1.3	3.4	3.4	4.8

Table 7.8: Observed numbers of two-photon events, background estimates and their errors, and expected numbers of two-photon events from two representative GGM SUSY models (details of MC simulation given in Chapter 8 and App. A) for the E_T bins used in the search. Errors on the background estimates are detailed in Tables 7.4, 7.5, 7.6, and 7.7. Errors on the expected numbers of GGM events are purely statistical.

Source	No. events				
	[50, 60)	[60, 70)	[70, 80)	[80, 100)	≥ 100
Observation ($\gamma\gamma$)	354	93	37	33	17
Predicted background ($ff + e\gamma$)	361 ± 51.5	113 ± 27.1	26.9 ± 14.5	23.9 ± 7.23	20.2 ± 10.9
$m_{\tilde{q}} = 720$ GeV $M_3 = 720$ GeV $M_1 = 375$ GeV	13.3 ± 2.13	17.7 ± 2.46	15.3 ± 2.33	42.9 ± 3.82	966 ± 18.3
$m_{\tilde{q}} = 1440$ GeV $M_3 = 1440$ GeV $M_1 = 375$ GeV	0.008 ± 0.003	0.009 ± 0.003	0.012 ± 0.003	0.030 ± 0.005	1.92 ± 0.04



(a) $ee + e\gamma$ and $ff + e\gamma$. The widths of the bands correspond to the errors given in Table 7.7, excluding the error associated with the difference between the ee and ff QCD estimates for the $ff + e\gamma$ E_T distribution.

(b) $ff + e\gamma$. The widths of the bands correspond to the errors given in Table 7.7, including the error associated with the difference between the ee and ff QCD estimates.

Figure 7.24: E_T distribution of the $\gamma\gamma + \geq 1$ jet search sample (black circles) along with the predicted E_T distributions of the QCD and electroweak backgrounds (blue band for ee QCD prediction + electroweak prediction, purple band for ff QCD prediction + electroweak prediction). The electroweak background prediction is shown in green. The bottom plots show the ratio of the $\gamma\gamma E_T$ distribution to the $ee + e\gamma$ background distribution (blue) and $ff + e\gamma$ background distribution (purple).

Table 7.9: Observed numbers of two-photon + ≥ 1 -jet events, background estimates and their errors, and expected numbers of two-photon + ≥ 1 -jet events from two representative GGM SUSY models (details of MC simulation given in Chapter 8 and App. A) for the \cancel{E}_T bins used in the search. Errors on the background estimates are detailed in Tables 7.4, 7.5, 7.6, and 7.7. Errors on the expected numbers of GGM events are purely statistical.

Source	No. events				
	[50, 60)	[60, 70)	[70, 80)	[80, 100)	≥ 100
Observation ($\gamma\gamma + \geq 1$ jet)	202	63	27	25	11
Predicted background ($ff + e\gamma$)	200 ± 35.4	77.7 ± 28.1	19.4 ± 8.55	14.7 ± 7.04	14.4 ± 5.59
$m_{\tilde{q}} = 720$ GeV $M_3 = 720$ GeV $M_1 = 375$ GeV	13.3 ± 2.13	17.7 ± 2.46	15.3 ± 2.33	42.9 ± 3.82	965 ± 18.3
$m_{\tilde{q}} = 1440$ GeV $M_3 = 1440$ GeV $M_1 = 375$ GeV	0.008 ± 0.003	0.009 ± 0.003	0.012 ± 0.003	0.031 ± 0.004	1.92 ± 0.04

¹⁹⁸⁹ **Chapter 8**

¹⁹⁹⁰ **Interpretation of Results in Terms**
¹⁹⁹¹ **of GMSB Models**

¹⁹⁹² As shown in Figs. 7.23 and 7.24 and Tables 7.8 and 7.9, no excess of events above
¹⁹⁹³ the Standard Model expectation is found in either the ≥ 0 - or ≥ 1 -jet analyses for the
¹⁹⁹⁴ GMSB-sensitive region $\cancel{E}_T \geq 50$ GeV. Therefore, upper limits on the production cross
¹⁹⁹⁵ sections of various GMSB models are calculated and then translated into statements of
¹⁹⁹⁶ exclusion. Section 8.1 describes the GMSB models that were generated with MC and
¹⁹⁹⁷ tested for exclusion. The upper limit calculation and translation to model exclusions
¹⁹⁹⁸ is laid out in Section 8.2. The upper limits themselves are presented in Section 8.3,
¹⁹⁹⁹ and, finally, the exclusions are presented in Section 8.4.

²⁰⁰⁰ **8.1 Simplified Models**

²⁰⁰¹ The exclusion reach of the two-photon search is presented for three different two-
²⁰⁰² dimensional scans in GMSB parameter space. The first scan covers the bino NLSP
²⁰⁰³ scenario of Sec. 3.5. In this scan, M_2 , which controls the amount of wino mixing, is
²⁰⁰⁴ set to 3.5 TeV. M_1 , which controls the amount of bino mixing, is set to 375 GeV.
²⁰⁰⁵ This insures that all gauginos except the lightest neutralino are too heavy to be

2006 produced in significant numbers at the LHC. All other mass parameters except for
 2007 M_3 (\sim gluino mass) and $m_{\tilde{q}}$ (\sim first- and second-generation squark mass) are set to
 2008 3.5 TeV, which insures that squark/gluino decay to intermediate states such as third-
 2009 generation squarks or any flavor of lepton is strongly suppressed. M_3 and $m_{\tilde{q}}$ are
 2010 scanned over from $M_3 = m_{\tilde{q}} = 400$ GeV to $M_3 = m_{\tilde{q}} = 2$ TeV in 80-GeV steps.
 2011 The resulting simplified model consists only of a gluino, first- and second-generation
 2012 squarks, and the lightest neutralino and its decay products (the gravitino is forced to
 2013 be the LSP). The scan in M_3 - $m_{\tilde{q}}$ space illuminates the sensitivity of the two-photon
 2014 search to different levels of signal hadronic activity.

2015 The second scan is identical to the first except that the values of M_1 and M_2
 2016 are inverted ($M_1 = 3.5$ TeV and $M_2 = 375$ GeV). This corresponds to the wino
 2017 NLSP scenario of Sec. 3.5. Now, both the lightest neutralino and the lightest chargino
 2018 have masses of order 375 GeV, and are therefore produced with approximately equal
 2019 frequency in the gluino and squark decays. The chargino decays to $W + \tilde{G}$, so final
 2020 states in this scan often include leptons or large jet multiplicity. Since there is no
 2021 guarantee that two neutralinos will be produced and will decay to two photons, this
 2022 search is not well optimized for the wino NLSP scenario. However, a related CMS
 2023 search with one photon and ≥ 3 jets has an exclusion reach of ~ 1 TeV in M_3 and
 2024 $m_{\tilde{q}}$ for this scenario [28].

2025 The third scan is M_3 vs. M_1 for $m_{\tilde{q}}$, M_2 , and all other mass parameters equal to
 2026 2.5 TeV. M_3 is scanned from 160 GeV to 2 TeV in 80-GeV steps, while M_1 is scanned
 2027 from 150 GeV to 1050 GeV in 100-GeV steps. $M_3 < M_1$ is not allowed, as this would
 2028 imply that the gluino, not the lightest neutralino, is the NLSP. This scan highlights
 2029 the performance of the two-photon search as a function of M_1 (i.e. as a function of
 2030 decays open to the neutralino), whereas the previous two scans keep M_1 fixed.

2031 For each scan, the sparticle mass spectrum is generated with SuSpect 2.41 [120]
 2032 and the decay widths with SDECAY 1.3 [121]. The event data (including produc-

2033 tion, unstable particle decay, parton showering, and hadronization) is generated with
 2034 Pythia 6.422 [125], using the sparticle mass spectra and decay widths as inputs. The
 2035 gravitino is always forced to be the LSP. The simulated data are reconstructed with
 2036 CMSSWv4.2.2, which uses a detector simulation based on GEANT 4 [122]. Next to
 2037 leading order cross sections are calculated with PROSPINO 2.1 [123], and shown in
 2038 Figure 8.1 for the three signal MC scenarios.

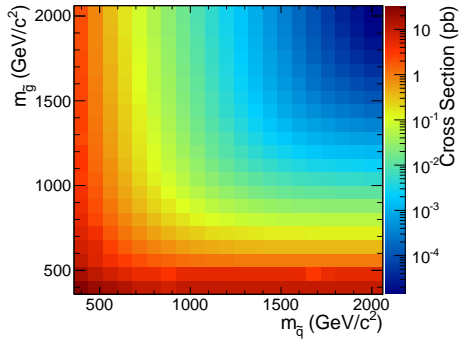
2039 **8.2 Upper Limit Calculation and Model Exclusion**

2040 The upper limits are calculated according to the prescription followed for the 2011
 2041 ATLAS + CMS Higgs limit combination [110]. This prescription utilizes the frequen-
 2042 tist CL_s method [111] with profile likelihood test statistic [112]. The CL_s method and
 2043 the profile likelihood are explained in Section 8.2.2, using specific signal MC points to
 2044 illustrate the procedure. First, however, the signal MC acceptance \times efficiency, which
 2045 is an input to the limit setting procedure, is presented in Section 8.2.1.

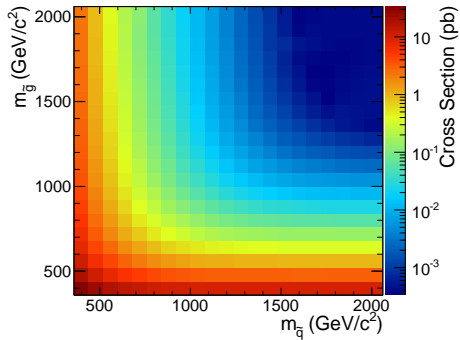
2046 **8.2.1 Signal Acceptance \times Efficiency**

2047 The signal acceptance \times efficiency (denoted $\mathcal{A} \times \epsilon$), defined for each signal point as
 2048 the number of $\gamma\gamma$ events selected with $\cancel{E}_T \geq 50$ GeV divided by the total number of
 2049 events generated, is shown in Figure 8.2 for the three different scenarios described in
 2050 Sec. 8.1.

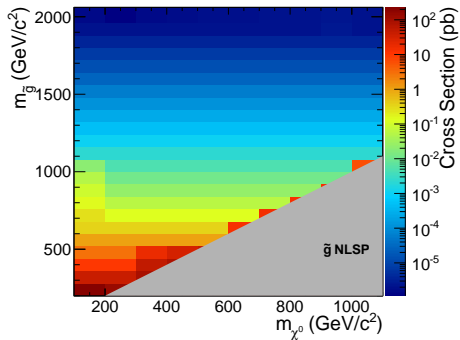
2051 In Figs. 8.2a and 8.2b, the large drop in $\mathcal{A} \times \epsilon$ for $m_{\tilde{q}} > M_3$ is due to an increase
 2052 in the number of jets produced per event and a consequent reduction in the number
 2053 of photons that pass the $I_{\text{comb}} < 6$ GeV cut. For $m_{\tilde{q}} > M_3$, there is more phase space
 2054 available to produce gluinos in the hard scatter than squarks. However, since gluinos
 2055 must decay via squarks, and in these models all squarks are heavier than the gluino,
 2056 only the two-jet decay $\tilde{g} \rightarrow qq\tilde{\chi}^0$ is available. Conversely, when $m_{\tilde{q}} < M_3$, there is



(a) M_2 decoupled ($M_2 = 3.5$ TeV), $M_1 = 375$ GeV, M_3 vs. $m_{\tilde{q}}$.



(b) M_1 decoupled ($M_1 = 3.5$ TeV), $M_2 = 375$ GeV, M_3 vs. $m_{\tilde{q}}$.



(c) $m_{\tilde{q}}$ decoupled ($m_{\tilde{q}} = 2.5$ TeV), M_3 vs. M_1 .

Figure 8.1: Next to leading order cross sections for the three different MC scenarios described in the text.

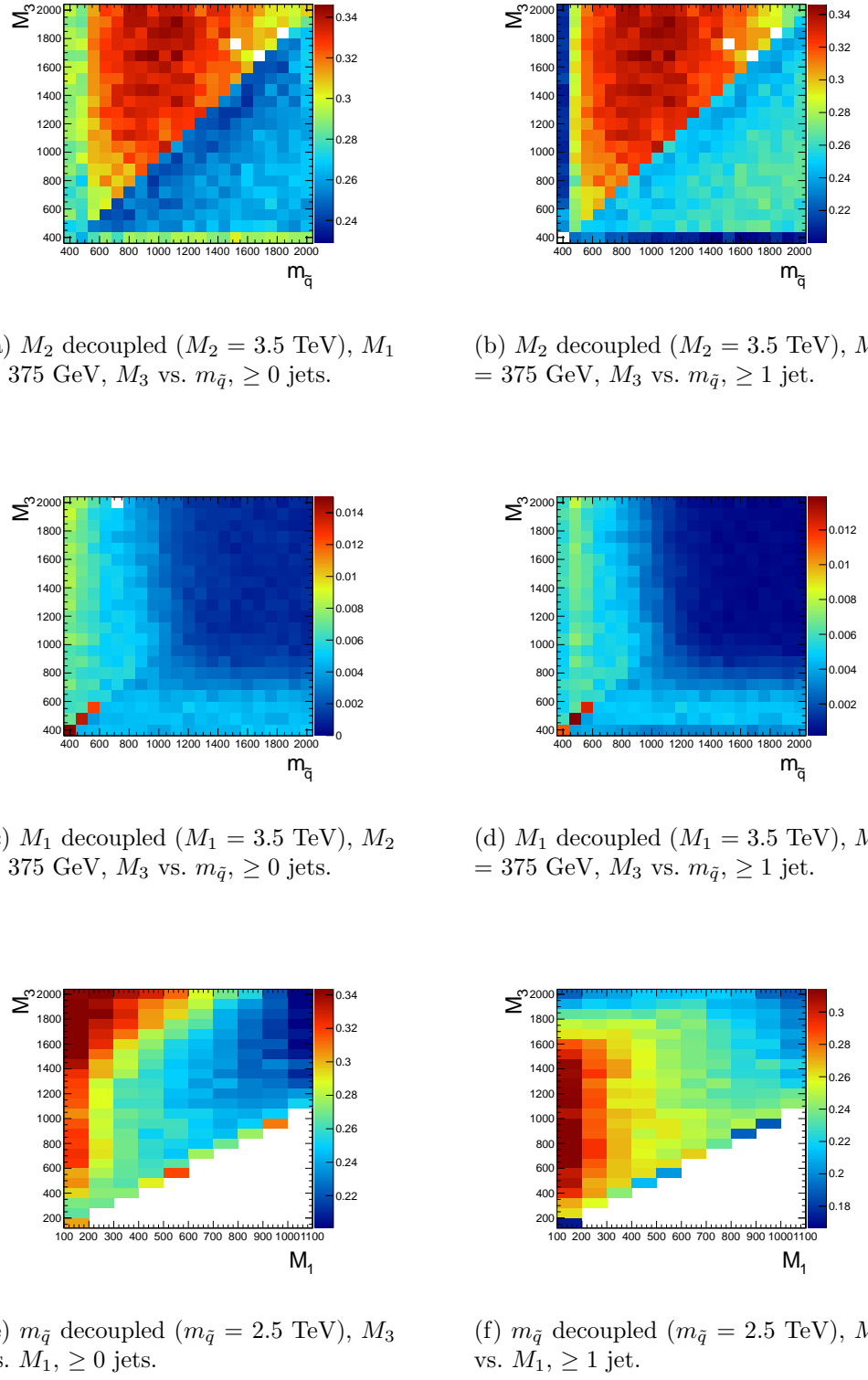


Figure 8.2: Signal acceptance \times efficiency (defined in the text) for the three different scenarios described in Sec. 8.1.

more phase space available to produce squarks, which may then decay via one jet as $\tilde{q} \rightarrow q\tilde{\chi}^0$. Jets in SUSY events may be very close to the neutralino decay photons, and as a result the photons may fail the strict isolation requirements, leading to lower $\mathcal{A} \times \epsilon$ for jet-rich events. The worsened acceptance along $M_3 = 400$ GeV and $m_{\tilde{q}} = 400$ GeV in Fig. 8.2b is due to efficiency of the jet cut, which decreases drastically as M_3 and $m_{\tilde{q}}$ approach M_1 because of shrinking phase space to produce hard jets in the squark and gluino decays to neutralinos.

The broad peak in $\mathcal{A} \times \epsilon$ shown in Fig. 8.2a for $m_{\tilde{q}} < M_3$ and ~ 600 GeV $< m_{\tilde{q}} < \sim 1600$ GeV is due to the $\cancel{E}_T > 50$ GeV cut. The efficiency of the cut decreases as $m_{\tilde{q}}$ decreases because of the fixed M_1 of 375 GeV. If the squark-neutralino mass splitting gets too small, the likelihood of producing an energetic enough gravitino to pass the \cancel{E}_T cut decreases.

$\mathcal{A} \times \epsilon$ is generally much lower for the $M_2 = 375$ GeV grid (Figs. 8.2c and 8.2d) due to the larger contribution from chargino decays to $W + \tilde{G}$, which do not give rise to photons in the final state. The increased acceptance for $M_3 > m_{\tilde{q}}$ is due to the same jet multiplicity issue affecting the $M_1 = 375$ GeV grid. As M_3 and $m_{\tilde{q}}$ increase relative to the fixed M_2 , the jets from squark and gluino decay get more energetic, increasing the chance that they will overlap with the neutralino decay photon and cause it to fail the isolation cut. For $m_{\tilde{q}} \gtrsim 1$ TeV and $M_3 \gtrsim 800$ GeV, the acceptance is so low that not enough events were simulated to see the acceptance decrease over the statistical error.

In Fig. 8.2e, the neutralino is always heavy enough to guarantee decay to a photon that can pass the 40 GeV p_T cut. $\mathcal{A} \times \epsilon$ increases as M_3 increases because the larger gluino-neutralino mass splitting gives the neutralino a larger kinetic energy, increasing the chance that it will decay to a photon with 40 GeV p_T or higher. After the bino mass increases beyond the threshold needed to produce high p_T photons, $\mathcal{A} \times \epsilon$ decreases with increasing M_1 , independent of gluino mass, because higher M_1 means more phase

2084 space is open to decays of the form $\tilde{\chi}_1^0 \rightarrow Z\tilde{G}$ and $\tilde{\chi}_1^0 \rightarrow H\tilde{G}$. The two-photon search
 2085 is naturally not as efficient for these decays.

Added

2086 There is a small chance that some real GMSB signal events could be reconstructed signal
 2087 as ff events in the data. To correct the signal acceptance for this effect, the number contamination
 2088 of signal events reconstructed as ff events is subtracted from the number of signal $\gamma\gamma$ ination
 2089 events, effectively reducing the signal acceptance. This is generally a small correction par.
 2090 ($\sim 5\%$).

2091 8.2.2 CL_s and the Profile Likelihood Test Statistic

2092 The process of setting a cross section upper limit entails (1) defining a test statistic,
 2093 (2) generating a distribution for that test statistic under the signal + background
 2094 and background-only hypotheses, and (3) deciding whether or not the observed value
 2095 of the test statistic is more compatible with the signal + background (i.e. weaker
 2096 upper limit) or background-only (i.e. stronger upper limit) hypotheses by considering
 2097 where it falls within the test statistic distributions. An important requirement on the
 2098 choice of test statistic is that it be able to effectively discriminate between the signal
 2099 + background and background-only hypotheses, i.e. the shape of its distribution for
 2100 these two hypotheses should be different. The procedure for determining the exclud-
 2101 ability of a particular model given the value of the test statistic observed should not
 2102 give rise to pathological behavior in the presence of small signals, low statistics, or
 2103 weak sensitivity to models, as is commonly the case in high energy physics. These
 2104 demands on the test statistic and the limit setting procedure itself dictate the choice
 2105 of the profile likelihood test statistic and CL_s procedure.

2106 In the remainder of this section, the notation is taken from ref. [110].

2107 **Profile Likelihood**

2108 For a specific model of GMSB, the limit setting procedure concerns the question of
 2109 whether to reject the signal + background hypothesis $\mu s + b$ in favor of the background-
 2110 only (Standard Model) hypothesis of b ($\mu = 0$). μ is a dimensionless signal strength
 2111 parameter. s is the expected number of signal events, calculated from MC simulated
 2112 signal events as in Secs. 8.1 and 8.2.1. b is the expected number of background events,
 2113 estimated in Chap. 7. By the Neyman-Pearson lemma [113], the ratio of the likelihood
 2114 of $\mu s + b$ to the likelihood of b is the test statistic with the highest power to reject $\mu s + b$
 2115 at whatever confidence level is desired. In practice, this means that the likelihood ratio
 2116 is the best discriminator between the GMSB and Standard Model hypotheses.

2117 The likelihood of the signal + background hypothesis as a function of the data
 2118 (either real or generated) is defined as

$$\mathcal{L}(\text{data}|\mu, \theta) = \prod_{i=1}^N \frac{(\mu s_i(\theta) + b_i(\theta))^{n_i}}{n_i!} e^{-\mu s_i(\theta) - b_i(\theta)} p(\tilde{\theta}|\theta) \quad (8.1)$$

2119 where $N = 5$ is the number of E_T bins used in the analysis ([50, 60) GeV, [60,
 2120 70) GeV, [70, 80) GeV, [80, 100) GeV, and [100, ∞) GeV); $s_i(\theta)$ and $b_i(\theta)$ are the
 2121 expected number of signal and background events in E_T bin i , respectively; n_i is the
 2122 number of events observed in E_T bin i ; and θ represents all the nuisance parameters
 2123 (uncertainties). $p(\tilde{\theta}|\theta)$ represents the product of probability distribution functions
 2124 (PDFs) for the nuisance parameters, where $\tilde{\theta}$ is the default value of the nuisance
 2125 parameter. In this analysis, there are eight experimental nuisance parameters per E_T
 2126 bin, given here as relative errors on the expected number of signal events:

- 2127 • Uncertainty on the measured integrated luminosity (4.5% in all bins) [114]
- 2128 • Uncertainty on the signal acceptance due to $\epsilon_e^{\text{data}}/\epsilon_e^{\text{MC}}$ and the pixel veto effi-
 2129 ciency error (cf. Sec. 6.4.2) (8% in all bins)

- 2130 ● Uncertainty on the signal acceptance due to imperfect pileup simulation (2.6%
2131 in all bins)
 - 2132 ● Systematic uncertainty on QCD background prediction due to difference be-
2133 tween ff and ee estimates (5.5%-53% of the QCD background depending on
2134 bin)
 - 2135 ● Systematic uncertainty on electroweak background prediction due to p_T depen-
2136 dence of $f_{e \rightarrow \gamma}$ (29%-30% of the electroweak background depending on bin)
 - 2137 ● Statistical uncertainty on the signal acceptance (1.8%-100% depending on model
2138 and bin)
 - 2139 ● Statistical uncertainty on the QCD background prediction (7.2%-38% of the
2140 QCD background depending on bin)
 - 2141 ● Statistical uncertainty on the electroweak background prediction (3.6%-7.2% of
2142 the electroweak background depending on bin)
- 2143 and one very small theoretical nuisance parameter: the uncertainty on the signal
2144 acceptance due to underlying parton distribution function (PDF) uncertainties. In
2145 the limit-setting code, the uncertainties on signal acceptance due to photon efficiency
2146 and PDF errors are added in quadrature and treated as one. The uncertainty on the
2147 signal acceptance due to jet energy correction uncertainties is negligible, due to the
2148 presence of many hard jets in GMSB signal events. The uncertainties on integrated
2149 luminosity and pileup are 100% correlated between \cancel{E}_T bins, and the uncertainty on
2150 signal acceptance can usually be treated similarly because the error on $\epsilon_e^{\text{data}}/\epsilon_e^{\text{MC}}$ often
2151 dominates the PDF error on acceptance (although these three uncertainties are 0%
2152 correlated with each other).

2153 To estimate the uncertainty due to imperfect simulation of LHC pileup, the square
2154 of the average data efficiency for photons over the range 1-15 reconstructed primary

vertices (see Fig. 6.17a), weighted by the number of $\gamma\gamma$ events per primary vertex bin, is calculated. The efficiency per primary vertex bin is estimated from a linear fit to Fig. 6.17a. The process is repeated for MC using the entire range of primary vertices in Fig. 6.17a (all MC signal points have the same pileup simulation). The error is taken as $2 \times |\text{avg. data efficiency squared} - \text{avg. MC efficiency squared}| / (\text{avg. data efficiency squared} + \text{avg. MC efficiency squared})$.

Each nuisance parameter PDF is modeled by a log-normal distribution:

$$p(\tilde{\theta}|\theta) = \frac{1}{\sqrt{2\pi} \ln \kappa} \exp\left(-\frac{(\ln \tilde{\theta}/\theta)^2}{2(\ln \kappa)^2}\right) \frac{1}{\tilde{\theta}} \quad (8.2)$$

where $\tilde{\theta} = 1$ and $\kappa = 1 +$ the one-standard-deviation relative error on the nuisance parameter (e.g. for the 4.5% error due to integrated luminosity, $\kappa = 1.045$).

Similarly, the likelihood of the background-only hypothesis as a function of the data (either real or generated) is defined as

$$\mathcal{L}(\text{data}|0, \theta) = \prod_{i=1}^N \frac{b_i(\theta)^{n_i}}{n_i!} e^{-b_i(\theta)} p(\tilde{\theta}|\theta) \quad (8.3)$$

The profile likelihood test statistic is defined as

$$\tilde{q}_\mu = -2 \ln \frac{\mathcal{L}(\text{data}|\mu, \hat{\theta}_\mu)}{\mathcal{L}(\text{data}|\hat{\mu}, \hat{\theta})}, 0 \leq \hat{\mu} \leq \mu \quad (8.4)$$

where the $\hat{\theta}_\mu$ maximize $\mathcal{L}(\text{data}|\mu, \hat{\theta}_\mu)$ when it is evaluated at a particular μ , and $\hat{\mu}$ and $\hat{\theta}$ are the global maximum likelihood estimators of μ and θ . The condition $\hat{\mu} \leq \mu$ insures that the obtained cross section upper limit is one-sided, i.e. there is no possibility to find a lower limit on the cross section. The profile likelihood test

2171 statistic has the nice property that in the asymptotic (large statistics) limit its PDF
 2172 can be approximated by analytic formulae, eliminating the need to generate multiple
 2173 toy experiments to get the PDF. However, the approximation breaks down for small
 2174 numbers of observed events, so in practice the asymptotic limit is only used as a first
 2175 guess at the location of the true limit.

2176 The PDFs $f(\tilde{q}_\mu | \mu, \hat{\theta}_\mu^{\text{obs}})$ and $f(\tilde{q}_\mu | 0, \hat{\theta}_0^{\text{obs}})$ for the profile likelihood test statistic
 2177 under the signal + background and background-only hypotheses, respectively, are
 2178 obtained by generating toy MC pseudo-experiments. $\hat{\theta}_\mu^{\text{obs}}$ and $\hat{\theta}_0^{\text{obs}}$ maximize Eqs. 8.1
 2179 and 8.3, respectively, when they are evaluated for the observed data. For each μ (and
 2180 the background-only hypothesis $\mu = 0$), the pseudo-experiments are generated by
 2181 picking random values of s and b from a Poisson distribution with the θ fixed as just
 2182 described.

2183 **CL_s**

2184 In the classical frequentist approach, a signal model may be excluded at the 95%
 2185 confidence level (CL) if the probability of any measurement of the test statistic to be
 2186 greater than or equal to the observed value given the signal + background hypothesis
 2187 is 5%. This means that the observed value of the test statistic is so incompatible
 2188 with what one would expect to observe if the signal model were true that, under the
 2189 assumption that the signal model *is* true, the chance of observing a test statistic even
 2190 further afield from the signal expectation is only 5%. Mathematically,

$$\begin{aligned} p_\mu &\equiv P(\tilde{q}_\mu \geq \tilde{q}_\mu^{\text{obs}} | \mu s + b) = \int_{\tilde{q}_\mu^{\text{obs}}}^{\infty} f(\tilde{q}_\mu | \mu, \hat{\theta}_\mu^{\text{obs}}) d\tilde{q}_\mu \\ p_\mu &\leq 0.05 \Rightarrow \text{exclude } \mu \end{aligned} \quad (8.5)$$

2191 where $\tilde{q}_\mu^{\text{obs}}$ is the observed value of the test statistic and p_μ is the p-value. As indicated
 2192 in Eq. 8.5, the p-value is simply the integral of the PDF of \tilde{q}_μ from $\tilde{q}_\mu^{\text{obs}}$ to infinity.

2193 By construction, the classical 95% CL frequentist approach described above will
 2194 reject a true signal + background hypothesis 5% of the time. This can happen if the
 2195 experiment gets “unlucky” and the observation fluctuates low, causing $\tilde{q}_\mu^{\text{obs}}$ to fall in
 2196 the tail of the \tilde{q}_μ distribution. This poses a problem for the case of very weak signals
 2197 ($\mu \sim 0$), because it will lead to spurious exclusions of models to which the experiment
 2198 has little sensitivity. To avoid this pitfall, the CL_s limit setting method is used.

2199 In the CL_s method, the classical frequentist p-value of Eq. 8.5 is simply divided by
 2200 one minus the p-value of the background-only hypothesis, and it is this ratio, rather
 2201 than the p-value of the signal + background hypothesis alone, that is required to be
 2202 ≤ 0.05 . Mathematically,

$$1 - p_0 \equiv P(\tilde{q}_\mu \geq \tilde{q}_\mu^{\text{obs}} | b) = \int_{\tilde{q}_\mu^{\text{obs}}}^{\infty} f(\tilde{q}_\mu | 0, \hat{\theta}_0^{\text{obs}}) d\tilde{q}_\mu \quad (8.6)$$

$$\text{CL}_s(\mu) \equiv \frac{p_\mu}{1 - p_0} \quad (8.7)$$

$$\text{CL}_s(\mu) \leq 0.05 \Rightarrow \text{exclude } \mu$$

2203 where p_0 is the p-value for the background-only hypothesis ($\mu = 0$). In the case of
 2204 low sensitivity to μ , $p_\mu \lesssim 1 - p_0$, so $\text{CL}_s(\mu) \lesssim 1$ and μ will not be excluded. On the
 2205 contrary, for high sensitivity to μ ($\mu s \gg \sigma_b$), $p_\mu \ll 1 - p_0$, so models that can be
 2206 excluded by the criterion $p_\mu \leq 0.05$ will also be excluded by the criterion $\text{CL}_s \leq 0.05$.
 2207 Compared to the classical frequentist method, CL_s limits can be a little stronger in
 2208 the case of low signal sensitivity [110].

2209 To determine the upper limit on the cross section of a particular model, the lowest
 2210 value of μ for which $\text{CL}_s(\mu) \leq 0.05$, denoted $\mu^{95\% \text{CL}}$, is found. The cross section upper
 2211 limit of that model is then simply $\mu^{95\% \text{CL}}$ multiplied by the expected cross section of

2212 the model (cf. Fig. 8.1).

2213 In contrast to the observed upper limit, the expected upper limit is calculated from
 2214 an ensemble of background-only MC pseudo-experiments. The distribution $f(\mu_{\text{pseudo}}^{\text{95%CL}})$
 2215 is plotted (one entry per pseudo-experiment). The median expected upper limits and
 2216 $\pm 1\sigma$ and $\pm 2\sigma$ bands are defined as

$$0.5 = \int_0^{\mu_{\text{exp}}^{\text{95%CL}}} f(\mu_{\text{pseudo}}^{\text{95%CL}}) d\mu_{\text{pseudo}}^{\text{95%CL}} \quad (8.8)$$

$$0.16 = \int_0^{\mu_{-1\sigma,\text{exp}}^{\text{95%CL}}} f(\mu_{\text{pseudo}}^{\text{95%CL}}) d\mu_{\text{pseudo}}^{\text{95%CL}} \quad (8.9)$$

$$0.84 = \int_0^{\mu_{+1\sigma,\text{exp}}^{\text{95%CL}}} f(\mu_{\text{pseudo}}^{\text{95%CL}}) d\mu_{\text{pseudo}}^{\text{95%CL}} \quad (8.10)$$

$$0.025 = \int_0^{\mu_{-2\sigma,\text{exp}}^{\text{95%CL}}} f(\mu_{\text{pseudo}}^{\text{95%CL}}) d\mu_{\text{pseudo}}^{\text{95%CL}} \quad (8.11)$$

$$0.975 = \int_0^{\mu_{+2\sigma,\text{exp}}^{\text{95%CL}}} f(\mu_{\text{pseudo}}^{\text{95%CL}}) d\mu_{\text{pseudo}}^{\text{95%CL}} \quad (8.12)$$

2217 The technical procedure followed to calculate the 95% CL cross section upper
 2218 limits for each GMSB model tested is given below.

- 2219 1. Calculate a guess for the median expected limit and $\pm 2\sigma$ error bands ($\mu_{\pm 2\sigma,\text{guess}}^{\text{95%CL}}$)
 2220 using the asymptotic formulae for $f(\tilde{q}_\mu | 0, \hat{\theta}_0^{\text{obs}})$.
- 2221 2. Calculate observed ($\mu_{\text{obs,asym}}^{\text{95%CL}}$), median expected ($\mu_{\text{exp,asym}}^{\text{95%CL}}$), and $\pm 1\sigma$ ($\mu_{\pm 1\sigma,\text{asym}}^{\text{95%CL}}$)
 2222 and $\pm 2\sigma$ ($\mu_{\pm 2\sigma,\text{asym}}^{\text{95%CL}}$) expected CL_s limits using the asymptotic formulae for
 2223 $f(\tilde{q}_\mu | \mu, \hat{\theta}_\mu^{\text{obs}})$ and $f(\tilde{q}_\mu | 0, \hat{\theta}_0^{\text{obs}})$. Restrict the range of $\mu_{\text{obs,asym}}^{\text{95%CL}}$ and $\mu_{\text{exp,asym}}^{\text{95%CL}}$ to
 2224 $[0, 5 \times \mu_{\pm 2\sigma,\text{guess}}^{\text{95%CL}}]$ (this avoids pathological behavior of the limit-setting code
 2225 when the expected number of signal events is much greater than the observed
 2226 number of events and only introduces a $\sim 5\%$ upward bias in the observed limit,
 2227 well within the $\pm 1\sigma$ error bands).
- 2228 3. Calculate median expected ($\mu_{\text{exp}}^{\text{95%CL}}$) and $\pm 1\sigma$ ($\mu_{\pm 1\sigma}^{\text{95%CL}}$) and $\pm 2\sigma$ ($\mu_{\pm 2\sigma}^{\text{95%CL}}$) ex-

2229 pected CL_s limits using 100 toy MC pseudo-experiments to generate $f(\tilde{q}_\mu|\mu, \hat{\theta}_\mu^{\text{obs}})$
 2230 and $f(\tilde{q}_\mu|0, \hat{\theta}_0^{\text{obs}})$. Restrict the range of $\mu_{\text{exp}}^{95\%\text{CL}}$ to $[0, 5 \times \mu_{\pm 2\sigma, \text{guess}}^{95\%\text{CL}}]$.

2231 4. If $\mu_{\pm 2\sigma}^{95\%\text{CL}}$ could not be calculated, set $\mu_{\pm 2\sigma}^{95\%\text{CL}} = \mu_{\pm 2\sigma, \text{asym}}^{95\%\text{CL}}$ instead.

2232 5. If $\mu_{+2\sigma}^{95\%\text{CL}} \neq \mu_{-2\sigma}^{95\%\text{CL}}$ and $\mu_{\text{obs}, \text{asym}}^{95\%\text{CL}} > 0.0001$:

2233 • If $\mu_{\text{obs}, \text{asym}}^{95\%\text{CL}} > \mu_{+2\sigma}^{95\%\text{CL}}$, set $\mu_{+2\sigma}^{95\%\text{CL}} = 1.3 \times \mu_{\text{obs}, \text{asym}}^{95\%\text{CL}}$.

2234 • If $\mu_{\text{obs}, \text{asym}}^{95\%\text{CL}} < \mu_{-2\sigma}^{95\%\text{CL}}$, set $\mu_{-2\sigma}^{95\%\text{CL}} = 0.7 \times \mu_{\text{obs}, \text{asym}}^{95\%\text{CL}}$.

2235 6. If $\mu_{+2\sigma}^{95\%\text{CL}} = \mu_{-2\sigma}^{95\%\text{CL}}$, set $\mu_{\pm 2\sigma}^{95\%\text{CL}} = \mu_{\pm 2\sigma, \text{asym}}^{95\%\text{CL}}$ instead.

2236 7. Scan over 100 equally spaced test values of μ between $\mu_{-2\sigma}^{95\%\text{CL}}$ and $\mu_{+2\sigma}^{95\%\text{CL}}$ and,
 2237 if $\mu > 0.0001$, calculate the CL_s p-value (p_μ) for this test value of μ to 10^{-6}
 2238 precision using a minimum of 500 toy experiments to generate $f(\tilde{q}_\mu|\mu, \hat{\theta}_\mu^{\text{obs}})$ and
 2239 $f(\tilde{q}_\mu|0, \hat{\theta}_0^{\text{obs}})$.

2240 8. Determine the observed ($\mu_{\text{obs}, \text{scan}}^{95\%\text{CL}}$), median expected ($\mu_{\text{exp}, \text{scan}}^{95\%\text{CL}}$), and $\pm 1\sigma$ ($\mu_{\pm 1\sigma, \text{scan}}^{95\%\text{CL}}$)
 2241 and $\pm 2\sigma$ ($\mu_{\pm 2\sigma, \text{scan}}^{95\%\text{CL}}$) expected CL_s limits from the scan p-values for the signal
 2242 + background and background-only pseudo-experiments.

2243 Finally, a particular GMSB model is excluded if the upper limit on the cross
 2244 section for that model is less than the expected theoretical cross section.

2245 8.3 Cross Section Upper Limits

2246 Figure 8.3 shows the observed upper limits on the cross sections for the models de-
 2247 scribed in Sec. 8.1. In some ($\mathcal{O}(10^{-3})$) cases, the upper limit is zero due to a com-
 2248 putational failure. The upper limit for these points is estimated from the average of the
 2249 upper limits of the four neighboring points, as shown in Figure 8.4. If any of the four
 2250 points is also missing a valid upper limit, it is dropped from the average. The errors

2251 on the individual upper limits used in the estimate are propagated to the error on
 2252 the average.

2253 8.4 Exclusion Contours

2254 Exclusion contours for the GMSB models discussed above are shown in Figure 8.5. The
 2255 contours are derived from plots of predicted cross section minus cross section upper
 2256 limit ($\sigma \times (1 - \mu^{95\%CL})$), where σ is the nominal value of the predicted cross section
 2257 for a given GMSB model) vs. the two model parameters of interest, so the values are
 2258 either negative (not excluded) or positive (excluded). Sometimes, a particular point
 2259 may have a different sign than its four same-sign neighbors (cf. Fig. 8.4) due to a
 2260 fluctuation. In these cases, $\sigma \times (1 - \mu^{95\%CL})$ for the anomalous point is estimated
 2261 as the average $\sigma \times (1 - \mu^{95\%CL})$ of the four neighboring points. The errors on the
 2262 individual values of $\sigma \times (1 - \mu^{95\%CL})$ used in the estimate are propagated to the error
 2263 on the average.

2264 In the plots in Fig. 8.5, the expected limit (i.e. the contour derived from $\sigma \times (1 -$
 2265 $\mu_{\text{exp,scan}}^{95\%CL})$) is drawn in dark orange and the 1σ experimental band around the expected
 2266 limit (i.e. the shaded region between the contours derived from $\sigma \times (1 - \mu_{\pm 1\sigma, \text{scan}}^{95\%CL})$) is
 2267 drawn in light orange. The values of $\mu_{\text{exp,scan}}^{95\%CL}$ and $\mu_{\pm 1\sigma, \text{scan}}^{95\%CL}$ only reflect the experimental
 2268 uncertainties given in Sec. 8.2.2.

2269 The observed limits (derived from $\sigma \times (1 - \mu_{\text{obs,scan}}^{95\%CL})$) and 1σ theoretical error
 2270 bands around the observed limits in Fig. 8.5 are drawn in blue. The contours that
 2271 define this band are derived from $\pm(\sigma_{\pm 1\sigma} - \sigma \mu_{\text{obs,scan}}^{95\%CL})$, where $\sigma_{\pm 1\sigma}$ is the nominal
 2272 value of the predicted cross section \pm the one-standard-deviation theoretical error on
 2273 the predicted cross section. In this way, the experimental and theoretical errors, the
 2274 latter due to imperfect knowledge of the predicted cross section, are shown separately.
 2275 Comparing with Fig. 8.1, one can easily see that the shapes of the exclusion curves

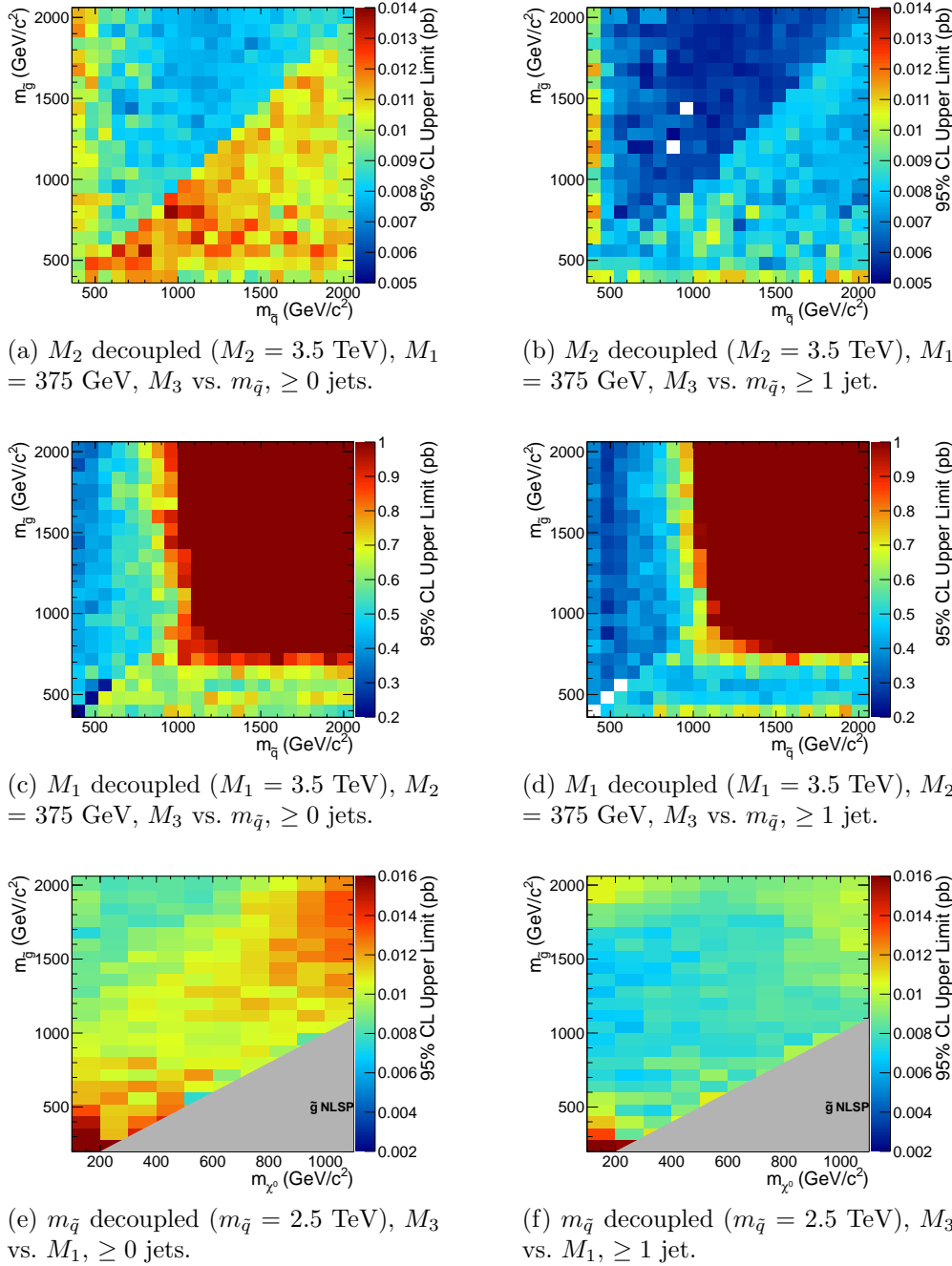


Figure 8.3: Cross section upper limits for the three different scenarios described in Sec. 8.1.

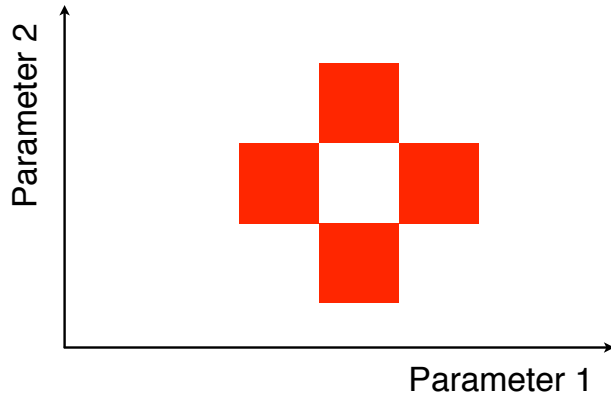


Figure 8.4: Diagram of the points (red squares) used in the estimation of an upper limit when a computational failure occurs (middle white square).

²²⁷⁶ are driven by the contours in the expected cross section plane.

²²⁷⁷ The dominant theoretical uncertainties on the GMSB cross sections are due to:

- ²²⁷⁸ • PDF uncertainty (4%-100% depending on model)
- ²²⁷⁹ • Renormalization scale uncertainty (0.036%-25% depending on model)

²²⁸⁰ The PDF4LHC [115] recommendations are used to calculate the effect of these un-
²²⁸¹ certainties on the GMSB cross sections. The recommendations state that PDF sets
²²⁸² from MSTW08 [116], CTEQ6.6 [117], and NNPDF2.0 [118] should be considered in
²²⁸³ the determination of the PDF uncertainties, because these three PDF sets include
²²⁸⁴ constraints from the Tevatron and from fixed target experiments, as well as from
²²⁸⁵ HERA [?], and are thus the most complete.

²²⁸⁶ Each collaboration's PDF prediction comes from a global fit to experimental data
²²⁸⁷ with a certain number of free parameters. The best fit parameters come from mini-
²²⁸⁸ mizing the χ^2 ; increasing the χ^2 by one from its minimum can be written in terms of
²²⁸⁹ the N -dimensional Hessian error matrix [?] where N is the number of free parameters.

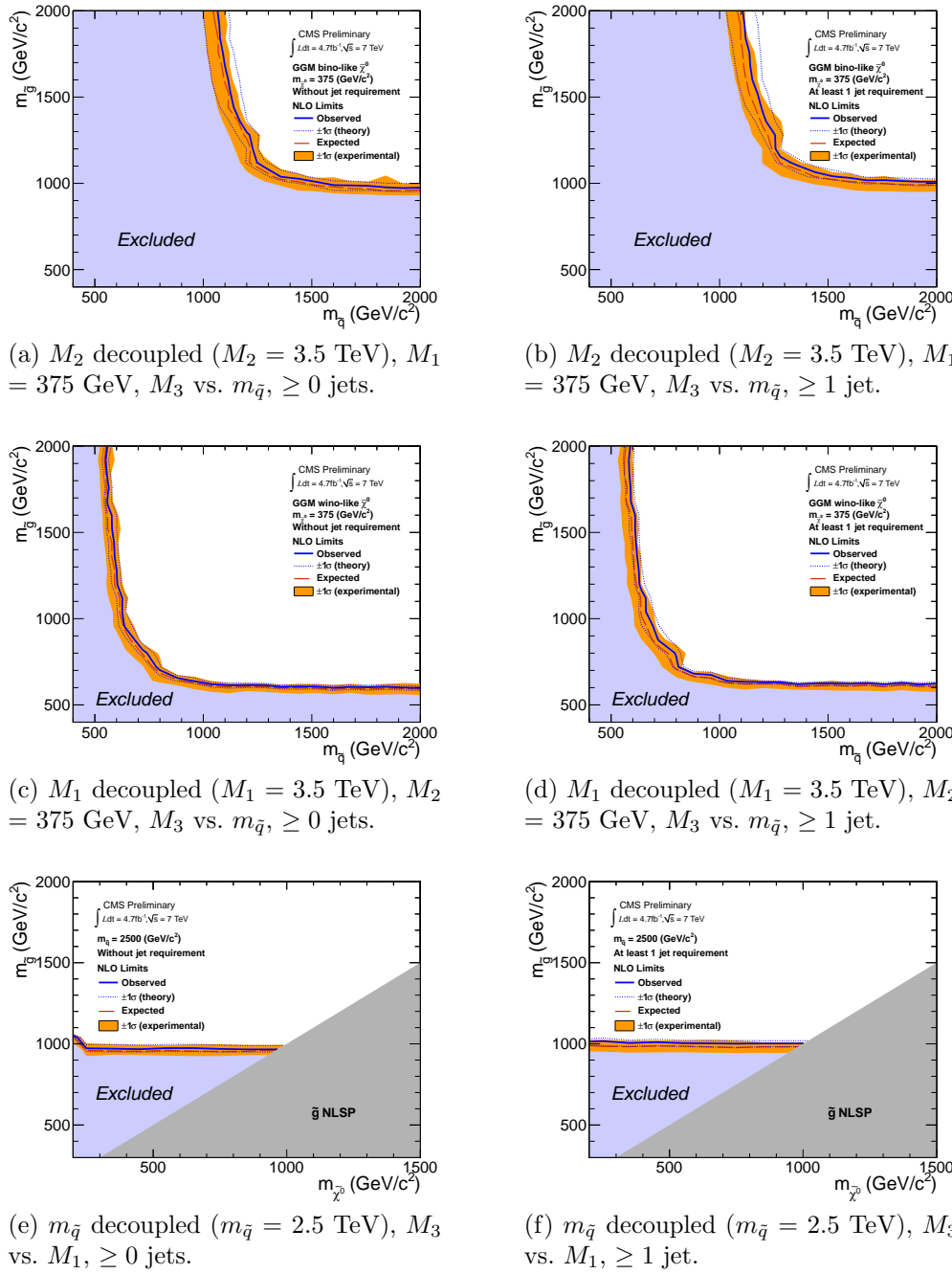


Figure 8.5: Exclusion contours for the three different scenarios described in Sec. 8.1.

2290 To form the i^{th} pair of members of the PDF set, the PDF is evaluated once at the
 2291 parameter values given by the i^{th} eigenvector of the Hessian matrix, and then again
 2292 at the parameter values given by the negative of the i^{th} eigenvector. Each PDF set
 2293 therefore contains $2N$ members, corresponding to the positive and negative values of
 2294 the N eigenvectors [119].

2295 To calculate the PDF uncertainties for a given GMSB model, the leading order
 2296 Pythia cross section is reweighted by a factor of the error PDF divided by the leading
 2297 order PDF with which the model was generated. This is repeated for each error PDF
 2298 in a given PDF set. The $\pm 1\sigma$ deviations are proportional to the maximum difference
 2299 between cross sections obtained this way. The actual equation for the $\pm 1\sigma$ errors is
 2300 Eq. (43) of ref. [119]. In the same way, the $\pm 1\sigma$ errors are calculated for the CTEQ6.6,
 2301 MSTW08, and NNPDF2.0 PDF sets. The total error is given by the half the difference
 2302 between the largest $+1\sigma$ deviation and the smallest -1σ deviation [115].

2303 The uncertainties on the signal cross sections due to the choice of renormaliza-
 2304 tion/factorization scale ($\alpha_S(M_Z)$) are evaluated by calculating the PROSPINO next
 2305 to leading order cross section once with $\alpha_S(M_Z)$ halved, then once with $\alpha_S(M_Z)$ dou-
 2306 bled. The lower error on the cross section is taken as the absolute difference between
 2307 the nominal and halved-scale values of the cross section, while the upper error is taken
 2308 as the absolute difference between the nominal and doubled-scale values. The PDF
 2309 and α_S uncertainties are added in quadrature to give the total PDF uncertainty.

2310 Note that the quoted GMSB cross sections are evaluated at next to leading order
 2311 using PROSPINO, but it is the leading order Pythia cross sections that are reweighted
 2312 to the next to leading order MSTW08, CTEQ6.6, and NNPDF2.0 PDFs to get the
 2313 error bands. In addition, since to a good approximation the GMSB production cross
 2314 sections for the M_3 - $m_{\tilde{q}}$ scans only depend on M_3 and $m_{\tilde{q}}$, the same PDF errors per
 2315 point are used for the \tilde{B} -like and \tilde{W} -like grids.

²³¹⁶ **Appendix A**

²³¹⁷ **Monte Carlo Samples**

²³¹⁸ A number of MC samples are utilized in this analysis and referred to throughout the
²³¹⁹ text. Below is a list of the MC samples used and an explanation of what the sample
²³²⁰ names mean.

²³²¹ **A.0.1 List of Samples**

²³²² 1. Drell-Yan:

²³²³ /DYJetsToLL_TuneZ2_M-50_7TeV-madgraph-tauola/
²³²⁴ Fall11-PU_S6_START42_V14B-v1/AODSIM

²³²⁵ 2. QCD enriched with B and D meson decays to electrons:

²³²⁶ /QCD_Pt-20to30_BCToE_TuneZ2_7TeV-pythia6/
²³²⁷ Fall11-PU_S6_START42_V14B-v1/AODSIM,
²³²⁸ /QCD_Pt-30to80_BCToE_TuneZ2_7TeV-pythia6/
²³²⁹ Fall11-PU_S6_START42_V14B-v1/AODSIM,
²³³⁰ /QCD_Pt-80to170_BCToE_TuneZ2_7TeV-pythia6/
²³³¹ Fall11-PU_S6_START42_V14B-v1/AODSIM

²³³² 3. Photon + jet doubly enriched with jets passing an EM filter:

```

2333 /GJet_Pt-20_doubleEMEnriched_TuneZ2_7TeV-pythia6/
2334 Fall11-PU_S6_START42_V14B-v1/AODSIM

2335 4.  $W$  leptonic decays:
2336 /WJetsToLNu_TuneZ2_7TeV-madgraph-tauola/
2337 Fall11-PU_S6_START42_V14B-v1/AODSIM

2338 5.  $t\bar{t}$ :
2339 /TTJets_TuneZ2_7TeV-madgraph-tauola/
2340 Fall11-PU_S6_START42_V14B-v2/AODSIM

```

2341 A.0.2 Explanation of Naming Conventions

- 2342 • L: charged lepton
- 2343 • B: B hadron
- 2344 • C: D , or charmed, hadron
- 2345 • E: electron or positron
- 2346 • G: photon
- 2347 • W: W boson
- 2348 • Nu: neutrino
- 2349 • T: top quark
- 2350 • TuneZ2: Pythia tune incorporating 2010 LHC data with CTEQ6L1 [117] PDFs
[124]
- 2352 • M-50: Generated l^+l^- invariant mass threshold of 50 GeV
- 2353 • 7TeV: Generated center-of-mass energy 7 TeV

- 2354 ● **pythia6**: Parton showering and hadronization simulated with Pythia v6.424
- 2355 [125]
- 2356 ● **madgraph**: Hard interaction generated with MadGraph [126]
- 2357 ● **tauola**: τ decays generated with Tauola [127]
- 2358 ● **PU_S6**: Generated with S6 pileup scenario
- 2359 ● **START42_V14B**: Reconstructed with best alignment and calibration constants
2360 and magnetic field conditions as of August 3, 2011
- 2361 ● **Pt_XtoY**: $X \leq$ generated $\hat{p}_T < Y$
- 2362 ● **BCToE**: Enriched in B and D meson decays to electrons
- 2363 ● **doubleEMEnriched**: Enriched in electromagnetic jets

²³⁶⁴ Bibliography

- ²³⁶⁵ [1] <http://cms.web.cern.ch/news/cms-detector-design> (2011).
- ²³⁶⁶ [2] S.L. Glashow, J. Iliopoulos, and L. Maiani, *Phys. Rev. D* **2** (1970) 1285; S.L. Glashow, *Nucl. Phys.* **22(4)** (1961) 579; J. Goldstone, A. Salam, and S. Weinberg, *Phys. Rev.* **127** (1962) 965; S. Weinberg, *Phys. Rev. Lett.* **19** (1967) 1264; A. Salam and J.C. Ward, *Phys. Lett.* **13(2)** (1964) 168.
- ²³⁷⁰ [3] M. Gell-Mann, *Phys. Lett.* **8** (1964) 214; G. Zweig, *CERN 8419/TH. 412* (1964) (unpublished).
- ²³⁷² [4] J. Drees, *Int. J. Mod. Phys.* **A17** (2002) 3259.
- ²³⁷³ [5] P.W. Higgs, *Phys. Lett.* **12(2)** (1964) 132; P.W. Higgs, *Phys. Rev. Lett.* **13** (1964) 508; P.W. Higgs, *Phys. Rev.* **145** (1966) 1156.
- ²³⁷⁵ [6] I. Aitchison, *Supersymmetry in Particle Physics: An Elementary Introduction* (Cambridge University Press, Cambridge 2007), p. 4.
- ²³⁷⁷ [7] C. Quigg, in *Flavor Physics for the Millennium: TASI 2000, Boulder, 2000*, edit by J. L. Rosner (World Scientific, Singapore, 2001), p. 3.
- ²³⁷⁹ [8] L. Álvarez-Gaumé and J. Ellis, *Nature Phys.* **7** (2011) 2.
- ²³⁸⁰ [9] G. Arnison et al. (UA1 Collaboration), *Phys. Lett.* **B122** (1983) 103.
- ²³⁸¹ [10] G. Arnison et al. (UA1 Collaboration), *Phys. Lett.* **B126** (1983) 398.

- 2382 [11] J. Gunion, H.E. Haber, G. L. Kane, and S. Dawson, *The Higgs Hunter's Guide*,
 2383 (Addison-Wesley, Redwood City, 1990).
- 2384 [12] S. P. Martin, *A Supersymmetry Primer* **v4** (2006) 86. [arXiv:hep-ph/9709356](https://arxiv.org/abs/hep-ph/9709356).
- 2385 [13] K. Nakamura et al. (Particle Data Group), *J. Phys.* **G37** (2010) 075021.
- 2386 [14] S. Chatrchyan et al. (CMS Collaboration), *Phys. Lett.* **B710** (2012) 26.
- 2387 [15] G. Aad et al. (ATLAS Collaboration), *Phys. Lett.* **B710** (2012) 49.
- 2388 [16] M. Dine and W. Fischler, *Phys. Lett.* **B110** (1982) 227; C.R. Nappi and B.A.
 2389 Ovrut, *Phys. Lett.* **B113** (1982) 175; L. Alvarez-Gaumé, M. Claudson, and M.B.
 2390 Wise, *Nucl. Phys.* **B207** (1982) 96; M. Dine and A.E. Nelson, *Phys. Rev.* **D48**
 2391 (1993) 1277; M. Dine, A.E. Nelson, and Y. Shirman, *Phys. Rev.* **D51** (1995)
 2392 1362; M. Dine, A.E. Nelson, Y. Nir, and Y. Shirman, *Phys. Rev.* **D53** (1996)
 2393 2658.
- 2394 [17] A.H. Chamseddine, R. Arnowitt, and P. Nath, *Phys. Rev. Lett.* **49** (1982) 970; R.
 2395 Barbieri, S. Ferrara, and C.A. Savoy, *Phys. Lett.* **B119** (1982) 343; L.E. Ibáñez,
 2396 *Phys. Lett.* **B118** (1982) 73; L.J. Hall, J.D. Lykken, and S. Weinberg, *Phys. Rev.*
 2397 **D27** (1983) 2359; N. Ohta, *Prog. Theor. Phys.* **70** (1983) 542; J. Ellis, D.V.
 2398 Nanopoulos, and K. Tamvakis, *Phys. Lett.* **B121** (1983) 123; L. Alvarez-Gaumé,
 2399 J. Polchinski, and M. Wise, *Nucl. Phys.* **B221** (1983) 495.
- 2400 [18] P. Meade, N. Seiberg, and D. Shih, *Progr. Theor. Phys. Suppl.* **177** (2009) 143.
- 2401 [19] G. Aad et al., *CERN-PH-EP-2011-160* (2011).
- 2402 [20] T. Aaltonen et al., *Phys. Rev. Lett.* **104** (2010) 011801.
- 2403 [21] CMS Collaboration, *CMS-PAS-SUS-11-009* (2011).
- 2404 [22] <http://en.wikipedia.org/wiki/Tevatron>.

- 2405 [23] E. Fernandez et al., *Phys. Rev. Lett.* **54** (1985) 1118; E. Fernandez et al., *Phys.*
 2406 *Rev.* **D35** (1987) 374; D. Decamp et al., *Phys. Lett.* **B237(2)** (1990) 291; F.
 2407 Abe et al., *Phys. Rev. Lett.* **75** (1995) 613; S. Abachi et al., *Phys. Rev. Lett.* **75**
 2408 (1995) 618; G. Alexander et al., *Phys. Lett.* **B377(4)** (1996) 273; S. Aid et al.,
 2409 *Z. Phys.* **C71(2)** (1996) 211; S. Aid et al., *Phys. Lett.* **B380(3-4)** (1996) 461; B.
 2410 Aubert et al., *Phys. Rev. Lett.* **95** (2005) 041802.
- 2411 [24] O. Buchmueller et al., *CERN-PH-TH/2011-220* (2011).
- 2412 [25] <https://twiki.cern.ch/twiki/bin/view/CMSPublic/PhysicsResultsSUS>.
- 2413 [26] G. Aad et al., *JINST* **3** (2008) S08003.
- 2414 [27] B.C. Allanach et al., *Eur. Phys. J.* **C25** (2002) 113.
- 2415 [28] CMS Collaboration, *CMS-PAS-SUS-12-001* (2012).
- 2416 [29] A. Boyarsky, J. Lesgourgues, O. Ruchayskiy, and M. Viel, *CERN-PH-TH/2008-*
 2417 *234* (2009).
- 2418 [30] E. Komatsu et al., *Astrophys. J. Suppl. Ser.* **180** (2009) 330.
- 2419 [31] C.-H. Chen and J.F. Gunion, *Physical Review* **D58** (1998) 075005.
- 2420 [32] F. Staub, W. Porod, J. Niemeyer, *JHEP* **1001** (2010) 058.
- 2421 [33] L. Evans and P. Bryant (eds.), *JINST* **3** (2008) S08001.
- 2422 [34] <http://cms.web.cern.ch/news/summary-2011-p-p-running> (2011).
- 2423 [35] <http://public.web.cern.ch/public/en/lhc/Facts-en.html> (2008).
- 2424 [36] CERN, <http://cdsweb.cern.ch/record/833187> (2005).
- 2425 [37] RGBStock.com, <http://www.rgbstock.com/photo/n7EsabW/Airplane> (2011).

- 2426 [38] R. Flükiger, S. Y. Hariharan, R. Küntzler, H. L. Luo, F. Weiss, T. Wolf, and J.
 2427 Q. Xu, in *Landolt-Börnstein: Numerical Data and Functional Relationships in*
 2428 *Science and Technology*, edited by R. Flükiger and W. Klose (Springer, 2012).
- 2429 [39] Y.-P. Sun, F. Zimmermann, and R. Tomás, in Proceedings of the 23rd Particle Ac-
 2430 celerator Conference, Vancouver, 2009, [http://accnet.web.cern.ch/accnet/](http://accnet.web.cern.ch/accnet/Literature/2009/TH5PFP016-Sunpdf.pdf)
 2431 Literature/2009/TH5PFP016-Sunpdf.pdf (unpublished).
- 2432 [40] O.S. Brüning et al. (eds.), *CERN-2004-003-V-1*, <http://lhc.web.cern.ch/lhc/LHC-DesignReport.html> (2004).
- 2434 [41] CERN, <http://cdsweb.cern.ch/record/841568/files/> (1993).
- 2435 [42] P. Komorowski and D. Tommasini, in *Proceedings of the 1998 International*
 2436 *Computational Accelerator Physics Conference, Monterey, 1998*, edited by K.
 2437 Ko and R. Ryne (SLAC, Stanford, 1998), p. 192, http://www.slac.stanford.edu/econf/C980914/papers/ICAP98_eConf.pdf.
- 2439 [43] <http://lhc-machine-outreach.web.cern.ch/lhc-machine-outreach/components/magnets.htm> (2008).
- 2441 [44] S. Chatrchyan et al. (CMS Collaboration), *JINST* **3** (2008) S08004.
- 2442 [45] G.L. Bayatian et al. (CMS Collaboration), *CERN/LHCC 2006-001*, edited by
 2443 D. Acosta (2006).
- 2444 [46] M. Ivova, talk given at the Swiss Ph.D. School on Particle and Astroparticle
 2445 Physics (CHIPP), Monte Verita' (2010).
- 2446 [47] G. Bolla et al., *Nucl. Instr. Meth. Res. A* **461** (2001) 182.
- 2447 [48] https://twiki.cern.ch/twiki/pub/CMSPublic/DPGResultsTRK/_imgf9e0ee48ebca770d7774454532b4b4ee.png (2011).

- 2449 [49] https://twiki.cern.ch/twiki/pub/CMSPublic/DPGResultsTRK/_img7569b7652b3f7c15030a11a4223e631c.png (2011).
- 2450
- 2451 [50] https://twiki.cern.ch/twiki/pub//CMSPublic/DPGResultsTRK/hv11_d1.png (2011).
- 2452
- 2453 [51] https://twiki.cern.ch/twiki/pub/CMSPublic/DPGResultsTRK/_imga571742cbed3a14a9e2581ae95efa54c.gif (2011).
- 2454
- 2455 [52] <https://twiki.cern.ch/twiki/pub//CMSPublic/DPGResultsTRK/StripHitRes2.gif> (2011).
- 2456
- 2457 [53] https://twiki.cern.ch/twiki/pub//CMSPublic/EcalDPGResults/histories2_laser.png (2012).
- 2458
- 2459 [54] https://twiki.cern.ch/twiki/pub//CMSPublic/EcalDPGResults/electronres_eb_inclusive.png (2012).
- 2460
- 2461 [55] https://twiki.cern.ch/twiki/pub//CMSPublic/EcalDPGResults/electronres_ee_inclusive.png (2012).
- 2462
- 2463 [56] <https://twiki.cern.ch/twiki/pub//CMSPublic/EcalDPGResults/seed-time.EEEE.png> (2012).
- 2464
- 2465 [57] N. Akchurin and R. Wigmans, *Rev. Sci. Instrum.* **74** (2003) 2955.
- 2466 [58] CMS Collaboration, *CMS-DP 2010-025* (2010).
- 2467 [59] https://twiki.cern.ch/twiki/pub/CMSPublic/PhysicsResultsMUO/dimuMass_2011Run_1fb_20July2011.pdf (2011).
- 2468
- 2469 [60] S. Chatrchyan et al. (CMS Collaboration), *JHEP* **4** (2012) 33.

- 2470 [61] W.H. Smith, P. Chumney, S. Dasu, F. Di Lodovico, M. Jaworski, J.R. Lackey, and
 2471 P. Robl in *Proceedings of the 7th Workshop on Electronics for LHC Experiments,*
 2472 *Stockholm, 2001*, edited by C. Isabella (CERN, Geneva, 2001), p. 238.
- 2473 [62] R. Brun and F. Rademakers, *Nucl. Inst. Meth. Res.* **A389** (1997) 81. See also
 2474 <http://root.cern.ch/>.
- 2475 [63] J. Guteleber and L. Orsini, *Cluster Comput.* **5** (2002) 55.
- 2476 [64] D. Box, D. Ehnebuske, G. Kakivaya, A. Layman, N. Mendelsohn, H.F.
 2477 Nielsen, S. Thatte, and D. Winer, *W3C Note 08*, <http://www.w3.org/TR/2000/NOTE-SOAP-20000508/> (2000).
- 2479 [65] R. Arcidiacono et al., talk given at the 10th ICAL-EPCS International Conference
 2480 on Accelerator and Large Experiment Physics Control Systems, Geneva (2005).
- 2481 [66] J. Knobloch et al., *CERN-LHCC-2005-024* (2005).
- 2482 [67] R. Brunelière, *Nucl. Instr. Meth. Res.* **A572** (2007) 33.
- 2483 [68] S. Chatrchyan et al. (CMS Collaboration), *JINST* **5** (2010) T03011.
- 2484 [69] CMS Collaboration, *CMS PAS EGM-10-002* (2010).
- 2485 [70] P. Meridiani and C. Seez, *CMS IN-2011/002* (2011).
- 2486 [71] P. Adzic et al. (CMS Electromagnetic Calorimeter Group), *Eur. Phys. J.* **C44S2**
 2487 (2006) 1.
- 2488 [72] P. Adzic et al. (CMS Electromagnetic Calorimeter Group), *JINST* **3** (2008)
 2489 P10007.
- 2490 [73] M. Malberti, *Nuc. Sci. Symposium Conference Record NSS/MIC IEEE* (2009)
 2491 2264.

- 2492 [74] S. Chatrchyan et al. (CMS Collaboration), *JINST* **5** (2010) T03010.
- 2493 [75] R. Paramatti, *J. Phys. Conf. Ser.* **293** (2011) 012045.
- 2494 [76] Y. Yang, http://www.hep.caltech.edu/cms/posters/Pi0Poster_CMSWeekDec2011.pdf (2011).
- 2495 [77] M. Anderson, A. Askew, A.F. Barfuss, D. Evans, F. Ferri, K. Kaadze, Y. Maravin,
2497 P. Meridiani, and C. Seez, *CMS IN-2010/008* (2010).
- 2498 [78] <https://twiki.cern.ch/twiki/bin/view/CMS/ECALEnergyScaleCorrections>.
- 2499 [79] The H $\rightarrow \gamma\gamma$ working group, *CMS AN-2011/426* (2011).
- 2500 [80] M. Cacciari, *LPTHE-P06-04* (2006).
- 2501 [81] M. Cacciari, G.P. Salam, and G. Soyez, *CERN-PH-TH-2011-297* (2011).
- 2502 [82] S. Chatrchyan et al. (CMS Collaboration), *Phys. Rev. Lett.* **106** (2011) 082001.
- 2503 [83] A. Askew, B. Cox, D. Elvira, Y. Gershtein, M. Hildreth, D. Jang, Y.-F. Liu, D.
2504 Mason, D. Morse, U. Nauenberg, M. Paulini, R. Stringer, R. Yohay, and S.L.
2505 Zang, *CMS AN-2011/515* (2011).
- 2506 [84] F. Beaudette, D. Benedetti, P. Janot, and M. Pioppi, *CMS AN-2010/034* (2010).
- 2507 [85] M. Konecki, in Proceedings of the European Physical Society Europhysics Con-
2508 ference on High Energy Physics, Krakow, 2009, Eur. Phys.Soc. Mulhouse (ed.)
2509 (unpublished).
- 2510 [86] W. Adam, R. Früwirth, A. Strandlie, and T. Todorov, *J. Phys.* **G31** No. 9 (2005).
- 2511 [87] CMS Collaboration, *CMS PAS PFT-09-001* (2009).
- 2512 [88] CMS Collaboration, *CMS PAS PFT-10-002* (2010).

- 2513 [89] S. Chatrchyan et al., *JINST* **6** (2011) P11002.
- 2514 [90] CMS Collaboration, *CERN-PH-EP* **2011-102** (2011).
- 2515 [91] M. Cacciari, G.P. Salam, and G. Soyez, *JHEP* **0804** (2008) 063.
- 2516 [92] G. Salam, talk given at CERN Theory Institute: SM and BSM Physics at the
2517 LHC (2009).
- 2518 [93] C.W. Fabjan and R. Wigmans, *Rep. Prog. Phys.* **52** (1989) 1519.
- 2519 [94] <http://www-cdf.fnal.gov/physics/new/top/2004/jets/cdfpublic.html>
2520 (visited on 16 January 2011).
- 2521 [95] S. Chatrchyan et al. (CMS Collaboration), *JINST* **6** (2011) P09001.
- 2522 [96] CMS Collaboration, *CMS PAS JME-09-002* (2009).
- 2523 [97] T. Sjöstrand, S. Mrenna, and P. Z. Skands, *Comput. Phys. Commun.* **178** (2008)
2524 852.
- 2525 [98] S. Chatrchyan et al. (CMS Collaboration), *JINST* **5** (2010) T03014.
- 2526 [99] J. P. Chou, S. Eno, S. Kunori, S. Sharma, and J. Wang, *CMS IN-2010/006*
2527 (2010).
- 2528 [100] Y. Chen, talk given at a meeting of the CMS JetMET group (2011).
- 2529 [101] R. Korzekwa et al., *iEEE Trans. Elec. Dev.* **38** (1991) 745.
- 2530 [102] W. Adam, Th. Speer, B. Mangano, and T.Todorov, *CMS NOTE* **2006/041**
2531 (2006).
- 2532 [103] G. Daskalakis, D. Evans, C.S. Hill, J. Jackson, P. Vanlaer, J. Berryhill, J. Haupt,
2533 D. Futyan, C. Seez, C. Timlin, and D. Wardrope, *CMS AN-2007/019* (2007).

- 2534 [104] F. James and M. Roos, *Comput. Phys. Commun.* **10** (1975) 343.
- 2535 [105] W. Verkerke and D.P. Kirkby, *CHEP-2003-MOLT007* (2003).
- 2536 [106] J.E. Gaiser, Ph.D. thesis, Stanford University (1982).
- 2537 [107] A. Askew, S. Arora, Y. Gershtein, S. Thomas, G. Hanson, R. Stringer, W.
2538 Flanagan, B. Heyburn, U. Nauenberg, S.L. Zang, R. Nandi, D. Elvira, D. Mason,
2539 M. Balazs, B. Cox, B. Francis, A. Ledovskoy, and R. Yohay, *CMS AN* **2010/271**
2540 (2010).
- 2541 [108] Information about all CMS datasets is available from the CMS Data Aggrega-
2542 tion System (DAS), located at the URL <https://cmsweb.cern.ch/das/>.
- 2543 [109] S. Chatrchyan et al., *Phys. Rev. Lett.* **106** (2011) 211802.
- 2544 [110] G. Aad et al. (ATLAS Collaboration), S. Chatrchyan et al. (CMS Collabora-
2545 tion), and LHC Higgs Combination Group, *CMS-NOTE-2011/005* (2011).
- 2546 [111] A.L. Read, in *Proceedings of the First Workshop on Confidence Limits, Geneva,*
2547 *2000*, edited by L. Lyons, Y. Perrin, and F.E. James (CERN, Geneva, 2000), p.
2548 81.
- 2549 [112] G. Cowan, K. Cranmer, E. Gross, and O. Vitells, *Eur. Phys. J.* **C71** (2011)
2550 1554.
- 2551 [113] J. Neyman and E.S. Pearson, *Phil. Trans. R. Soc. Lond.* **A231** (1933) 289.
- 2552 [114] CMS Collaboration, *CMS PAS EWK-11-001* (2011).
- 2553 [115] S. Alekhin et al. (The PDF4LHC Working Group), [arXiv:1101.0536 \[hep-ph\]](https://arxiv.org/abs/1101.0536);
2554 M. Botje et al. (The PDF4LHC Working Group), [arXiv:1101.0538 \[hep-ph\]](https://arxiv.org/abs/1101.0538);
2555 <http://www.hep.ucl.ac.uk/pdf4lhc/index.html>.

- 2556 [116] A.D. Martin, W.J. Stirling, R.S. Thorne, and G. Watt, *Eur. Phys. J.* **C63**
 2557 (2009) 189.
- 2558 [117] P. M. Nadolsky, H.-L. Lai, Q.-H. Cao, J. Huston, J. Pumplin, D. Stump, W.-K.
 2559 Tung, and C.-P. Yuan, *Phys. Rev.* **D78** (2008) 013004.
- 2560 [118] R.D. Ball, L. Del Debbio, S. Forte, A. Guffanti, J.I. Latorre, J. Rojo, and M.
 2561 Ubiali, *Nucl. Phys.* **B838** (2010) 136.
- 2562 [119] J.M. Campbell, J.W. Huston, and W.J. Stirling, *Rep. Prog. Phys.* **70** (2007) 89.
- 2563 [120] A. Djouadi, J.-L. Kneur, G. Moultaka, [arXiv:hep-ph/0211331](#) (2005).
- 2564 [121] M. Muhlleitner, A. Djouadi, Y. Mambrini, *Comput. Phys. Commun.* **168** (2005)
 2565 46.
- 2566 [122] J. Allison et al., *IEEE Trans. Nucl. Sci.* **53(1)** (2006) 270.
- 2567 [123] W. Beenakker, R. Hoepker, M. Spira, [arXiv:hep-ph/9611232](#) (1996).
- 2568 [124] R. Field, talk given at LHC Physics Centre at CERN Minimum Bias and Un-
 2569 derlying Event Working Group Meeting (2011).
- 2570 [125] T. Sjöstrand, S. Mrenna, and P. Z. Skands, *JHEP* **0605** (2006) 026.
- 2571 [126] dummy
- 2572 [127] dummy